

Understanding sol–gel processing: Hierarchical silica monoliths towards applications in chemical reaction engineering

Kumulative Dissertation

zur Erlangung des Doktorgrades
der Naturwissenschaften (Dr. rer. nat.)

dem Fachbereich Chemie
der Philipps-Universität Marburg

vorgelegt von

Richard Kohns, M.Sc.

geboren am 17.10.1992 in Nordhausen

Marburg an der Lahn, 2020

Abgabedatum: _____

Vom Fachbereich Chemie der Philipps-Universität Marburg (Hochschulkennziffer 1180) als
Dissertation angenommen am: _____

Erstgutachter: Prof. Dr. Ulrich Tallarek

Zweitgutachter: Prof. Dr. Dirk Enke

Tag der mündlichen Prüfung: _____

Die vorliegende Arbeit wurde im Zeitraum von Januar 2017 bis April 2020 am Fachbereich
Chemie der Philipps-Universität Marburg unter Leitung von Herrn Prof. Dr. Ulrich Tallarek
angefertigt.

Teile der Dissertation wurden bereits in folgenden wissenschaftlichen Artikeln veröffentlicht:

- [1] R. Kohns, C. P. Haas, A. Hörtzel, C. Splith, D. Enke, U. Tallarek
“Hierarchical silica monoliths with submicron macropores as continuous-flow microreactors for reaction kinetic and mechanistic studies in heterogeneous catalysis”
React. Chem. Eng., **2018**, 3, 353–364.
DOI: 10.1039/c8re00037a

- [2] R. Kohns, N. Anders, D. Enke, U. Tallarek
“Influence of Pore Space Hierarchy on the Efficiency of an Acetylcholinesterase-Based Support for Biosensorics”
Adv. Mater. Interfaces, **2020**, *accepted*.
DOI: 10.1002/admi.202000163

- [3] R. Kohns, R. Meyer, M. Wenzel, J. Matysik, D. Enke, U. Tallarek
“*In situ* synthesis and characterization of sulfonic acid functionalized hierarchical silica monoliths”
J. Sol-Gel Sci. Technol., **2020**, *submitted*.

Danksagung

Mein besonderer Dank gilt Herrn Prof. Dr. Ulrich Tallarek für die Betreuung meiner Promotion und die Möglichkeit, diese interessante und anspruchsvolle Thematik in seinem Arbeitskreis bearbeiten zu dürfen. Des Weiteren möchte ich mich für die zahlreichen fachlichen Diskussionen sowie Ratschläge, das Vertrauen, die wissenschaftliche Freiheit und die jederzeit gewährte Unterstützung bedanken.

Nicht minder möchte ich mich bei Herrn Prof. Dr. Dirk Enke für die Übernahme des Zweitgutachtens, die fachlichen Anregungen sowie für die prägende Zeit im Verlaufe meiner universitären Laufbahn bedanken. Zusätzlich danke ich Herrn Prof. Dr. Norbert Hampp dafür, als drittes Mitglied die Prüfungskommission zu vervollständigen.

Herzlichen Dank möchte ich der gesamten Arbeitsgruppe von Prof. Dr. U. Tallarek für die angenehme Arbeitsatmosphäre, die gemeinschaftlichen Unternehmungen und die konstruktiven Diskussionen aussprechen. Mein besonderer Dank gilt dabei Herrn Christian Haas für die freundschaftliche Integration in die Arbeitsgruppe Tallarek, die wissenschaftlichen Auseinandersetzungen jeglicher Art und die Bearbeitung gemeinsamer Projekte. Für die Unterstützung bei organisatorischen und bürokratischen Fragestellungen bin ich Frau Kirsten Bubenheim sehr dankbar. Allen Mitarbeitern des Arbeitskreises von Prof. Dr. D. Enke danke ich für die gemeinsame Zeit, die wissenschaftlichen Anregungen und die hilfreiche Zusammenarbeit, welche im Rahmen der Kooperation zustande kamen. Meine Dankbarkeit möchte ich auch gegenüber allen Studenten zum Ausdruck bringen, welche ich während meiner Promotionszeit bei ihren Forschungspraktika oder als Tutor betreuen und unterrichten durfte.

Abschließend möchte ich meiner Familie, die mich auf diesem Weg immer unterstützt und getragen hat, meinen tiefsten Dank aussprechen. Nur durch sie konnte ich all das erreichen, was ich bis zu diesem Zeitpunkt angestrebt habe. Diesen Dank richte ich ebenfalls an meine Freunde, welche mein Leben, vor allem außerhalb meiner wissenschaftlichen Tätigkeit, durch die unterschiedlichsten Aktivitäten bereichert und geprägt haben.

Contents

I	Zusammenfassung	1
II	Abstract	5
III	Introduction	9
III.I	Hierarchically structured porous materials	9
III.II	The sol–gel process	14
III.III	Applications for hierarchical silica monoliths	22
Chapter 1	35
1.1	Introduction	37
1.2	Experimental	38
1.2.1	Chemicals.....	38
1.2.2	Support synthesis	39
1.2.3	Surface modification and enzyme immobilization	40
1.2.4	Characterization	41
1.3	Results and discussion	42
1.3.1	Synthesis of porous silica membranes	42
1.3.2	Functionalization of the silica surface	45
1.3.3	Impact of pore space hierarchy on transport efficiency	47
1.4	Conclusions	52
1.5	Supporting Information	53
Chapter 2	72
2.1	Introduction	74
2.2	Experimental	76
2.2.1	Chemicals.....	76
2.2.2	Synthesis of hierarchical silica monoliths.....	76
2.2.3	Characterization of macro- and mesoporosity	77
2.2.4	Cladding and functionalization of sample Urea-7	78
2.2.5	Continuous-flow microreactor and catalytic testing	78
2.3	Results and discussion	79

2.3.1	Synthesis of hierarchical silica monoliths with urea-controlled macro- and mesopore size	79
2.3.2	Role of urea in the formation of macropores and silica skeleton	82
2.3.3	Monolith cladding and column permeability	84
2.3.4	Continuous-flow microreactor for reaction kinetic and mechanistic studies	86
2.4	Conclusions	90
2.5	Supporting Information	91
2.5.1	Estimation of the Thiele modulus for the silica monolithic microreactor	94
Chapter 3	103
3.1	Introduction	105
3.2	Experimental	106
3.2.1	Chemicals	106
3.2.2	Synthesis	107
3.2.3	Characterization	107
3.3	Results and discussion	109
3.3.1	Pore space properties of the functionalized materials	109
3.3.2	Efficiency of the <i>in situ</i> functionalization and extraction procedure	113
3.3.2.1	Elemental analysis and SEM-EDX measurements	113
3.3.2.2	FT-IR spectroscopy and thermogravimetric analysis	116
3.3.2.3	MAS NMR spectroscopy	118
3.3.3	Inverse gas chromatography (IGC)	121
3.4	Conclusions	125
3.5	Supporting Information	126
3.5.1	Determination of the total surface energy	130
IV	Conclusions and perspective.....	139
V	Appendix	148
V.I	Curriculum Vitae	148
V.II	Publikationsverzeichnis	149
V.III	Erklärungen	150

I Zusammenfassung

Hierarchisch strukturierte, poröse Materialien in Form von makro–mesoporösen Silica-Monolithen sind ideale Trägermaterialien, die in einer Vielzahl von Anwendungen wie beispielsweise in chemischen Trennungsvorgängen, heterogener Katalyse, elektrochemischen Prozessen sowie als Wärmeisolationmaterialien und zur CO₂-Adsorption eingesetzt werden. Für diese Anwendungen eignen sie sich hervorragend, da die Makroporen einen schnellen, advektionsdominierten Transport durch das Material gewährleisten und das mesoporöse Skelett eine große externe Oberfläche für den Stofftransport zwischen makro- und mesoporösen Domänen sowie eine große interne Oberfläche für mögliche Funktionalisierungen zur Verfügung stellt. In diesem Zusammenhang befasst sich diese Arbeit mit der Erzeugung von Hierarchien in auf dem Sol–Gel-Verfahren basierenden porösen Silica-Materialien sowie der Bestimmung und Interpretation ihrer Eigenschaften hinsichtlich anwendungsbezogener, reaktionstechnischer Applikationen. Dabei wird der gesamte Herstellungsprozess durch Feinjustierung jedes einzelnen Teilschritts zur Generierung stabiler, hierarchisch strukturierter Sol–Gel-Monolithe modifiziert, um den Anforderungen angepasste, zeiteffektive und, in ihrer Handbarkeit, simple Syntheserouten zu entwickeln. Zudem ist das Verständnis über die chemischen und physikalischen Abläufe in diesen Prozessen unerlässlich. So erlaubt die Kontrolle und Feinjustierung einer Vielzahl an Syntheseparametern eine bewusste Steuerung der Materialeigenschaften. Zu diesem Zweck werden neuartige experimentelle Methoden und Strategien gezeigt, die den laboratorischen Arbeitsaufwand minimieren und zusätzlich die herausragenden Eigenschaften dieser Materialien gezielt herausstellen. Das Potential der hierarchisch strukturierten Sol–Gel-Monolithe wird anhand von Applikationen in der heterogenen Katalyse und Biokatalyse demonstriert. Im Folgenden werden die jeweiligen Konzepte dieser Arbeit zusammengefasst.

Im ersten Kapitel wird das Konzept der Hierarchie untersucht und mit monomodalen Porensystemen verglichen, um die Vorzüge eines hierarchisch strukturierten Porensystems bezüglich dessen Stofftransporteigenschaften aufzuzeigen. Dafür wird ein auf Silica-Membranen aufbauendes Modellsystem vorgestellt, welches die Vor- aber auch Nachteile rein mesoporöser, rein makroporöser und hierarchischer Porenstrukturen offenlegt. Die monolithischen Trägermaterialien werden mit Hilfe des Sol–Gel-Verfahrens synthetisiert, da dieser Prozess durch seine Variabilität in der Erzeugung unterschiedlichster Porenstrukturen und -größen sowie der Möglichkeit post-synthetischer Funktionalisierung der Silica-Oberfläche als sehr geeignet gilt. Zur Herstellung von mechanisch stabilen und vergleichbaren Sol–Gel-Membranen kommt eine neuartige und in ihren Grundzügen simple Trocknungsmethode zum Einsatz. Durch Variation der Zusammensetzungen, Synthesebedingungen und Nachbehandlungen werden eine Vielzahl verschiedenster Silica-Membranen hergestellt, welche sich nur in ihren porösen Eigenschaften unterscheiden. So werden monomodale strukturierte Materialien (rein meso- oder makroporös) mit mittleren Porengrößenbereichen von 20–40 nm sowie 350–3250 nm und hierarchisch strukturierte Materialien aus der

Kombination dieser Porengrößenbereiche angefertigt. Die anschließend durchgeführte post-synthetische Funktionalisierung mit dem bifunktionellen Reagenz 3-Glycidoxypropyl-dimethylmethoxysilan verhilft zu einer kovalenten Immobilisierung des Enzyms Acetylcholinesterase (AChE) unter Ringöffnung der Epoxidgruppe des Silans. In diesem Zusammenhang erfolgt eine Beschränkung auf drei Porensysteme, wobei je eines die rein mesoporöse, die rein makroporöse und die hierarchische Porenstruktur darstellt, damit diese Porensysteme bezüglich ihrer Beladungskapazität an Enzym und ihrer Ansprechzeit verglichen werden können. Aufgrund der porengrößenabhängigen spezifischen Oberfläche unterscheiden sich die Beladungskapazitäten der Porensysteme signifikant, sodass bei makroporösen Membranen eine Beladung von 4.1 µg/Membran und bei monomodal mesoporösen Membranen eine Beladung von 38.5 µg/Membran an AChE vorliegt, wobei das hierarchisch strukturierte Porensystem mit äquivalenten Porengrößenbereichen eine Beladungskapazität von 15.5 µg/Membran aufweist. Über die Ansprechzeit der enzymkatalysierten Substratabbaureaktion von Acetylcholin zu Cholin und Essigsäure werden Reaktionsgeschwindigkeiten bestimmt, mit welcher die Effizienz der einzelnen Porensysteme beschrieben wird und somit Rückschlüsse auf intrinsische Diffusionslimitierungen gezogen werden können. Um die Vergleichbarkeit zu gewährleisten, erfolgen diese Untersuchungen für alle drei Porensysteme bei konstant gleicher Enzymbeladung. Bei einer Beladung von 4.1 µg AChE pro Membran zeigt das rein makroporöse Porensystem einen leichten Vorteil gegenüber dem hierarchisch strukturierten Material, da es die schnellste Reaktion hervorruft, was auf die geringsten Stofftransportlimitierungen zurückzuführen ist. Durch eine Erhöhung der Beladung auf 12.9 µg für die monomodal mesoporösen und die hierarchisch strukturierten Membranen wird deutlich, dass das hierarchische Porensystem mit einer signifikanten Verkürzung der Ansprechzeit gegenüber dem rein mesoporösen Material überlegen ist, da es die Vorteile der beiden monomodalen Systeme, den verbesserten Stofftransport und die höhere Enzymbeladung vereint. Als Fazit zeigt diese Studie systematische Untersuchungen zur Herausstellung der Vorteile eines hierarchisch strukturierten Porensystems, welches sich durch die Kombination aus Transporteffizienz und hoher Beladungskapazität auszeichnet.

Das zweite Kapitel beschäftigt sich mit der Synthese hierarchisch strukturierter Silica-Monolithe, deren Überführung in ein geeignetes Säulensystem und anschließender Funktionalisierung der Trägeroberfläche, um sie so als Flow-Mikroreaktoren zu verwenden. Die Generierung der Hierarchie erfolgt über die polymerinduzierte Phasenseparation, welche einen wichtigen Teilschritt des Sol–Gel-Prozesses darstellt. Die Silicagele werden unter der Verwendung von Harnstoff synthetisiert, um zum einen eine mesoporöse Domäne zu erzeugen und zum anderen das Makroporensystem gezielt zu kontrollieren. Der Einfluss von Harnstoff auf die mittlere Mesoporengröße ist bereits in der Literatur beschrieben und basiert auf der Zersetzung zu Ammoniak und Kohlenstoffdioxid bei erhöhter Temperatur. Durch den somit steigenden pH-Wert erhöht sich die Löslichkeit des Siliciumdioxids, wodurch Auflösungs- und Abscheidungsprozesse dafür sorgen, dass das anfänglich mikroporöse Silica-Skelett aufgeweitet wird und daraus resultierend Mesoporen generiert werden. Eine wissenschaftlich

übliche Herangehensweise ist es, dass Harnstoff bereits zur wässrigen Startlösung hinzugefügt und somit direkt in das Hydrogel eingebracht wird, wodurch anschließend eine homogene Porenaufweitung durch eine hydrothermale Nachbehandlung stattfinden kann. Dabei zeigt sich, dass Harnstoff zusätzlich einen starken Einfluss auf die Makroporengröße und die Skelettdicke des erzeugten Sol–Gel-Monolithen besitzt. Mit steigendem Harnstoffgehalt wird die mittlere Makroporengröße drastisch bis in den Submikrometer-Bereich verringert. Harnstoff beeinflusst aufgrund einer pH-Werterhöhung des Sols, welche bereits vor der signifikanten Zersetzung eintritt und einer Einflussnahme auf dessen Polarität, die zeitlichen Abfolgen der Gelierung und der Phasenseparation. Der Gelierungspunkt tritt somit zu einer früheren Entwicklungsphase der spinodalen Entmischung ein, wodurch ein kleineres Makroporensystem fixiert wird. Die somit synthetisierten Monolithe mit Makroporengrößen im Submikrometer-Bereich sind hervorragend für Untersuchungen intrinsischer Reaktionskinetiken geeignet, da externe und interne Diffusionslimitierungen eliminiert werden und zudem die hydrodynamische Rückvermischung in einem Maße reduziert wird, dass eine ideale Pfropfenströmung erhalten werden kann. Um diese Sol–Gel-Monolithe dafür zugänglich und als Flow-Mikroreaktoren nutzbar zu machen, wird eine Methodik zur Einhausung bzw. Ummantelung vorgestellt, welche Gegendrücken von >100 bar standhält. Mittels einer eigens entwickelten stop-flow-Funktionalisierungsmethode werden Aminopropylgruppen auf die Silica-Oberfläche aufgebracht, womit eine katalytisch aktive Säule generiert wird. Die Erfassung der Reaktionsdaten für die Reaktionskinetik der Knoevenagel-Kondensation zwischen Benzaldehyd und Cyanessigsäureethylester zu *trans*- α -Cyanzimtsäureethylester, welche eine literaturbekannte Testreaktion für basische Katalysatoren darstellt, erfolgt mithilfe zweidimensionaler HPLC-Instrumentation, welche in der ersten Dimension die Einstellung der gewünschten Reaktionsparameter automatisiert und in der zweiten Dimension die vollständige Quantifizierung des Reaktionsergebnisses mit Hilfe online HPLC ermöglicht. Für fünf unterschiedliche Reaktionszeiten bei je sieben verschiedenen Reaktionstemperaturen wird die gesamte Reaktionskinetik der aminokatalysierten Knoevenagel-Kondensation in nur etwa 400 Minuten aufgenommen. Die Reaktionsergebnisse ergeben eine Kinetik pseudo-erster Ordnung, welche in dem zweistufigen Reaktionsmechanismus begründet liegt. Die Reaktionsdaten liefern ein Reaktionsverhalten unter quasi-homogenen Bedingungen, was die gänzliche Eliminierung von Transportlimitierungen attestiert. Resümierend werden in dieser Studie hierarchisch strukturierte Sol–Gel-Monolithe unter der Verwendung von Harnstoff synthetisiert, welcher die gezielte Mesoporen- und Makroporengrößenkontrolle ermöglicht und somit eine katalytische Säule mit hoher aktiver Oberfläche und ohne Transportlimitierungen erzeugt.

Das dritte Kapitel beschreibt eine neue Herangehensweise zur Herstellung hierarchisch strukturierter, Sulfonsäure-modifizierter Silica-Monolithe basierend auf dem Sol–Gel-Prozess, wobei die Funktionalisierung *in situ* – während der Gelierung – in das Porensystem eingebracht wird. Dabei wird sich dem Prinzip der Co-Kondensation bedient, in welchem zusätzlich zum reinen Silica-Präkursor ein Alkoxysilan mit einer Propylthiol-Funktion (3-Mercaptopropyl-

trimethoxysilan, MPTMS), für die Solbildung verwendet wird. Die Synthese solcher organisch-anorganischen Hybridmaterialien ist in der Literatur weit verbreitet, jedoch nicht für hierarchisch strukturierte Sol–Gel-Materialien. Denn wie bereits in Kapitel 1 und 2 wird die Hierarchie über die polymerinduzierte Phasenseparation erzeugt. Das so in das Gel inkorporierte Polymer wird üblicherweise über einen Teilschritt, welcher auch als Kalzinierung bezeichnet wird, bei hohen Temperaturen aus dem Material entfernt, um das reine Silica-Produkt zu erhalten. Durch diesen Prozess verbrennt jegliche Organik, wodurch die ebenfalls eingebrachte Funktionalisierung verloren geht. Aufgrund dessen wird das Polymer in dieser Studie aus dem Material extrahiert, um dem Verlust der kovalent gebundenen Funktionalisierung auf der Trägeroberfläche zu entgehen. Dazu wird ein Extraktionsmittel aus Wasserstoffperoxid und Salpetersäure verwendet, welches gleichzeitig die eingebrachten Thiolgruppen in die gewünschten Sulfonsäurefunktionen überführt, was in einer zeiteffektiven Syntheseroute resultiert. Mittels Variation der Zusammensetzung bezüglich des Polymer- und Funktionalisierungsreagenzgehalts wird die mittlere Makroporengröße kontrolliert, wobei das Funktionalisierungsreagenz einen signifikanten Einfluss auf den Eintritt der Phasenseparation und somit auf die resultierende Makroporengröße nimmt. Ferner findet eine starke Beeinflussung des Aufweitungsprozesses zur Bildung der Mesoporen statt, wodurch sich sehr schmale Mesoporenverteilungen <10 nm ergeben, resultierend in spezifischen Oberflächen von bis zu $576 \text{ m}^2 \text{ g}^{-1}$. Die Untersuchung und Charakterisierung der Effektivität der Extraktion sowie die Generierung einer Sulfonsäure-modifizierten Silica-Oberfläche ist in diesem Zusammenhang unabdingbar, um die vorgestellte Herangehensweise zu evaluieren. So wird mit steigendem Anteil an MPTMS der Schwefelgehalt und somit die Beladung an homogen verteilter Sulfonsäure im monolithischen Hybridmaterial bis auf 1.2 mmol g^{-1} erhöht, ohne dass ein signifikanter Verlust durch die Extraktion auftritt. Zusätzlich kommt es zu einer nahezu vollständigen Entfernung des Polymers. Die kovalente Anbindung der Funktionalisierung und die erfolgreiche Oxidation des Schwefels zur Bildung von Sulfonsäurefunktionen wird anhand Infrarot- sowie ^{13}C und ^{29}Si MAS NMR-Spektroskopie nachgewiesen. Zusätzlich lassen Untersuchungen mittels Inverser Gas Chromatographie einen Schluss über Oberflächenwechselwirkungen und Säurestärke zu. So weisen die funktionalisierten Hybridmonolithe signifikant höhere Oberflächenenergien auf, wobei der spezifische, polare Anteil gegenüber dem dispersiven Anteil prävalent ist. Darüber hinaus zeigt sich, dass diese Materialien an Säurestärke gewinnen, welche durch die eingebrachte Sulfonsäure generiert wird. Zusammenfassend wird eine neuartige und effiziente Syntheseroute zur Herstellung hierarchisch strukturierter Sol–Gel-Monolithe mit homogen verteilter Sulfonsäurefunktionalisierung vorgestellt.

Abschließend lässt sich zusammenfassen, dass diese Arbeit die einzelnen Teilschritte der Präparation hierarchisch strukturierter Silica-Materialien basierend auf den Prinzipien des Sol–Gel-Prozesses untersucht und diese Erkenntnisse in Hinblick auf die vielseitig möglichen Anwendungen diskutiert. Sie trägt somit dazu bei, Silica-Materialien mit hoher Variabilität an die unterschiedlichsten Anforderungen und Problemstellungen anzupassen.

II Abstract

Hierarchically structured, porous materials in the form of macro–mesoporous silica monoliths represent ideal support materials for a variety of applications such as chemical separation, heterogeneous catalysis, thermal insulation, electrochemical processes and CO₂ adsorption. They are well suited for this purpose since the macropores enable fast, advection-dominated transport through the material whilst the mesoporous skeleton provides a large external surface area for mass transfer between the macro- and the mesoporous domains, as well as a large, internal surface area for possible functionalization. In this context, this thesis focuses on the generation of hierarchy in sol–gel based porous silica materials, as well as the determination and interpretation of their properties with respect to applications in reaction technology. For the entire preparation process each individual step is fine-tuned in terms of practicability, time-effectiveness and simplicity to obtain robust and straightforward synthetic routes towards stable, hierarchically structured sol–gel monoliths. The understanding of the chemical and physical processes involved in these steps allows the precise control of the material characteristics. Novel experimental methods and strategies are presented, which minimize the laboratory workload and additionally highlight the superior properties of these materials. The potential of hierarchically structured sol–gel monoliths is demonstrated by applications in heterogeneous catalysis and biocatalysis. In the following, the respective concepts of this thesis are briefly summarized.

Chapter 1 examines the concept of hierarchy itself and highlights the advantages of a hierarchically structured pore system in comparison with monomodal pore systems, especially with regard to its mass transport properties. A model system based on silica membranes is presented, which discloses the advantages and disadvantages of purely mesoporous, purely macroporous and hierarchical pore structures. The monolithic support materials are synthesized using the sol–gel process, as this technique is considered as highly variable in the generation of different pore structures and sizes and it enables post-synthetic functionalization of the silica surface. In order to prepare mechanically stable and comparable sol–gel membranes, a novel and simplified drying method is presented. By varying the synthesis compositions, synthesis conditions and post-synthetic treatments, a variety of silica membranes are produced, which differ only in their porous properties. Monomodal structured materials with mean pore sizes in the range from 20 to 40 nm (mesoporous) and 350 to 3250 nm (macroporous) are produced as well as hierarchically structured materials combining these pore size ranges. All surfaces are functionalized post-synthetically with the bifunctional reagent 3-(glycidoxypropyl)-dimethylmethoxysilane to realize the covalent immobilization of the enzyme acetylcholinesterase (AChE) under ring opening of the epoxy group of the silane. In the following, the three different pore systems are compared in terms of their enzyme loading capacity and their response times. Due to the pore-size-dependent specific surface area, the loading capacities of the representative pore systems differ significantly, resulting in a loading of 4.1 µg of AChE per membrane with a macropore size of 3250 nm and an AChE loading of

38.5 μg per membrane for a mesopore size of 20 nm, whereby the hierarchically structured pore system with equivalent pore size ranges has a loading capacity of 15.5 μg AChE per membrane. The response time of the enzyme-catalyzed substrate degradation reaction of acetylcholine to choline and acetic acid is used to determine the apparent reaction rate, which is used to describe the efficiency of the individual pore structure and thus allows conclusions on intrinsic diffusion limitations. These investigations are conducted for all three pore systems at a constant enzyme loading to ensure comparability. At a loading of 4.1 μg AChE per membrane, the purely macroporous pore system exhibits a slight advantage over the hierarchically structured material, as it causes the fastest reaction, which is due to the lowest mass transfer limitations. By increasing the enzyme loading to 12.9 μg per membrane, it is evident that the hierarchically structured pore system shows a significant reduction of the response time, and thus is superior to the purely mesoporous material, as it combines the advantages of both monomodal systems, the improved mass transport and the higher enzyme loading. In conclusion, this study demonstrates systematic investigations to highlight the advantages of pore space hierarchy, which is characterized by combined functionality and transport efficiency.

Chapter 2 presents the urea-controlled synthesis of hierarchically structured silica monoliths, their transfer into a suitable column system and subsequent functionalization of the support surface in order to use them as flow microreactors. The hierarchy is generated by polymer-induced phase separation, which is an important step in the sol-gel process. The silica gels were synthesized using urea to create a mesoporous domain and to control the macroporous system. The influence of urea on the mean mesopore size is based on the base releasing property of urea by decomposition to ammonia and carbon dioxide under elevated temperature and has already been described in the literature. The resulting raise in pH increases the solubility of silica, whereby dissolution and deposition processes ensure that the initially microporous silica skeleton is expanded, resulting in a mesoporous domain. A common scientific approach is to add urea to the aqueous starting solution for a direct incorporation into the hydrogel to ensure a homogeneous pore expansion in the hydrothermal treatment. However, it is found that urea also has a strong influence on the macropore size and skeleton thickness of the obtained sol-gel monolith. With increasing urea content, the average macropore size is significantly reduced down to the submicron range. Urea influences the time sequences of gelation and phase separation due to an increase in the pH of the sol, which already occurs before substantial decomposition and additionally influences its polarity. Therefore, the gelation point occurs at an earlier stage of spinodal decomposition, which fixes a smaller macropore system. The synthesized monoliths with macropores in the submicron range are well-suited for the investigation of intrinsic reaction kinetics, since external and internal diffusion limitations are eliminated and hydrodynamic backmixing is reduced to a degree that a hydrodynamic plug flow behavior can be reached. For the application as flow microreactor, a novel cladding procedure is presented, which enables seamless housing of the sol-gel monolith in stainless steel tubing to withstand column backpressures >100 bar. By a special stop-flow functionalization method, aminopropyl groups are coated onto the silica surface generating a catalytically active column.

The acquisition of reaction data for the reaction kinetics of the Knoevenagel condensation between benzaldehyde and ethyl cyanoacetate to *trans*- α -ethyl cyanocinnamate, which is a well-known test reaction for basic catalysts, is realized with a two-dimensional HPLC setup. The first dimension automates the adjustment of the desired reaction parameters for the microreactor and the second dimension allows the complete quantification of the reaction data by online HPLC. The entire reaction kinetics of the amino-catalyzed Knoevenagel condensation for five different reaction times at seven different reaction temperatures each is recorded in only about 400 minutes. The reaction data results in a pseudo first order reaction kinetics, which is due to the two-step reaction mechanism. The reaction data reveal a reaction behavior under quasi-homogeneous conditions, which confirms the absence of any transport limitations. In conclusion, hierarchically structured sol-gel monoliths are synthesized using urea as pore size controlling agent to obtain catalytic microreactors with a high active surface area, which allow for the investigation of intrinsic reaction kinetics without transport limitations.

Chapter 3 describes a new approach for the preparation of hierarchically structured, sulfonic acid modified silica monoliths based on the sol-gel process, whereby the functionalization is introduced into the pore system *in situ* during gelation. By using the co-condensation method, an alkoxy silane with a propylthiol function, ((3-mercaptopropyl)trimethoxysilane, MPTMS), is added together with the unfunctionalized silica precursor for sol formation. The synthesis of such organic-inorganic hybrid materials is widely used in the literature, but not for hierarchically structured sol-gel materials, where the hierarchy is generated *via* polymer-induced phase separation. Here, the incorporated polymer is usually removed from the material at high temperatures by an additional step, called calcination, to obtain the pure silica product. This treatment pyrolyzes any organic matter, which would also result in a loss of incorporated functionality. Therefore, this study presents an extraction of the polymer to avoid the loss of the covalently bound functionalization on the support surface, which simultaneously converts the introduced thiol groups into sulfonic acid functions, resulting in a time-efficient synthesis route. For this purpose, an extracting agent consisting of hydrogen peroxide and nitric acid is used. Macropore size control is demonstrated by the variation of polymer and functionalization reagent compositions, whereby the functionalization reagent has a significant influence on the onset of phase separation and consequently on the final macropore size. Furthermore, the widening process to form the mesoporous domain is strongly affected, resulting in very narrow mesopore distributions <10 nm with specific surface areas of up to 576 m² g⁻¹. The efficiency of the extraction procedure and the successful generation of sulfonic acid modified silica is extensively investigated and characterized to evaluate the presented approach. It is shown that, as the amount of MPTMS increases, the sulfur content and thus the loading of homogeneously distributed sulfonic acid groups is increased up to 1.2 mmol g⁻¹ without significant loss due to the extraction. The polymer, however, is removed to a high degree during the extraction process. The covalent binding of the functionalization and the successful oxidation of the sulfur to form sulfonic acid functions is demonstrated by IR as well as ¹³C and ²⁹Si MAS NMR spectroscopy. Moreover, investigations using inverse gas chromatography allow to investigate

surface interactions and acid strength. The functionalized organic-inorganic hybrid monoliths have significantly higher surface energies, with the specific (polar) component being more dominant as the dispersive component. Furthermore, it is shown that these materials gain acid strength, which is generated by the incorporated sulfonic acid groups. In summary, a novel and efficient synthesis route for the preparation of hierarchically structured sol–gel monoliths with homogeneously distributed sulfonic acid functionalization is introduced.

In conclusion, this thesis improves the understanding of the individual steps of the sol–gel process for the preparation of hierarchically structured silica-based materials. These results are presented in the context of different possible applications, since their variability allows them to be adapted to diverse requirements and problems.

III Introduction

The word hierarchy has its origin in the Greek expression *hierarchia* (ἱεραρχία), which can be translated as “rule of a high priest“ from *hieros* (ἱερός) “holy“ and *arche* (ἀρχή) “go first, rule“. A free translation could mean “holy rule“. Pseudo-Dionysius the Areopagite was, as far as it can be retraced, possibly the first person to use this word in relation to the celestial and ecclesiastical hierarchy.¹ He introduced the term for the classification of priestly classes, which determined an order of priestly ministry (inspired by the Bible²), with the word “hierarchia“ standing for the position of the high priest. With that, a word for the pyramidal order of ranks was coined.

Although the word hierarchy goes back to religion, it is omnipresent nowadays. We encounter this phenomenon in our family, at work, in the supermarket, in politics, in military, in science, in nature, and even in ourselves, in the human body. In the end, our entire cosmos is based on hierarchical concepts and structures. Mankind mainly learned from nature how “hierarchy“ originates, operates and, most importantly, can be practiced. Natural hierarchical structures are based on the self-organization of molecular units assembled with other sections that are again self-organized on a different scale. These structures can be found in almost endless quantities. From simple unicellular organisms to plants, wood, sponges, cotton, and bones.³⁻⁶ The natural hierarchical structures exhibit the most diverse functions and properties, but there is one feature many of them have in common: They are porous.

III.I Hierarchically structured porous materials

Nature is one step ahead of us in almost all aspects. We only try to understand the tools nature provides to us and use it for our benefit. One of the most important German authors of the Enlightenment, Christoph Martin Wieland, once said: Who else can we ask than nature, to know how we should live in order to live well? (translation by the author from: „Wen anders als die Natur können wir fragen, um zu wissen, wie wir leben sollen, um wohl zu leben“).⁷ In natural materials, which are considered to be ideally hierarchically structured, growth mechanisms have been observed that only use weak interactions and ambient conditions, a fact that should be exploited in research.⁸ There is no deficiency of natural concepts that can serve as a basis for orientation. The properties and functions that nature offers by means of porous, hierarchical materials are manifold (Figure III.1).

The human bone, for example, is a natural material exhibiting several hierarchical structures.⁹ At the microstructural level are the osteons, which are large hollow fibers composed of concentric lamellae and pores. The lamellae consist of fibers, which in turn contain fibrils. At the nanoscale, the fibers are a composite of the mineral hydroxyapatite and the protein collagen, which is the main reason for their stiffness.⁹⁻¹¹ The multifaceted bamboo is a natural model for hierarchical structures. It consists in its basic features of three fundamental tissues: epidermis, vascular bundles, and parenchyma. The thick epidermis is the shell of the bamboo, while the

vascular bundles are the longitudinal tissues that support the bamboo, and the base parenchyma comprises the rest of the organism. In each vascular bundle, the vessels and phloem transport water and nutrients while they are all surrounded by fibers.^{12,13}

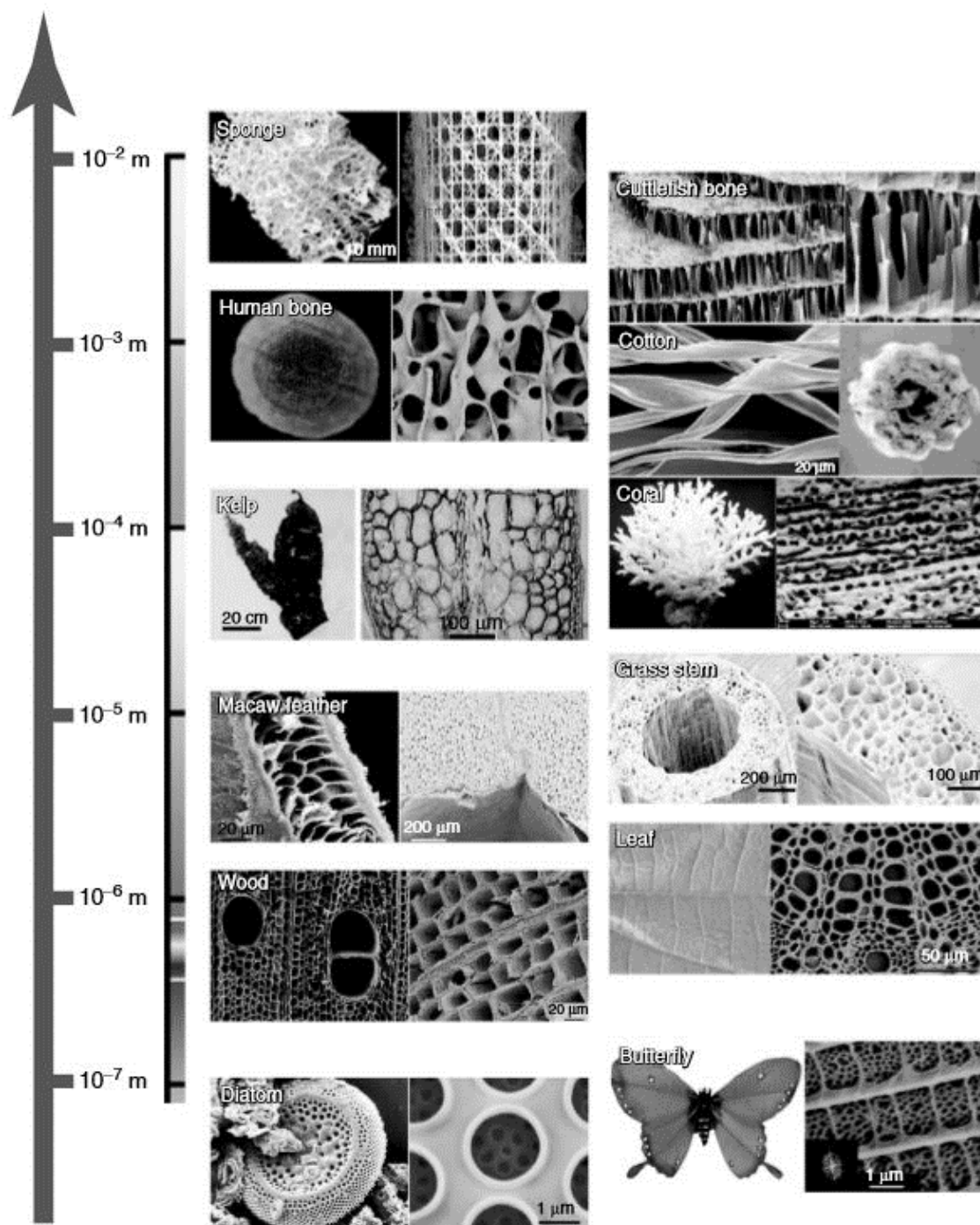


Figure III.1. Optical and scanning electron microscopy images of natural hierarchically structured, porous materials arranged according to their critical dimensions from bottom to top: diatom, butterfly, wood, leaf, macaw feather, blade of grass, kelp, coral, cotton, human bone, cuttlefish bone, and sponge. Reprinted with permission from Ref. 14. Copyright © 2012 Wiley-VCH Verlag GmbH & Co. KGaA.

The principle many scientists from various disciplines adapt to create new synthetic hierarchical materials is therefore based on “learning from nature“. This requires an understanding of the structure of the natural material and its specific functionalities, whereby structural parameters must be studied over several length scales, from the atomic to the macro level. However, it is crucial that this knowledge can also be implemented, and therefore it is necessary to develop new synthesis and manufacturing routes enabling the production of hierarchical materials. It is not self-evident that the architecture produced by nature is immediately transferable to the design of new synthetic materials, because the engineer uses a far more comprehensive toolbox than nature. Elements such as iron, aluminum, nickel, chromium, etc., are rarely biologically available in nature. Although iron is the most common element on earth¹⁵, nature uses rather light elements such as hydrogen, carbon, nitrogen, oxygen, silicon, phosphorus, sulfur, calcium, etc., for its hierarchical materials.³ For this reason, there are many opportunities to create man-made hierarchical materials that imitate the superior structures and characteristics of nature. Thereby the biological material can be utilized as biotemplate (*cf.* Figure III.1), or the properties can be realized by completely new approaches.

The scientific community is continuously interested in the development of new or improvement of established hierarchically structured porous materials, whereby the three-dimensional structures can be assembled with different sized pores, ranging from micropores (<2 nm) to mesopores (2–50 nm) to macropores (>50 nm). In general, the macropores are large enough to offer fast, advection-dominated, mass transfer through a material and the micro- and mesopores, accessible by diffusion, generate a large surface area for adsorption or reaction. The creation of hierarchical structures in porous materials can be realized by several techniques.

Depending on the physical and chemical characteristics of the desired product and the type of hierarchy to be introduced, the manufacturing approach will be specific. In particular, many template methods have been developed to form this type of materials, as they offer effective control of the structural and textural properties. Here, a differentiation is made between endotemplating processes, in which templates are embedded in the solid being formed, and exotemplating processes, in which a rigid porous solid serves as framework for shaping the product. The porous material is obtained by subsequently removing the template.¹⁶ For example, using uniformly dispersed oil droplets and surfactants in an emulsion-templating strategy yields hierarchically structured transition metal oxides and polymers.^{17–20} As template, many different substances or materials can be involved, such as gas bubbles,^{21,22} ice crystals,^{23,24} salts,²⁵ supramolecular aggregates,^{26–29} and, as already mentioned, biomaterials.^{30–33} Colloidal crystals can serve as macrotemplates, also in combination with supramolecular templates.³⁴ The small particles of the colloid, with at least one specific size, aggregate to spheres followed by an infiltration of a precursor and surfactant (or copolymer) micellar solution into the gaps with immediate condensation and crystallization processes. After surfactant removal by extraction or high-temperature calcination a three-dimensional ordered macro–mesoporous material is

obtained. Similar strategies can be adopted to design hierarchical silica materials with MCM-48 or MCM-41 type mesostructures.³⁵⁻³⁷

However, modifications in chemical and physical parameters of a method, *e.g.*, the control of process conditions (synthesis and aging), as well as post-treatments can also lead to hierarchical structures.³⁸⁻⁴⁴ Furthermore, replica techniques have been successfully implemented, in which a porous skeleton (silica) is impregnated with a carbon precursor followed by a carbonization under non-oxidizing conditions, resulting in a hierarchical carbon material. A positive replica on the micrometer scale and a negative replica on the nanometer scale then forms from the silica skeleton.⁴⁵⁻⁴⁷ It was also found that macro-mesoporous materials, especially metal oxides, can be synthesized by an innovative self-assembly procedure without the use of any macrotemplate. The generated structures are composed of parallel macropores with integrated micro/mesopores in the walls. Only a surfactant supports the formation of a large macroporous domain, although this is not always necessary.^{48,49} Also, there are several synthesis strategies for the introduction of hierarchy into porous glass monoliths, including sintering and fusion of alkali borosilicate initial glasses as well as the partial or complete pseudomorphic transformation of porous glasses into zeolites or ordered mesoporous materials.^{50,51} A very efficient and convenient strategy to create hierarchical structures is the phase separation. This method is based on hydrolysis and condensation reactions of inorganic precursors in an aqueous domain of a microphase-separated medium, originating from the self-assembly phase of the template used. The phase separation is induced by a polymer and results in a macroporous pore system with micro- or mesopores in its skeleton.⁵² This technique is mainly used in the so-called sol-gel process to prepare macro-mesoporous materials for many different applications.

An overview of the most relevant preparation strategies with the corresponding possible porous structures and material compositions is given in Table III.1.

Table III.1. Synthesis strategies for various hierarchically structured porous materials. Adapted from Ref. 14. Copyright © 2012 Wiley-VCH Verlag GmbH & Co. KGaA.

Methods	Porous structure	Compositions
<i>Templating via</i>		
Biomaterials ^{30–33}	Meso–macro	Oxides
Colloidal crystals ^{34,37}	Micro–macro, meso–macro	Polymer, Aluminosilicate, Oxides
Gas bubbles ^{21,22}	Meso–macro	Oxides
Small liquid drops (emulsion) ^{17–20}	Meso–macro	Oxides
Small nanoparticles (salts, ice, etc.) ^{23–25}	Meso–macro	Oxides
Supramolecular aggregates (dually micellar) ^{26–29,53–55}	Micro–meso, meso–meso, meso–Macro	Aluminosilicate, Oxides
<i>Process modifications</i>		
Aging and synthesis controlling ^{38,39}	Micro–meso, meso–macro	Aluminosilicate, Oxides
Post-treatment ^{43,44}	Micro–meso, meso–meso, meso–macro	Aluminosilicate, Oxides
<i>Other</i>		
Core-shell methodology ^{40–42}	Micro–meso, meso–macro, Micro@hollow, Meso@hollow, Micro@amorphous, Meso@amorphous	Aluminosilicate, Oxides, Carbon
Phase separation and sol–gel process ⁵²	Micro–macro, meso–macro	Oxides
Pseudomorphic transformation and sintering ^{35,36,50,51}	Meso–macro	Oxides
Selective leaching ^{56,57}	Meso–macro	Oxides
Template-free ^{48,49}	Micro–macro, meso–macro, micro–meso–macro	Aluminosilicate, Oxides, Carbon
Template replication ^{45–47}	Meso–macro	Carbon

III.II The sol–gel process

The sol–gel method has attracted great attention in several decades of scientific research, as it promises the synthesis of materials such as glasses, ceramics, polymers, and organic-inorganic hybrids.^{58–65} In 1846, M. Ebelmann laid the foundations for this interesting methodology when he found that the hydrolysis of tetraethyl orthosilicate led to SiO₂ as a glass-like substance under acidic conditions.⁶⁶ The basis of this process are hydrolysis reactions of (mostly) inorganic precursors in an aqueous medium, which form a sol and result in a gel by condensation reactions among themselves. The resulting gel is micro- or mesoporous. The macroporous domain of the hierarchy is created by the addition of a polymer during the sol formation, inducing a phase separation.⁶⁷ A wide variety of water-soluble polymers such as poly(ethylene oxide) or poly(acrylic acid) can be used for phase separation, controlling the gelation kinetics and thus the macroporous structure.

Phase separation is driven by the repulsive interactions between the hydrophobic polymer-inorganic species oligomer complex and the hydrophilic solvent. The most common and extensively studied system is pure silica, SiO₂, mainly because of its strong tendency to gel formation regardless of the origin of the precursor sol. Silicon precursors such as tetraethyl orthosilicate, tetramethyl orthosilicate or bis(trimethoxysilyl)ethane are widely used to create an amorphous silica gel.⁶⁸ Also modified variants like (3-aminopropyl)trimethoxysilanes or (3-mercaptopropyl)trimethoxysilanes are added to prepare organic-inorganic hybrid gels.^{69,70} Furthermore, the interest in gels based on metal and transition metal oxides has strongly increased, whereby alkoxide precursors of aluminum, zinc, titanium, nickel or cobalt are required.^{71–74} The result of this process is a three-dimensional flexible or rigid network representing the solid phase and is surrounded by the liquid phase in the cavities and interstices. The terms hydrogel, alcogel, or (more rarely) aquagel are employed to describe this state. By removing the solvent *via* suitable drying processes, a monolithic solid is obtained which can be designated as xerogel or aerogel, whereby the designations can be generally distinguished by the material properties and drying conditions.⁵⁹

The approaches of the overall synthesis procedure can differ considerably, depending on the properties that the final product is intended to have, or the application for which it should be used. For the preparation of monolithic, hierarchically structured porous materials, the sol–gel process can be divided into specific sub-steps (Figure III.2):⁵² (1) the sol–gel transition with concurrent, polymer-induced phase separation to form a macro–microporous gel (including hydrolysis and condensation); (2) the widening process by hydrothermal treatment to enlarge micropores to mesopores and ripening the pore structure; (3) solvent exchange and drying, which should yield a dry, mechanically stable monolith; and (4) removal of the organic template (polymer) lurking in the pores.

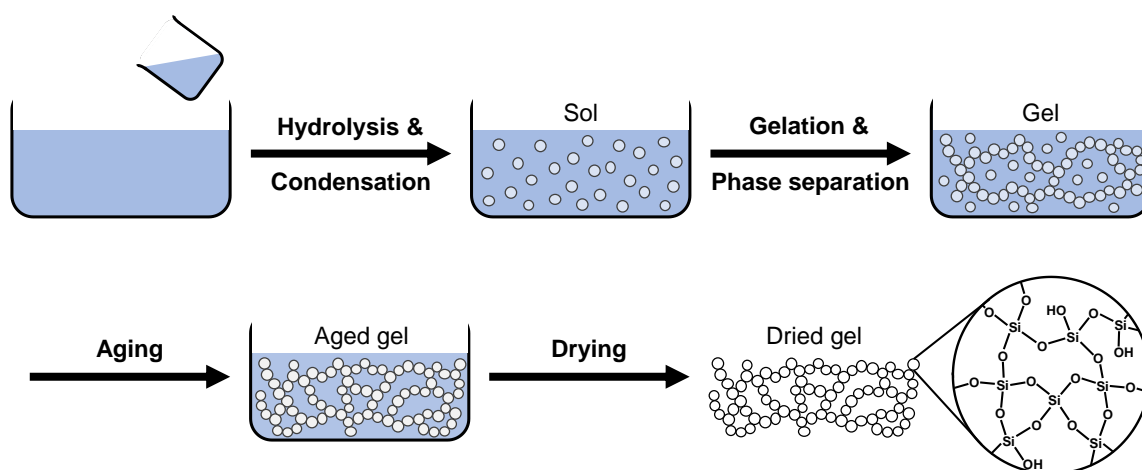


Figure III.2. Schematic illustration of the stepwise sol–gel process from the educt solution to the dried gel exemplified for silica (SiO_2).

In the following, the individual steps of the classical sol–gel process (hydrolysis, condensation, gelation, polymer-induced phase separation, gel aging, and gel drying) are described in more detail, mainly focusing on the silicon dioxide system and with reference to the extensive descriptions from the literature.^{52,59,67,68,74–81}

The first step of the sol–gel process is hydrolysis, in which metalloids or metal precursors are hydrolyzed under acidic, neutral, or basic conditions. The rate of hydrolysis is mainly determined by the pH value, with very slow hydrolysis at $\text{pH} = 7$ and very fast at $\text{pH} = 0$ or $\text{pH} = 14$. Usually metal salts or metal alkoxides are chosen as precursors, whereby the alkoxides allow a much better control of the hydrolysis because they exhibit a high reactivity towards hydrolysis and condensation due to the support of nucleophilic attacks (S_N mechanism) by stabilizing the metal in the highest oxidation state. The precursor has a direct influence on the hydrolysis rate, as longer and more branched alkoxide residues cause slower hydrolysis rates due to the increase in steric hindrance with increasing chain length and the associated shielding of the metal center against nucleophilic attacks. The reaction of hydrolysis proceeds in different nucleophilic substitution reaction mechanisms depending on the pH value. In an acidic medium the oxygen of the alkoxy group is protonated. This results in a charge displacement, forming an alcohol as a good leaving group, while the oxygen of water attacks as nucleophile from behind. A trigonal bipyramid is adopted as transition state, which is caused by the formation of a negatively charged molecule with weakly bound axial ligands (Figure III.3). In basic hydrolysis a hydroxide ion acts as a good nucleophile directly on the silicon and initiates the cleavage of the alcoholate. Under neutral conditions only water serves as a weaker nucleophile in the reaction, which causes a lower hydrolysis rate. The degree of hydrolysis is determined by the available water concentration, which is described by the r -value. The r -value indicates the molar ratio between water and precursor and has to be at least as high as the number of ligands on the metal precursor to allow complete hydrolysis. The higher the r -value, the higher the hydrolysis rate. As the hydrolysis advances, the cross-linking (condensation) of the silica framework starts to become dominating.

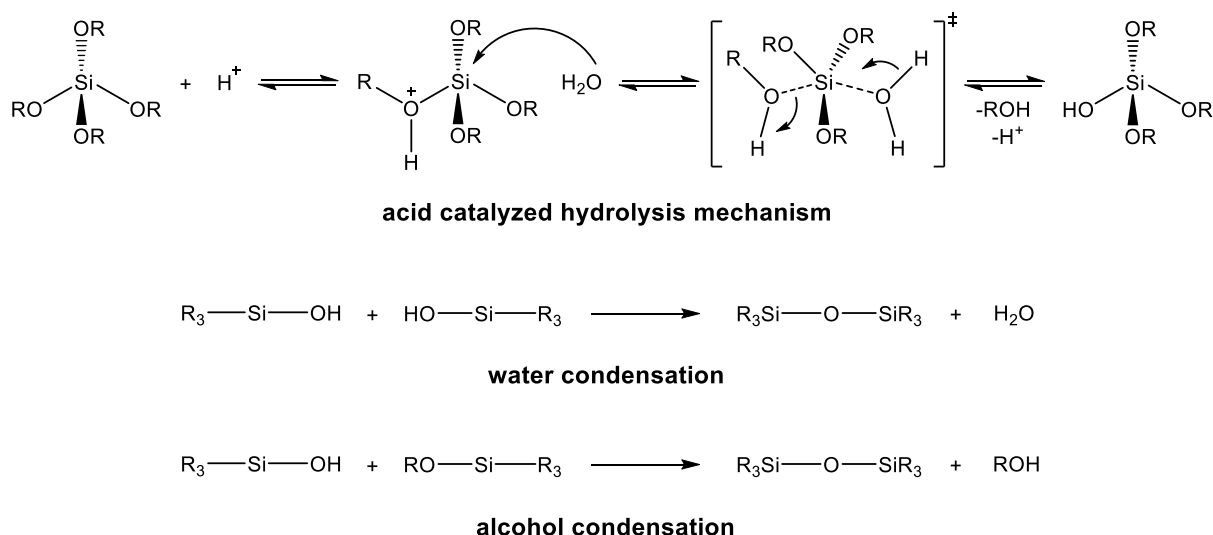


Figure III.3. Acid catalyzed hydrolysis mechanism and condensation reactions exemplified by a silicon alkoxide precursor.

The gelation describes the transformation from a sol to a gel, which is the growth and cross-linking of the hydrolyzed and condensed particles to a three-dimensional macromolecule. Condensation reactions of the hydrolyzed species under elimination of water or the corresponding alcohol (Figure III.3) form dimers, trimers, and finally, oligomers. A colloidal solution with finely distributed solid nanoparticles, the sol, is formed. Interactions between the oligomers among each other and with the solvent result in a floating state which prevents the particles from sedimentation. The cross-linking of the sol particles is affected by hydroxy- or oxo-groups present on the surface, which connect themselves by condensation reactions (likewise olation and oxolation). The sol particles aggregate to short chains and with increasing chain length further particles are accumulated. In this way, three-dimensional networks are created. Still unbound sol particles attach themselves to this network forming microgel regions, which are known as gel phases. Each gel phase grows by further accumulation of sol particles from the surrounding liquid phase. Finally, all gel phases connect to create a continuous network. The moment at which the last bond is formed is called gel point, at which the viscosity rises abruptly and generates the rigid gel. During this process, particle growth is significantly influenced by the pH value, since the condensation reactions are very slow in the weakly acidic and strongly basic range. Thus, the condensation reaction is the rate limiting step in a strongly acidic medium. Under these conditions, particle growth follows the “reaction-limited cluster aggregation”, in which network-like gels are formed, due to the preferred condensation at terminal silanol groups by electronic impulses. Raising the pH value increases the nucleophilicity due to the deprotonation of the silanol groups. At this point, hydrolysis is the rate limiting step. Condensation is now favored at central silicon atoms of the oligomers resulting in the formation of individual larger particles. Oligomer growth is promoted by the condensation of hydrolyzed monomers and is designated as “reaction-limited monomer cluster growth”. This allows the oligomers to react more easily and form larger particles.

After reaching the gel point, structural changes can still occur as the gel is still in contact with the liquid phase. In general, any change in the gel caused by liquid inside the pores can be considered as gel aging. A differentiation is established between polycondensation, syneresis and, Ostwald ripening or coarsening. Again, the pH has a considerable influence on the effect of these processes, since they are favored by the increase in the solubility of SiO_2 in the basic medium. Polycondensation describes the further cross-linking of reactive hydroxyl groups, which are located on the gel surface. These reactions enhance the connectivity of the network, *i.e.*, it is stiffened and strengthened, increasing its mechanical stability. Syneresis refers to the shrinkage of the gel network combined with a simultaneous displacement of liquid out of the pores due to polycondensation reactions. It is based on the reaction of two hydroxyl groups to form an oxo-group, which is called siloxane bond in the case of silicon. Therefore, two different cases are distinguished. Firstly, when two adjacent hydroxyl groups on the surface react (Figure III.4a) and secondly when two flexible gel chains come so close that they react irreversibly with each other (Figure III.4b). In both cases, the network shrinks, because two hydroxyl groups occupy more space than one siloxane bond. The second effect is more pronounced, because the reaction of the flexible chains with each other reduces their flexibility and strengthens the network. This process continues as long as chains are sufficiently flexible. Ostwald ripening is based on the solubility of metal oxides depending on the radius of curvature of the surface. Generally, the solubility of convex surfaces (positive radii of curvature) is higher compared to concave ones (negative radii of curvature). Thus, the material is dissolved at convex locations and is deposited at concave surfaces (Figure III.4c). This process enlarges the contact area between the individual aggregated particles for the gel network. Considering the whole system, an increase in the mean pore size and consequently a decrease in the specific surface area can be observed. In addition, due to the growth of the contact area between the particles, a further stiffening of the gel network occurs.

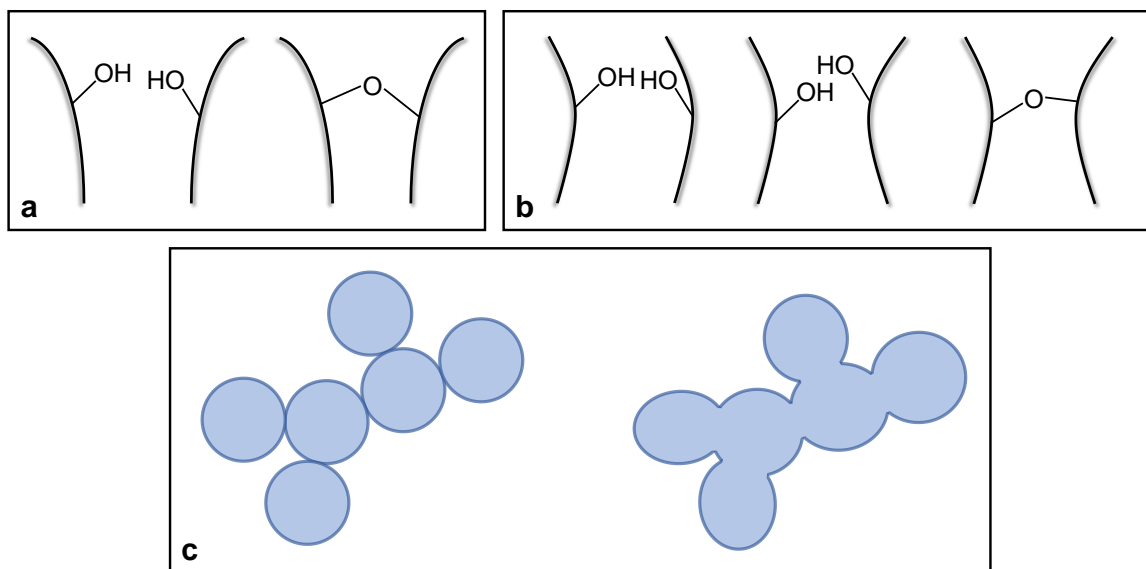


Figure III.4. Schematic representation of the aging processes to stiffen and coarsen the gel network: polycondensation and syneresis (a,b) and Ostwald ripening (c).

Due to the pH dependence, these processes can be adjusted to control the structural and textural properties of the material. For this purpose, a separate process step is introduced after gelation, in which the pH is set to a basic level to stiffen the silica skeleton and widen the micropores (or even very small mesopores) to mesopores. The basic atmosphere accelerates these processes through the increased solubility of SiO₂.⁸² Specific mesopore sizes can be adjusted, depending on the concentration of OH⁻ ions and the duration of the aging process. The longer the process takes and the higher the pH value, the larger the mesopores become. However, if the conditions are too harsh, the gel can dissolve completely with the loss of a stable network. These processes can be further enhanced by increasing the temperature, hence hydrothermal widening processes are often applied. The pH change can be achieved by solvent exchange or by basic precursors such as urea, which are already present in the liquid phase during sol formation and decompose to basic substances at elevated temperature. Aging has a decisive influence on the stability of the gel network and on the mesopore size. The macropore size, in contrast, is only weakly influenced by the hydrothermal treatment (depending on the conditions).

The pore widening process can become of major importance for the last step of the synthesis, the drying. Drying probably represents the most crucial step for the preparation of stable, crack-free, monolithic materials. During this process, strong capillary forces can lead to cracks in the gel body, if the gel is unstable, or through unsuitable drying methods. Furthermore, the removal of the solvent causes a volumetric reduction of the gel, the shrinkage, which creates tensions in the three-dimensional network and can thus initiate crack formation. Drying can only occur if the vapor pressure of the liquid p_v is lower than the equilibrium vapor pressure p_0 . Using the Gibbs–Thompson equation (III.1) with the ideal gas constant R , the temperature T , and V_m , the molar volume of the gas, the capillary tension P can be expressed as a function of the vapor pressure p_v of the liquid:⁸³

$$P = -\frac{RT}{V_m} \ln \frac{p_v}{p_0} \quad (\text{III.1})$$

The drying process can generally be divided into three steps. In the first step the liquid surrounding the gel body evaporates. If only a thin film of liquid remains on the outer surface, the second step, meniscus formation at the pore openings with radius r_m occurs, which results from the surface tension γ of the pore liquid. In the last step, the liquid evaporates from the pores, causing the meniscus to drop. A very thin film of liquid with thickness δ_f remains on the pore walls above the meniscus. The thickness of this liquid film decreases as the meniscus falls to the point where all the liquid is removed from the pores. Such a meniscus is comparable to the formation of a spherical drop of water on a surface. The curved surface of this droplet causes capillary stress. This capillary tension corresponds to a negative pressure and can be described in a generalized way according to the Young–Laplace equation (III.2), with γ as the surface tension of the liquid:

$$P = \frac{2\gamma}{r} \quad (\text{III.2})$$

The spherical radius r is equivalent to r_m and thus corresponds to the pore radius r_p . The maximum possible capillary stress P_m can be described by Equation (III.3):

$$P_m = \frac{2\gamma\cos\theta}{r_p} \quad (\text{III.3})$$

This derivation demonstrates that the capillary tension during drying can be influenced by the parameters r_p , γ , T , V_m , and p_v . For crack-free drying, the stress should be as low as possible so that an increase in vapor pressure p_v , pore radius r_p or temperature T reduces the capillary stress P , as well as a reduction of the surface tension of the pore liquid γ .^{83–85}

A variety of drying methods are available for the preparation of crack-free monoliths. A conventional drying method is supercritical drying, in which the gel shape is almost completely preserved. Here, either the pore fluid itself is converted to the supercritical state or it is displaced from the pore system by a supercritical fluid like CO_2 .^{86–88} By using supercritical media, the surface tension of the pore fluid is eliminated to ensure that no force is exerted to the pore network. Supercritically dried gels are known as aerogels and are characterized by their stability and shape preservation without crack formation. Another type is subcritical drying, which can be performed in several ways to produce monolithic xerogels. One possibility is single or double solvent exchange.^{62,89} Here, the aqueous pore liquid of the synthesized hydrogel/alcogel is replaced by ethanol or propanol. Subsequently, a second solvent exchange with, *e.g.*, diethyl ether, *n*-heptane, *n*-hexane or *n*-pentane can follow. Finally, the gel is dried in a vessel with a small puncture at room temperature and atmospheric pressure. If only the first solvent exchange is performed, drying is conducted at slightly elevated temperature.

After drying, the polymer, which was necessary for the polymer-induced phase separation, is usually removed in a separate step to preserve the pure inorganic framework. This is commonly realized by combustion (calcination) at high temperatures (500–650 °C), whereby the organic matter is first pyrolyzed to elemental carbon and then oxidized to CO_2 . The texture is not affected by this procedure. Alternatively, the polymer can be extracted with suitable solvents, whereas a slight influence on the texture cannot be excluded.

The implementation of the macroporous domain in hierarchically structured sol–gel materials is realized by polymer-induced phase separation. By adding a polymer to the starting solution, an additional phase separation is integrated into the process. Different polymers can be used for this purpose, whereas the most common is poly(ethylene oxide). This process defines the final structure of the gel and depends on the precise interplay between gelation and phase separation. If phase separation is too slow (or gelation too fast), a structure is frozen without the formation of transport pores. In contrast, if phase separation is too far evolved, particulate aggregates are generated instead of a three-dimensional network, often ending up in a mechanical labile gel. Regulating the reaction conditions and the resulting influence on both the gelation and phase separation allows to control the gel structure and the respective macroporous domain within a specific range.

The miscibility of the reaction mixture depends on both temperature and chemical composition. The change of the free mixing enthalpy ΔG can be described thermodynamically using the Gibbs–Helmholtz equation

$$\Delta G = \Delta H - T\Delta S \quad (\text{III.4})$$

where ΔH denotes the change of the enthalpy of mixing, T is the temperature and ΔS the change of the entropy of mixing. This can be expressed in more detail by using the Flory–Huggins equation for the description of thermodynamic polymer solutions

$$\Delta G = RT \left[\frac{\phi_1}{P_1} \ln \phi_1 + \frac{\phi_2}{P_2} \ln \phi_2 + \chi_{12} \phi_1 \phi_2 \right] \quad (\text{III.5})$$

where ϕ_i denotes the volume fractions, P_i the degrees of polymerization, and χ is the Flory–Huggins interaction parameter.⁹⁰ The first two summands in the brackets represent the entropic part and the last the enthalpic part. If $\Delta G < 0$, the system is present as a homogeneous mixture. Consequently, ΔG must become positive to initiate phase separation. This is achieved by reducing the temperature in the system by physical cooling. As can be seen in Equation (III.4), the decrease in temperature causes an increase of ΔG , *i.e.*, the system of the mixture becomes more unstable. When the temperature decreases to the extent that ΔG turns positive, the thermodynamic driving force for phase separation is reached and the homogeneous mixture separates. Polymer-induced phase separation is not caused by a reduction in temperature but by a polymerization reaction, *i.e.*, a composition change. An increase of the enthalpy of mixing and/or a decrease of the entropy of mixing can therefore be designated as the chemical cooling (Figure III.5). A proceeding gelation of the hydrolyzed silica aggregates results in an increase of the polymerization degrees P_i (Equation (III.5)), which corresponds to a reduction of the entropy. The solubility is further reduced as silica polymerization progresses and the system begins the phase separation. As silicate particles grow, it becomes energetically more favorable for the polymer (poly(ethylene oxide)) to exchange its hydrate shell for a silica shell. The polymer interacts with the silica surface (hydrogen bonds) as the driving force reduces the solubility in the aqueous phase, because of an enthalpy gain. Due to the coordination of the polymer on the polar silica surface, the hydrophobic backbone ($-\text{CH}_2-\text{CH}_2-$) is directed to the solvent and the phases separate. In addition, the polarity decreases as more and more hydroxyl groups are connected to form siloxane bonds. Due to the repulsive interactions between hydrophobic and hydrophilic phase, spontaneous separation into two phases occurs. There is no direct distinction between the driving forces that dominate in phase separation. Nevertheless, it is distinguished between entropic and enthalpic driven systems. This classification merely means that in the respective cases one of these driving forces clearly predominates. The reaction conditions can be used to set the gelation point in the zone of phase separation. From the gel point onwards, the state seems to be "frozen" and thus the gel consisting of metal oxide/polymer phase and solvent phase (alcohol and water). This can be achieved *via* the polymer composition, the gelation temperature or chemicals that influence the polarity.

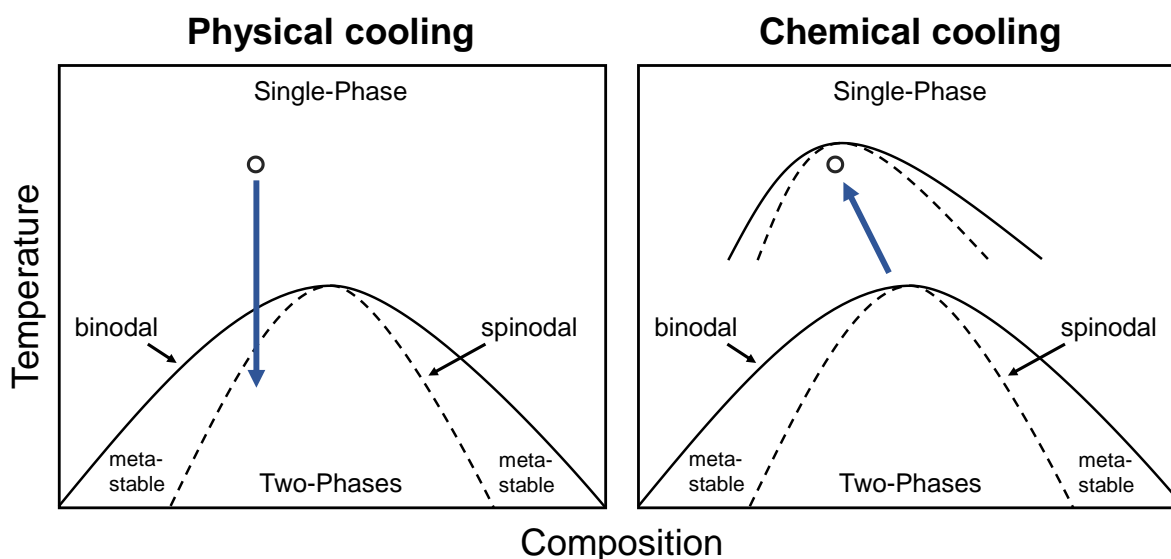


Figure III.5. Comparison between physical and chemical cooling according to Nakanishi.⁵²

As already mentioned, the phase separation determines the shape of the porous structure. If the phase separation is in accordance with the gelation, a fixed pore network is formed, which can differ in design. Depending on the decomposition mechanism, isolated pores, particulate aggregates, interconnected structures, spherodized structures, and combinations of these can be formed. Dependent on the desired application the different structures can have advantages or disadvantages. However, the interconnected pore system is the most studied and implemented system among them. These structures can be described as sponge-like and the relation to nature becomes obvious. These structures can be conserved *via* the state of spinodal decomposition. In a two-phase system there are three states of mixing (Figure III.5). Above the binodal curve is a homogeneous phase. Between the binodal and the spinodal is a metastable state in which a phase transition would consume energy. Below the spinodal, the phase transition would be spontaneous (unstable state), *i.e.*, in this region the components of the system are no longer soluble in each other and phase separation into two phases occurs spontaneously. If at this point the system is stabilized by gelation, the interconnected pore system is formed. If an early stage of spinodal decomposition is fixed, finer structures and smaller macropores are generated. In a very late stage of spinodal decomposition, spherodized structures are obtained. In contrast, the nucleation and growth mechanism (metastable range) forms particulate aggregates or isolated pores. In the interface region from the metastable to the unstable area, particulate interconnected structures are generated. The macropore size of the interconnected pores can be influenced directly by the polymer content. In enthalpy driven systems, such as those with poly(ethylene oxide) or poly(acrylamide), larger amounts of the polymer create smaller macropores and vice versa. At higher concentrations, an earlier stage of spinodal decomposition is frozen, resulting in smaller pores, because the onset of phase separation is more retarded compared to the onset of the sol–gel transition. In entropic driven systems (*e.g.*, poly(acrylic acid) or poly(sodium-4-styrene sulfonate)) it is reversed. A higher polymer concentration leads to larger mean pore diameters of the macropores.

Overall, the sol–gel process is extremely sensitive to parameter changes, so that even slight modifications regarding, *e.g.*, the polarity or pH in the sol solutions, slightest mass differences, temperature variations, pressure changes, and contaminations affect the properties of the resulting monoliths. Therefore, it is necessary to perform the preparative work as uniformly as possible in order to achieve reproducible results. An understanding of the chemical and physical processes and fundamentals of this technique is essential for those who want to produce and use hierarchically structured sol–gel materials, as well as those who want to develop new or improve existing methods. Tailoring and fine-tuning textural, structural, and chemical features require insight into the individual steps in order to modify and adapt them for the requirements of the specific challenge or application.

III.III Applications for hierarchical silica monoliths

Monolithic silica supports are characterized by a continuous three-dimensional structure, *i.e.*, a single body of porous material, which offers direct access to the active surface sites specifically designed and tailored for a variety of applications. Hierarchically structured porous silica monoliths are widely used for chemical separation, thermal insulation, biomedical screening, electrochemical processes, CO₂ adsorption and heterogeneous catalysis, as well as for supercapacitors and sensors.^{62,91–102} For example, hierarchically structured dielectric silica with embedded nanostructured germanium based on the marine diatom *Pinnularia* sp. is expected to have great potential for optoelectronic applications such as semiconductor capacitors.¹⁰³ Furthermore, photochemical bioreactors based on the immobilization of biological species in hierarchically structured porous and transparent SiO₂, designed for the conversion of sunlight to chemical energy *via* photosynthesis, are attracting much attention.^{14,104} In addition, organo-functionalized, hierarchically porous silica monoliths with diglycolamide groups prepared by the sol–gel process have demonstrated excellent performance for the separation and recovery of Th(IV) from mineral leachates.¹⁰⁵

Macro–mesoporous silica monoliths, in particular, are ideal support structures in most of these applications, because the macropores enable fast, advection-dominated transport through the material and the mesoporous skeleton provides a large external surface (thus, a large contact area) for efficient mass transfer between macroporous and mesoporous domains, as well as a large internal surface available for functionalization.¹⁰⁶ Due to their silanol groups, the surface of the silica monoliths can be easily modified, *e.g.*, with organosilanes or inorganic precursors. In addition, silica monoliths are also characterized by more homogeneous structural features (distribution of pore size and skeleton thickness) than alternative bimodal support structures like packed beds of mesoporous particles (which show constrictions due to the cusp regions near the contact points between the particles), which in turn improves transport and overall performance.¹⁰⁷ Due to their characteristics like high porosity, high pore interconnectivity, low bulk density, large surface area, and high mechanical and thermal stability, as well as high

resistance to most solvents, silica monoliths can be easily approached with different functionalization strategies, as required in order to gain functionality.^{108,109}

Macro–mesoporous silica monoliths are particularly suited for high-performance liquid chromatography (HPLC) and solid–liquid heterogeneous catalysis, because the interskeleton macropores ensure fast pressure-driven flow through the material and the intraskeleton mesopores, which are only accessible by diffusion, generate a high surface area for adsorption or reaction.¹¹⁰ Furthermore, they enable a wide range of textural properties and functionalities. The main reason for using these monoliths, *e.g.*, as continuous-flow microreactors is the significant reduction of pressure drops and that they offer more degrees of freedom in their hierarchical design compared to (particulate) packed-bed reactors.¹¹¹ A bimodal pore structure with flow-through macropores ($\sim 1\ \mu\text{m}$) and a mesoporous skeleton enables mechanically stable beds with a high external porosity, resulting in hydraulic permeabilities (flow resistance) comparable to those of columns packed with particles of about 5–6 μm in size in the porosity range typical for mechanically stable particle packings (external porosity $\approx 0.36\text{--}0.42$).^{112,113} The high permeability allows for short analysis times, fulfilling the requirements of high-throughput screening applications.

However, the silica monoliths in continuous-flow applications combine three main advantages. They provide a large specific surface area (A_{spec}) and, thus, a high loading capacity for reaction and/or adsorption. They are characterized by short diffusion lengths (L_{diff}) in spatial domains where the transport is diffusion-limited and reaction and/or adsorption occurs. And finally, the hydraulic permeability of the monoliths is defined by their flow-through channel size (L_{flow}).¹⁰⁶ L_{diff} describes the diffusive transport in the pore space offering the active surface. L_{flow} represents the hydrodynamic transport through the monolith as well as the lateral diffusion from the pore center to the pore walls, where the reactants interact with the active surface. Due to the independent adjustment of L_{diff} and L_{flow} , short diffusion lengths can be combined with flow-through channels allowing minimal pressure drops and well-defined residence times.

Through the sol–gel process, all three dimensions (L_{flow} , L_{diff} , A_{spec}) can be precisely adjusted through control of the synthesis parameters, which makes this process ideally suited to match structural features to various requirements from targeted applications. Macropore size, skeleton thickness, and macroporosity can be tailor-made to reduce backmixing, and thus enhance heat and mass transfer to achieve both highly efficient and selective catalysis in short-contact-time reactors. Especially the homogeneous macroporous domain in such continuous flow reactors enables the separate optimization of transport properties, hydrodynamics, and intrinsic reaction kinetics.

In the literature such silica monoliths have been tested as flow-through microreactors for the synthesis of fine chemicals. The Knoevenagel condensation between benzaldehyde and ethyl cyanoacetate (amino functionalization), and the transesterification of triacetine by methanol (sulfonic acid functionalization) were investigated with modified silica monoliths.⁴⁷ It was

demonstrated that continuous flow systems realize significantly higher productivities than packed-bed reactors and especially compared to batch experiments. However, the housing and the implementation of a column design is challenging to operate with monoliths in flow experiments. Since a porous silica rod shrinks during polycondensation, it cannot be gelled directly into a tube as it would not stick to the tube wall. The resulting column would be useless if the mobile phase could not be forced to flow through the pores. Cladding options, like wrapping the rods in thermoshrinking poly(tetrafluoroethylene) (PTFE) and encapsulating the wrapped rods in tubes made of PTFE or poly(arylether ether ketone) (PEEK), or combining these methods with polymer resins are widely reported in the literature.^{47,91,114–116} Unfortunately, these materials do not permit all possible operating conditions in terms of resistance to pressure and solvents. In this respect, stainless steel could be well suited to withstand the challenging conditions in HPLC experiments.

References

- (1) A. van Hove, *The Catholic Encyclopedia*, Robert Appleton Company, New York, NY, **1910**.
- (2) 1Chr 24, 1–19, *Einheitsübersetzung der Heiligen Schrift*, Stuttgart, **2016**.
- (3) P. Fratzl, R. Weinkamer, Nature's hierarchical materials. *Prog. Mater. Sci.*, **2007**, *52*, 1263–1334.
DOI: 10.1016/j.pmatsci.2007.06.001.
- (4) R. J. Thomas, Wood: Structure and chemical composition. *ACS Symp. Ser.*, **1977**, *43*, 1–23.
DOI: 10.1021/bk-1977-0043.ch001.
- (5) K. E. Easterling, R. Harrysson, L. J. Gibson, M. F. Ashby, On the mechanics of balsa and other woods. *Proc. Royal Soc. A*, **1982**, *383*, 31–41.
DOI: 10.1098/rspa.1982.0118.
- (6) D. Vashishth, Hierarchy of bone microdamage at multiple length scales. *Int. J. Fatigue*, **2007**, *29*, 1024–1033.
DOI: 10.1016/j.ijfatigue.2006.09.010.
- (7) C. M. Wieland, *Geschichte des Agathon*, Philipp Reclam jun. Verlag GmbH & Co., Stuttgart, **1979** (first published 1766).
- (8) J. Aizenberg, P. Fratzl, Biological and biomimetic materials, *Adv. Mater.*, **2009**, *21*, 387–388.
DOI: 10.1002/adma.200803699.
- (9) N. M. Hancox, *Biology of Bones*, Cambridge University Press, London, Great Britain, **1972**.
- (10) P. Frasca, R. A. Harper, J. L. Katz, Isolation of single osteons and osteon lamellae. *Acta Anat.*, **1976**, *95*, 122–129.
DOI: 10.1159/000144608.

-
- (11) J. L. Katz, Hard tissue as a composite material – I. Bounds on the elastic behavior. *J. Biomech.*, **1971**, *4*, 455–473.
DOI: 10.1016/0021-9290(71)90064-9.
- (12) T. Y. Lo, H. Z. Cui, H. C. Leung, The effect of fiber density on strength capacity of bamboo. *Mater. Lett.*, **2004**, *58*, 2295–2598.
DOI: 10.1016/j.matlet.2004.03.029.
- (13) M. K. Habibi, Y. Lu, Crack propagation in bamboo’s hierarchical cellular structure. *Sci. Rep.*, **2014**, *4*, 5598.
DOI: 10.1038/srep05598.
- (14) B.-L. Su, C. Sanchez, X.-Y. Yang, Hierarchically Structured Porous Materials: From Nanoscience to Catalysis, Separation, Optics, Energy, and Life Science, Wiley-VCH, Weinheim, Germany, **2012**.
- (15) U. von Rauchhaupt, *Die Ordnung der Stoffe*, S. Fischer Verlag, Frankfurt am Main, Deutschland, **2009**.
- (16) F. Schüth, Endo- and Exotemplating to create high-surface-area inorganic materials. *Angew. Chem. Int. Ed.*, **2003**, *42*, 3604–3622.
DOI: 10.1002/ange.200300593.
- (17) T. Sen, G. J. T. Tiddy, J. L. Casci, M. W. Anderson, Macro-cellular silica foams: synthesis during the natural creaming process of an oil-in-water emulsion. *Chem. Commun.*, **2003**, *9*, 2182–2183.
DOI: 10.1039/B303349J.
- (18) F. Carn, A. Colin, M.-F. Achard, H. Deleuze, E. Sellier, M. Birot, R. Backov, Inorganic monoliths hierarchically textured *via* concentrated direct emulsion and micellar templates. *J. Mater. Chem.*, **2004**, *14*, 1370–1376.
DOI: 10.1039/B400984C.
- (19) H. Zhang, A. I. Cooper, Synthesis and applications of emulsion-templated porous materials. *Soft Matter*, **2005**, *1*, 107–113.
DOI: 10.1039/B502551F.
- (20) T. Zhang, R. A. Sanguramath, S. Israel, M. S. Silverstein, Emulsion templating: Porous polymers and beyond. *Macromolecules*, **2019**, *52*, 5445–5479.
DOI: 10.1021/acs.macromol.8b02576.
- (21) K. Suzuki, K. Ikari, H. Imai, Synthesis of mesoporous silica foams with hierarchical trimodal pore structures. *J. Mater. Chem.*, **2003**, *13*, 1812–1816.
DOI: 10.1039/B302466K.
- (22) F. Carn, A. Colin, M.-F. Achard, H. Deleuze, C. Sanchez, R. Backov, Anatase and rutile TiO₂ macrocellular foams: Air–liquid foaming sol–gel process towards controlling cell sizes, morphologies, and topologies. *Adv. Mater.*, **2005**, *17*, 62–66.
DOI: 10.1002/adma.200401080.
- (23) H. Nishihara, S. R. Mukai, D. Yamashita, H. Tamon, Ordered macroporous silica ice templating. *Chem. Mater.*, **2005**, *17*, 683–689.
DOI: 10.1021/cm048725f.

-
- (24) S. Deville, Ice-templating, freeze casting: Beyond materials processing. *J. Mater. Res.*, **2013**, 28, 2202–2219.
DOI: 10.1557/jmr.2013.105.
- (25) A.-H. Lu, W.-C. Li, W. Schmidt, F. Schüth, Fabrication of hierarchically structured carbon monoliths via self-binding and salt templating. *Microporous Mesoporous Mater.*, **2006**, 95, 187–192.
DOI: 10.1016/j.micromeso.2006.05.024.
- (26) K. W. Tan, U. Wiesner, Block copolymer self-assembly directed hierarchically structured materials from nonequilibrium transient laser heating. *Macromolecules*, **2019**, 52, 395–409.
DOI: 10.1021/acs.macromol.8b01766.
- (27) W. Shang, H. Du, Y. u, J. Xu, F. Ran, Hierarchical porous nanofibers of carbon@nickel oxide nanoparticles derived from polymer/block copolymer system. *Chin. Chem. Lett.*, **2019**.
DOI: 10.1016/j.cclet.2019.10.017.
- (28) A. Ianiro, M. Chi, M. M. R. M. Hendrix, A. V. Koç, E. D. Eren, M. Sztucki, A. V. Petukhov, G. de With, A. C. C. Esteves, R. Tuinier, Block copolymer hierarchical structures from the interplay of multiple assembly pathway. *Polym. Chem.*, **2020**, 11, 2305–2311.
DOI: 10.1039/D0PY00081G.
- (29) B. Reinhardt, J. Herwig, S. Rannabauer, M. Scheffler, D. Enke, Hierarchically structured glass monoliths based on polyurethane foams as template. *J. Eur. Ceram. Soc.*, **2014**, 34, 1465–1470.
DOI: 10.1016/j.jeurceramsoc.2013.11.042.
- (30) Y. Wie, H. Chen, H. Jiang, B. Wang, H. Liu, Y. Zhang, H. Wu, Biotemplate-based engineering of high-temperature stable anatase TiO₂ nanofiber bundles with impregnated CeO₂ nanocrystals for enhanced lithium storage. *ACS Sust. Chem. Eng.*, **2019**, 7, 7823–7832.
DOI: 10.1021/acssuschemeng.9b00012.
- (31) Y. Liu, G. Wang, W. Yang, J. Li, Biotemplated synthesis of hierarchically porous ZnAl-CLDH/FeWO₄ for effective removal of dyes from water. *Water Air Soil Pollut.*, **2019**, 230, 89.
DOI: 10.1007/s11270-019-4134-9.
- (32) C. Wang, J. Li, E. Paineau, A. Laachachi, C. Colbeau-Justin, H. Remita, M. N. Ghazzal, A sol–gel biotemplating route with cellulose nanocrystals to design a photocatalyst for improving hydrogen generation. *J. Mater. Chem. A*, **2020**.
DOI: 10.1039/C9TA12665A.
- (33) Z. Yang, J. Kang, L. Li, L. Guo, A biotemplating route for the synthesis of hierarchical Fe₂O₃ with highly dispersed carbon as electron-transfer channel. *ChemPlusChem*, **2020**, 85, 258–263.
DOI: 10.1002/cplu.201900641.

-
- (34) P. Yang, T. Deng, D. Zhao, P. Feng, D. Pine, B. F. Chmelka, G. M. Whitesides, G. D. Stucky, Hierarchically ordered oxides. *Science*, **1998**, 282, 2244–2246.
DOI: 10.1126/science.282.5397.2244.
- (35) H. Uhlig, T. Münster, G. Kloess, S. Ebbinghaus, W.-D. Einicke, R. Gläser, D. Enke, Synthesis of MCM-48 granules with bimodal pore systems via pseudomorphic transformation of porous glass. *Microporous Mesoporous Mater.*, **2008**, 257, 185–192.
DOI: 10.1016/j.micromeso.2017.08.033.
- (36) C. Küster, B. Reinhardt, M. Fröba, D. Enke, Hierarchically structured MCM-41 silica beds via nanocasting in combination with “pore-protected” pseudomorphic transformation. *Z. Anorg. Allg. Chem.*, **2014**, 640, 565–569.
DOI: 10.1002/zaac.201300456.
- (37) C.-G. Oh, Y. Baek, S.-K. Ihm, Synthesis of skeletal-structured biporous silicate powders through microcolloidal crystal templating. *Adv. Mater.*, **2005**, 17, 270–273.
DOI: 10.1002/adma.200400192.
- (38) R. Ryoo, C. H. Ko, M. Kruk, V. Antochschuk, M. Jaroniec, Block-copolymer-templated ordered mesoporous silica: Array of uniform mesopores or mesopore-micropore network? *J. Phy. Chem. B*, **2000**, 104, 11465–11471.
DOI: 10.1021/jp002597a.
- (39) A. Galarneau, H. Cambon, F. Di Renzo, R. Ryoo, M. Choi, F. Fajula, Microporosity and connections between pores in SBA-15 mesostructured silicas as a function of the temperature of synthesis. *New J. Chem.*, **2003**, 27, 73–79.
DOI: 10.1039/B207378C.
- (40) K.-J. Lin, L.-J. Chen, M. R. Prasad, C.-Y. Cheng, Core-shell synthesis of a novel, spherical, mesoporous silica/platinum nanocomposite: Pt/PVP@MCM-41. *Adv. Mater.*, **2004**, 16, 1845–1849.
DOI: 10.1002/anie.200501500.
- (41) Y. Zhu, J. Shi, W. Shen, X. Dong, J. Feng, M. Ruan, Y. Li, Stimuli-responsive controlled drug release from a hollow mesoporous silica sphere/polyelectrolyte multilayer core-shell structure. *Angew. Chem. Int. Ed.*, **2005**, 44, 5083–5087.
DOI: 10.1002/anie.200501500.
- (42) J.-S. Yu, S. B. Yoon, Y. J. Lee, K. B. Yoon, Fabrication of bimodal porous silicate with silicate-1 core/mesoporous shell structures and synthesis of nonspherical carbon and silica nanocases with hollow core/mesoporous shell structures. *J. Phys. Chem. B*, **2005**, 109, 7040–7045.
DOI: 10.1021/jp044730v.
- (43) Z. Han, F. Zhou, J. Zhao, Y. Liu, H. Ma, G. Wu, Synthesis of hierarchical GaZSM-5 zeolites by a post-treatment method and their catalytic conversion of methanol to olefins. *Microporous Mesoporous Mater.*, **2020**, 110194.
DOI: 10.1016/j.micromeso.2020.110194.

-
- (44) J. Zhou, F. Zheng, H. Li, J. Wang, N. Bu, P. Hu, J. Gao, Q. Zhen, S. Bashir, J. L. Liu, Optimization of post-treatment variables to produce hierarchical porous zeolites from coal gangue to enhance adsorption performance. *Chem. Eng. J.*, **2020**, *381*, 122698. DOI: 10.1016/j.cej.2019.122698.
- (45) A. Taguchi, J.-H. Smått, M- Lindén, Carbon monoliths possessing a hierarchical, fully interconnected porosity, *Adv. Mater.*, **2003**, *15*, 1209–1211. DOI: 10.1002/adma.200304848.
- (46) J. Xu, Z. Tan, W. Zeng, G. Chen, S. Wu, Y. Zhao, K. Ni, Z. Tao, M. Ikram, H. Ji, Y. Zhu, A hierarchical carbon derived from sponge-templated activation of graphene oxide for high-performance supercapacitor electrodes. *Adv. Mater.*, **2016**, *28*, 5222–5228. DOI: 10.1002/adma.201600586.
- (47) X. Li, B. Y. Guan, S. Gao, X. W. D. Lou, A general dual templating approach to biomass-derived hierarchically porous heteroatom-doped carbon materials for enhanced electrocatalytic oxygen reduction. *Energy Environ. Sci.*, **2019**, *12*, 648–655. DOI: 10.1039/C8EE02779J.
- (48) Z.-Y. Yuan, A. Vantomme, A. Léonard, B.-L. Su, Surfactant-assisted synthesis of unprecedented hierarchical meso-macrostructured zirconia. *Chem. Commun.*, **2003**, 1558–1559. DOI: 10.1039/B303272H.
- (49) Z.-Y. Yuan, T. Z. Ren, A. Azioune, J. J. Pireaux, B.-L. Su, Self-assembly of hierarchically mesoporous-macroporous phosphate nanocrystalline aluminum (oxyhydr)oxide materials. *Chem. Mater.*, **2006**, *18*, 1753–1762. DOI: 10.1021/cm0520160.
- (50) A. Inayat, B. Reinhardt, H. Uhlig, W.-D. Einicke, D. Enke, Silica monoliths with hierarchical porosity obtained from porous glasses. **2013**, *42*, 3753–3764. DOI: 10.1039/c2cs35304k.
- (51) A. Inayat, B. Reinhardt, J. Herwig, C. Küster, H. Uhlig, S. Krenkel, E. Raedlein, D. Enke, Recent advances in the synthesis of hierarchically porous silica materials on the basis of porous glasses. *New J. Chem.*, **2016**, *40*, 4095–4114. DOI: 10.1039/C5NJ03591K.
- (52) K. Nakanishi, Pore structure control of silica gels based on phase separation. *J. Porous Mater.*, **1997**, *4*, 67–112. DOI: 10.1023/A:1009627216939.
- (53) J.-H. Sun, Z. Shan, T. Maschmeyer, M.-O. Coppens, Synthesis of bimodal nanostructured silicas with independently controlled small and large mesopore sizes. *Langmuir*, **2003**, *19*, 8395–8402. DOI: 10.1021/la0351156.
- (54) M. Groenewolt, M. Antonietti, S. Polarz, Mixed micellar phases of nonmiscible surfactants: Mesoporous silica with bimodal pore size distribution via the nanocasting process. *Langmuir*, **2004**, *18*, 7811–7819. DOI: 10.1021/la049147k.

-
- (55) J. H. Schattka, E. H.-M. Wong, M. Antonietti, R. A. Caruso, Sol–gel templating of membranes to form thick, porous titania, titania/zirconia and titania/silica films. *J. Mater. Chem.*, **2006**, *16*, 1414–1420.
DOI: 10.1039/B515421A.
- (56) E. S. Toberer, A. Joshi, R. Seshadri, Template-free routes to macroporous monoliths of nickel and iron oxides: Toward porous metals and conformally coated pore walls. *Chem. Mater.*, **2005**, *17*, 2142–2147.
DOI: 10.1021/cm0401342.
- (57) E. S. Toberer, R. Seshadri, Template-free routes to porous inorganic materials. *Chem. Commun.*, **2006**, *30*, 3159–3165.
DOI: 10.1039/B602153K.
- (58) M. Yamane, S. Aso, T. Sakaino, Preparation of a gel from metal alkoxide and its properties as a precursor of oxide glass. *J. Mater. Sci.*, **1978**, *13*, 865–870.
DOI: 10.1007/BF00570525.
- (59) C. J. Brinker, G. W. Scherer, *Sol–Gel Science: The Physics and Chemistry of Sol–Gel Processing*, Academic Press, New York, NY, **1990**.
- (60) J. Jang, H. Park, *In situ* sol–gel process of polystyrene/silica hybrid materials: Effect of silane-coupling agents. *J. Appl. Polym. Sci.*, **2002**, *85*, 2074–2083.
DOI: 10.1002/app.10747.
- (61) Q.-Z. Chen, Y. Li, Y.-Y. Jin, J. M. W. Quinn, P. A. Komesaroff, A new sol–gel process for producing Na₂O containing bioactive glass ceramics. *Acta Biomater.*, **2010**, *6*, 4143–4153.
DOI: 10.1016/j.actbio.2010.04.022.
- (62) G. Hayase, K. Kugimiya, M. Ogawa, Y. Kodera, K. Kanamori, K. Nakanishi, The thermal conductivity of polymethylsilsesquioxane aerogels and xerogels with varied pore sizes for practical application as thermal superinsulators. *J. Mater. Chem. A*, **2014**, *2*, 6525–6525.
DOI: 10.1039/c3ta15094a.
- (63) R. Meinus, R. Ellinghaus, K. Hormann, U. Tallarek, B. M. Smarsly, On the underestimated impact of the gelation temperature on macro- and mesoporosity in monolithic silica. *Phy. Chem. Chem. Phys.*, **2017**, *19*, 14821–14834.
DOI: 10.1039/c7cp01846k.
- (64) C. Jiang, W. Liu, Y. Sun, C. Liu, M. Yang, Z. Wang, Fabrication of durable superhydrophobic and superoleophilic cotton fabric with fluorinated silica via sol–gel process. *J. Appl. Polym. Sci.*, **2019**, *136*, 47005.
DOI: 10.1002/app.47005.
- (65) M. Catauro, F. Barrino, G. D. Poggetto, F. Pacifico, S. Piccolella, S. Pacifico, Chlorogenic acid/PEG-based organic-inorganic hybrids: A versatile sol–gel synthesis route for new bioactive materials. *Mater. Sci. Eng. C*, **2019**, *100*, 837–844.
DOI: 10.1016/j.msec.2019.03.035.
- (66) M. Ebelmann, *Ann. Chim. Phys.*, **1846**, *16*, 129.

- (67) K. Nakanishi, N. Soga, Phase separation in silica sol–gel system containing polyacrylic acid I. Gel formation behavior and effect of solvent composition. *J. Non Cryst. Solids*, **1992**, *139*, 1–13.
DOI: 10.1016/S0022-3093(05)80800-2.
- (68) A. Feinle, M. S. Elsaesser, N. Hüsing, Sol–gel synthesis of monolithic materials with hierarchical porosity. *Chem. Soc. Rev.*, **2016**, *45*, 3377–3399.
DOI: 10.1039/C5CS00710K.
- (69) K. Thenmozhi, S. Sriman Narayanan, Surface renewable sol–gel composite electrode derived from 3-aminopropyl trimethoxy silane with covalently immobilized thionin. *Biosens. Bioelectron.*, **2007**, *23*, 606–612.
DOI: 10.1016/j.bios.2007.06.003.
- (70) K. Wilson, A. F. Lee, D. J. Macquarrie, J. H. Clark, Structure and reactivity of sol–gel sulphonic acid silicas. *Appl. Catal. A*, **2002**, *228*, 127–133.
DOI: 10.1016/S0926-860X(01)00956-5.
- (71) M. C. Advincula, F. G. Rahemtulla, R. C. Advincula, E. T. Ada, J. E. Lemons, S. L. Bells, Osteoblast adhesion and matrix mineralization on sol–gel derived titanium oxide. *Biomaterials*, **2006**, *27*, 2201–2212.
DOI: 10.1016/j.biomaterials.2005.11.014.
- (72) J. Herwig, J. Titus, J. Kullmann, N. Wilde, T. Hahn, R. Gläser, D. Enke, Hierarchically structured porous spinels via epoxide-mediated sol–gel process accompanied by polymerization-induced phase separation. *ACS Omega*, **2016**, *3*, 1201–1212.
DOI: 10.1021/acsomega.7b01621.
- (73) C. Carstens, D. Enke, Investigation of the formation process of highly porous α -Al₂O₃ via citric acid-assisted sol–gel synthesis. *J. Eur. Cer. Soc.*, **2019**, *39*, 2493–2502.
DOI: 10.1016/j.jeurceramsoc.2019.01.043.
- (74) X. Lu, K. Kanamori, K. Nakanishi, Preparation of zinc oxide with a three dimensionally interconnected macroporous structure via sol–gel method accompanied by phase separation, *New J. Chem.*, **2019**, *43*, 11720–11726.
DOI: 10.1039/C9NJ02373A.
- (75) D. W. Schaefer, Polymers, fractals, and ceramic materials. *Science*, **1989**, *243*, 1023–1027.
DOI: 10.1126/science.243.4894.1023.
- (76) K. Nakanishi, N. Soga, Phase separation in silica sol–gel system containing polyacrylic acid II. Effects of molecular weight and temperature. *K. Non Cryst. Solids*, **1992**, *139*, 14–24.
DOI: 10.1016/S0022-3093(05)80801-4.
- (77) K. Nakanishi, H. Komura, R. Takahashi, N. Soga, Phase separation in silica sol–gel system containing poly(ethylene oxide). I. Phase relation and gel morphology. *Bull. Chem. Soc. Jpn.*, **1994**, *67*, 1327–1335.
DOI: 10.1246/bcsj.67.1327.

- (78) G. W. Scherer, D. M. Smith, Cavitation during drying of a gel. *J. Non Cryst. Solids*, **1995**, *189*, 197–211.
DOI: 10.1016/0022-3093(95)00222-7.
- (79) K. Nakanishi, N. Soga, Phase separation in silica sol–gel system containing poly(ethylene oxide) II. Effects of molecular weight and temperature. *Bull. Chem. Soc. Jpn.*, **1997**, *70*, 587–592.
DOI: 10.1246/bcsj.70.587.
- (80) R. Takahashi, K. Nakanishi, N. Soga, Aggregation behavior of alkoxide-derived silica in sol–gel process in presence of poly(ethylene oxide). *J. Sol-Gel Sci. Technol.*, **2000**, *17*, 7–18.
DOI: 10.1023/A:1008753718586.
- (81) O. V. Gorbunova, O. N. Baklanova, T. I. Gulyaeva, M. V. Trenikhin, V. A. Drozdov, Poly(ethylene glycol) as structure directing agent in sol–gel synthesis of amorphous silica. *Microporous Mesoporous Mater.*, **2014**, *190*, 146–151.
DOI: 10.1016/j.micromeso.2014.02.013.
- (82) C. W. Correns, *Einführung in die Mineralogie, Kristallographie und Petrologie*, 2nd Ed., Springer Verlag, Berlin, Germany, **1968**.
- (83) G. W. Scherer, D. M. Smith, Cavitation during drying of a gel. *J. Non Cryst. Solids*, **1995**, *189*, 197–211.
- (84) T. K. Sherwood, The drying of solids–I. *Ind. Eng. Chem.*, **1929**, *21*, 12–16.
DOI: 10.1021/ie50229a004.
- (85) T. K. Sherwood, The drying of solids–II. *Ind. Eng. Chem.*, **1929**, *21*, 976–980.
DOI: 10.1021/ie50238a021.
- (86) S. S. Kistler, Coherent expanded-aerogels. *J. Phys. Chem.*, **1932**, *36*, 52–64.
DOI: 10.1021/j150331a003.
- (87) N. Hüsing, F. Schwertfeger, W. Tappert, U. Schubert, Influence of supercritical drying fluid on structure and properties of organically modified silica aerogels. *J. Non Cryst. Solids*, **1995**, *186*, 37–43.
DOI: 10.1016/0022-3093(95)00031-3.
- (88) N. Hüsing, U. Schubert, Aerogels–airy materials: Chemistry, structure, and properties. *Angew. Chem. Int. Ed.*, **1998**, *37*, 22–45.
DOI: 10.1002/(SICI)1521-3773(19980202)37:1/2<22::AID-ANIE22>3.0.CO;2-I.
- (89) K. Kanamori, M. Aizawa, K. Nakanishi, T. Hanada, Elastic organic-inorganic hybrid aerogels and xerogels. *J. Sol-Gel Sci. Technol.*, **2008**, *48*, 172–181.
DOI: 10.1007/s10971-008-1756-6.
- (90) Y. C. Bae, J. J. Shim, D. S. Soane, J. M. Prausnitz, Representation of vapor-liquid and liquid-liquid equilibria for binary systems containing polymers: Applicability of an extended flory-huggins equation. *J. Appl. Polym. Sci.*, **1993**, *47*, 1193–1206.
DOI: 10.1002/app.1993.070470707.

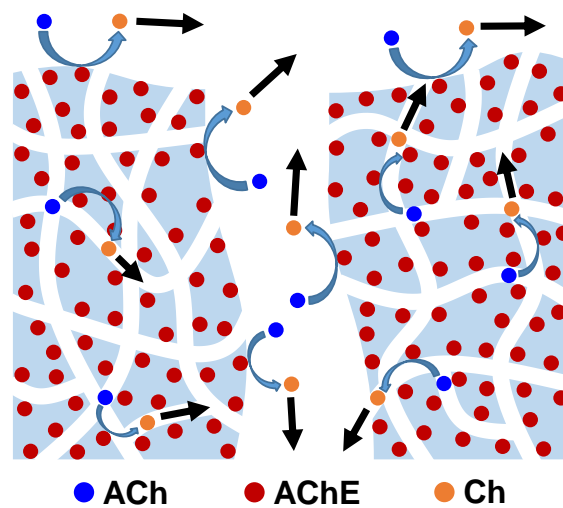
-
- (91) K. Nakanishi, N. Tanaka, Sol-gel with phase separation. Hierarchically porous materials optimized for high-performance liquid chromatography separations. *Acc. Chem. Res.*, **2007**, *40*, 863–873.
DOI: 10.1021/ar600034p.
- (92) I. Tan, Z. Zarafshani, J.-F. Lutz, M.-M. Titirici, PEGylated chromatography: Efficient bioseparation on silica monoliths grafted with smart biocompatible polymers. *ACS Appl. Mater. Interfaces*, **2009**, *1*, 1869–1872.
DOI: 10.1021/am900461a.
- (93) X. Du, C. Wang, T. Li, M. Chen, Studies on the performances of silica aerogel electrodes for the application of supercapacitor. *Ionics*, **2009**, *15*, 561–565.
DOI: 10.1007/s11581-009-0315-7.
- (94) A. Sachse, A. Galarneau, F. Fajula, F. Di Renzo, P. Creux, B. Coq, Functional silica monoliths with hierarchical uniform porosity as continuous flow catalytic reactors. *Microporous Mesoporous Mater.*, **2011**, *140*, 58–68.
DOI: 10.1016/j.micromeso.2010.10.044.
- (95) E. Cuce, P. M. Cuce, C. J. Wood, S. B. Riffat, Toward aerogel based thermal superinsulation in buildings: A comprehensive review. *Renew. Sust. Energ. Rev.*, **2014**, *34*, 273–299.
DOI: 10.1016/j.rser.2014.03.017.
- (96) Y. G. Ko, H. J. Lee, J. Y. Kim, U. S. Choi, Hierarchically porous aminosilica monolith as a CO₂ adsorbent. *ACS Appl. Mater. Interfaces*, **2014**, *6*, 12988–12996.
DOI: 10.1021/am5029022.
- (97) F. Svec, Y. Lv, Advances and recent trends in the field of monolithic columns for chromatography. *Anal. Chem.*, **2015**, *87*, 250–273.
DOI: 10.1021/ac504059c.
- (98) M. von der Lehr, C. F. Seidler, D. H. Taffa, M. Wark, B. M. Smarsly, R. Marshall, Proton conduction in sulfonated organic-inorganic hybrid monoliths with hierarchical pore structure. *ACS Appl. Mater. Interfaces*, **2016**, *8*, 25476–25488.
DOI: 10.1021/acsami.6b08477.
- (99) A. Galarneau, A. Sachse, B. Said, C.-H. Péliesson, P. Boscaro, N. Brun, L. Courtheoux, N. Olivi-Tran, B. Coasne, F. Fajula, Hierarchical porous silica monoliths: A novel class of microreactors for process intensification in catalysis and adsorption. *C. R. Chimie*, **2016**, *19*, 231–247.
DOI: 10.1016/j.crci.2015.05.017.
- (100) H. Maleki, N. Hüsing, Current status, opportunities and challenges in catalytic and photocatalytic applications of aerogels: Environmental protection aspects. *Appl. Catal. B*, **2018**, *221*, 530–555.
DOI: 10.1016/j.apcatb.2017.08.012.
- (101) A. Walcarius, Silica-based electrochemical sensors and biosensors: Recent trends. *Curr. Opin. Electrochem.*, **2018**, *10*, 88–97.
DOI: 10.1016/j.coelec.2018.03.017.

-
- (102) M. Vafi, G. H. Rounaghi, Z. Es'haghi, Z. Moradi, Design and application of an optical pH sensor based on thionine doped modified sol–gel film. *Russ. J. Phys. Chem.*, **2019**, *93*, 1389–1393.
DOI: 10.1134/S0036024419070173.
- (103) C. Jeffryes, T. Gutu, J. Jiao, G. L. Rorrer, Two-stage photobioreactor process for the metabolic insertion of nanostructured germanium into the silica microstructure of the diatom *Pinnularia* sp. *Mater. Sci. Eng. C*, **2008**, *28*, 107–118.
DOI: 10.1016/j.msec.2007.01.002.
- (104) C. F. Meunier, J. C. Rooke, A. Léonard, P. Van Cutsem, B.-L. Su, Design of photochemical materials for carbohydrate production *via* the immobilization of whole plant cells into porous silica matrix. *J. Mater. Chem.*, **2009**, *20*, 929–936.
DOI: 10.1039/B919763J.
- (105) Y. Hu, S. Giret, R. Meinus, J. Han, F.-G. Fontaine, F. Kleitz, D. Larivière, Selective separation and preconcentration of Th(IV) using organo-functionalized, hierarchically porous silica monoliths. *J. Mater. Chem. A*, **2019**, *7*, 289–302.
DOI: 10.1039/C8TA07952H.
- (106) D. Enke, R. Gläser, U. Tallarek, Sol–gel and porous glass-based silica monoliths with hierarchical pore structure for solid-liquid catalysis. *Chem. Ing. Tech.*, **2016**, *88*, 1561–1585.
DOI: 10.1002/cite.201600049.
- (107) T. Müllner, K. K. Unger, U. Tallarek, Characterization of microscopic disorder in reconstructed porous materials and assessment of mass transport-relevant structural descriptions. *New J. Chem.*, **2016**, *40*, 3993–4015.
DOI: 10.1039/C5NJ03346B.
- (108) T. Noisser, G. Reichenauer, N. Hüsing, In situ modification of the silica backbone leading to highly porous monolithic hybrid organic-inorganic materials via ambient pressure drying. *ACS Appl. Mater. Interfaces*, **2014**, *6*, 1025–1029.
DOI: 10.1021/am404005g.
- (109) D. Stoeckel, C. Kübel, K. Hormann, A. Hölzel, B. M. Smarsly, U. Tallarek, Morphological analysis of disordered macroporous-mesoporous solids based on physical reconstruction by nanoscale tomography. *Langmuir*, **2014**, *30*, 9022–9027.
DOI: 10.1021/la502381m.
- (110) K. K. Unger, N. Tanaka, E. Machtejevas, *Monolithic Silica in Separation Science: Concepts, Syntheses, Characterization, Modeling and Applications*, Wiley-VCH, Weinheim, Germany, **2011**.
- (111) K. Szymańska, M. Pietrowska, J. Kocurek, K. Maresz, A. Koreniuk, J. Miroyiec-Białoń, P. Widłak, E. Magner, A. Jarzębski, Low back-pressure hierarchically structured multichannel microfluidic bioreactors for rapid protein digestion—Proof of concept. *Chem. Eng. J.*, **2016**, *287*, 148–154.
DOI: 10.1016/j.cej.2015.10.120.

- (112) K. Hormann, T. Müllner, S. Bruns, A. Höltzel, U. Tallarek, Morphology and separation efficiency of a new generation of analytical silica monoliths. *J. Chromatogr. A*, **2012**, *1222*, 46–58.
DOI: 10.1016/j.chroma.2011.12.008.
- (113) K. Hormann, U. Tallarek, Analytical silica monoliths with submicron macropores: Current limitations to a direct morphology-column efficiency scaling. *J. Chromatogr. A*, **2013**, *1312*, 26–36.
DOI: 10.1016/j.chroma.2013.08.087.
- (114) N. Tanaka, H. Kobayashi, N. Ishizuka, H. Minakuchi, K. Nakanishi, K. Hosoya, T. Ikegami, Monolithic silica columns for high-efficiency chromatographic separations. *J. Chromatogr. A*, **2002**, *965*, 35–49.
DOI: 10.1016/S0021-9673(01)01582-5.
- (115) G. Guiochon, Monolithic columns in high-performance liquid chromatography. *J. Chromatogr. A*, **2007**, *1168*, 101–168.
DOI: 10.1016/j.chroma.2007.05.090.
- (116) K. Szymańska, W. Pudło, J. Miroyiec-Białoń, A. Czardybon, J. Kocurek, A. Jarzębski, Immobilization of invertase on silica monoliths with hierarchical pore structure to obtain continuous flow enzymatic microreactors of high performance. *Microporous Mesoporous Mater.*, **2013**, *170*, 75–82.
DOI: 10.1016/j.micromeso.2012.11.037.

Chapter 1

Influence of Pore Space Hierarchy on the Efficiency of an Acetylcholinesterase-Based Support for Biosensorics



Authors

Richard Kohns, Nicole Anders, Dirk Enke and Ulrich Tallarek

State of Publication

Accepted 26 March 2020 in *Advanced Materials Interfaces*.

DOI: 10.1002/admi.202000163

Abstract

The influence of a hierarchically structured pore system of a silica sol–gel support for application as a functional component in an acetylcholinesterase-based enzyme array, with respect to its efficiency (response time, in particular) is investigated. Careful adjustment of synthesis parameters and a novel drying method allow to prepare monolithic silica sol–gel membranes with monomodal or hierarchical pore structures. These supports enable direct comparison regarding the influence of morphological properties on maximum AChE loading by a membrane and on the apparent reaction rate of the AChE-catalyzed degradation of acetylcholine at identical enzyme loading. It is shown for the first time that the hierarchical, macro–mesoporous material is superior over the monomodal structures (of either mesopores or macropores) regarding combined functionality and transport efficiency, as reflected in the apparent reaction rates. The advantage of the mesopores in a hierarchical system is manifested in higher maximum enzyme loading than for purely macroporous material, while the presence of macropores results in less obstructed transport than for a purely mesoporous material, which in turn reduces the response time.

1.1 Introduction

Due to their potential for miniaturized designs, biosensors are a cost-effective alternative to classical analytical platforms.¹ The spatial proximity of biological (functional) components, transducer and signal converter, as well as the integration of a reaction unit optimized to handle small sample amounts are advantages over conventional detection and characterization schemes. Biosensors are not only used in clinical diagnostics but also in environmental analysis, military technology, food science, and process control.¹⁻⁶

The enzyme class of cholinesterases occurs in all multicellular organisms and is one of the most important enzyme classes in biosensorics next to the glucosidases. Acetylcholinesterase (AChE), the best-known representative of the cholinesterases, acts in the vegetative and central nervous system and in neuromuscular synapses in the transmission of stimuli. To guarantee the transmission of stimuli to the neurons in a short time, the degradation of acetylcholine (ACh) into choline and acetic acid belongs to the fastest reactions. Because of this vital effect of AChE also in the human body, it is important that the mechanism of stimulus transmission is not disturbed.^{6,7} The degeneration of the nervous system can cause diseases like Alzheimer and forms of muscle weakness, which can as well be attributed to a disturbed AChE mechanism.⁸ Some pesticides and various chemical warfare agents also rely on the inhibition of the AChE mechanism, so that environmental influences (contaminated food or drinking water) also contribute to enzyme inhibition and may even lead to paralysis of the muscles and death of the organism.⁹ With an AChE-based sensor, decisions can be reached about the effect of a medical product, of pesticides, or chemical warfare agents on humans and animals. Therefore, AChE-based sensors are used at early stages of drug and plant protection agent development, as well as in environmental and food analysis for the detection of pesticide residues in food or drinking water samples.¹⁰⁻¹²

Proper function of AChE-based sensors relies on a constant enzyme activity, as seen in the substrate decomposition under defined reaction conditions. The degradation of ACh takes place by ester hydrolysis into choline and acetic acid. AChE acts as catalyst and is immobilized on a support for better storage and transport, easier sensor handling and straightforward separation from analytes.^{13,14} The enzyme-support assembly is directly connected to a transducer, *e.g.*, an optoelectronic sensor or potentiometric electrodes.¹⁵

To guarantee optimal biosensor function high demands are placed on a potential support for immobilization of the biologically active component. AChE is an ellipsoidal molecule of about 4.5 nm × 6.0 nm × 6.5 nm.¹⁶ 12 β -sheets are arranged in slightly convex form and surrounded by 14 α -helices similar to a sandwich structure. This arrangement of the secondary structure enables formation of a slightly twisted, helical tertiary structure of the molecule, which requires a pore size of the support of at least 10 nm so that unfolding of the enzyme and thus its activity are not impaired.¹⁷ In addition, the support material should have a high specific surface area (for high loading capacities) combined with high mechanical and thermal stability. Due to these

requirements, porous materials are often the first choice. In addition to agarose and polymers such as acrylamide or polyethylene glycol, nanoparticles or nanoporous layers of gold, titanium dioxide, zirconium or cadmium sulfide and silicon dioxide are often used in biosensors.^{15,18–20} In this case, additional demands are placed on the support regarding little obstructed transport of solutes within the pore system, because short response times should remain one of the main advantages of biosensors.

The combination of mesopores (with large specific surface area for reaction) and macropores (highly permeable flow-through pores enabling advection-dominated transport) as hierarchical architecture in a support material ensures optimized mass transfer in many applications.^{21–24} Hierarchical supports can be prepared, *e.g.*, *via* thermally-induced phase separation in sodium borosilicate glasses. Hierarchy is also realized by employing sintering processes in combination with the replica process using tube bundles or with foaming processes.^{25–27} Hierarchical silica materials can be prepared based on sol–gel chemistry, which is achieved by polymer-induced phase separation during the sol–gel process.^{28–32} Sol–gel materials are already employed in several applications including biosensorics and microfluidic devices, but often with monomodal pore structure. In microfluidic chips for DNA isolation or as flow-through cells for an optical biosensor and also in combination with AChE the devices are operated using purely monomodal (macroporous) sol–gel materials.^{33–36} We therefore study closer morphological effects of the support material that will have an impact on the performance in such applications.

In this work, we investigate the impact of a hierarchical pore system on the efficiency (mass transfer resistance and response time) of a functional support based on AChE for biosensorics compared to materials with monomodal pore systems. By adapting a general sol–gel synthesis protocol purely mesoporous, purely macroporous, and bimodal (macro–mesoporous) supports have been synthesized. These three basic pore architectures were compared in a model system to determine the maximum loading of AChE as well as the apparent reaction rate of the AChE-catalyzed degradation of ACh at identical enzyme loading. We highlight the conditions when a hierarchical support is indispensable and when a purely macroporous material suffices.

1.2 Experimental

1.2.1 Chemicals

Tetraethyl orthosilicate (TEOS, 99%) came from abcr (Karlsruhe, Germany). AChCl (99%), bromothymol blue, and poly(ethylene oxide) (PEO, average molecular weight: 100,000) were received from Alfa Aesar (Haverhill, MA). Sulfuric acid (95%) came from VWR International (Darmstadt, Germany). Ammonium hydroxide solution (25%) and hydrochloric acid (37%) were purchased from AppliChem (Darmstadt, Germany). Potassium bromide (IR-grade), *n*-butylamine (97%), and sodium dihydrogen phosphate dihydrate came from Merck (Darmstadt, Germany). 3-(glycidoxypropyl)dimethylmethoxysilane (97%), AChE (electrophorus electricus, 518 U/mg), ethanol (analytical standard), and disodium hydrogen phosphate were

obtained from Sigma–Aldrich (St. Louis, MO). Chemicals were used without further purification.

1.2.2 Support synthesis

For the sol–gel based synthesis of the materials with different pore systems (Figure 1.1) the following molar ratios of starting components have been employed: 1.0 mol H₂O : 0.025 mol H₂SO₄ : x mol PEO : 0.070 mol TEOS.

First, sulfuric acid (2.54 g) and PEO (0–3 g) were added to distilled water (18 g) under vigorous stirring. After stirring for 30 min at room temperature, the reaction mixture was cooled with an ice bath to 4 °C and TEOS (14.6 g) was added. When (after an additional 30 min of vigorous stirring) solutions became transparent, each mixture was poured into a 15 mL centrifugal tube. Before gelation, the mixtures were evacuated (2 min, 0.1 bar) to remove air bubbles. Gelation was performed in an oven for 24–72 h at 50 °C under helium atmosphere at constant pressure of 7 bar. After cooling, the wet gels were washed for 18 h with distilled water to neutral pH. Pore widening of mesoporous and hierarchical materials was carried out in small lab autoclaves with solid–solvent ratio of 1:10 at 120 °C/180 °C for 3 to 48 h using 7 M ammonia solution. A washing step with distilled water (18 h) was added. Hierarchical materials were dried at room temperature for 1 d. Samples with monomodal pore structure were placed into their starting plastic vessels and covered with water. The centrifugal tubes were closed, the lid provided with a leak, and the materials dried in an oven at 120 °C for 12 h. Samples with organic residues were calcined for 4 h using a heating rate of 3 °C min⁻¹ from room temperature up to 550 °C. Macroporous materials were additionally sintered at 900 °C for 1 h in a muffle furnace (Nabertherm, Lilienthal, Germany) with a heating rate of 3 °C min⁻¹ to remove any mesoporosity. Using a core drill (Guede, Wolpertshausen, Germany) and a SAW 15 from Logitech (Lausanne, Switzerland) membranes with a diameter of 6 mm and a thickness of 0.5 mm were prepared.

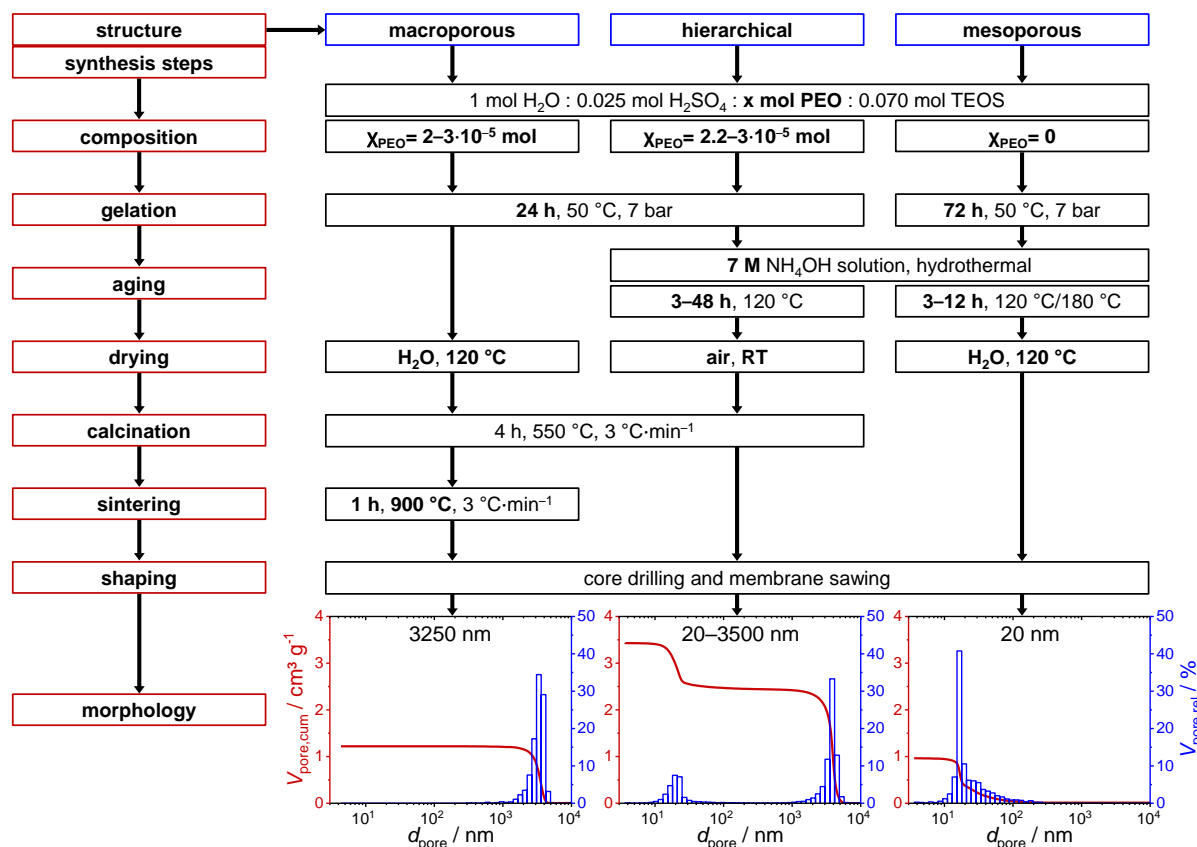


Figure 1.1. Adapted synthesis route to purely mesoporous, purely macroporous, and hierarchical (macro–mesoporous) supports. Highlighted (bold) synthesis parameters offer the possibility to tailor morphological details. Mercury intrusion curves and pore size distributions (cumulative and relative pore volumes, respectively) for silica monoliths selected from each route are shown as examples (*cf.* Table 1.1).

1.2.3 Surface modification and enzyme immobilization

Before surface functionalization, samples were rehydroxylated in water (3 h, room temperature) and dried in an oven at 120 °C. Activated membranes were mixed with a fresh 3-(glycidoxypropyl)dimethylmethoxysilane solution (1 wt.%) in a polypropylene vessel at a ratio of 1:20. A 1:4 (v/v) water/ethanol mixture was used as solvent for the silane solution. Reaction took place at 60 °C in a water bath under careful shaking for 6 h. After washing the membranes for 5 min with solvent under shaking, a drying step for the post-condensation of physisorbed molecules was carried out at 120 °C for 2 h. The membranes were finally washed with solvent three times for 10 min and dried at 120 °C for 2 h.

For enzyme immobilization, each functionalized membrane was transferred into a 2 mL reaction vessel and mixed with 150 μ L enzyme buffer solution in an ice bath at 0 °C. The enzyme concentration varied from 4 to 60 μ g mL⁻¹. To ensure complete filling of the pore system, reaction vessels were placed in an ice bath in a vacuum oven and evacuated for 15 min at 0.1 bar. Subsequently, immobilization took place in a closed vessel at 4 °C in the refrigerator for 16 h. After washing each membrane three times for 5 min with 500 μ L buffer solution, the

membranes were stored in the reaction vessels (covered with 50 μ L buffer solution) in the refrigerator at 4 °C. A 0.01 M phosphate buffer (pH 8) was used as buffer solution. All materials and solutions used for enzyme immobilization were autoclaved at 120 °C. Although we always worked with freshly prepared samples, the final membranes with immobilized enzyme can still be used after a few months when properly stored at 4 °C in the buffer solution under exclusion of light. With these conditions, an activity loss of ~10% was observed after 2 months.

1.2.4 Characterization

Mercury intrusion porosimetry was run on a Poremaster[®] (Quantachrome Instruments, Boynton Beach, FL) from 0.15 to 400 MPa. Pore size distributions were derived from the MIP data with Quantachrome software according to the Washburn equation, setting the mercury contact angle to 140°. The measured pressure range corresponds to pore diameters between 3.5 nm and 10 μ m. Nitrogen physisorption data were acquired on an ASAP 2000 (Micromeritics, Norcross, GA). Prior to the measurements samples were activated for 24 h at 120 °C under vacuum (10^{-5} bar). Specific surface areas were calculated using the Brunauer–Emmett–Teller equation ($p/p_0 = 0.05–0.35$). Silica membranes were examined under a Leo Gemini 1530 scanning electron microscope (Zeiss, Oberkochen, Germany), for which Au was vapor-deposited onto sample pieces at 10 kV. Elemental analysis was conducted on a vario Micro cube (Elementar, Langensfeld, Germany).

To verify functionalization, DRIFT spectra were recorded on a Vector 22 (Bruker, Billerica, MA) from 4000 to 1500 cm^{-1} . Prior to the measurements samples were ground (to receive a particle size <5 μ m) and diluted with potassium bromide to reduce absorption. For quantitative analysis, 500 mg sample were mixed with 25 mL of 0.01 M *n*-butylamine solution for 1 h at 60 °C and titrated by dropwise addition of 0.01 M HCl (indicator: bromothymol blue). The number of functional surface species ($N_{\text{glycidoxy}}$) was calculated from the sample mass and required volume of hydrochloric acid. The epoxide groups react with *n*-butylamine under ring opening and remaining *n*-butylamine is back-titrated with HCl (see Supporting Information for further details). To derive enzyme concentration in the reaction solutions before and after immobilization, spectrophotometric studies were conducted using a Pierce BCA Protein Assay Kit (Thermo Scientific, Waltham, MA) and a UV-1600PC spectrophotometer from VWR International (Darmstadt, Germany) at 562 nm. Potentiometric pH analysis of AChE-catalyzed ACh degradation was performed with the pH electrode InLab Ultra Micro pH and the measuring device Seven Easy pH from Mettler Toledo (Columbus, OH), both for free and immobilized enzyme. Degradation was carried out from pH 8.0 to 7.0. For each test, 1 mL AChCl solution at the respective concentration (0.005, 0.01, 0.05, and 0.1 mol L^{-1}) was prepared, for which the pH was adjusted to 8.0 using a 0.05 M disodium hydrogen phosphate solution. For constant conditions, a suitable measurement setup has been configured (Figure 1.S1). All solutions for the measurements were tempered to 25 °C. The general procedure and more detailed information on the potentiometric analysis can be found in the Supporting Information (Table 1.S1).

1.3 Results and discussion

1.3.1 Synthesis of porous silica membranes

To identify positive effects of a hierarchical pore structure compared to monomodal pore systems, we adapted the strategy from Figure 1.1. A hierarchical (macro–mesoporous) support is required when higher enzyme loadings are needed than realizable with a purely macroporous material. They can be achieved by an increase of the specific surface area with the additional mesopores inside the silica skeleton.

Starting sols comprised a sulfuric acid solution with tetraethyl orthosilicate (TEOS) as silica precursor, water as solvent and, for the macroporous and hierarchical materials, poly(ethylene oxide) (PEO) as porogen.²⁸ After several synthesis steps (gelation, hydrothermal treatment, washing, drying, calcination, sintering, shaping) silica membranes were received.^{28–30,37} They are denoted according to their respective pore system and mean pore size, *e.g.*, as 20_nm for a purely mesoporous material, or with 20–3500_nm (rounded) in the case of a macro–mesoporous material. For monomodal pore systems, mean pore sizes in the range from 10 to 39 nm (meso) and from 270 to 3272 nm (macro) could be realized. As expected, specific surface areas (S_{BET}) increased with decreasing pore diameter and ranged between 66 and 343 m² g⁻¹ (Table 1.1). The relatively high surface area of the macroporous material (66 m² g⁻¹) is attributed to a small amount of micropores that could not be completely removed during the sintering process. The fact that AChE is larger than 3 nm implies that these micropores become unaccessible and the material can be effectively described as macroporous. For supports with hierarchical pore structure, combinations of reaction pores (mesopores) in a range from 20 to 40 nm (see Figure 1S2 in the Supporting Information for nitrogen physisorption measurements on sample 20–3500_nm) and larger transport pores (macropores) with a mean size from 360 to 3781 nm were realized. They have specific surface areas between 105 and 262 m² g⁻¹ (Table 1.1).

Table 1.1. Preparation conditions and porosimetry data for selected monolithic silica samples.

Sample	Preparation Conditions	$d_{\text{macro}}^{\text{a}}$ / μm	$V_{\text{macro}}^{\text{a}}$ / cm ³ g ⁻¹	$d_{\text{meso}}^{\text{a}}$ / nm	$V_{\text{meso}}^{\text{a}}$ / cm ³ g ⁻¹	$\epsilon_{\text{total}}^{\text{a}}$ / –	$S_{\text{BET}}^{\text{b}}$ / m ² g ⁻¹
20_nm	0g-P-A-7M-120-6h-oH ₂ O	–	–	20	1.02	0.69	343
20–3500_nm	2.3g-P-A-7M-120-3h-oH ₂ O-c	3574	2.50	20	0.93	0.88	205
3250_nm	2.0g-P-oH ₂ O-s	3272	1.22	–	–	0.73	66*

^a Macropore size (d_{macro}) and volume (V_{macro}), mesopore size (d_{meso}) and volume (V_{meso}), as well as total porosity (ϵ_{total}) calculated from mercury intrusion porosimetry (MIP) data. d_{macro} and d_{meso} correspond to the average median pore diameter (corresponding to 50% of the total intrusion volume increment).

^b BET surface area (S_{BET}) based on nitrogen physisorption measurements.

* Based on nitrogen physisorption measurements and MIP data.

To compare supports with monomodal and hierarchical pore structure regarding their performance as potential sensor component, the following representative samples have been selected: 20_nm (mono-meso), 20–3500_nm (meso-macro), and 3250_nm (mono-macro). Silica membranes were examined by scanning electron microscopy (SEM) (Figure 1.S3, Supporting Information) and subjected to porosimetry (Table 1.1). The sol–gel process generates reproducible materials (~5% tolerance regarding mean pore diameter and pore volume) when using exactly the same procedure. The terminology for the preparation conditions is as follows: xg -P stands for the initial weight of PEO. A-7M-120- xh represents the conditions of the hydrothermal treatment in 7 M ammonia solution at 120 °C for x hours. Drying was carried out in an oven from overheated water (oH₂O). Abbreviations s and c denote sintering and calcination.

The shrinkage of the sol–gel materials is influenced by their synthesis conditions (*e.g.*, aging and drying) and their textural properties can therefore vary significantly. Consequently, larger cylindrical and crack-free monoliths were synthesized and shaped by further processing (core drilling and membrane sawing) into sol–gel membranes with defined geometry. The drying process is crucial for the preparation of crack-free silica monoliths, because unfavorable drying conditions can lead to complete degradation of the gel network. Stress on the network during drying is mainly caused by capillary tension. In addition, solvent removal leads to a decrease of the gel volume, referred to as shrinkage. Thereby occurring syneresis causes a stiffening of the gel network and the rigid network is prone to breaking. In their classical textbook, Brinker and Scherer describe the drying of porous gels in more detail.³⁸

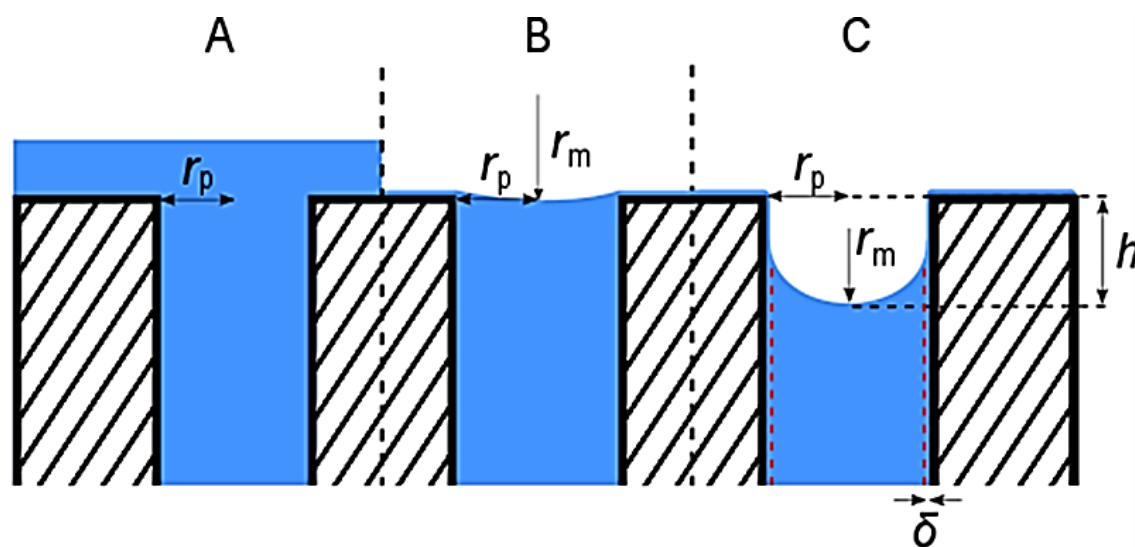


Figure 1.2. Schematic sequence of the drying process of porous materials according to Scherer and Smith.³⁹ (A) Initial stage of drying, (B) origin of menisci inside the pores, and (C) emptying of the pores leaving a thin film on the surface (r_p : pore radius, r_m : meniscus radius, h : depth of the evaporation front, δ : width of solvent film).

Evaporation occurs when the vapor pressure of the solvent p_v is smaller than the equilibrium vapor pressure p_0 . A tension P develops in the solvent phase, which is related to the vapor pressure of the corresponding liquid according to the Gibbs–Thomson equation

$$P = -\frac{RT}{V_m} \cdot \ln \frac{p_v}{p_0} \quad (1.1)$$

where R denotes the ideal gas constant, T is the temperature and V_m the molar volume of the liquid.³⁹ Figure 1.2 depicts the drying of a gel with cylindrical pores of radius r_p schematically.

At first, the gel-surrounding solvent evaporates (Figure 1.2A), while the liquid vapor interface is flat. In the case of a spreading liquid (with a contact angle between liquid and solid phase of $\theta = 0^\circ$), a thin film (of width δ) remains on the surface of the solid. Afterwards, the liquid in the pores starts to evaporate. If the contact angle between pore liquid and pore wall is $\theta < 90^\circ$, a concave meniscus is formed due to P , the described tension in the fluid (Figure 1.2B). P depends on the interfacial energy between liquid and vapor phase γ_{LV} and on the radius of the meniscus r_m . This relationship can be characterized by the Young–Laplace equation³⁹

$$P = -\frac{2\gamma_{LV}}{r_m} \quad (1.2)$$

The capillary tension draws the compliant network into the liquid and the occurring volume shrinkage is equal to the volume of evaporated liquid. This is referred to as the first stage of drying (constant-rate period).^{38,40–42} In the beginning, r_m is much larger than the pore radius r_p . Further drying decreases r_m and rises the tension correspondingly. The network becomes rigid by formation of new bonds. At a certain point, the solid phase is stiff enough to overcome the tension and no further shrinkage occurs. The radius of the meniscus r_m reaches its minimum and becomes equal to $r_p - \delta$. In the reverse, the capillary stress reaches its maximum value P_c and can be expressed through the following equation³⁹

$$P_c = \frac{2\gamma_{LV}}{r_p - \delta} \quad (1.3)$$

This point is critical and cracking most likely. From here onwards, the first falling-rate period takes place, where the depth h of the meniscus recedes into the pores, still leaving a thin film of solvent on the surface (Figure 1.2C). Through this film, the solvent flows to the exterior surface constantly, where most evaporation takes place.^{38,41,42} With increasing h , fluid flow becomes slower up to the point where remaining fluid leaves the pore system only by diffusion of its vapor, which is the final stage of drying, the second falling-rate period. According to Equations (1.1)–(1.3), the stress during drying is influenced by several parameters like r_p , γ , T , V_m , and p_v . A number of approaches have been developed to reduce the capillary stress P_c and obtain crack-free silica monoliths from sol–gel processing.^{43–45}

In this work, we introduce a cost and time efficient drying process together with an easy and safe experimental setup. For that purpose, the wet gel – placed in a closed plastic vessel – was

covered with water (two-fold volume of the monolith) to prevent partial drying during heating to 120 °C. It was subsequently dried at this temperature, *i.e.*, above the boiling point of water at normal pressure. The high temperature was important to minimize the interfacial energy γ of water.⁴⁶ Since evaporating water can leave the vessel only slowly through the small, defined puncture in the lid, the vapor pressure p_v should be kept close to its equilibrium value p_0 . This would decrease the evaporation rate as well as capillary tension according to the Gibbs–Thomson equation, *cf.* Equation (1.1).^{38,47,48} In addition to the preceding aging step, the hydrothermal conditions during drying could also contribute to the network strength, which should suppress shrinkage during the constant-rate period.⁴⁴ The pore widening caused by the hydrothermal aging also benefits the drying of monolithic silica gels according to Equation (1.3).^{43–45} The presented drying method guarantees fast, crack-free drying of silica monoliths even with mesopore sizes <15 nm – otherwise only possible by using complex drying methods like supercritical drying or ambient pressure drying.⁴⁹

Supercritical drying prevents capillary stress completely by exceeding the critical point of the pore liquid to eliminate the liquid–vapor interface and phase transitions during the process.^{50–53} Ambient pressure drying reduces capillary stress due to the lower interfacial energy γ_{LV} and larger molar volume V_m of the employed organic solvent.^{51,52,54,55} Despite the possibility to dry almost without shrinkage (<1%), both methods suffer from drawbacks when considering the costs and duration of the drying process as well as requirements regarding safety issues and environmentally benign green chemistry. Kirkbir *et al.*⁵⁶ succeeded in drying monolithic silica gels under subcritical conditions with low shrinkage (<1%), however, solvent exchange as well as a pressure chamber were still required. In this regard, the drying procedure presented here is reliable for fast drying of silica monoliths with a relatively easy setup, though it is accompanied by moderate overall shrinkage (20–25%). This drying method is of great importance especially for the purely mesoporous materials, because here capillary stress is significantly higher due to the small pore size. Without this drying procedure the purely mesoporous materials could not have been obtained in a stable manner, or only by significantly more complex drying methods. For comparability, purely macroporous and hierarchical monoliths were also dried by this method, as it cannot be excluded that additional pore widening occurs despite hydrothermal treatment.

1.3.2 Functionalization of the silica surface

Immobilization of AChE was performed through functionalization of the silica surface with 3-(glycidoxypropyl)dimethylmethoxysilane. On the one hand, the monomethoxy modification of the silane prevents its polymerization, and on the other hand, the glycidoxy group binds the enzyme directly to the surface without needing an additional spacer, *e.g.*, glutardialdehyde.⁵⁷ Concentrations between 0.3 and 100 vol.% can be applied for surface functionalization with silanization reagents.⁵⁸ Preliminary studies have shown that the materials become hydrophobic after using a 3 or 5 wt.% 3-(glycidoxypropyl)dimethylmethoxysilane solution, preventing their use in aqueous medium (Table 1S2, Supporting Information). For this reason, and because pore-

blocking should be avoided, a concentration of 1 wt.% was used. Prior to functionalization, all materials were gently rehydroxylated in water for 3 h at 25 °C to achieve a high and comparable concentration of surface hydroxyl groups. The concentration of hydroxyl groups on the pore surface was calculated by thermogravimetric measurements. Based on the mass loss and taking into account the specific surface area, five hydroxyl groups per nm² could be generated with the rehydroxylation step. Diffuse reflectance infrared fourier transform spectroscopy (DRIFTS) was used to study the functionalization with 3-(glycidoxypropyl)dimethylmethoxysilane and associated changes in the surface properties. A rehydroxylated sample was used for comparison (Figure 1.3).

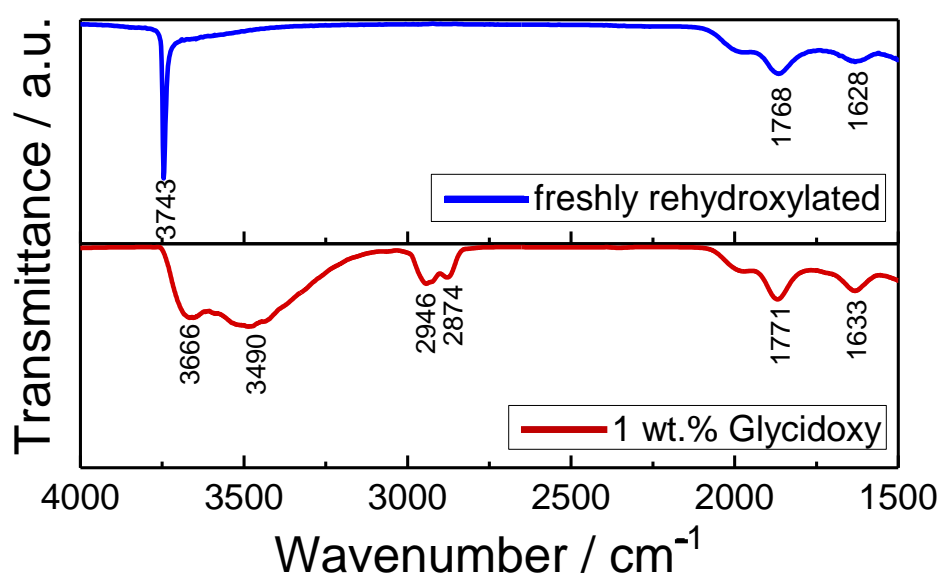


Figure 1.3. DRIFT-IR spectrum of a freshly rehydroxylated, purely macroporous membrane (top) and after functionalization with a 1 wt.% 3-(glycidoxypropyl)dimethylmethoxysilane solution (bottom).

Because of the deformation vibrations of the SiO₂ framework the fingerprint region in which, *e.g.*, ring deformation vibrations of the epoxy group of the functionalization reagent are found (950–815 cm⁻¹), could not be used for evidence. The spectrum of the rehydroxylated material provides a sharp band at 3743 cm⁻¹ (stretching vibrations of isolated hydroxyl groups). Based on its intensity only a small amount of water is physisorbed on the surface. The bands at 1768 and 1628 cm⁻¹ cannot be unambiguously assigned. They may represent deformation vibrations of the SiO₂ framework, as they are also present in the spectrum for the functionalized material. The successful binding of the functionalization reagent is demonstrated by the bands corresponding to the asymmetric and symmetric stretching vibrations of the -CH₂ groups of the propyl chain and the methyl groups of the silane (from 3100 to 2700 cm⁻¹). The sharp, intense band for the hydroxyl groups is now obscured by a broad band from physisorbed water (3700–3250 cm⁻¹). This qualitative proof is supported by the elemental analysis (Table 1.S2) and SEM-EDX images (Figure 1.S4).

Further, we determined the number of functional surface species ($N_{\text{glycidoxy}}$) quantitatively by titration (Table 1.2 and Table 1.S3 in the Supporting Information). Given values represent the mean from three individual investigations. It should be mentioned that for each membrane the same amount of modification reagent (corresponding to the same number of silane molecules) was used to ensure comparability. The data in Table 1.2 ($N_{\text{glycidoxy}}/\text{nm}^2$) reveal that the offered 1 wt.% 3-(glycidoxypropyl)dimethylmethoxysilane solution presents an overshoot for the macroporous membranes (sample 3250_nm) and an undershoot for the mesoporous membranes (sample 20_nm).

Table 1.2. Number of functional groups ($N_{\text{glycidoxy}}$) on the support materials.

Sample	$S_{\text{BET}} /$ $\text{m}^2 \text{g}^{-1}$	$N_{\text{glycidoxy}} /$ $\mu\text{mol g}^{-1}$	$N_{\text{glycidoxy}}^{\text{a}} /$ nm^{-2}
20_nm	343	419±6	0.7±0.01
20–3500_nm	205	392±5	1.2±0.01
3250_nm	66*	255±4	2.3±0.03

^a Calculated using Avogadro's constant.

* Based on nitrogen physisorption measurements and MIP data.

The influence of the pore system can already be seen at this stage, as the macroporous sample contains significantly less functional groups per mass ($255 \mu\text{mol g}^{-1}$) than the mesoporous sample ($419 \mu\text{mol g}^{-1}$). The hierarchical support combines features of these two materials and demonstrates the positive effect of a macro–mesoporous architecture by an intermediate concentration ($392 \mu\text{mol g}^{-1}$). As the same amount of silanization reagent has been employed for all samples, their area-normalized functionalization is inversely proportional to their S_{BET} -values. For example, $N_{\text{glycidoxy}}/\text{nm}^2$ for sample 20–3500_nm is by a factor of 1.7 higher than for the mesoporous sample 20_nm and its specific surface area is smaller by nearly the same factor (*cf.* Table 1.2).

1.3.3 Impact of pore space hierarchy on transport efficiency

By analyzing the maximum amount of immobilized AChE as a function of pore size and membrane morphology, the focus was on the reaction pores (mesopores). The determination of enzyme loading onto a support with the protein assay kit is based on a reduction of Cu^{2+} to Cu^+ ions. Bicinchoninic acid was used to complex the monovalent copper ions. Extinction of the solutions (Table 1.S4, Supporting Information) was determined at 562 nm and converted into enzyme loading (C_{ACHE}) by calibration. The successful enzyme immobilization is confirmed by SEM-EDX measurements (Figure 1.S4).

For comparability, the determination of the maximum loading concentration (c_{\max}) for AChE was carried out per membrane with fixed geometry, because it reflects envisioned operation of these materials as geometrical unit (with given dimensions) in a flow-through reactor or sensor design. Total porosities of these membranes expectedly varied according to the individual pore systems (*cf.* ϵ_{total} in Table 1.1). From the data in Table 1.3 it is clear that also c_{\max} (AChE) depends on the morphology of a pore system, because the surface area of a membrane (S) available for immobilization is intrinsically related to it.

Table 1.3. Maximum AChE loading concentrations (c_{\max}) for membranes with identical geometry, but different pore space morphology and surface area S .

Sample	S / m ² /membrane	c_{theor} (AChE) / μg/membrane	c_{\max} (AChE) / μg/membrane
20_nm	4.4 ^a	60	38.5±0.8
20–3500_nm	1.0 ^a	40	15.5±0.4
3250_nm	0.02 ^b	40	4.1±0.2

^a Based on nitrogen physisorption measurements.

^b Based on the MIP data only.

The analyzed data reveal that the amount of enzyme bound to a support (c_{\max} , average of three individual measurements on different membranes for a given pore system) is less than the enzyme amount offered with the starting solutions (c_{theor}). Depending on the pore system and pore size, however, this only happens for higher theoretical concentrations (Table 1.S4). For the pore system containing only mesopores, the low loading can be attributed to pore blocking effects and associated obstruction of parts of the pore space. The mesopore network represents a tubular, three-dimensional interconnected structure which – due to the size of the enzyme and bottle-necking effects – can impose severe steric hindrance and ultimately prevent the access of the enzyme to major parts of the surface. The simulation of hindered diffusion in physical reconstructions of the mesoporous skeleton from hierarchical, macro–mesoporous silica monoliths has revealed that only ~40% of the mesoporosity (mean mesopore size: 20 nm) remains accessible for molecules with a size of 6 nm.⁵⁹ This situation is similar to that considered here regarding mean mesopore size and size of the AChE molecules. Compared with the 20_nm sample (mono-meso), the 3250_nm sample (mono-macro) offers a *ca.* 99% smaller surface area (Table 1.3). Still, a c_{\max} of 4.1 μg/membrane is achieved, corresponding to *ca.* 10% of c_{\max} for the mesoporous material (38.5 μg/membrane). Obviously, this originates in a quantitative exploitation of the macropore surface by the enzyme under conditions when steric hindrance is practically absent.

While a purely macroporous material offers excellent properties regarding liquid-phase mass transfer, *i.e.*, relatively unhindered diffusion of large molecules and also little obstructed, highly permeable flow (when used in a flow-through design),^{21,22} it can bind only much fewer enzyme

molecules compared to purely mesoporous supports. As shown, a maximum loading of 38.5 μg AChE per membrane is obtained for the purely mesoporous material (Table 1.3), but in this case mass transfer into the membrane and within its mesopore system becomes limiting. Due to the small pore size the material is unsuitable, *e.g.*, as geometrical element of a flow-through reactor, because enormous pressures will be needed to realize advection-dominated mass transfer in the mesopores (and through the membrane).^{22,30,37} Further, purely diffusive liquid-phase transport through a relatively thick (0.5 mm) membrane is slow. In contrast, the material with hierarchical, macro–mesoporous system will allow to combine enhanced diffusion and advection-dominated mass transfer in the macropores with the larger amount of covalently bound enzyme molecules in a thin, only *ca.* 1 μm -thick mesoporous skeleton (*cf.* Figure 1.S3). Sample 20–3500_nm could immobilize almost 4 times the AChE amount (15.5 $\mu\text{g}/\text{membrane}$) of the purely macroporous material. The hierarchical system offers a large specific surface area (S_{BET}) and a large external surface of the silica skeleton. The latter provides intense contact area between stagnant and flowing fluids in the mesoporous skeleton and the macropore space, respectively. Moreover, independent manipulation of macropore size and skeleton thickness allows to control diffusive mass transfer resistance in the mesoporous skeleton beyond mesopore size and thereby fine-tune transport to and from the enzyme in the mesopores. Since enzyme immobilization is based on a reaction between surface epoxide groups and amino groups of amino acids in AChE, the immobilization process and trends observed for the individual pore systems should be similarly applicable to a number of other enzymes.

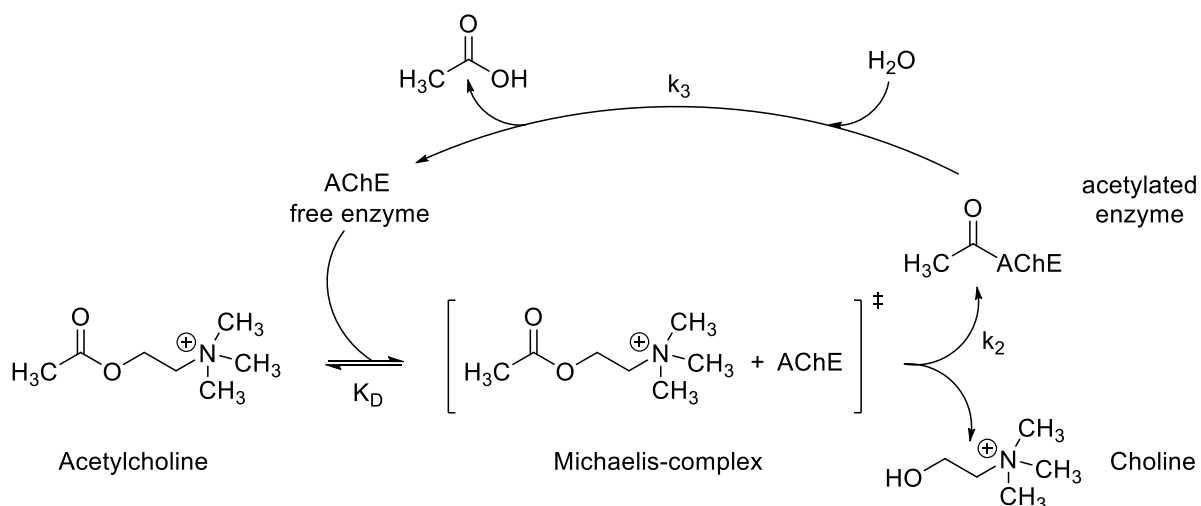


Figure 1.4. AChE-catalyzed ACh degradation with attribution of the rate constants and resulting products.^{60,61}

ACh is degraded by AChE into choline and acetic acid (Figure 1.4), so that the reaction can be monitored by potentiometric pH measurement. Enzyme activity strongly depends on the pH; beyond the pH optimum enzyme activity decreases up to complete activity loss and associated denaturation or a permanent damage of the enzyme.⁶² The pH optimum for AChE is in the range of 7–9, thus, a disodium hydrogen phosphate buffer solution was used to adjust the starting pH

to 8.⁶³ To determine the response time of a sensor membrane by pH changes from 8 to 7 as a function of ACh concentration and calculate apparent reaction rates, the experimental setup in Figure 1.S1 (Supporting Information) was held constant regarding all relevant aspects, *e.g.*, membrane geometry, solution volume, and stirring speed. Differences in response times could therefore be attributed to the impact of the individual pore systems. The response time is used to estimate an apparent reaction rate of the ACh degradation according to

$$v_{r,app} = \frac{n_{HAC}}{t_{8-7}} \quad (1.4)$$

In Equation (1.4), n_{HAC} is the amount of formed acetic acid (back-calculated from the potentiometric pH measurements) and t_{8-7} denotes the response time for a pH change from 8 to 7. The degradation of ACh and the activity of free AChE were monitored in advance (Figure 1.S5, Supporting Information). With 4 μg of free AChE a reaction time of $t_{8-7} = 106 \text{ s}$ was found for the targeted pH change. Based on Equation (1.4), the reaction rate is 31 nmol s^{-1} , equivalent to an activity of 1.8 U ($= 1.8 \mu\text{mol min}^{-1}$), close to the specification by the manufacturer ($518 \text{ U mg}^{-1} \cdot 0.004 \text{ mg} = 2.1 \text{ U}$).

The impact of the pore system (morphology) on response time and apparent reaction rate of the developed model system was investigated at an AChE loading of $4.1 \mu\text{g}/\text{membrane}$ for all three pore systems, a value that reflects c_{max} for the purely macroporous sample (*cf.* Table 1.3). That loading was chosen as a consequence of the conditions in this work and corresponds to the highest common loading in a comparison including all three pore systems. This means that the three materials (membranes) had the same amount of enzyme molecules ($4.1 \mu\text{g}$) distributed over their intrinsically different pore systems. Experimental results summarized in Table 1.S5 (Supporting Information) reveal that for materials with monomodal pore structure (mono-meso, mono-macro) the response times increased with increasing ACh concentration up to a saturation point. Concomitantly, the apparent ACh degradation rates approached a maximum (Figure 1.S6, Supporting Information), which is typical in enzyme kinetics.⁶⁴ A similar effect is seen for the hierarchical materials (data not shown). These kinetic data were used to determine maximum apparent reaction rates v_{max} from the corresponding Lineweaver-Burk plots (Figure 1.S7 and Table 1.S6, Supporting Information).⁶⁵ It should be emphasized that the recorded apparent kinetic data reflect both the intrinsic reaction kinetics and eventual transport limitations by an individual pore system. Figure 1.5 reveals only a slight disadvantage for the hierarchical pore system (20–3500_nm) compared to the macroporous structure (3250_nm), as seen in their close v_{max} -data (red circles). Clearly, transport into the macroporous membrane is least obstructed and its response is fastest. The purely mesoporous membrane shows a much slower response time (*cf.* Table 1.S5), indicating a substantially obstructed transport into and through its pore system, even though mesoporous and macroporous systems share similar porosities ($\epsilon_{total} = 0.69$ and 0.73 , Table 1.1).

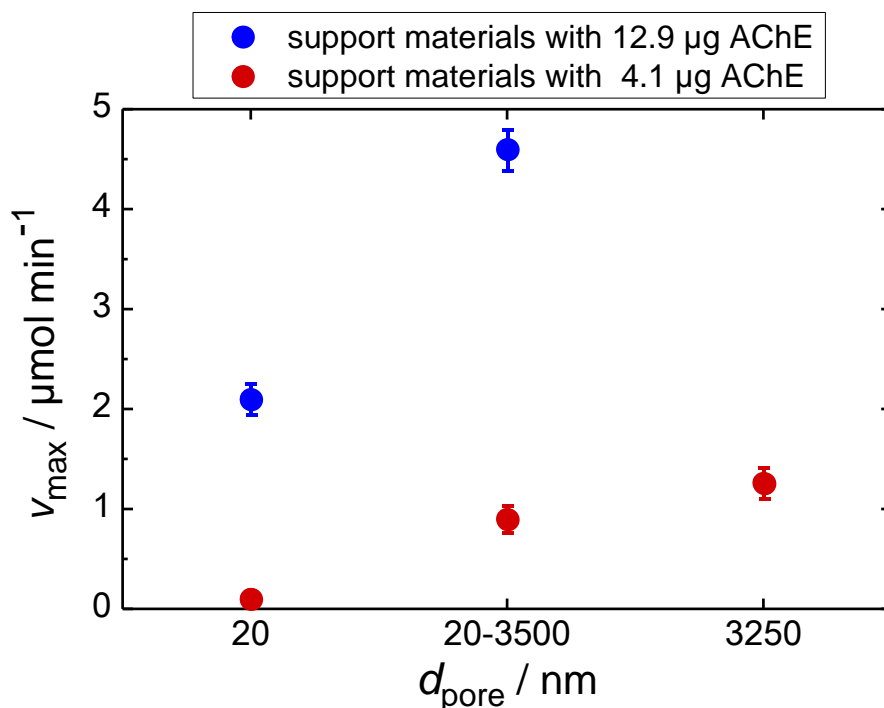


Figure 1.5. Maximum apparent reaction rates v_{max} for the AChE-catalyzed ACh degradation depending on morphology of the pore system and AChE loading. v_{max} -values were determined from the Lineweaver–Burk plots of the apparent kinetic data (*cf.* Figure 1.S6). Error ranges for mesoporous materials at 4.1 $\mu\text{g}/\text{membrane}$ could not be presented due to the small deviations (*cf.* Table 1.S5).

For the purely macroporous material the actual enzyme loading (also its maximum loading) is sufficient and transport through the macropore network least obstructed compared with the hierarchical and the purely mesoporous material. Consequently, its efficiency is also highest. On the other hand, the maximum enzyme loading of the purely macroporous membrane may not suffice in certain applications like the detection of pesticides in food products. For example, $\sim 12.9 \mu\text{g AChE}$ per membrane are needed for the detection of the legally prescribed maximum residue level of the pesticide carbofuran.⁶⁶ These 12.9 μg of AChE (3.2 times higher than c_{max} of the purely macroporous material) correspond to $\sim 34\%$ and $\sim 83\%$ of the maximum loadings for the mesoporous sample 20_nm and the hierarchical sample 20–3500_nm, respectively (*cf.* Table 1.3). Importantly, purely macroporous membranes with decreased macropore size and therefore larger macropore surface as well as higher c_{max} compared to sample 3250_nm cannot achieve the targeted AChE loading of 12.9 μg (*cf.* Table 1.S4).

With results for 12.9 $\mu\text{g AChE}$ per membrane (blue circles, Figure 1.5) the purely mesoporous material demonstrates an impact of the enzyme loading on the reaction rate. It can be attributed to faster substrate conversion due to a larger number of active centers and decreased diffusion lengths of substrate to the enzyme and of products out of the pore network. Also for the support with hierarchical structure reaction rates increase at higher loading, *i.e.*, v_{max} is increased by a factor of 5 for the 3.2 times higher AChE loading (Figure 1.5). The beneficial effect of pore

space hierarchy is clearly documented here – the hierarchical pore system responds more than twice as fast as the purely mesoporous material. A biosensor equipped with the hierarchical support can therefore demonstrate improved efficiency.

Looking ahead, these studies may be transferred to a flow-through design. Then, due to pressure-driven flow through the hierarchical material, transport in its macropores moves from diffusion-limited to advection-dominated and pure diffusion takes place only inside a thin mesoporous skeleton. This operation will also allow to move from the apparent to the intrinsic reaction kinetics (as transport limitations are removed) and access parameters like the reaction order, rate constants, and activation energies.³⁰ On the other hand, with an adequate enzyme loading in the macropores, a purely macroporous material may suffice as functional component in biosensor applications and at the same time take full advantage of the fast mass transfer due to forced advection in a flow-through design. If required, the surface area (and thus, enzyme loading) of the macropores can be increased to some extent by reducing the macropore size and increasing the macroporosity.²²

1.4 Conclusions

The effect of a hierarchical pore system on the diffusive response of sol–gel based materials was systematically studied and compared with corresponding monomodal (purely mesoporous and macroporous) pore systems for the first time. Supports in the form of membranes (6 mm-diameter × 0.5 mm thickness) were prepared by the sol–gel process to address the impact of the three different pore systems on features of the functional components derived by subsequent enzyme immobilization. A general preparation scheme was adapted with varying composition of the starting synthesis mixture as well as various additional treatments such as sintering and alkaline aging. Mesoporous materials have been prepared as stable, shaped bodies by a novel drying method. Hierarchical systems were prepared *via* polymer-induced phase separation with mesopores and macropores from the same size ranges as realized for the monomodal pore systems. All surfaces were functionalized with 3-(glycidoxypropyl)dimethylmethoxysilane and AChE was then immobilized covalently *via* the epoxide group of the silane. The immobilized enzyme amounts depended on the specific surface area of the materials. Membrane preparation, surface functionalization, and enzyme immobilization were realized in good reproducibility, which underlines the suitability of the adapted synthesis strategy.

It has been shown that a membrane with hierarchical pore system and a macropore size similar to a purely macroporous support exhibits a much higher AChE loading capacity due to the additional mesopores. Further, it was investigated if the hierarchy has an impact on the response time of AChE-based functional membranes. At this stage, studies remained limited to purely diffusive membrane transport, so that apparent reaction rates reflected intrinsic diffusion limitations of a pore system in addition to the intrinsic reaction kinetics. Response times of the prepared membranes were determined for the AChE-catalyzed degradation of ACh to choline and acetic acid. With 4.1 µg AChE per membrane the purely macroporous material revealed a

slight advantage over the hierarchical pore system; exclusive transport in the macropores is least obstructed giving the fastest response. On the other hand, for the detection of the legal residue level of carbofuran $\sim 12.9 \mu\text{g AChE}$ per membrane are required (exceeding c_{max} of the purely macroporous material). Then, the hierarchical pore system gives the fastest response by combining advantages of the two monomodal systems, *i.e.*, enhanced mass transfer and higher enzyme loading.

Gained insight will help to tailor new hybrid materials based on a functional component and an inorganic support, *e.g.*, in chemo- and biosensor technology to improve sensor performance. The gain could be particularly impressive as the application is realized in a flow-through design and full advantage is taken of both a highly permeable (flow-through) macropore system and negligible resistance to diffusion through a thin (just $\sim 1 \mu\text{m}$ thick) mesoporous skeleton in a hierarchical support.

1.5 Supporting Information

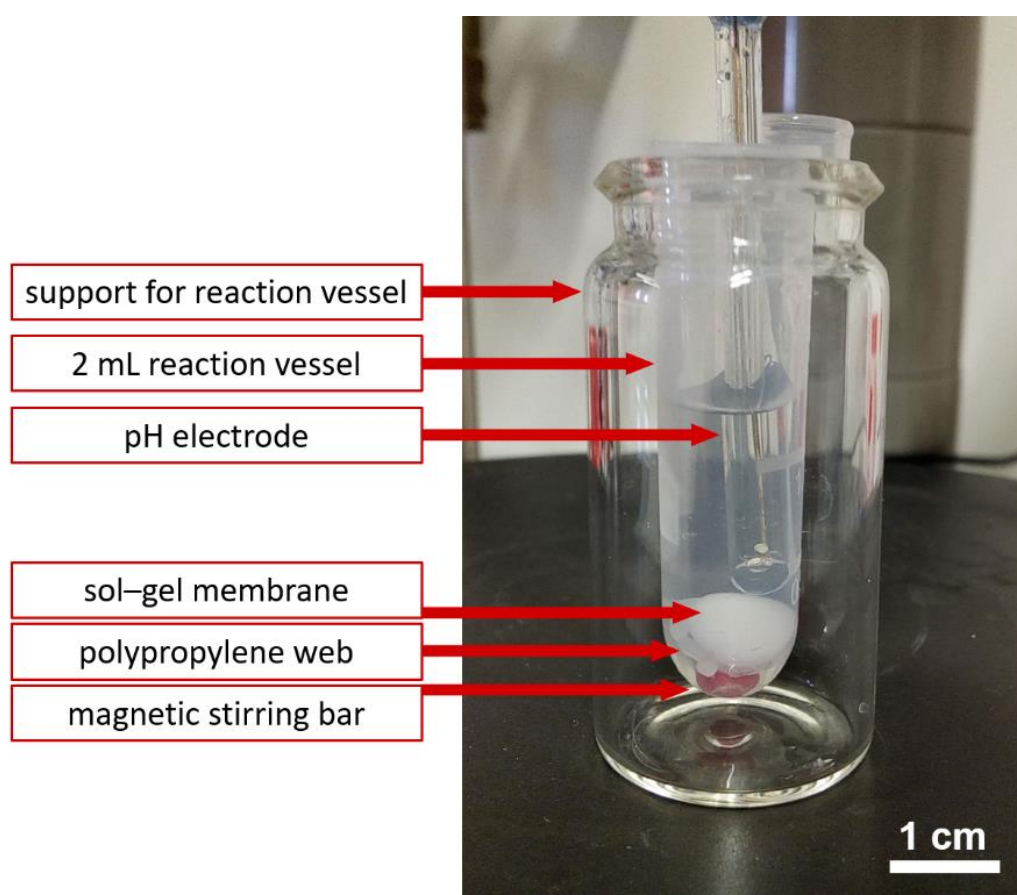


Figure 1.S1. Experimental setup for potentiometric pH determination during the AChE-catalyzed ACh degradation.

Table 1.S1. Composition of AChCl solutions used for the verification of pH changes.

$c_{\text{AChCl}} /$ mol L^{-1}	$V_{\text{H}_2\text{O}} /$ μL	$V_{\text{AChCl}} /$ μL	pH	$V_{\text{Na}_2\text{HPO}_4} /$ μL	pH	$V_{\text{HAc}} /$ μL	pH
0.005	993.7	5	4.89	1.25	7.99	0.45	6.99
0.01	986.0	10	4.82	4.00	7.96	0.90	7.02
0.05	938.0	50	4.04	12.0	8.00	3.50	6.97
0.1	875.4	100	3.95	24.6	8.05	6.50	7.03

Potentiometric pH measurements for the enzyme-catalyzed degradation of ACh to choline and acetic acid were used to evaluate effects of pore space morphology on apparent reaction rate. It was important to employ an experimental setup (*cf.* Figure 1.S1) that ensures high reproducibility to correlate revealed trends to the influence of the actual pore system.

General procedure

Potentiometric pH measurements were performed for all membranes in 1 mL of substrate solution, which corresponded to a constant filling height of 2 cm in the reaction vessel. This ensured that the pH electrode with an immersion depth of 1 cm was always at the same distance from the membrane. The stirring speed of the magnetic stirrer was fixed at 150 rpm. To protect the membrane, a polypropylene net was placed above the magnetic stirring rod.

Analysis of the AChE-catalyzed ACh degradation was conducted with the pH electrode InLab Ultra Micro pH and the measuring instrument Seven Easy pH from Mettler Toledo (Columbus, OH). One measured value per second was recorded with the aid of the Terra Term Pro software. AChE activity was determined both for the free enzyme and for the immobilized samples. For that purpose, a fresh AChCl solution was used. During preparation of the solution, it was taken into account that AChCl acts as a weak acid in an aqueous solution, whereby the solution pH becomes concentration-dependent. Because the pH optimum of AChE is in the range of 7–9, the pH value of the substrate solution was adjusted to 8.0 using a 0.05 M disodium hydrogen phosphate solution.^{S1} All required reagents and devices were maintained at a temperature of 25 °C for the measurements. To determine response times, the measurement range was fixed to the pH change from 8.0 to 7.0.

In preliminary studies, it was verified how much acetic acid (HAc) needs to be produced during ACh degradation in dependence of the concentration of the AChCl solution in order to achieve the targeted pH change from 8.0 to 7.0. A 0.5 M acetic acid solution was used for this purpose. Table 1.S1 shows that with increasing AChCl concentration more acetic acid must be produced to effect the same drop in the pH-value.

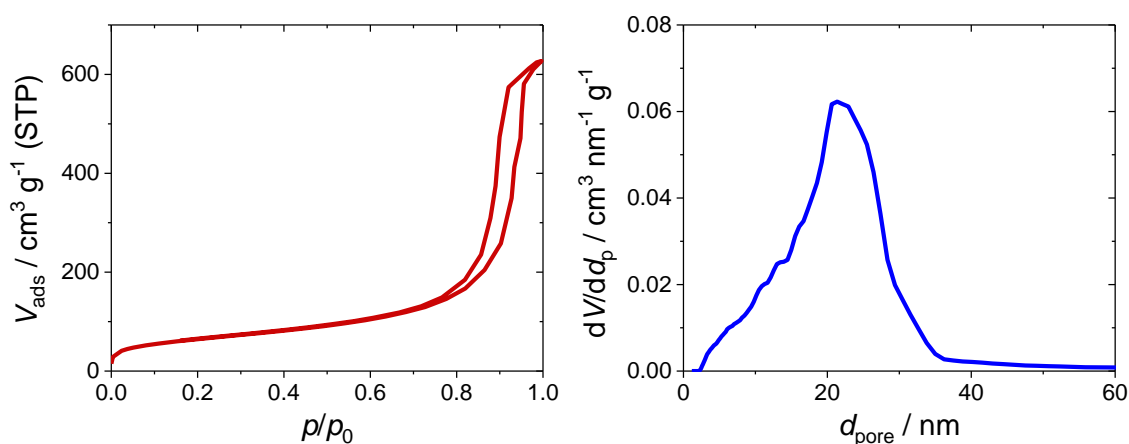


Figure 1.S2. Nitrogen physisorption isotherms (left) and resulting pore size distribution (right) for the hierarchical, macro–mesoporous sample 20–3500_nm. The pore size distribution was derived from the adsorption branch by using the non-local density functional theory (NLDFT) method and assuming a cylindrical pore model.^{S2} The average mesopore diameter of 21 nm correlates well with the d_{meso} estimate based on MIP analysis (Table 1.1, main text).

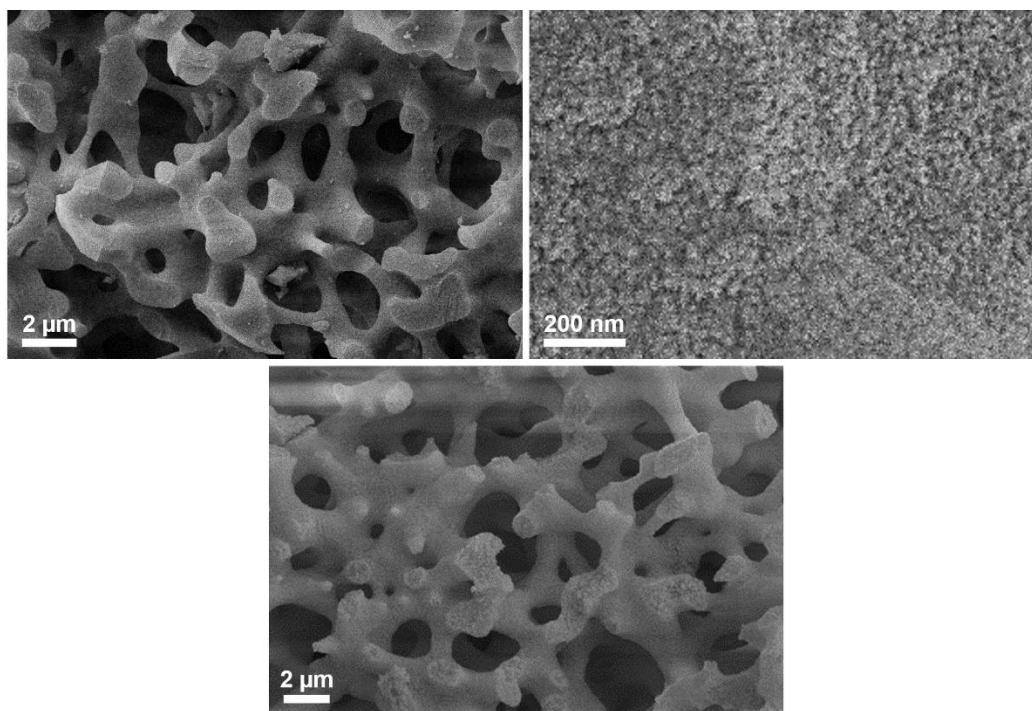


Figure 1.S3. SEM images of the three different pore space morphologies. Sample 20–3500_nm (bottom), illustrating the interconnected macropore space of the support with hierarchical pore structure. The mesopores are located inside the silica skeleton and are representative as well for the purely mesoporous material shown in the top-right panel. The purely macroporous material (top left) has a similar structure as the hierarchical material after thermal post-treatment applied to remove the mesoporosity. A detailed analysis of the mesopore space morphology of these silica materials is reported in a previous study, in which their structure was three-dimensionally reconstructed using electron tomography.^{S3}

Table 1.S2. Results of the elemental analysis for the functionalized and the enzyme-immobilized hierarchical materials (20–3500 nm).

Sample	N / %	H / %	C / %
1wt.%_Glycidoxy	0.1	0.5	1.2
1wt.%_Glycidoxy_Enzyme	0.4	1.0	4.8
2wt.%_Glycidoxy_Enzyme	0.3	0.9	2.9

Elemental analysis was run on a vario Micro cube (Elementar, Langensfeld, Germany); given values are the average from two individual measurements.

Carbon contents of the functionalized sample 1wt.%_Glycidoxy and the enzyme-immobilized sample 1wt.%_Glycidoxy_Enzyme indicate that functionalization and enzyme immobilization were successful. An increase in the concentration of functionalization reagent to 2 wt.% has an adverse effect on the subsequent enzyme immobilization (at the same enzyme loading of 4.1 $\mu\text{g}/\text{membrane}$), since the carbon content drops significantly. With this higher concentration of functionalization reagent the hydrophobicity of the silica surface increases, inhibiting enzyme immobilization that takes place from an aqueous solution.

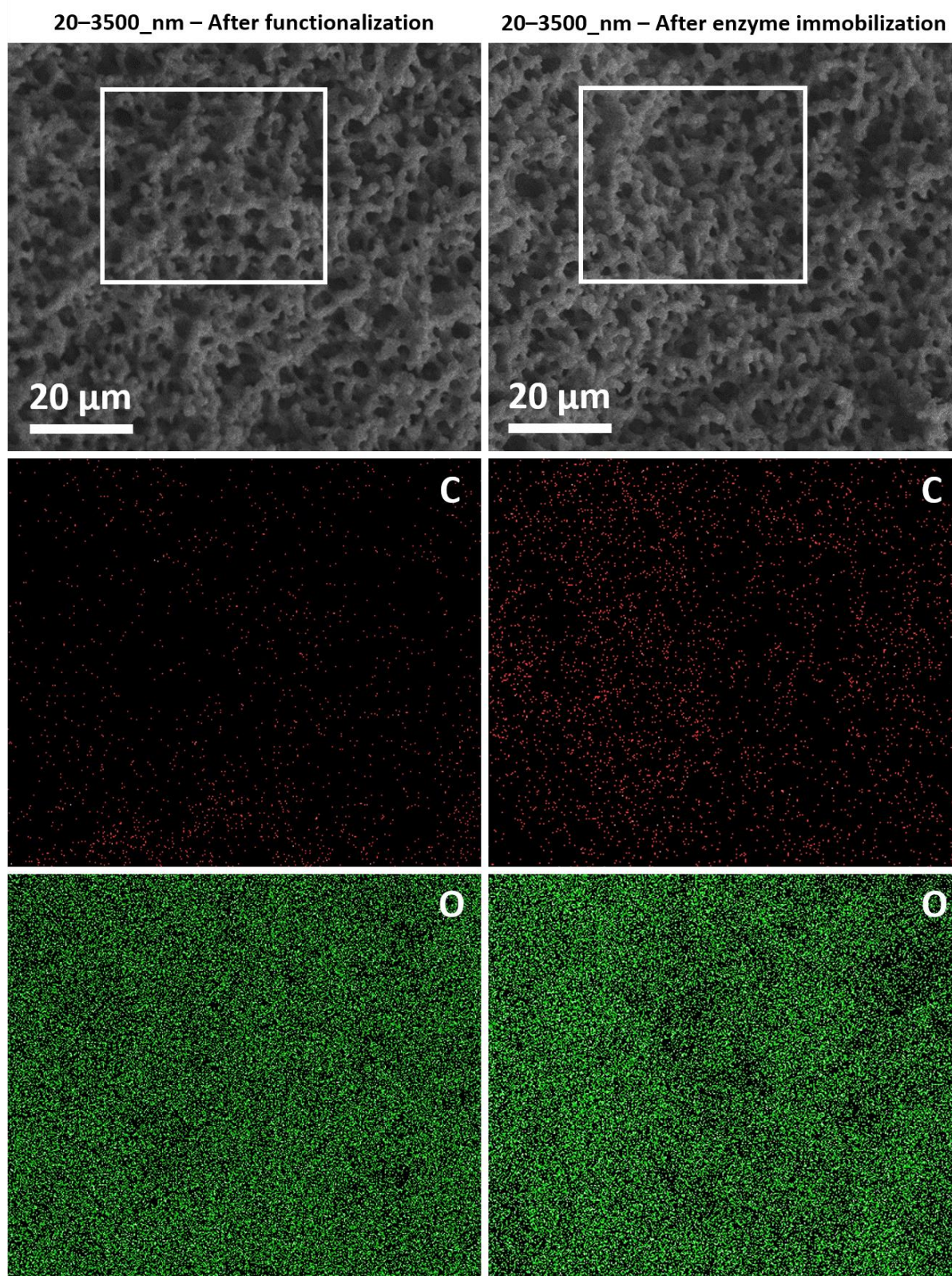


Figure 1.S4. SEM-EDX images of hierarchically structured material (20–3500_nm) after surface functionalization (left) and after the additional enzyme immobilization (right) reveal the carbon (red) and the oxygen (green) content.

Red dots represent the presence of carbon atoms on the surface attributed to functionalization, since the membranes do not contain organic material after calcination. Green dots indicate the oxygen atoms on the material surface and serve as a reference for the calculation of the atom contents. The detection limit for nitrogen atoms was not reached, which is in line with the results of the elemental analysis (Table 1.S1). The ratio of carbon to oxygen atoms on the surface after functionalization is 4.6 at.% C to 95.4 at.% O, which corresponds to 3.5 wt.% C to 96.5 wt.% O. After enzyme immobilization the ratio is 9.3 wt.% C to 90.7 wt.% O (11.9 at.% C to 88.1 at.% O). The increased carbon content reveals that enzyme has been successfully immobilized on the surface of the membrane. The moderate increase can be explained by the fact that the hierarchically structured material still contains a significant amount of free linker, since only 4.1 μg of enzyme were offered to each membrane.

Table 1.S3. Number of functional groups ($N_{\text{glycidoxy}}$) on the support materials determined by acid–base titration.

Sample	ΔV_{HCl} / mL	m_{sample} / mg	$\langle m_{\text{mem}} \rangle$ / mg/membrane	S_{BET} / $\text{m}^2 \text{g}^{-1}$	$N_{\text{glycidoxy}}$ / $\mu\text{mol g}^{-1}$	$N_{\text{glycidoxy}}^{\text{a}}$ / nm^{-2}
20_nm	0.57	533	13.3	343	419 \pm 6	0.7 \pm 0.01
20–3500_nm	0.83	537	5.0	205	392 \pm 5	1.2 \pm 0.01
3250_nm	2.40	553	11.7	66*	255 \pm 4	2.3 \pm 0.03

^a Number of 3-(glycidoxypropyl)dimethylmethoxy groups calculated using Avogadro's constant.

* Calculated from nitrogen physisorption measurements and additional MIP data.

Due to the low concentration of the functionalization species (depending on the specific surface of the materials) sample quantities m_{sample} of 500–600 mg became necessary. For this purpose, between 40 and 120 membranes with $\langle m_{\text{mem}} \rangle$ were collected, which differed by less than 50 μm in diameter and by less than 10 μm in height. The standard deviation for $\langle m_{\text{mem}} \rangle$ was 3.3–4.5%. Experiments were performed three times and the mean value is given with the corresponding standard deviation.

Epoxy groups react with acids and bases (*e.g.*, amines) under ring opening. The reaction of the *n*-butylamine with the functional groups on the support allows back-titration of the remaining *n*-butylamine concentration with an acid (*e.g.*, HCl), whereby the number of epoxide groups on the surface can be determined. For this purpose, about 500 mg of the membranes were mixed with 25 mL of a 0.01 M *n*-butylamine solution for 1 h at 60 °C in a water bath. Subsequently, 5 ml of the solution were titrated with a 0.01 M HCl solution (three repetitions). Bromothymol blue was used as indicator.

Table 1.S4. Photometrically determined absorbances of the enzyme solutions and the resulting enzyme concentrations per membrane.

Sample	C_{ACHE} / $\mu\text{g}/\text{membrane}$		Extinction				C_{ACHE} / $\mu\text{g}/\text{membrane}$		
	theor.	start	end	WS1	WS2	WS3	sorb.	WS	corr.
20_nm	4	0.1118	0.0044	0.0025	0	0	4.0	0.3	3.7±0.4
	10	0.3053	0.0378	0.0021	0	0	9.9	0.2	9.6±0.2
	20	0.5444	0.0106	0.0077	0.0009	0	19.7	0.5	19.3±0.6
	40	1.0842	0.0303	0.0089	0.0041	0.0006	39.0	0.7	38.3±0.8
	60	1.5956	0.5193	0.0199	0.0082	0.0031	39.8	1.3	38.5±0.8
40_nm	4	0.1114	0.0020	0.0034	0	0	4.0	0.3	3.8±0.3
	10	0.3042	0.0289	0.0087	0	0	10.2	0.5	9.7±0.3
	20	0.5449	0.0017	0.0037	0.0025	0	20.1	0.4	19.7±0.5
	40	1.0857	0.1022	0.0125	0.0030	0.0009	36.4	0.8	35.6±0.7
	60	1.5899	0.5784	0.0253	0.0094	0.0027	37.4	1.5	35.8±0.6
20–1000_nm	4	0.1108	0.0025	0.0017	0	0	4.0	0.2	3.8±0.2
	10	0.2961	0.0104	0.0038	0	0	10.6	0.3	10.3±0.1
	20	0.5435	0.0098	0.0056	0.0006	0	19.7	0.4	19.3±0.6
	40	1.0840	0.5344	0.0172	0.0047	0.0013	20.3	1.0	19.3±0.4
20–3500_nm	4	0.1103	0.0021	0.0028	0	0	4.0	0.3	3.7±0.3
	10	0.2967	0.0077	0.0032	0	0	10.7	0.3	10.4±0.2
	20	0.5436	0.1108	0.0074	0.0007	0	16.0	0.5	15.5±0.5
	40	1.0835	0.6402	0.0163	0.0043	0.0011	16.4	1.0	15.5±0.4
40–3500_nm	4	0.1100	0.0037	0.0007	0	0	3.9	0.2	3.7±0.2
	10	0.2963	0.0111	0.0043	0	0	10.5	0.3	10.2±0.3
	20	0.5431	0.1756	0.0099	0.0011	0	13.6	0.6	13.0±0.1
350_nm	40	1.0842	0.7016	0.0238	0.0049	0.0009	14.1	1.3	12.9±0.3
	4	0.1140	0.0073	0.0009	0	0	3.9	0.2	3.7±0.4
	10	0.2771	0.0054	0.0082	0	0	10.0	0.5	9.6±0.6
	20	0.5436	0.2393	0.0126	0.0034	0	11.2	0.8	10.5±0.3
1000_nm	40	1.0879	0.7792	0.0145	0.0021	0	11.4	0.8	10.6±0.5
	4	0.1154	0.0048	0.0034	0	0	4.1	0.3	3.8±0.4
	10	0.2988	0.0533	0.0076	0.0023	0	9.1	0.5	8.5±0.6
3250_nm	20	0.5449	0.2994	0.0115	0.0026	0	9.1	0.7	8.4±0.5
	40	1.0813	0.8083	0.0297	0.0067	0.0021	10.1	1.6	8.5±0.6
	4	0.1144	0.0041	0.0037	0	0	4.1	0.3	3.8±0.3
	10	0.3069	0.1786	0.0119	0.0036	0	4.7	0.7	4.0±0.4
3250_nm	20	0.5447	0.4144	0.0142	0.0029	0	4.8	0.8	4.0±0.5
	40	1.0847	0.9211	0.0359	0.0097	0.0029	6.0	2.0	4.1±0.2

The concentration obtained immediately after the loading is referred to as "adsorbed enzyme" (sorb.), because – in addition to covalently bound molecules – physisorbed molecules may also be present in the pore system. The loading concentration for the adsorbed enzyme results from the difference between the start and end concentrations in the buffer solutions. The enzyme concentration in the washing solutions (WS) is the sum of the non-covalently bound enzyme amount in the washing solutions. The real loading concentration (corr.) per membrane is the difference between loading of adsorbed enzyme (sorb.) and non-covalently bound enzyme (sum of WS 1–3) and corresponds to the actual loading of the covalently bound AChE per membrane. Used membranes have the same weight to achieve comparable results. All values correspond to the average of three individual measurements (standard deviations of the determined AChE concentrations are indicated).

To determine enzyme concentrations in the reaction solutions before and after immobilization, spectrophotometric analysis was run using a Pierce BCA Protein Assay Kit (Thermo Scientific, Waltham, MA) and a UV-1600PC spectrophotometer from VWR International (Darmstadt, Germany) at a wavelength of 562 nm.

The BCA Protein Assay is based on reduction of Cu^{2+} to Cu^+ by a protein in alkaline medium, which is combined with the highly sensitive and selective colorimetric detection of the cuprous cation (Cu^+) by bicinchoninic acid.^{S4} First, the protein forms a light blue chelate complex with the copper in an alkaline environment. In this reaction, known as the biuret reaction, peptides containing three or more amino acid residues form a colored chelate complex with cupric ions in an alkaline medium containing sodium potassium tartrate. The second step of the color development reaction is the reaction of bicinchoninic acid (BCA) with the reduced cuprous cation that was formed in step one. Two BCA molecules form a new chelate complex with Cu^+ , which results in an intense purple-colored reaction product. The reaction leading to BCA color formation is strongly influenced by four amino acid residues (cysteine or cystine, tyrosine, tryptophan) in the amino acid sequence of the protein. The water-soluble BCA/copper complex shows strong linear absorption at 562 nm with increasing protein concentrations and is *ca.* 100 times more sensitive than the light blue color of the first reaction product.

Calculation of enzyme coverage on the different pore surfaces

With the known maximum concentration of AChE it is possible to calculate how many enzyme molecules have been immobilized on the surface of the respective support and how much space the enzymes occupy. In the following, this is examined for the three different pore systems using an exemplary calculation for the hierarchical material. For this purpose, the maximum concentration of enzyme c_{AChE} and the surface S per membrane (*cf.* Table 1.3) of the respective pore structures become involved.

$$N_{\text{AChE}} = \frac{c_{\text{AChE}}}{M_{\text{AChE}}} \cdot N_{\text{A}}$$

$$N_{\text{AChE}} = \frac{15.5 \cdot 10^{-6} \text{ g} \cdot \text{membrane}^{-1}}{\frac{1 \text{ m}^2 \cdot \text{membrane}^{-1}}{280000 \text{ g} \cdot \text{mol}^{-1}}} \cdot 6.022 \cdot 10^{23} \text{ mol}^{-1}$$

$$N_{\text{AChE}} = 3.33 \cdot 10^{13} \text{ m}^{-2} = 33.3 \cdot 10^{-6} \text{ nm}^{-2}$$

The number N_{AChE} of AChE molecules per nm^2 in the hierarchical membrane 20–3500_nm is $33.3 \cdot 10^{-6} \text{ nm}^{-2}$. For the purely mesoporous membrane 20_nm it is $18.8 \cdot 10^{-6} \text{ nm}^{-2}$ and for the purely macroporous membrane 3250_nm we find $N_{\text{AChE}} = 441 \cdot 10^{-6} \text{ nm}^{-2}$. Differences in these values reflect the different surfaces of the pore systems. For example, the purely mesoporous membrane has a significantly higher surface area but the same amount of functionalization reagent, so that the enzyme is distributed more widely.

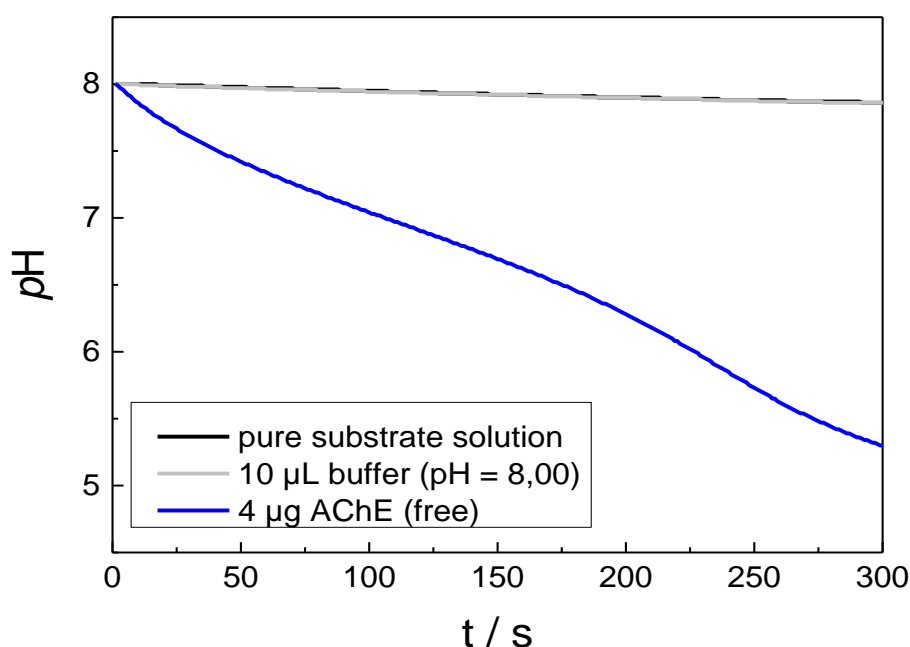


Figure 1.S5. pH response of the analytical solution during the ACh degradation with 4 µg of free AChE over 5 min. Conditions: 1 mL, 0.1 M AChCl solution; 25 °C. The pH of the pure AChCl solution (without AChE) and of the pure buffer solution is monitored as reference.

The change of solution pH during ACh degradation with AChE as free enzyme was monitored. Figure 1.S5 reveals that a self-decomposition of the substrate AChCl and the buffer solution have no significant influence on the pH measurements over 5 minutes. 4 µg of free AChE were used, which results in a reaction time of $t_{8-7} = 106 \text{ s}$ for the targeted pH change. Based on Equation (1.4) (main text), the reaction rate for the ACh degradation was 31 nmol s^{-1} . This is equivalent to an activity of 1.8 U (= $1.8 \text{ µmol min}^{-1}$), which approximately corresponds to the specification from the manufacturer ($518 \text{ U mg}^{-1} \cdot 0.004 \text{ mg} = 2.1 \text{ U}$).

Table 1.S5. Response time (t_{8-7}) and apparent reaction rate ($v_{r,app}$) for the AChE-catalyzed ACh degradation depending on substrate concentration (c_{AChCl}) and pore system. Enzyme loading: 4.1 μg per membrane.

c_{AChCl}	0.005 mol L ⁻¹		0.01 mol L ⁻¹		0.05 mol L ⁻¹		0.10 mol L ⁻¹		
n_{HAc}	0.225 μmol		0.45 μmol		1.75 μmol		3.25 μmol		
Sample	$t_{8-7} /$ s	$v_{r,app} /$ $\mu\text{mol min}^{-1}$	$t_{8-7} /$ s	$v_{r,app} /$ $\mu\text{mol min}^{-1}$	$t_{8-7} /$ s	$v_{r,app} /$ $\mu\text{mol min}^{-1}$	$t_{8-7} /$ s	$v_{r,app} /$ $\mu\text{mol min}^{-1}$	
20_nm	1	168	0.08	276	0.10	706	0.15	1530	0.13
	2	147	0.09	288	0.09	743	0.14	1548	0.13
	3	156	0.09	300	0.09	718	0.15	1582	0.12
	∅	157	0.09	288	0.09	722	0.15	1553	0.13
		± 11	± 0.006	± 12	± 0.004	± 12	± 0.004	± 24	± 0.002
20-3500_nm	1	33	0.41	65	0.42	150	0.70	169	1.15
	2	36	0.38	69	0.40	144	0.73	175	1.11
	3	41	0.33	61	0.44	130	0.81	183	1.07
	∅	37	0.37	65	0.42	141	0.74	176	1.11
		± 4	± 0.04	± 4	± 0.03	± 10	± 0.06	± 7	± 0.04
3250_nm	1	13	1.04	36	0.75	94	1.12	157	1.24
	2	21	0.64	34	0.79	82	1.28	135	1.44
	3	18	0.75	28	0.96	89	1.18	149	1.31
	∅	17	0.78	33	0.83	88	1.19	147	1.33
		± 4	± 0.20	± 4	± 0.11	± 6	± 0.08	± 11	± 0.10

The measurements for the determination of response times were repeated three times, the results averaged and indicated by the corresponding standard deviation. The error of apparent reaction rates is 2–26%. Especially at shorter response times a larger error occurs, because even small deviations in the timing are decisive. Since the geometries of the membranes were the same and measuring conditions constant, differences in response times (and thus in the apparent reaction rates) were attributable to the impact of the pore system (morphology) in a membrane.

With the resulting values of the apparent reaction rates $v_{r,app}$ at an AChCl concentration of 0.1 mol L⁻¹ (see the values in the last column of Table 1.S5) the activity of the free enzyme (1.8 $\mu\text{mol min}^{-1}$, also determined at an AChCl concentration of 0.1 mol L⁻¹, Figure 1.S5) can be related to that of the immobilized enzyme. It is obvious that the immobilized enzyme generally shows a lower activity. This can be explained by the restricted diffusion of the substrate molecules in the support structures and a possibly hindered accessibility of the active site of the enzyme by the substrate (due to the immobilization of the enzyme on a surface) compared to the relatively unrestricted diffusion and unhindered access in free solution.

At the same time, it is also clear that the reduction of the activity of the immobilized enzyme from 1.33 $\mu\text{mol min}^{-1}$ (mono-macro) to 1.11 $\mu\text{mol min}^{-1}$ (meso-macro) and to only

$0.13 \mu\text{mol min}^{-1}$ (mono-meso), as documented in the last column of Table 1.S5, reflects the increasing transport limitations engendered by the respective pore systems.

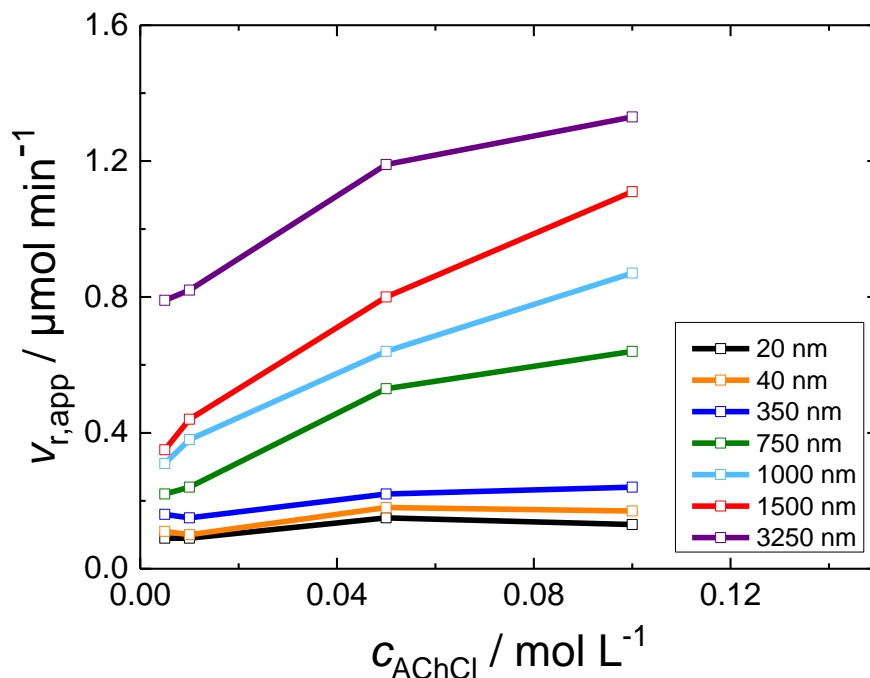


Figure 1.S6. Apparent reaction rate ($v_{r,\text{app}}$) of the AChE-catalyzed ACh degradation as a function of mean pore size for materials with monomodal pore system. Conditions: $4.1 \mu\text{g}$ loading of AChE per membrane; 1 mL, x M AChCl solution; 25°C . After plotting $1/v_{r,\text{app}}$ against $1/c_{\text{AChCl}}$ for each material, the maximum apparent rate v_{max} is determined as $1/v_{\text{max}}$ from the y-intercept of the straight line fitted to the data (see Figure 1.S7 and Table 1.S6).

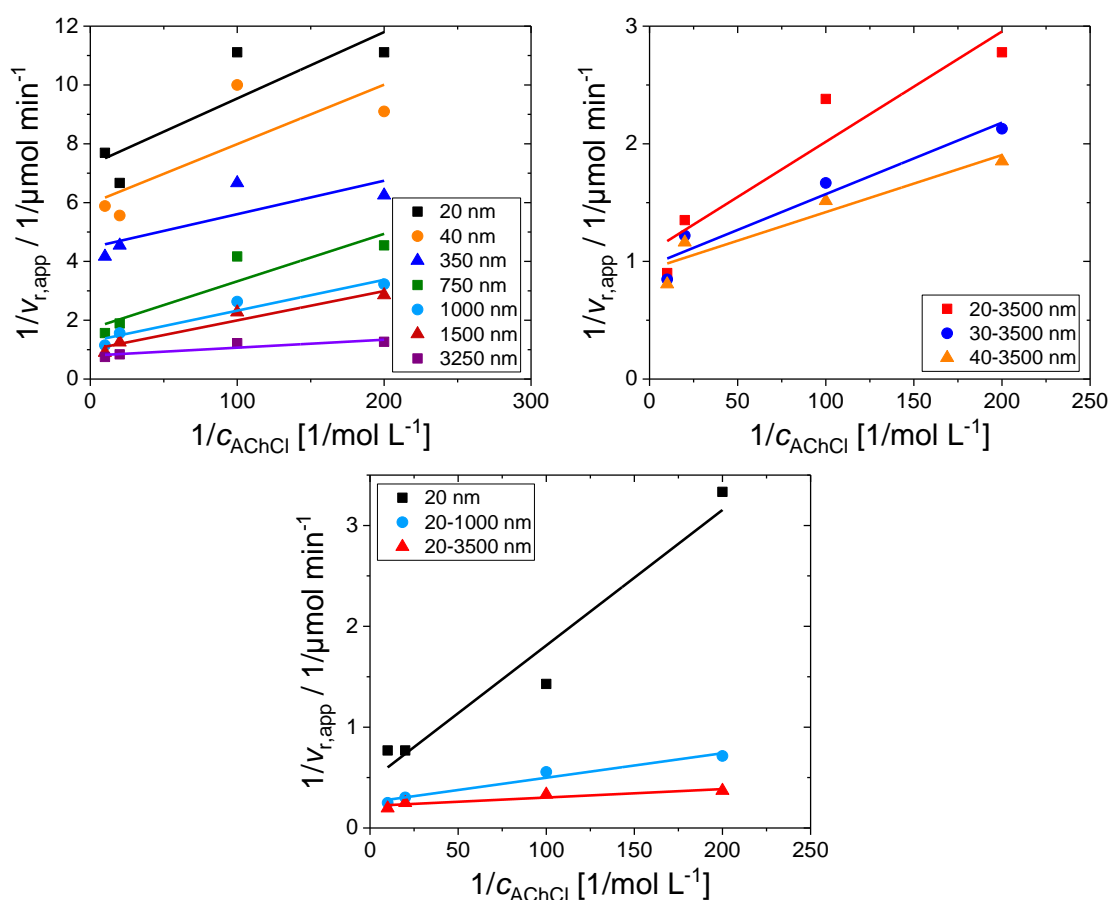


Figure 1.S7. Lineweaver–Burk plots for materials with monomodal pore structure at an enzyme loading of 4.1 μg per membrane (top left), for materials with hierarchical pore structure at an enzyme loading of 4.1 μg per membrane (top right), and for materials with hierarchical pore structure in comparison to the purely mesoporous material at an enzyme loading of 12.9 μg per membrane (bottom). These plots are used for the determination of v_{max} from the y-intercept of the straight line fitted to the data (providing $1/v_{\text{max}}$).

Calculation of maximum apparent reaction rates and Michaelis–Menten constants

The maximum apparent reaction rate (v_{max}) and the Michaelis–Menten constant (K_{M}) can be estimated for our systems after transforming the Michaelis–Menten equation into a straight-line plot of $1/v_{r,app}$ against $1/c_{\text{AChCl}}$, that is, into a double-reciprocal or Lineweaver–Burk plot,^{S5} as shown in Figure 1.S7:

$$\frac{1}{v_{r,app}} = \frac{K_{\text{M}}}{v_{\text{max}}} \cdot \frac{1}{c_{\text{AChCl}}} + \frac{1}{v_{\text{max}}}$$

Importantly, the slope of this plot is $K_{\text{M}}/v_{\text{max}}$, the intercept on the vertical axis is $1/v_{\text{max}}$, and the intercept on the horizontal axis is $-1/K_{\text{M}}$. The parameters resulting from the Lineweaver–Burk plots are summarized in Table 1.S6 below and converted into v_{max} and K_{M} for the respective pore system with its specific enzyme loading.

Table 1.S6. Determination of the maximum apparent reaction rates v_{\max} and Michaelis–Menten constants K_M from Lineweaver–Burk plots for materials with monomodal and hierarchical pore systems at enzyme loadings of 4.1 and 12.9 μg per membrane.

Sample	$c_{\text{AChE}} /$ $\mu\text{g}/\text{mem}$	Slope / $\text{mol L}^{-1}/\mu\text{mol min}^{-1}$	$1/v_{\max} /$ $1/\mu\text{mol min}^{-1}$	$v_{\max} /$ $\mu\text{mol min}^{-1}$	$K_M /$ mol L^{-1}
20_nm	4.1	0.0226	7.282	0.14	0.003
40_nm	4.1	0.0202	5.968	0.17	0.003
350_nm	4.1	0.0114	4.468	0.22	0.003
750_nm	4.1	0.0162	1.708	0.59	0.009
1000_nm	4.1	0.0105	1.277	0.78	0.008
1500_nm	4.1	0.0010	0.998	1.00	0.010
3250_nm	4.1	0.0027	0.796	1.26	0.003
20-3500_nm	4.1	0.0094	1.079	0.93	0.009
30-3500_nm	4.1	0.0061	0.964	1.04	0.006
40-3500_nm	4.1	0.0049	0.934	1.07	0.005
20_nm	12.9	0.0134	0.466	2.14	0.029
20-1000_nm	12.9	0.0024	0.255	3.92	0.010
20-3500_nm	12.9	0.0008	0.218	4.58	0.004

References

- (1) M. N. Velasco-Garcia, T. Mottram, Biosensor technology addressing agricultural problems. *Biosyst. Eng.*, **2003**, *84*, 1–12.
DOI: 10.1016/S1537-5110(02)00236-2.
- (2) A. J. Bäumner, R. D. Schmid, Development of a new immunosensor for pesticide detection: a disposable system with liposome-enhancement and amperometric detection. *Biosens. Bioelectron.*, **1998**, *13*, 519–529.
DOI: 10.1016/s0956-5663(97)00131-0.
- (3) E. A. H. Hall, J. J. Gooding, C. E. Hall, Redox enzyme linked electrochemical sensors: Theory meets practice. *Microchim. Acta*, **1995**, *121*, 119–145.
DOI: 10.1007/BF01248246.
- (4) K. R. Rogers, L. R. Williams, Biosensors for environmental monitoring: a regulatory perspective. *Trends Anal. Chem.*, **1995**, *14*, 289–294.
DOI: 10.1016/0165-9936(95)97054-5.
- (5) H. H. Weetall, Biosensor technology What? Where? When? and Why? *Biosens. Bioelectron.*, **1996**, *11*, 1–2.
DOI: 10.1016/0956-5663(96)83729-8.

-
- (6) D. H. Small, S. Michaelson, G. Sberna, Non-classical actions of cholinesterases: Role in cellular differentiation, tumorigenesis and Alzheimer's disease. *Neurochem. Int.*, **1996**, 28, 453–483.
DOI: 10.1016/0197-0186(95)00099-2.
- (7) R. Aldunate, J. C. Casar, E. Brandan, N. C. Inestrosa, Structural and functional organization of synaptic acetylcholinesterase. *Brain Res. Rev.*, **2004**, 47, 96–104.
DOI: 10.1016/j.brainresrev.2004.07.019.
- (8) S. Greenfield, Non-classical actions of cholinesterases: role in cellular differentiation, tumorigenesis and Alzheimer's disease. *Neurochem. Int.*, **1996**, 28, 485–490.
DOI: 10.1016/0197-0186(95)00100-x.
- (9) T. C. Kwong, Organophosphate pesticides: Biochemistry and clinical Toxicology. *Ther. Drug Monit.*, **2002**, 24, 144–149.
DOI: 10.1097/00007691-200202000-00022.
- (10) G. D. Moores, X. Gao, I. Denholm, A. L. Devonshire, Characterisation of insensitive acetylcholinesterase in insecticide-resistant cotton aphids, *Aphis gossypii* glover (Homoptera: Aphididae). *Pestic. Biochem. Physiol.*, **1996**, 56, 102–110.
DOI: 10.1006/pest.1996.0064.
- (11) L. Wang, Y. Zhao, Y. Zhang, T. Zhang, J. Kool, G. W. Somsen, Q. Wang, Z. Jiang, Online screening of acetylcholinesterase inhibitors in natural products using monolith-based immobilized capillary enzyme reactors combined with liquid chromatography-mass spectrometry. *J. Chromatogr. A*, **2018**, 1563, 135–149.
DOI: 10.1016/j.chroma.2018.05.069.
- (12) L. Drechsel, M. Schulz, F. von Stetten, C. Moldovan, R. Zengerle, N. Paust, Electrochemical pesticide detection with AutoDip—a portable platform for automation of crude sample analyses. *Lab Chip*, **2015**, 15, 704–710.
DOI: 10.1039/C4LC01214C.
- (13) D. I. Fried, F. J. Brieler, M. Fröba, Designing inorganic porous materials for enzyme adsorption and applications in biocatalysis. *ChemCatChem.*, **2013**, 5, 862–884.
DOI: 10.1002/cctc.201200640.
- (14) M. Dreifke, M. Fröba, Immobilisierung von Enzymen: Spielerei oder biotechnologischer Fortschritt? *BIOspektrum*, **2017**, 23, 95–97.
DOI: 10.1007/s12268-017-0769-5.
- (15) S. Andreescu, J.-L. Marty, Twenty years research in cholinesterase biosensors: From basic research to practical applications. *Biomol. Eng.*, **2006**, 23, 1–15.
DOI: 10.1016/j.bioeng.2006.01.001.
- (16) H. Dvir, I. Silman, M. Harel, T. L. Rosenberry, J. L. Sussman, Acetylcholinesterase: from 3D structure to function. *Chem. Biol. Interact.*, **2010**, 187, 10–22.
DOI: 10.1016/j.cbi.2010.01.042.
- (17) G. Johnson, S. W. Moore, The peripheral anionic site of acetylcholinesterase: Structure, functions and potential role in rational drug design. *Curr. Pharm. Design*, **2006**, 12, 217–225.

- DOI: 10.2174/138161206775193127.
- (18) C. Bernal, P. Urrutia, A. Illanes, L. Wilson, Hierarchical macro–mesoporous silica grafted with glyoxyl groups: opportunities for covalent immobilization of enzymes. *New Biotechnol.*, **2013**, *30*, 500–506.
DOI: 10.1016/j.nbt.2013.01.011.
- (19) K. Dutta, D. Bhattacharyay, A. Mukherjee, S. J. Setford, A. P. F. Turner, P. Sarkar, Detection of pesticide by polymeric enzyme electrodes. *Ecotoxicol. Environ. Saf.*, **2008**, *69*, 556–561.
DOI: 10.1016/j.ecoenv.2007.01.004.
- (20) V. K. Yadavalli, W. G. Koh, G. J. Lazur, M. V. Pishko, Microfabricated protein-containing poly(ethylene glycol) hydrogel arrays for biosensing. *Sens. Actuators B Chem.*, **2004**, *97*, 290–297.
DOI: 10.1016/j.snb.2003.08.030.
- (21) C. P. Haas, T. Müllner, R. Kohns, D. Enke, U. Tallarek, High-performance monoliths in heterogeneous catalysis with single-phase liquid flow. *React. Chem. Eng.*, **2017**, *2*, 498–511.
DOI: 10.1039/C7RE00042A.
- (22) D. Enke, R. Gläser, U. Tallarek, Sol–gel and porous glass-based silica monoliths with hierarchical pore structure for solid-liquid catalysis. *Chem. Ing. Tech.*, **2016**, *88*, 1561–1585.
DOI: 10.1002/cite.201600049.
- (23) D. Schneider, D. Mehlhorn, P. Zeigermann, J. Kärger, R. Valiullin, Transport properties of hierarchical micro-mesoporous materials. *Chem. Soc. Rev.*, **2016**, *45*, 3439–3447.
DOI: 10.1039/C5CS00715A.
- (24) W. Schwieger, A. G. Machoke, T. Weissenberger, A. Inayat, T. Selvam, M. Klumpp, A. Inayat, Hierarchy concepts: classification and preparation strategies for zeolite containing materials with hierarchical porosity. *Chem. Soc. Rev.*, **2015**, *45*, 3353–3376.
DOI: 10.1039/C5CS00599J.
- (25) B. Reinhardt, D. Enke, F. Syrowatka, Preparation of porous, hierarchically organized glass monoliths via combination of sintering and phase separation. *J. Am. Ceram. Soc.*, **2012**, *95*, 461–465.
DOI: 10.1111/j.1551-2916.2011.05013.x.
- (26) A. Inayat, B. Reinhardt, H. Uhlig, W.-D. Einicke, D. Enke, Silica monoliths with hierarchical porosity obtained from porous glasses. *Chem. Soc. Rev.*, **2013**, *42*, 3753–3764.
DOI: 10.1039/C2CS35304K.
- (27) P. Sepulveda, J. G. P. Binner, Processing of cellular ceramics by foaming and in situ polymerization of organic monomers. *J. Eur. Ceram. Soc.*, **1999**, *19*, 2059–2066.
DOI: 10.1016/S0955-2219(99)00024-2.
- (28) K. Nakanishi, Pore structure control of silica gels based on phase separation. *J. Porous Mater.*, **1997**, *4*, 67–112.

- DOI: 10.1023/A:1009627216939.
- (29) K. Nakanishi, N. Tanaka, Sol–gel with phase separation. Hierarchically porous materials optimized for high-performance liquid chromatography separations. *Acc. Chem. Res.*, **2007**, *40*, 863–873.
DOI: 10.1021/ar600034p.
- (30) R. Kohns, C. P. Haas, A. Höltzel, C. Splith, D. Enke, U. Tallarek, Hierarchical silica monoliths with submicron macropores as continuous-flow microreactors for reaction kinetic and mechanistic studies in heterogeneous catalysis. *React. Chem. Eng.*, **2018**, *3*, 353–364.
DOI: 10.1039/C8RE00037A.
- (31) C. Triantafillidis, M. S. Elsaesser, N. Hüsing, Chemical phase separation strategies towards silica monoliths with hierarchical porosity. *Chem. Soc. Rev.*, **2013**, *42*, 3833–3846.
DOI: 10.1039/C3CS35345A.
- (32) A. Feinle, M. S. Elsaesser, N. Hüsing, Sol–gel synthesis of monolithic materials with hierarchical porosity. *Chem. Soc. Rev.*, **2016**, *45*, 3377–3399.
DOI: 10.1039/C5CS00710K.
- (33) Q. Wu, J. M. Bienvenue, B. J. Hassan, Y. C. Kwok, B. C. Giordano, P. M. Norris, J. P. Landers, J. P. Ferrance, Microchip-based microporous silica sol–gel monolith for efficient isolation of DNA from clinical samples. *Anal. Chem.*, **2006**, *78*, 5704–5710.
DOI: 10.1021/ac060390t.
- (34) P. C. A. Jerónimo, A. N. Araújo, M. C. B. S. M. Montenegro, D. Satinský, P. Solich, Flow-through sol–gel optical biosensor for the colorimetric determination of acetazolamide. *Analyst*, **2005**, *130*, 1190–1197.
DOI: 10.1039/B504474J.
- (35) K. Anitha, S. Venkata Mohan, S. Jayarama Reddy, Development of acetylcholinesterase silica sol–gel immobilized biosensor - an application towards oxydementon methyl detection. *Biosens. Bioelectron.*, **2004**, *20*, 848–856.
DOI: 10.1016/j.bios.2004.03.024.
- (36) R.-A. Doong, H.-C. Tsai, Immobilization and characterization of sol–gel-encapsulated acetylcholinesterase fiber-optic biosensor. *Anal. Chim. Acta*, **2001**, *434*, 239–246.
DOI: 10.1016/S0003-2670(01)00853-4.
- (37) A. Galarneau, Z. Abid, B. Said, Y. Didi, K. Szymanska, A. Jarzębski, F. Tancret, H. Hamaizi, A. Bengueddach, F. Di Renzo, F. Fajula, Synthesis and textural characterization of mesoporous and meso-/microporous silica monoliths obtained by spinodal decomposition. *Inorganics*, **2016**, *4*, 9.
DOI: 10.3390/inorganics4020009.
- (38) C. J. Brinker, G. W. Scherer, *Sol–Gel Science: The Physics and Chemistry of Sol–Gel Processing*, Academic Press, New York, NY, **1990**.
- (39) G. W. Scherer, D. M. Smith, Cavitation during drying of a gel. *J. Non Cryst. Solids*, **1995**, *189*, 197–211.

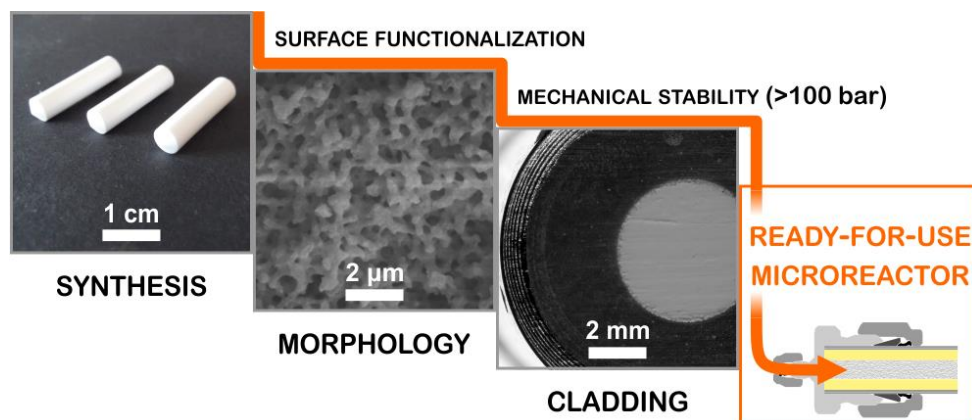
- DOI: 10.1016/0022-3093(95)00222-7.
- (40) D. M. Smith, D. Stein, J. M. Anderson, W. Ackerman, Preparation of flow-density xerogels at ambient pressure. *J. Non Cryst. Solids*, **1995**, *186*, 104–112.
DOI: 10.1016/0022-3093(95)00040-2.
- (41) T. K. Sherwood, The drying of solids—I. *Ind. Eng. Chem.*, **1929**, *21*, 12–16.
DOI: 10.1021/ie50229a004.
- (42) T. K. Sherwood, The drying of solids—II. *Ind. Eng. Chem.*, **1929**, *21*, 976–980.
DOI: 10.1021/ie50238a021.
- (43) F. Kirkbir, H. Murata, D. Meyers, S. R. Chaudhuri, A. Sarkar, Drying and sintering of sol–gel derived large SiO₂ monoliths. *J. Sol-Gel Sci. Technol.*, **1996**, *6*, 203–217.
DOI: 10.1007/BF00402691.
- (44) K. Kajihara, Recent advances in sol–gel synthesis of monolithic silica and silica-based glasses. *J. Asian Ceram. Soc.*, **2013**, *1*, 121–133.
DOI: 10.1016/j.jascer.2013.04.002.
- (45) A. Soleimani Dorcheh, M. H. Abbasi, Silica aerogel; synthesis, properties and characterization. *J. Mater. Process. Technol.*, **2008**, *199*, 10–26.
DOI: 10.1016/j.jmatprotec.2007.10.060.
- (46) H. Moser, Der Absolutwert der Oberflächenspannung des reinen Wassers nach der Bügelmethode und seine Abhängigkeit von der Temperatur. *Ann. Phys.*, **1927**, *387*, 993–1013.
DOI: 10.1002/andp.19273870706.
- (47) T. Kawaguchi, H. Hishikura, J. Iura, Y. Kokubu, Monolithic dried gels and silica glass prepared by the sol–gel process. *J. Non Cryst. Solids*, **1984**, *63*, 61–69.
DOI: 10.1016/0022-3093(84)90386-7.
- (48) W. Prüger, Die Verdampfungsgeschwindigkeit der Flüssigkeiten. *Z. Phys.*, **1940**, *115*, 202–244.
DOI: 10.1007/BF01341379.
- (49) R. Miyamoto, Y. Ando, C. Kurusu, H.-Z. Bai, K. Nakanishi, M. Ippommatsu, Fabrication of large-sized silica monolith exceeding 1000 mL with high structural homogeneity. *J. Sep. Sci.*, **2013**, *36*, 1890–1896.
DOI: 10.1002/jssc.201300123.
- (50) S. S. Kistler, Coherent expanded aerogels and jellies. *Nature*, **1931**, *127*, 741.
DOI: 10.1038/127741a0.
- (51) S. S. Prakash, C. J. Brinker, A. J. Hurd, Silica aerogel films at ambient pressure. *J. Non Cryst. Solids*, **1995**, *190*, 264–275.
DOI: 10.1016/0022-3093(95)00024-0.
- (52) S. S. Prakash, C. J. Brinker, A. J. Hurd, S. M. Rao, Silica aerogel films prepared at ambient pressure by using surface derivatization to induce reversible drying shrinkage. *Nature*, **1995**, *374*, 439–443.
DOI: 10.1038/374439a0.

- (53) M. von der Lehr, K. Hormann, A. Hölzel, L. S. White, A. E. Reising, M. F. Bertino, B. M. Smarsly, U. Tallarek, Mesopore etching under supercritical conditions – a shortcut to hierarchically porous silica monoliths. *Microporous Mesoporous Mater.*, **2017**, *243*, 247–253.
DOI: 10.1016/j.micromeso.2017.02.036.
- (54) A. Paravathy Rao, G. M. Pajonk, A. V. Rao, Effect of preparation conditions on the physical and hydrophobic properties of two step processed ambient pressure dried silica aerogels. *J. Mater. Sci.*, **2005**, *40*, 3481–3489.
DOI: 10.1007/s10853-005-2853-3.
- (55) S. D. Bhagat, Y.-H. Kim, Y.-S. Ahn, J.-G. Yeo, Textural properties of ambient pressure dried water-glass based silica aerogel beads: One day synthesis. *Microporous Mesoporous Mater.*, **2006**, *96*, 237–244.
DOI: 10.1016/j.micromeso.2006.07.002.
- (56) F. Kirkbir, H. Murata, D. Meyers, S. R. Chaudhuri, Drying of large monolithic aerogels between atmospheric and supercritical pressures. *J. Sol-Gel Sci. Technol.*, **1998**, *13*, 311–316.
DOI: 10.1023/A:1008668009340.
- (57) V. Vescovi, W. Kopp, J. M. Guisán, R. L. C. Giordano, A. A. Mendes, P. W. Tardioli, Improved catalytic properties of *Candida antarctica* lipase B multi-attached on tailor-made hydrophobic silica containing octyl and multifunctional amino- glutaraldehyde spacer arms. *Process Biochem.*, **2016**, *51*, 2055–2066.
DOI: 10.1016/j.procbio.2016.09.016.
- (58) Y. Liebes, L. Amir, R. S. Marks, M. Banai, Immobilization strategies of *Brucella* particles on optical fibers for use in chemiluminescence immunosensors. *Talanta*, **2009**, *80*, 338–345.
DOI: 10.1016/j.talanta.2009.06.070.
- (59) S.-J. Reich, A. Svidrytski, D. Hlushkou, D. Stoeckel, C. Kübel, A. Hölzel, U. Tallarek, Hindrance factor expression for diffusion in random mesoporous adsorbents obtained from pore-scale simulations in physical reconstructions. *Ind. Eng. Chem. Res.*, **2018**, *57*, 3031–3042.
DOI: 10.1021/acs.iecr.7b04840.
- (60) P. Zdražilová, Š. Štěpánková, M. Vránová, K. Komers, A. Komersová, A. Čegan, Kinetics of total enzymatic hydrolysis of acetylcholine and acetylthiocholine. *Z. Naturforsch. C*, **2006**, *61*, 289–294.
DOI: 10.1515/znc-2006-3-423.
- (61) J. Stenersen, *Chemical Pesticides Mode of Action and Toxicology*, CRC Press. Boca Raton, FL, USA, **2004**.
- (62) A. Schuchert-Shi, P. C. Hauser, Study of acetylcholinesterase inhibitors using CE with contactless conductivity detection. *Electrophoresis*, **2009**, *30*, 3442–3448.
DOI: 10.1002/elps.200900184.

- (63) R. J. Skaer, Acetylcholinesterase in human erythroid cells. *J. Cell Sci.*, **1973**, *12*, 911–923.
- (64) J. Teipel, D. E. Koshland, Significance of intermediary plateau regions in enzyme saturation curves. *Biochemistry*, **1996**, *8*, 4656–4663.
DOI: 10.1021/bi00839a064.
- (65) J. E. Dowd, D. S. Riggs, A comparison of estimates of Michaelis-Menten kinetic constants from various linear transformations. *J. Biol. Chem.*, **1965**, *240*, 863–869.
- (66) N. Anders, Untersuchungen zum Einfluss einer hierarchischen Porenstruktur am Beispiel einer Funktionskomponente in der Biosensorik. *Doctoral thesis*, Universität Leipzig, October **2016**.
- (S1) R. J. Skaer, Acetylcholinesterase in human erythroid cells. *J. Cell Sci.*, **1973**, *12*, 911–923.
- (S2) K. A. Cychosz, R. Guillet-Nicolas, J. García-Martínez, M. Thommes, Recent advances in the textural characterization of hierarchically structured nanoporous materials. *Chem. Soc. Rev.*, **2017**, *46*, 389–414.
DOI: 10.1039/C6CS00391E.
- (S3) S.-J. Reich, A. Svidrytski, D. Hlushkou, D. Stoeckel, C. Kübel, A. Höltzel, U. Tallarek, Hindrance factor expression for diffusion in random mesoporous adsorbents obtained from pore-scale simulations in physical reconstructions. *Ind. Eng. Chem. Res.*, **2018**, *57*, 3031–3042.
DOI: 10.1021/acs.iecr.7b04840.
- (S4) P. K. Smith, R. I. Krohn, G. T. Hermanson, A. K. Mallia, F. H. Gartner, M. D. Provenzano, E. K. Fujimoto, N. M. Goetze, B. J. Olson, D. C. Klenk, Measurement of protein using bicinchoninic acid. *Anal. Biochem.*, **1985**, *150*, 76–85.
DOI: 10.1016/0003-2697(85)90442-7.
- (S5) B. K. Hamilton, C. R. Gardner, C. K. Colton, Effect of diffusional limitations on Lineweaver-Burk plots for immobilized enzymes. *AIChE J.*, **1974**, *20*, 503–510.
DOI: 10.1002/aic.690200310.

Chapter 2

Hierarchical silica monoliths with submicron macropores as continuous-flow microreactors for reaction kinetic and mechanistic studies in heterogeneous catalysis



Authors

Richard Kohns, Christian P. Haas, Alexandra Hölzel, Christian Splith, Dirk Enke and Ulrich Tallarek

State of Publication

Published 17 April 2018 in *Reaction Chemistry & Engineering*, Vol. 3, 353–364.
DOI: 10.1039/c8re00037a

Abstract

Synthetic attempts towards submicron macropore and skeleton dimensions of hierarchical silica monoliths have so far been plagued by compromised structural homogeneity and/or mechanical stability. We overcome these problems by introducing urea as an agent to control macropore size and skeleton thickness (in addition to mesopore size) as well as a low-cost, straightforward method to achieve a seamless stainless-steel cladding of the monolithic silica rods tolerating pressures of >100 bar. Increasing the urea content of the starting sol comprising a sulfuric acid solution of tetraethoxysilane, poly(ethylene oxide), and urea from 3 to 24 wt.% decreases the macropore size from 2.3 to 0.6 μm , the skeleton thickness from 2.0 to 0.4 μm , and increases the mesopore size from 10 to 26 nm. We assume that with increasing urea content of the starting sol, phase separation and gelation are retarded as well as shifted closer together, so that the formed monolithic structures represent a less evolved state of spinodal decomposition, preserving smaller macropores and a thinner skeleton. After cladding, the surface functionalization with aminopropyl groups yields a continuous-flow microreactor (5 mm i.d. \times 4 cm length) used for heterogeneous catalysis of the Knoevenagel condensation between benzaldehyde and ethyl cyanoacetate. The catalytic testing and kinetic studies with an on-line coupled reaction–analysis system reveal plug-flow conditions in the microreactor and the elimination of diffusive transport limitations demonstrating the overall success of the preparation. The proposed scheme enables academic laboratories to prepare hierarchical silica monoliths with desirable morphological properties (addressing particularly submicron macropore size and skeleton thickness) and versatile surface functionalization for demanding applications in adsorption, separation, organic synthesis, and catalysis.

2.1 Introduction

Silica monoliths combine low bulk density, high porosity, and mechanical stability with a large surface area open to various functionalization options.^{1,2} As versatile materials, they are used for thermal insulation, CO₂ adsorption, chemical separations, and heterogeneous catalysis.^{3–12} Their hierarchical pore structure consisting, for example, of interskeleton macropores and intraskeleton mesopores allows for fast transport of solutes to and from the active sites, which is why they are preferably used in applications requiring high efficiencies.^{13,14} The macropores enable advective transport by pressure-driven flow and the mesoporous skeleton provides a large surface for active sites accessible by diffusion. Further, the large contact area between macropores and skeleton (the external surface) guarantees fast exchange between flowing and stagnant fluid. And finally, silica monoliths potentially exhibit more homogeneous structural features (pore size and shape, skeleton thickness) than alternative hierarchical support structures such as packed beds of porous particles, which again enhances the transport efficiency and overall performance.¹⁵

Despite their advantages, silica monoliths do not enjoy the widespread application they deserve, because there exists as yet no reliable route for academic laboratories to prepare silica monoliths with submicron macropores in functional devices that are ready for use. Decreasing the macropore size and skeleton thickness to below one micrometer results in an increased external surface area of the mesoporous silica skeleton, where flowing and stagnant mobile phases get in contact with each other, as well as in extremely low backmixing and intraskeleton mass transfer resistance. In addition, the independent adjustment of macropore size and skeleton thickness allows to decouple hydraulic permeability and advection-dominated dispersion (*i.e.*, properties of the flow-through macropore space) from diffusion-limited intraskeleton mass transfer, mesopore space loading capacity, and contact time. Present obstacles towards this goal are a simultaneous control over the macropore size, structural homogeneity, and mechanical stability of the monolith, and to seamlessly clad the monolithic rod into tubing that resists a variety of organic solvents as well as pressures >100 bar. Existing cladding options, like wrapping the rods in thermoshrinking poly(tetrafluoroethylene) (PTFE) and encapsulating the wrapped rods in tubes made of PTFE or poly(arylether ether ketone) (PEEK), do not allow the same range of operating conditions (in terms of resistance to pressure and solvents) as stainless steel.¹³ Whereas the need for mechanical stability and seamless cladding are self-evident, tight control over macropore size is a less obvious goal. Smaller macropores reduce hydrodynamic dispersion occurring with single-phase hydraulic flow due to the general pore-level flow nonuniformity, and a thinner mesoporous skeleton reduces mass transfer resistance due to the hindered diffusion of solutes through the mesopores containing stagnant mobile phase. These effects (smaller macropore size and thinner mesoporous skeleton) reduce the characteristic lengths for flow and diffusion, respectively, translating into a narrower residence time distribution of the solutes and ultimately an improved performance.¹⁴ Repeated attempts to shrink the macropore size were undertaken over the years, most frequently by the Kyoto group

around Nakanishi,^{3,13,16–19} who introduced the original process for silica monoliths with bimodal pore structure.^{20,21} Although the macropore size could be successfully decreased to 1–2 μm , further downsizing efforts resulted in a collapse of structural homogeneity and mechanical stability, yielding monoliths too brittle for cladding.²²

The Nakanishi process typically follows four steps:^{3,20} (1) the sol–gel transition with concurrent, polymer-induced phase separation to form a macro–microporous gel; (2) hydrothermal treatment of the gel to widen micropores to mesopores; (3) solvent exchange, ripening, and drying, which should yield a dry, mechanically stable monolith; and (4) calcination to remove organic matter lurking in the pores. The properties of the macropore space are determined in the first step; the silica precursor, an alkoxy silane, forms a sol by concurrent hydrolysis and condensation reactions in acidic aqueous solution. As the condensation proceeds, silanol groups become exposed to which the phase-separation inducing polymer, often poly(ethylene oxide) (PEO), forms hydrogen bonds. PEO adsorption on the growing silica surface directs the nonpolar backbone of PEO to the aqueous solution. Repulsive interactions between the aqueous solution and the PEO-adsorbed silica phase accumulate until the solution separates into a silica-rich phase (with adsorbed PEO) and a solvent-rich phase. Once phase separation has set in, the structural features of the silica-rich phase undergo a coarsening process; upon gelation, features are frozen in place. The longer the time span between phase separation and gelation is (and the faster coarsening proceeds), the larger are the structural features of the formed gel and thus macropore size and skeleton thickness of the final monolith. Control of macropore size and homogeneity thus means control over the sensitive timing of phase separation relative to gelation.²³

The components of the sol–gel step, namely, content of the silica precursor, pH of the starting sol, as well as chemical structure, molecular weight, and content of the polymer, plus some obvious experimental parameters like gelation temperature, have all been evaluated previously, separately as well as in combination. An optional component in the starting sol that has not been investigated so far is urea. Due to its base-releasing decomposition into carbon dioxide and ammonia at elevated temperatures, urea is used for pore widening in the hydrothermal treatment step. Adding urea to the starting sol is a common practice with two advantages: it provides a homogeneous distribution of the etching chemical in the wet gel, which is supposed to generate a spatially homogeneous mesopore size distribution in the monolith, and it allows hydrothermal treatment to proceed in the gelation mold, eliminating the need to handle the wet gel. A possible steering role of urea in the sol–gel step (apart from its effect on the pH of the solution) has never been considered, although experimental evidence suggests this possibility. Urea has been used as template for the sol–gel synthesis of monomodal, mesoporous silica gels with controlled mesopore size and volume; the templating effect was attributed to hydrogen bonds between urea and silica.²⁴ Hydrogen bonds between urea and hydrocarbons, including PEO, have also been reported.^{25,26} And finally, urea decreases the polarity of water by disrupting its solvent structure, which improves the solubility of hydrophobic compounds in

aqueous solution.^{27–30} With its ability for hydrogen-bond formation with silica as well as PEO and for enhancing the solubility of hydrophobic compounds in aqueous solution, urea can be expected to delay the onset of phase separation. We therefore regard urea as potential tool to control the macropore size *via* the timing of phase separation vs. gelation.

In this work, we explore urea as a macropore-size controlling agent to obtain mechanically stable silica monoliths with the targeted morphological properties (*i.e.*, submicron macropore size and skeleton thickness). We introduce a new cladding method for the monolithic rods that allows their operation at high pressure. After functionalization of the silica surface with aminopropyl groups, the performance of a 5 mm i.d. × 4 cm length continuous-flow microreactor is evaluated by adapting the Knoevenagel condensation as an established test reaction for diffusion- and/or reaction-limitations of basic catalysts. The comprehensive protocol that we present here to obtain ready-for-use microreactors not only offers great flexibility in surface functionalization, typical for silica, but also allows to fine-tune morphological features of monolithic microreactors. One key aspect is the minimization of backmixing desirable, *e.g.*, in consecutive reaction schemes when selectivity is important (since backmixing reduces the driving force for heat and mass transfer and reaction). Another boost will be hopefully seen in the systematic decoupling as well as separate optimization of the intrinsic reaction kinetics, relevant (eventually limiting) transport phenomena, and hydrodynamics.

2.2 Experimental

2.2.1 Chemicals

Tetraethoxysilane (TEOS, 99%) was purchased from abcr (Karlsruhe, Germany). PEO with an average molecular weight of 100,000 was obtained from Alfa Aesar (Haverhill, MA). Urea was bought at Caesar & Loretz (Hilden, Germany). Sulfuric acid (95%) and absolute ethanol (AnalaR NORMAPUR[®] ACS, Reag. Ph. Eur.) came from VWR International (Darmstadt, Germany). (3-Aminopropyl)triethoxysilane (APTES), benzaldehyde (BA, ReagentPlus[®], ≥99%), and ethyl *trans*- α -cyanocinnamate (ECC, 99%) were purchased from Sigma–Aldrich (St. Louis, MO). Ethyl cyanoacetate (ECA, 99%) was bought at Fluorochem (Hadfield, U.K.). All chemicals were used as received. HPLC-grade water was obtained from a Milli-Q gradient purification system (Millipore, Bedford, MA).

2.2.2 Synthesis of hierarchical silica monoliths

Eight monolithic silica rods were prepared from eight starting sols with different urea content. The synthesis was carried out in parallel fashion and took ~4 days (Figure 2.1). First, PEO (2.0 g) and urea (1.05, 2.10, 3.16, 4.21, 5.27, 6.31, 7.36, or 8.43 g) were added to distilled water (18 g) under vigorous stirring. When, after stirring for 30 min at room temperature, the solutions became transparent, sulfuric acid (2.54 g) and TEOS (14.6 g) were added. After an additional

30 min of vigorous stirring, each mixture was poured into a PTFE tube (7 mm i.d., filled to 10-cm height). For gelation, the eight tubes were placed in a small lab autoclave (with a plastic insert for eight tubes) and the autoclave was put into an oven for gelation (24 h at 50 °C) and the subsequent hydrothermal treatment (20 h at 120 °C). After cooling, the wet gels were removed from the tubes and placed in marked positions around the perimeter of a wide glass vessel (2-L volume). The gels were washed by submersion in stirred water, refreshed three to four times until the pH was neutral, which took about 5 h. Each gel was then placed in its own plastic vessel, submerged with water, and dried in an oven (24 h at 120 °C). The dried rods were calcined for 8 h, using a heating rate of 3 °C min⁻¹ from room temperature to 600 °C. The finished monolithic silica rods had a diameter of ~0.5 cm and a length of ~9 cm.

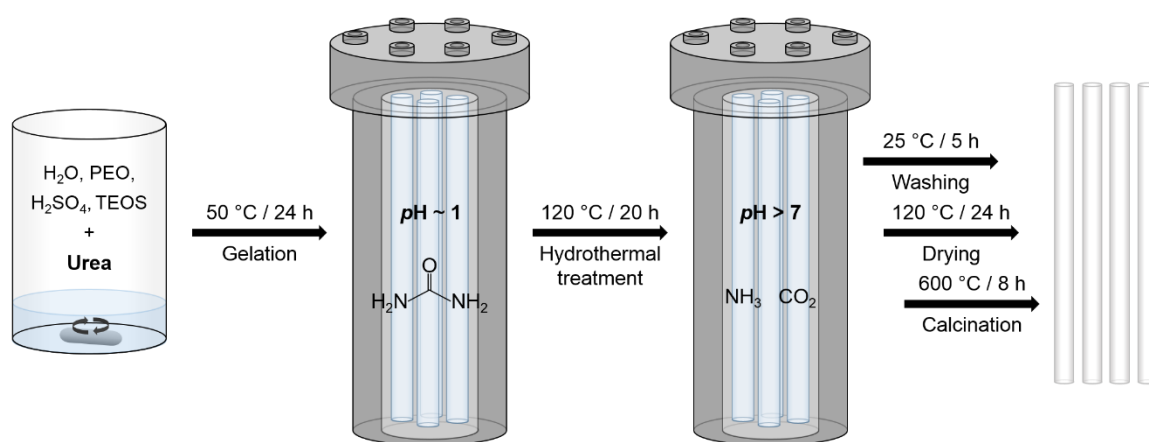


Figure 2.1. Parallel synthesis of monolithic silica rods with urea-controlled, bimodal pore size distributions.

2.2.3 Characterization of macro- and mesoporosity

The monolithic silica rods were examined under a Leo Gemini 1530 scanning electron microscope (Zeiss, Oberkochen, Germany), for which sample pieces were vapor-deposited with Au at 10 kV. Mercury intrusion porosimetry (MIP) measurements were carried out on a Pascal 140/440 porosimeter (Thermo Fisher Scientific, Waltham, MA) over a pressure range of 0.15–400 MPa. Pore size distributions were derived from the MIP data with the Pascal software according to the Washburn equation, setting the mercury contact angle to 141°; the measured pressure range corresponds to pore diameters between 3.7 nm and 10 μm. Nitrogen physisorption data were acquired on an Autosorb-iQ system (Quantachrome Instruments, Boynton Beach, FL). Prior to the measurements samples were evacuated for 10 h at 250 °C. Mesopore volume and BET surface area were calculated from the nitrogen adsorption isotherms recorded at –196 °C up to pressures of $p/p_0 = 0.98$. Pore size distributions were derived from the adsorption branches using the non-local density functional theory (NLDFT) method with a cylindrical pore model.³¹

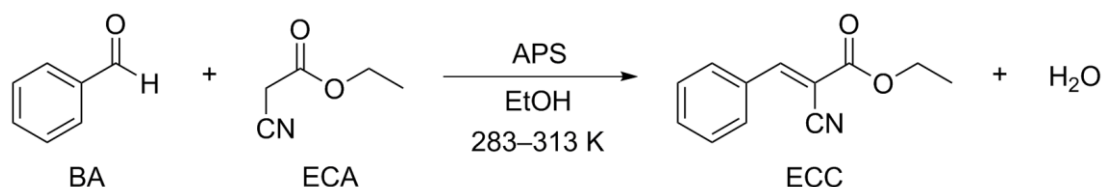
2.2.4 Cladding and functionalization of sample Urea-7

Of the prepared monolithic silica rods, sample Urea-7 with submicron macropore size and skeleton thickness was selected for further processing, that is, cladding of the rod and functionalization of the silica surface. The rod was first trimmed to 4-cm length to comply with the dimensions of the stainless-steel tubing (10.6 mm i.d./12.6 mm o.d. × 4 cm length; Swagelok, Solon, OH). The trimmed rod was centered in the tubing and embedded with UHU[®] PLUS 300 epoxy resin adhesive (UHU, Bühl, Germany) composed of 1:1 (v/v) tube binder and hardener. We chose this resin adhesive since it was cheap, easy to acquire, and showed the demanded physical properties like high mechanical stability, low thermal expansion coefficient, as well as the resistance against many solvents (including ethanol).³² After resin hardening overnight, the ends were cleaned from residual resin and then cut flat using conventional machine processing. By attaching zero-volume reducing unions (Swagelok) to the stainless-steel tube, the column was finished.

After cladding, the bare-silica surface of the monolith was functionalized with aminopropyl groups by flushing the column with ~3 mL APTES solution (0.25 M in ethanol) at a volumetric flow rate of $Q = 1.5 \text{ mL min}^{-1}$. The column was then disconnected from the pump, sealed on both ends, and placed in a water bath (70 °C for 3 h). Flushing the column with pure ethanol for several minutes completed the procedure. The coverage of the silica surface with aminopropyl groups was determined as $\sim 2.8 \mu\text{mol m}^{-2}$ by elemental analysis of a monolith piece removed from the column after catalytic testing. Elemental analysis also provided nitrogen and carbon contents of the monolith after hydrothermal treatment (no nitrogen, high carbon content) as well as after calcination and before functionalization (no nitrogen, low carbon content), which is discussed further in the ESI (Table 2.S1).

2.2.5 Continuous-flow microreactor and catalytic testing

The clad and aminopropylated silica (APS) monolith was used as continuous-flow microreactor to catalyze the Knoevenagel condensation between BA and ECA to ECC in ethanol (Scheme 2.1). The catalytic testing was performed in the temperature range of $T = 10\text{--}40 \text{ }^\circ\text{C}$.



Scheme 2.1. Knoevenagel condensation between benzaldehyde (BA) and ethyl cyanoacetate (ECA) to ethyl *trans*- α -cyanocinnamate (ECC) using an aminopropylated silica (APS) monolith as catalytic microreactor.

A commercial HPLC system from Agilent Technologies (Waldbronn, Germany) was adapted into a flow chemistry apparatus. Degassed ethanol solutions of BA (120 mmol L⁻¹) and ECA (100 mmol L⁻¹) were provided in separate bottles. The solutions were by a quaternary pump

mixed and delivered to the microreactor, fixed in a thermostated compartment (with a temperature accuracy of ± 0.8 °C and stability of ± 0.05 °C) that also served to preheat the solutions. An in-line diode-array detector (DAD) was used to indicate the steady-state of the microreactor after changing a reaction parameter. A two-position, six-port switching valve connected the microreactor assembly to an HPLC system consisting of a binary pump, a chromatographic column, and a DAD. An injection loop integrated in the valve allowed to transfer discrete, 1.3- μ L plugs of the microreactor effluent onto the column (Chromolith[®] HighResolution RP-18e 100–4.6 mm; Merck Millipore, Darmstadt, Germany). BA and ECC were baseline separated with an eluent of 50/50 (v/v) water/ethanol at a volumetric flow rate of $Q = 1.5$ mL min⁻¹ and detected at 250 nm (ECC) and 290 nm (BA). Standard calibration was used to calculate the concentration of BA and ECC from their absorbance.

2.3 Results and discussion

2.3.1 Synthesis of hierarchical silica monoliths with urea-controlled macro- and mesopore size

To explore the effect of urea on the macropore size of hierarchical silica monoliths, we followed the strategy outlined in Figure 2.1. The starting sol comprised a sulfuric acid solution of TEOS as silica precursor, PEO as porogen, and urea as pore-size controlling agent. Eight samples were prepared in parallel fashion by varying the urea content of the starting sol. Expressed as wt.% of the weight of water, PEO, and TEOS in the starting sol, the urea content was increased from 3 to 24 wt.% in 3-wt.% steps. After gelation, hydrothermal treatment, washing, drying, and calcination, eight monolithic rods were received, designated as samples Urea-1 to Urea-8 (the number indicates the value of m_{urea} , the weight of the amount of urea in the starting sol). The silica monoliths were examined by SEM and subjected to porosimetry analysis (Table 2.1).

Table 2.1. Preparation conditions and porosimetry data for the monolithic silica samples.

Sample	m_{urea} [g]	d_{macro} [μm] ^a	V_{macro} [$\text{cm}^3 \text{g}^{-1}$] ^a	ϵ_{macro} [-] ^a	d_{skel} [μm] ^b	d_{meso} [nm] ^{a (c)}	V_{meso} [$\text{cm}^3 \text{g}^{-1}$] ^{a (c)}	ϵ_{meso} [-] ^a	S_{BET} [$\text{m}^2 \text{g}^{-1}$] ^c
Urea-1	1.05	2.28	1.90	0.61	2.00	10 (5)	0.40 (0.72)	0.62	718
Urea-2	2.10	1.84	2.12	0.61	1.41	14 (14)	0.88 (0.94)	0.66	273
Urea-3	3.16	1.46	2.15	0.62	1.15	15 (16)	0.88 (0.94)	0.66	249
Urea-4	4.21	1.14	2.18	0.61	0.94	18 (16)	0.97 (0.92)	0.68	227
Urea-5	5.27	0.90	2.43	0.63	0.75	19 (18)	0.95 (0.98)	0.68	211
Urea-6	6.31	0.71	2.41	0.61	0.53	20 (21)	1.10 (1.09)	0.71	206
Urea-7	7.36	0.61	2.52	0.63	0.43	24 (25)	1.03 (1.07)	0.69	196
Urea-8	8.43	0.56	2.58	0.64	0.41	26 (23)	1.14 (1.14)	0.69	198

^a Macropore size (d_{macro}), volume (V_{macro}), and porosity (ϵ_{macro}), and mesopore size (d_{meso}), volume (V_{meso}), and porosity (ϵ_{meso}) calculated from MIP data.

^b Skeleton thickness (d_{skel}) estimated from SEM images.

^c Mesopore size (d_{meso}), mesopore volume (V_{meso}), and BET surface area (S_{BET}) based on nitrogen physisorption measurements.

Before discussing the porosimetry data of the entire series, we highlight the most important results through selected samples. Figure 2.2 shows SEM images and MIP results for samples Urea-3, Urea-5, and Urea-7. The SEM images visualize that the urea content of the starting sol has a strong influence on the structural features of the formed silica monoliths.

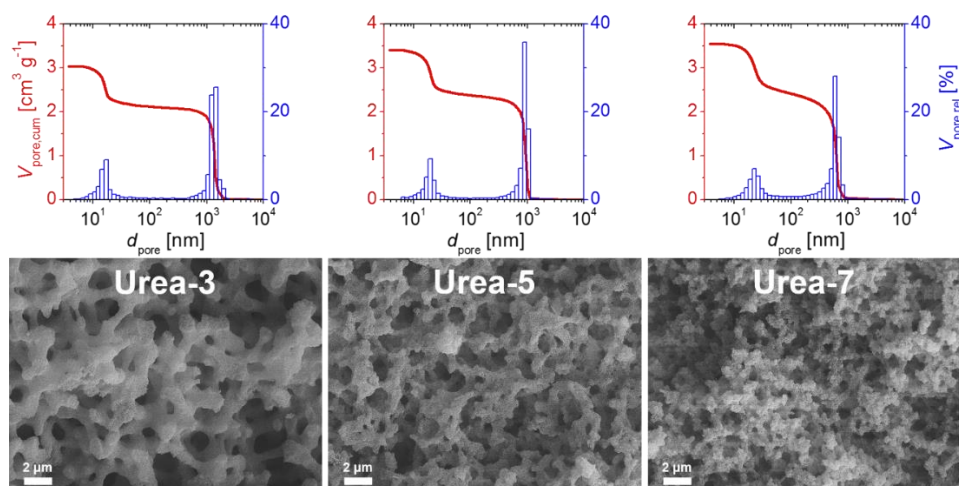


Figure 2.2. SEM images and results of the MIP analysis (mercury intrusion curves and derived pore size distributions as cumulative and relative pore volumes, respectively) for selected hierarchical silica monoliths (*cf.* Table 2.1). The urea content of the starting sol used for their preparation increases from the left to the right sample.

With increasing m_{urea} , the macropores and skeleton become finer while the general architecture of an interconnected pore space is conserved. The MIP curves and derived pore size distributions show a shrinking size difference between (interskeleton) macropore and

(intraskelton) mesopore space from sample Urea-3 to sample Urea-7. Figure 2.3 summarizes the effect of urea as pore-size controlling agent in the prepared series. The urea content of the starting sol influences macropore and mesopore size of the finished monolith in opposite directions: with increasing m_{urea} , the mean mesopore size (d_{meso}) increases while the mean macropore size (d_{macro}) decreases. The pore size range spanned by the samples according to MIP analysis comprises mean mesopore sizes between 10 and 26 nm and mean macropore sizes between 2.3 and 0.6 μm .

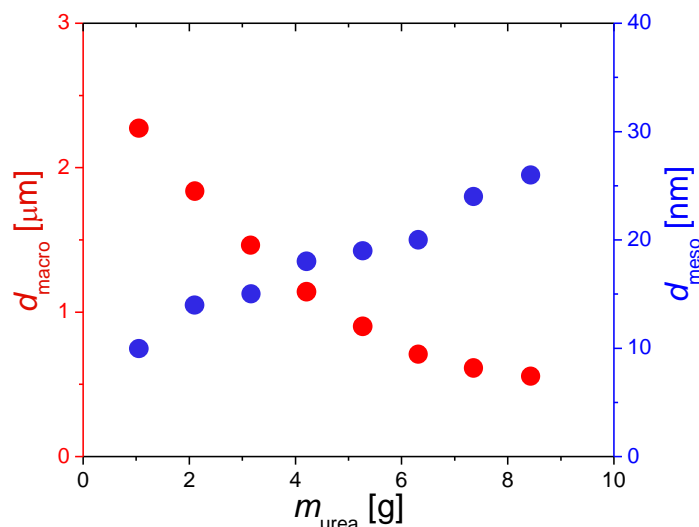


Figure 2.3. MIP-determined macro- and mesopore size (d_{macro} and d_{meso}) of hierarchical silica monoliths vs. weight of the amount of urea in the starting sol.

The effect of m_{urea} on d_{meso} and consequently on the mesopore volume (V_{meso}) of silica monoliths is known.³³ An increased m_{urea} reflects a higher concentration of the surface etching agent during hydrothermal treatment. As a consequence, the mesopores become larger and the specific surface area S_{BET} (essentially the internal surface area of the mesopores) decreases (Table 2.1). In the series, sample Urea-2 actually represents the lower limit of m_{urea} for obtaining a mechanically stable monolith; sample Urea-1 cracked during drying. The nitrogen sorption isotherm and MIP curve of sample Urea-1 differ visibly from those of the other samples (Figures 2.S1 and 2.S2 in the ESI); Urea-1 has very small mesopores and a substantial amount of micropores (*cf.* Figure 2.S1), resulting in a much larger surface area ($718 \text{ m}^2 \text{ g}^{-1}$) than for the rest of the series ($273\text{--}196 \text{ m}^2 \text{ g}^{-1}$). Obviously, the urea content of the starting sol used for sample Urea-1 was too low for a sufficient micropore widening during hydrothermal treatment. Another expected result of the series is the m_{urea} -related increase of the macropore volume (V_{macro}); increasing the urea content of the starting sol increases the volume fraction of the solvent-rich phase, which generally determines V_{macro} .³⁴ The unexpected result is the effect on d_{macro} and d_{skel} ; the data in Table 2.1 prove that mean macropore size and skeleton thickness of the finished monolith can be controlled through the urea content of the starting sol down into the submicron scale (samples Urea-5 to Urea-8).

2.3.2 Role of urea in the formation of macropores and silica skeleton

To understand how urea controls the size of the structural features of the monolith, we considered the possible influence of urea on the different processes during the first step of the synthesis. The gelation behavior of a silica sol is controlled by the reaction rates of hydrolysis and condensation, which are both very fast under strongly acidic conditions (Figure 2.S3 in the ESI).^{35,36} We monitored the turbidity of the starting sol before heating up to the gelation temperature. All starting sols became transparent after ~ 30 min, when the heat release from the solution stopped, which indicates that the hydrolysis rate of TEOS is not affected by the urea content of the starting sol. We then estimated the gelation time t_g of each starting sol by counting from the time of transparency until the gelation point was reached. This was done in a complementary experiment using translucent plastic vessels to visually determine the gelation time as the point when the sol loses its bulk fluidity. Figure 2.4 shows that the gelation time increases with the urea content of the starting sol, from $t_g = 160$ min for $m_{\text{urea}} = 1.05$ g (sample Urea-1) to $t_g = 410$ min for $m_{\text{urea}} = 8.43$ g (sample Urea-8). At gelation temperatures that support the decomposition of urea, urea acts as gelation accelerator, because basic conditions favor condensation over hydrolysis (Figure 2.S3). Urea decomposition should not occur at the gelation temperature of 50°C used in this work, which was verified by measuring the pH of the solution (containing urea, PEO, and sulfuric acid) before addition of TEOS as well as after gelation. As shown in Figure 2.4, the pH rises only slightly with the urea content of the starting sol, from pH 0.58 for $m_{\text{urea}} = 1.05$ g to pH 1.28 for $m_{\text{urea}} = 8.43$ g, and changes minimally upon gelation. While firmly remaining in the acidic range, increasing m_{urea} steers the pH closer to the isoelectric point of silica (pH ~ 2.5), where the condensation rate has a local minimum (Figure 2.S3).

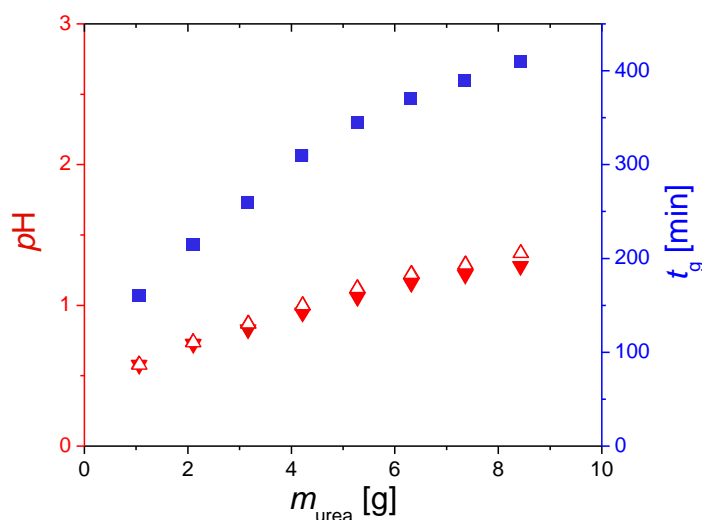


Figure 2.4. pH of the starting sol before addition of TEOS (solid triangles) and after gelation (open triangles) as well as gelation times t_g (solid squares) vs. weight of the amount of urea in the starting sol.

Consequently, increasing the urea content of the starting sol increases the gelation time. If the timing of phase separation is not affected, a longer gelation time generates monoliths with larger structural features, because the two phases evolve by coarsening between the onset of phase separation and gelation. Since the opposite is true for the prepared sample series, urea must have a direct effect on the phase separation. As noted before, urea forms hydrogen bonds with silica as well as PEO and enhances the solubility of hydrophobic compounds in aqueous solution. We assume that urea attaches through hydrogen bonds to PEO, which forms hydrogen bonds with the silanol groups emerging from hydrolysis of the silica precursor (Figure 2.5).

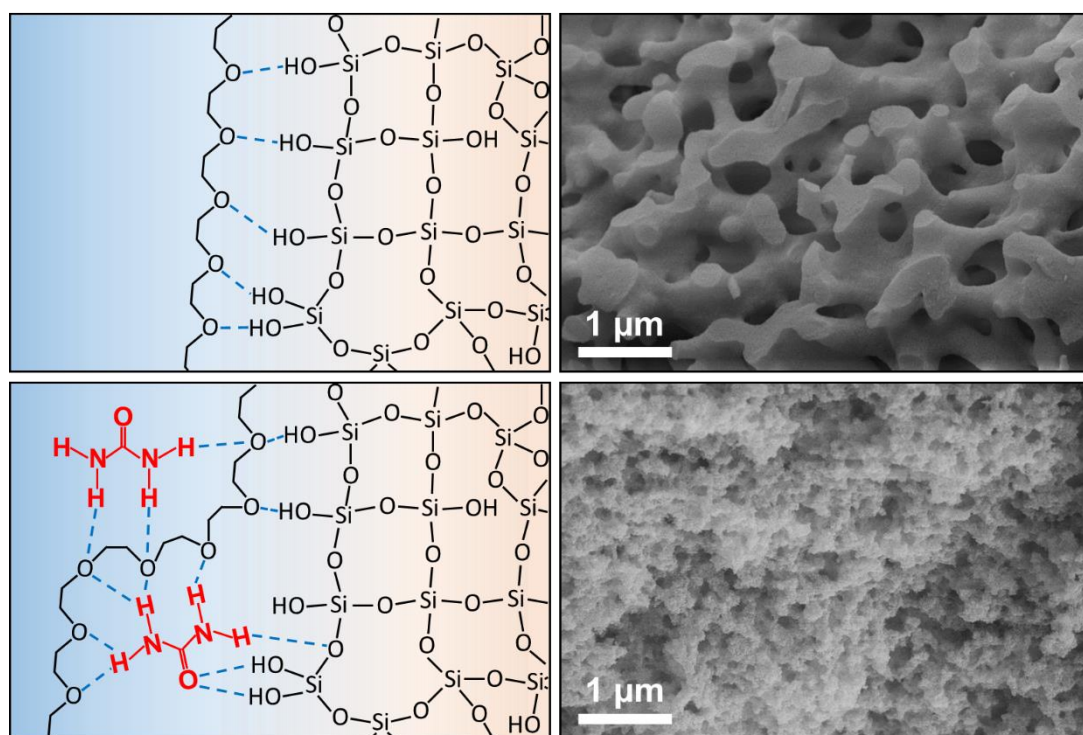


Figure 2.5. Proposed role of urea in the sol-gel step of silica monolith synthesis. Through hydrogen-bond formation, urea weakens PEO adsorption to the silica oligomers and increases the solubility of the PEO-adsorbed silica oligomers in aqueous solution. Both effects retard the onset of phase separation. Phase separation is shifted closer to the gelation point, resulting in monoliths with finer structural features (sample Urea-7, bottom right panel).

Through hydrogen-bond formation with PEO and the emerging silanol groups, urea weakens the adsorption of PEO to the silica oligomers and increases the solubility of the PEO-adsorbed silica oligomers in aqueous solution. Both effects retard the onset of phase separation. At the same time, the gelation time increases with m_{urea} (Figure 2.4) due to a slight pH-increase that lowers the condensation rate. Increasing the urea content of the starting sol thus shifts the timing of phase separation and gelation in the same direction, but not at the same rate, else we would not observe the m_{urea} -dependence of d_{macro} (Figure 2.3). The data suggest that phase separation and gelation are retarded with increasing m_{urea} , but phase separation more than gelation, so that phase separation is effectively shifted closer to the gelation point. The formed gel represents an

earlier frozen (and thus less evolved) state of spinodal decomposition, preserving smaller macropores and a thinner skeleton.

2.3.3 Monolith cladding and column permeability

From the synthesized eight silica rods, sample Urea-7 ($d_{\text{macro}} = 0.61 \mu\text{m}$ and $d_{\text{skel}} = 0.43 \mu\text{m}$) was selected for cladding. This choice reflects our goal to prepare monolithic devices with submicron macropore and skeleton dimensions, minimizing flow-driven dispersion in the macropore space and diffusive transport resistance in the mesoporous skeleton, respectively. These morphological features should lead to extremely narrow residence-time distributions on the catalytic support and, therefore, strong driving forces for mass and heat transfer as well as reaction. Consequently, plug-flow conditions are favoured in the microreactor (on a macroscopic scale) and diffusive transport limitations are eliminated; microreactor operation is shifted from diffusion to reaction control, providing direct access to the intrinsic reaction kinetics of the Knoevenagel condensation.^{14,37} Robust cladding is critical to the targeted use with liquid mobile phases, since a convenient flow rate ($Q \sim 1 \text{ mL min}^{-1}$) easily produces a column backpressure of ~ 100 bar (safely managed by HPLC systems). Sample Urea-7 was clad into stainless-steel tubing using epoxy resin adhesive. Figure 2.6 gives an impression of the seamless cladding and the physical dimensions of the compact column design.

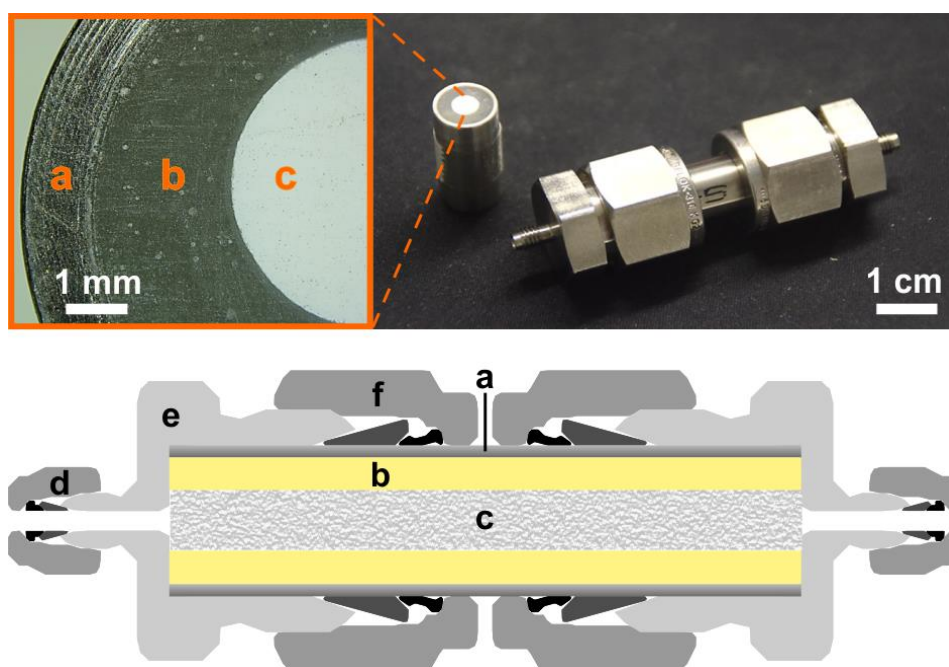


Figure 2.6. Ready-for-use column around a hierarchical silica monolith with submicron macropore size and skeleton thickness (sample Urea-7, *cf.* Table 2.1) for continuous-flow operation (Top right); the cut surface of the column (Top left) visualizes the leakproof contact between monolith and cladding. Schematic drawing of this configured column set-up (Bottom): (a) 1/2" o.d. stainless-steel tube (10.6 mm i.d. \times 4 cm length), (b) UHU[®] PLUS 300 epoxy resin adhesive, (c) monolithic silica rod (5 mm i.d. \times 4 cm length), (d) 5/16" nut hex with 1/16" o.d. tube, (e) 13/16" body hex, and (f) 7/8" nut hex with 1/2" o.d. tube.

Mechanical stability and hydraulic permeability of the configured column around sample Urea-7 were determined by analyzing the pressure drop–flow rate relationship, which characterizes the resistance to hydraulic flow. According to Darcy's law, the pressure drop over the monolithic bed length ($\Delta p/L$) is related to the superficial flow velocity u_{sf} as follows³⁶

$$\frac{\Delta p}{L} = \frac{\eta}{K_D} u_{sf} \quad \text{or} \quad K_D = \frac{u_{sf} L \eta}{\Delta p}, \quad (2.1)$$

where η is the viscosity of the liquid and K_D is the Darcy permeability. The superficial velocity u_{sf} is related to the volumetric flow rate Q and the average velocity u_{av} through

$$u_{av} = \frac{Q}{\varepsilon_{total} A} = \frac{u_{sf}}{\varepsilon_{total}}, \quad (2.2)$$

where A is the cross-sectional area of the rod (see (c) in Figure 2.6) and ε_{total} is the total porosity of the monolith, calculated from its macro- and mesoporosity (ε_{macro} and ε_{meso} , respectively) as $\varepsilon_{total} = \varepsilon_{macro} + (1 - \varepsilon_{macro})\varepsilon_{meso}$.

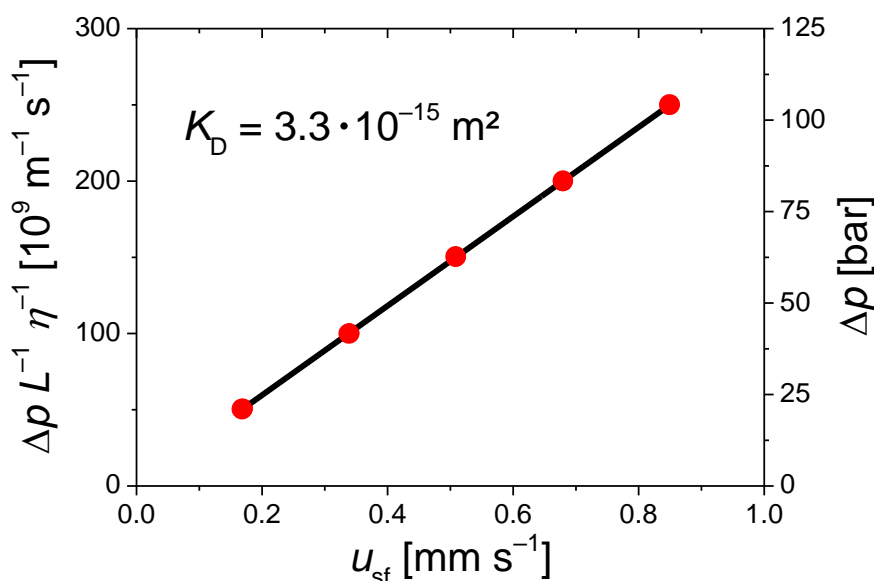


Figure 2.7. Pressure drop–flow rate relationship (Equation (2.1)) for the configured column (Figure 2.6, $L = 4$ cm) around a silica monolith with submicron macropores (sample Urea-7, *cf.* Table 2.1). Mobile phase: pure ethanol ($\eta = 1.04 \times 10^{-3} \text{ kg m}^{-1} \text{ s}^{-1}$ at $T = 20$ °C), range of volumetric flow rates: $Q = 0.2$ – 1.0 mL min^{-1} .

The hydraulic permeability data (Figure 2.7) were recorded for a mobile phase of pure ethanol, the solvent used for the Knoevenagel condensation. The data show excellent linearity up to a pressure drop of >100 bar over the 4-cm long monolithic bed (right ordinate in Figure 2.7). This linearity was maintained in repeated runs, which indicates a mechanically stable bed morphology, resistant to time and use. Fitting the data in Figure 2.7 to Equation (2.1) returned a Darcy permeability of $K_D = 3.3 \times 10^{-15} \text{ m}^2$ for the column.

In terms of hydraulic permeability, the monolithic column with $d_{\text{macro}} = 0.61 \mu\text{m}$ and $\varepsilon_{\text{macro}} = 0.63$ is equivalent to a column packed with $\sim 2 \mu\text{m}$ particles at a (typical) interparticle porosity of 0.37.³⁹ But the monolith offers the following advantages over the particulate bed at the same hydraulic permeability:¹⁴ First, the larger external surface area of the monolith translates to a larger contact area between flowing fluid (in the macropores) and stagnant fluid (in the mesopores), which intensifies mass transport to and from the active surface sites in the mesopores. And second, the interskeleton macropore space is more homogeneous and less constricted than the interparticle void space in the packing; therefore, hydrodynamic dispersion in the monolith is much smaller than in the packing (at the same flow velocity).

2.3.4 Continuous-flow microreactor for reaction kinetic and mechanistic studies

The mechanical stability of the engineered monolithic column allows the advanced operation as continuous-flow microreactor at >100 bar backpressure.³⁷ Figure 2.6 shows a ready-for-use column, but the silica surface of the monolith needs to be functionalized first for a specific application. We use the Knoevenagel condensation, since it is an important carbon–carbon bond forming reaction in organic synthesis and commonly employed to evaluate heterogeneous base catalysis in batch mode^{40,41} as well as in continuous-flow operation with fixed catalyst supports.^{42–50} To catalyze the Knoevenagel condensation of BA and ECA to ECC (Scheme 2.1), an APS surface is required. Aminopropylation of the column under stop-flow conditions yielded a surface coverage of $\sim 2.8 \mu\text{mol m}^{-2}$, comparable to commercial APS materials.³⁷

The microreactor was integrated into a flow-chemistry system on-line coupled through a switching valve to an analytical HPLC system. Catalytic testing was run as follows. Ethanol solutions of the reactants BA (120 mmol L^{-1}) and ECA (100 mmol L^{-1}) were mixed at a ratio of 1:1 (v/v), resulting in feed concentrations of 60 and 50 mmol L^{-1} , respectively, preheated, and pumped through the microreactor at varied volumetric flow rate and temperature (solutions were preheated by the thermostated column compartment that also contained the microreactor). For a given temperature T , the flow rate was varied at $Q = 0.2\text{--}1.0 \text{ mL min}^{-1}$, translating into average velocities of $u_{\text{av}} = 0.19\text{--}0.95 \text{ mm s}^{-1}$ through the monolith (Equation (2.2) with $\varepsilon_{\text{total}} \sim 0.89$ for sample Urea-7). This resulted in system backpressures of up to 165 bar (Figure 2.S4 in the ESI). Afterwards, the temperature was increased and the flow rate variation repeated. These processes were permanently monitored by the in-line DAD, which indicated when the microreactor reached steady-state after changing a reaction parameter (Q and/or T). When the steady-state for a given Q – T pair was reached, the two-position, six-port valve was switched to transfer a $1.3 \mu\text{L}$ -plug from the microreactor outlet (effluent) to the on-line coupled HPLC system, where reactants and product were baseline separated on a reversed-phase column with a mobile phase of 50/50 (v/v) water/ethanol. Each valve switch therefore produced a chromatogram (inset in Figure 2.8). Detected were the aromatic compounds BA and ECC, whose absorbances in the DAD were then used to quantify their concentrations in the effluent. The effect of varied input parameters (Q , T) on the reaction system were thus directly reflected

in the resulting output parameters (absorbance) of the HPLC analysis system. All input parameter variations and valve switches were programmed as function of the experiment time; once started, the experiment proceeded fully automated.

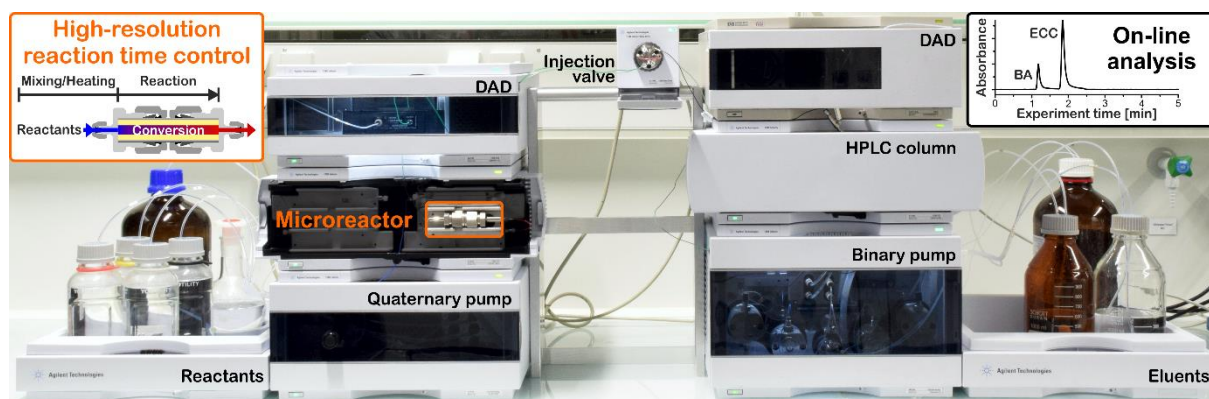


Figure 2.8. Prepared microreactor integrated into the reaction system (left half): a quaternary pump delivers a preheated mixture of the reactants in ethanol solution to the microreactor; the in-line DAD indicates when the microreactor has reached steady-state after a change of flow rate or temperature. With the two-position, six-port switching (injection) valve, the microreaction system is on-line coupled to an analytical HPLC system (right half) that separates reactants and product and quantifies their concentrations in the microreactor effluent.

Figure 2.9 summarizes the results of the catalytic testing, collected from a single experiment of ~400 min duration (left panels) and provides an analysis of the collected data (right panels). The dashed, vertical lines in the bottom-left panel indicate the valve switches (plug injections) that lead to the corresponding chromatograms in the top-left panel.

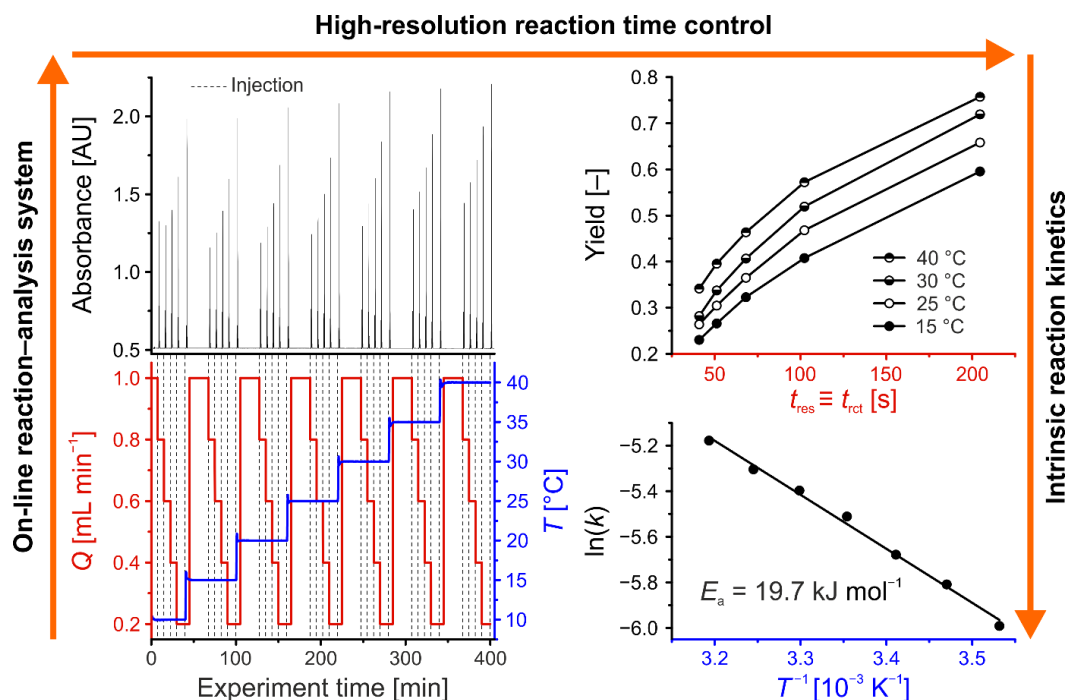


Figure 2.9. Catalytic testing with the on-line coupled reaction–analysis system shown in Figure 2.8. (Bottom left) Variation of flow rate Q (thus, reaction time) and temperature T in the microreactor. (Top left) The resulting seven sets of five chromatograms (seven temperatures at five flow rates each) corresponding to an overall experiment time of ~ 400 min. (Top right) Yield of the Knoevenagel condensation as a function of residence time t_{res} (which equals the reaction time t_{rct}) at four temperatures. (Bottom right) Arrhenius plot to determine the activation energy E_a of the Knoevenagel condensation between BA and ECA to ECC on the APS monolith (Scheme 2.1).

Through pore-scale simulations of flow and mass transport (using lattice-Boltzmann and random-walk methods) in three-dimensional reconstructions obtained by confocal laser scanning microscopy,^{51,52} we have previously shown that the intrinsic morphology engenders very little hydrodynamic dispersion in silica monoliths, which are similar to those analyzed here. In particular, D_L/D_m (the longitudinal dispersion coefficient normalized by the diffusion coefficient in the corresponding bulk liquid) for a passive, *i.e.*, nonadsorbing, nonreacting tracer increased weakly from ~ 0.7 at $u_{\text{av}} = 0.2 \text{ mm s}^{-1}$ (reflecting mostly diffusion through the tortuous pore space of the monolith) to ~ 5.8 at $u_{\text{av}} = 6.2 \text{ mm s}^{-1}$. The hydrodynamics remained in the laminar flow regime, with Reynolds numbers well below unity and Péclet numbers $Pe = u_{\text{av}}d_{\text{dom}}/D_m$ not exceeding 20, calculated using the domain size $d_{\text{dom}} = d_{\text{macro}} + d_{\text{skel}}$ of these monoliths.⁵² Their small flow-channels ($d_{\text{macro}} \sim 1.2 \text{ }\mu\text{m}$ and $\sim 1.9 \text{ }\mu\text{m}$) are therefore expected to result in extremely narrow residence time distributions on the support and ideal plug-flow behavior. This is illustrated with a look at typical Bodenstein numbers (Bo) characterizing reactor-based liquid-phase transport by flow relative to hydrodynamic dispersion along the flow direction.⁵³

$$Bo = \frac{u_{av}L}{D_L} \quad (2.3)$$

The longitudinal dispersion coefficient D_L in Equation (2.3) includes, in general, contributions from longitudinal diffusion as well as mechanical, boundary-layer, and hold-up dispersion.³⁸ Based on the simulated D_L - u_{av} data,^{51,52} values estimated for Bo in the range of Q (0.2–1.0 mL min⁻¹) and u_{av} (0.19–0.95 mm s⁻¹) encountered in the present work, with $L = 40$ mm, are on the order of 10^4 . Further, the monolith employed here as microreactor (Figure 2.6) has a still smaller macropore size and skeleton thickness than the monoliths considered earlier in the simulations,^{51,52} which is expected to result in an even lower D_L -value (higher Bo) at a given velocity. This analysis clearly indicates plug-flow conditions due to the unique morphology of these monoliths, which engenders very little longitudinal dispersion (resulting in the low D_L -values).

Plug-flow behavior allows to calculate the residence time t_{res} of solutes in the microreactor from the reactor void volume (given by the empty-reactor volume $V_{reactor} = \pi r^2 L$, where r and L denote radius and length of the monolithic silica rod, and the total porosity ϵ_{total} of the monolith) and the volumetric flow rate Q .³⁷ Because the catalyst is immobilized on the silica surface, reaction proceeds for as long as the reactants are inside the microreactor. Consequently, the reaction time t_{rct} equals the residence time t_{res} :

$$t_{rct} \equiv t_{res} = \frac{V_{reactor} \epsilon_{total}}{Q} \quad (2.4)$$

For a given monolithic microreactor, the reaction time t_{rct} depends only on Q , which is precisely controlled by the pump. The resulting high-resolution reaction time control allows to analyze multiple reaction times rapidly in a single experiment through variation of the flow rate.^{54,55} The top-right panel of Figure 2.9, for example, analyzes the dependence of the yield from reaction time (controlled through the flow rate) and temperature. The yield was calculated as the ratio between ECC concentration in the effluent and ECA concentration in the feed.

The bottom-right panel of Figure 2.9 illustrates the great potential of the monolithic microreactor for convenient reaction kinetic and mechanistic studies in heterogeneous catalysis. With its favorable morphology, diffusive transport limitations in the monolith are absent.³⁷ Submicron macropores and a very thin skeleton provide quick access to a large surface area (~ 200 m² g⁻¹) embedded into an only weakly obstructed network of mesopores, whose size is sufficient ($d_{meso} \sim 25$ nm) to offer little hindrance to diffusion.⁵⁶ We have found that the APS-catalyzed Knoevenagel condensation of BA and ECA follows a first-order reaction kinetics based on the proposed reaction mechanism: In a very fast first step, BA reacts with the aminopropyl groups to an imine (Schiff base); in the rate-determining second step, nucleophilic attack of ECA yields the product ECC.^{37,45} Working with excess BA compared to the ECA concentration, the aminopropyl groups are always saturated with BA. Quasi-immobilized on the surface, BA maintains a constant concentration corresponding to the concentration of

aminopropyl groups in the reactor volume. Thus, reaction rate only depends on ECA concentration. For the first-order kinetics, the rate constants k were calculated at different temperatures from the dependence of $\ln(c(\text{ECA}))$ on t_{rct} . Due to the use of dilute educt solutions, the quasi-isothermal microreactor operation³⁷ allowed to determine the activation energy E_a of the Knoevenagel condensation through the Arrhenius equation

$$k = A e^{-\frac{E_a}{RT}}, \quad (2.5)$$

where A is the pre-exponential factor and R the universal gas constant (bottom-right panel of Figure 2.9).

Compared with the literature, the low value of $E_a = 19.7 \text{ kJ mol}^{-1}$ derived for the heterogeneously-catalyzed Knoevenagel condensation reflects the near-instant access of the reactants to the large, active surface area of the monolithic microreactor (as if the catalytic centers were moving freely in solution).^{37,57} In other words, the excellent transport properties of the prepared hierarchical silica monolith with submicron structural features enable quasi-homogeneous catalysis in continuous-flow mode with a high-performance fixed-bed support. This is corroborated by an estimation of the values for the Thiele modulus, which are on the order of 10^{-4} (details of the calculation can be found in the ESI). These low values indicate the wide range of possible applications with the presented concept and material (still avoiding diffusive transport limitations). It includes, for example, much faster reactions than the Knoevenagel condensation adapted here (as a mere test reaction), the use of smaller intraskelton mesopores or even micropores (depending on application), or the immobilization of enzymes, *e.g.*, in the wider mesopores realized here ($d_{\text{meso}} = 25 \text{ nm}$), which will also allow a relatively unimpeded transport, in general, of bulkier molecules and species, like peptides and proteins, or even metal clusters and nanoparticles.⁵⁶

2.4 Conclusions

We have demonstrated how to prepare hierarchical silica monoliths ready-for-use as supports for continuous-flow applications. To synthesize mechanically stable, monolithic silica rods with the desirable morphology, namely submicrometer macropores and a thin mesoporous skeleton, we adapted the classical Nakanishi process. Through adjusting the urea content of the starting sol we achieved simultaneous control over macro- and mesopore size of the resulting rods. Raising the urea content of the starting sol from 3 to 24 wt.% decreased d_{macro} from 2.3 to 0.6 μm , d_{skel} from 2.0 to 0.4 μm , and increased d_{meso} from 10 to 26 nm. We assume that urea acts in the sol–gel step by retarding phase separation more than gelation, so that an earlier state of spinodal decomposition is frozen, which yields finer structural features. The use of urea as macropore-size controlling agent may be the key to mechanically stable, monolithic silica rods with submicron morphological features.

We introduced a low-cost, straightforward procedure to a seamless stainless-steel cladding of the monolithic silica rods that allows their operation as columns or microreactors with liquid mobile phases at convenient flow rates of $\sim 1 \text{ ml min}^{-1}$ and column backpressures $>100 \text{ bar}$. For reaction kinetic and mechanistic studies, a monolithic silica rod with submicrometer macropore size and skeleton thickness was cladded and, after surface functionalization, employed as continuous-flow microreactor in an on-line coupled reaction–analysis system enabling fully automated catalytic testing. High performance of the prepared monolithic support was demonstrated by investigating the reaction kinetics of the Knoevenagel condensation, suggesting an instantly available surface area of the intraskeleton mesopores and the absence of diffusion limitations.

Overall, the presented approach offers academic laboratories a reliable route to large-surface-area supports with tailored morphological and functional properties in a mechanically stable, compact column format, which are attractive for various applications like the fully automated screening of reaction mechanisms and kinetics.

2.5 Supporting Information

Table 2.S1. Results of the elemental analysis for sample Urea-7 after hydrothermal treatment, after calcination, as well as after functionalization.

	After hydrothermal treatment ^a	After calcination	After functionalization
N [%]	0	0.06	0.76
C [%]	12.40	0.29	5.58
H [%]	2.793	0.186	0.898

^a After hydrothermal treatment, the sample was washed several times with water (until the pH of the aqueous solution became neutral) and then dried under reduced pressure.

All elemental analyses were performed by the “Gerätezentrum für Massenspektrometrie und Elementaranalytik” at the Department of Chemistry, Philipps-Universität Marburg (Marburg, Germany), using the CHN(S)-analyzer vario MICRO cube (Elementar Analysensysteme, Hanau, Germany). The data suggest that all nitrogen containing molecules like urea or its decomposition products can be washed out already after hydrothermal treatment. During phase separation, urea and its decomposition products are therefore mainly in the aqueous phase; at least, they are not incorporated (and fixed) in the gelled silica-PEO system. After calcination, all organic residues are removed, so that the nitrogen content after functionalization can be exclusively attributed to the functionalization with aminopropyl groups on the silica surface.

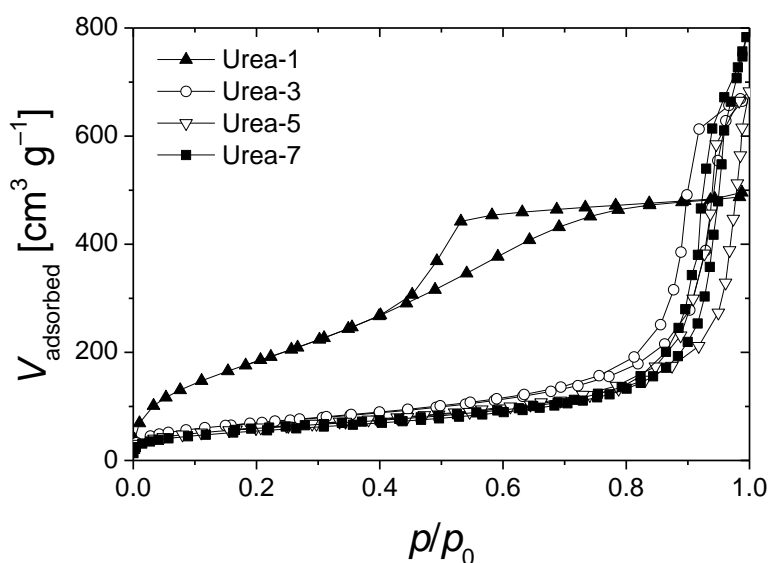


Figure 2.S1. Nitrogen sorption isotherms of bimodal silica monoliths prepared with different urea content of the starting sol (*cf.* Table 2.1 in the main text).

Isotherms in Figure 2.S1 can be classified as type IV isotherms.^{S1} Sample Urea-1 has a hysteresis type H2(a); a saturation plateau is reached and the hysteresis closes again at $p/p_0 = 0.42$. The other samples show a type H1 hysteresis. Here, the saturation plateau is not completely reached, which indicates incomplete filling of the pores. The change of hysteresis can be explained by the extent of mesopore widening during hydrothermal treatment, which depends on the urea content of the starting sol.

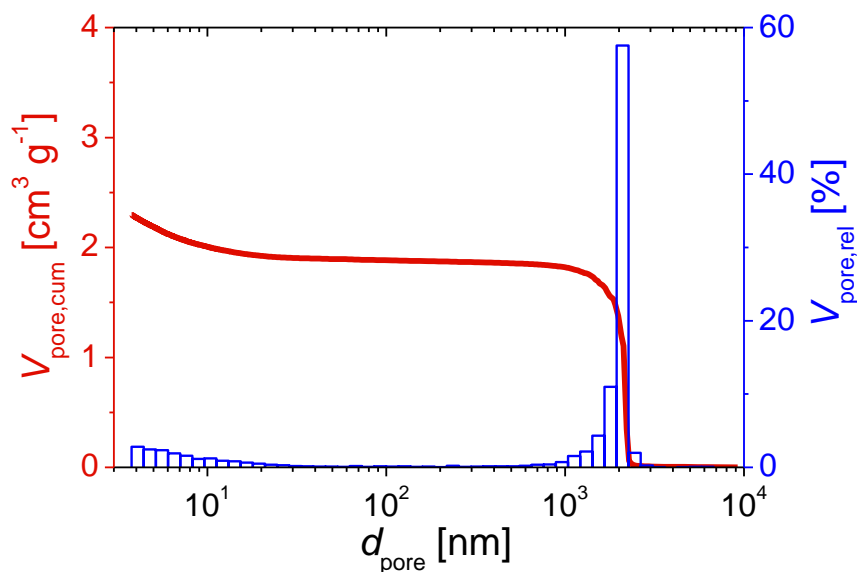


Figure 2.S2. Results of the MIP analysis (mercury intrusion curve and the derived pore size distribution as cumulative and relative pore volume, respectively) for sample Urea-1 (*cf.* Table 2.1 in the main text).

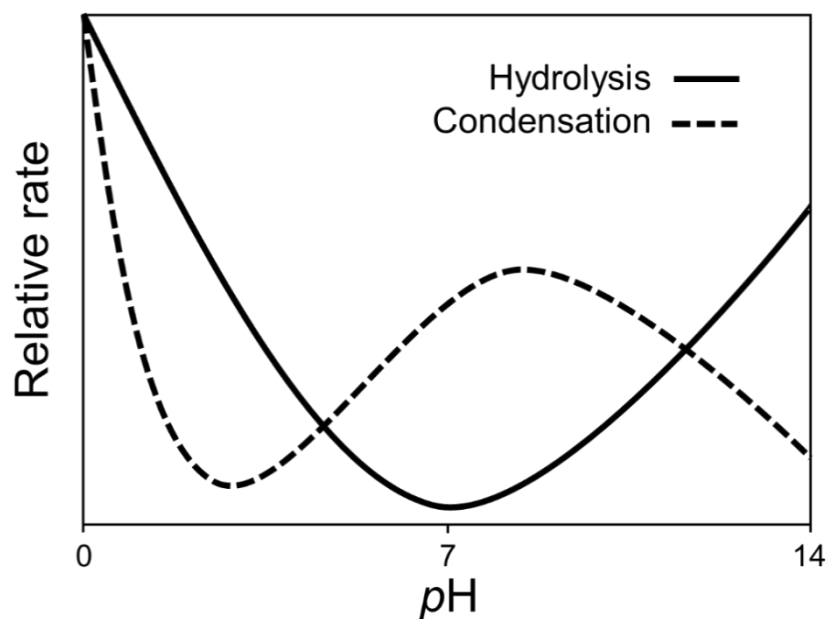


Figure 2.S3. pH dependence of hydrolysis and condensation rates in silicates. Adapted with permission from ref 35. Copyright © 1989 The American Association for the Advancement of Science.

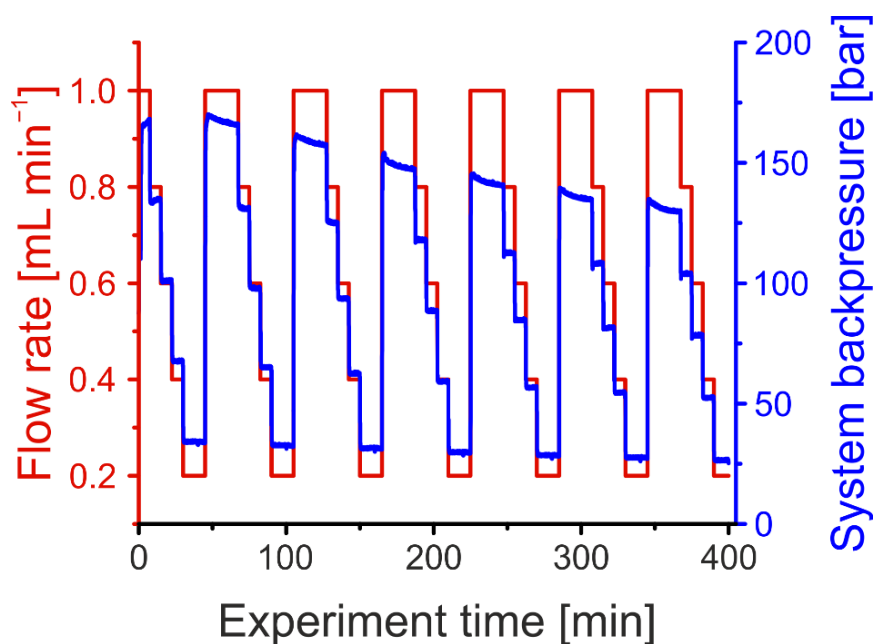


Figure 2.S5. Adjustments of the volumetric flow rate by the quaternary pump and resulting backpressure in the flow-chemistry system with the integrated microreactor (*cf.* Figure 2.8 in the main text, left half of the entire setup).

2.5.1 Estimation of the Thiele modulus for the silica monolithic microreactor

The Thiele modulus Φ accounts for the competition between the Knoevenagel reaction at the aminopropylated silica surface (represented by the rate constant k) and the limitation of transport of the reactant ECA by diffusion in the mesoporous skeleton of the monolith (represented by the effective diffusion coefficient D_{eff}):

$$\Phi = L_{\text{skel}} \sqrt{\frac{k}{D_{\text{eff}}}} = \frac{V_{\text{skel}}}{A_{\text{ext}}} \sqrt{\frac{k}{D_{\text{eff}}}} \quad (2.S1)$$

The characteristic diffusion length L_{diff} is generally defined through the volume-to-surface ratio of the spatial domain, in which diffusion-limited transport takes place. In this study, $L_{\text{skel}} \equiv L_{\text{diff}}$ in Equation (2.S1) refers to diffusive transport in the mesopores of the silica skeleton (the white-appearing skeleton of the silica monoliths seen, for example, in Figure 2.5 of the main text, contains a fine network of mesopores; the macropores, by contrast, in which liquid flow occurs through the silica monolith, are outside this skeleton).

We have shown earlier^{S3} that L_{skel} can be estimated from d_{skel} (the thickness of the typical worm-like silica skeleton in a monolith) by using the characteristic length parameter of a cylindrical pellet shape. Here, $d_{\text{skel}}/2$ corresponds to the radius of the assumed cylindrical (worm-like) structural element and the diffusion length then is one half of the cylinder radius:^{S4}

$$L_{\text{skel}} = \frac{d_{\text{skel}}}{2} \cdot \frac{1}{2} = 0.11 \mu\text{m} \quad (2.S2)$$

(Before continuing, it has to be realized that, due to the very fine morphology of the monolith, the characteristic diffusion length in its mesoporous skeleton is on the order of only 100 nanometers, as illustrated with Equation (2.S2).)

For calculation of D_{eff} in Equation (2.S1) we first estimate the size of ECA, which is ~ 0.7 nm. Regarding hindered diffusion of this molecule in the mesoporous skeleton of the monolith, we notice that the ratio of ECA-size to the mean mesopore size in sample Urea-7 ($d_{\text{meso}} = 25$ nm) is as low as 0.028. We can thus simplify the general formula derived for hindered diffusion of finite-size tracers in mesoporous silica^{S5} to that for point-like tracers [see, for example, equation (10) with $\lambda = d_{\text{tracer}}/d_{\text{meso}} = 0$ in S.-J. Reich, A. Svidrytski, D. Hlushkou, D. Stoeckel, C. Kübel, A. Höltzel and U. Tallarek, Hindrance factor expression for diffusion in random mesoporous adsorbents obtained from pore-scale simulations in physical reconstructions. *Ind. Eng. Chem. Res.*, **2018**, *57*, 3031–3042.]:

$$D_{\text{eff}} = D_{\text{m}} \frac{\varepsilon_{\text{meso}}}{\tau_{\text{meso}}} \quad (2.S3)$$

In Equation (2.S3), $\varepsilon_{\text{meso}}$ and τ_{meso} denote the porosity and diffusive tortuosity of the mesopore space accessible to point-like tracers, and D_{m} is the diffusion coefficient in the bulk liquid. Intraskelton porosity for sample Urea-7 is $\varepsilon_{\text{meso}} = 0.69$ (given in Table 2.1 of the main

text). For a very similar porosity (0.70) and mesopore size (25.7 nm), diffusion simulations in reconstructed mesoporous silica from these monoliths gave a diffusive tortuosity for point-like tracers of $\tau_{\text{meso}} = 1.35^{S5}$ [cf. the data for sample Si26 in Table 3 in S.-J. Reich, A. Svidrytski, D. Hlushkou, D. Stoeckel, C. Kübel, A. Höltzel and U. Tallarek, *Ind. Eng. Chem. Res.*, **2018**, *57*, 3031–3042.]. The (electron tomographic) reconstruction employed in these diffusion simulations has been received from the mesoporous skeleton of such silica monoliths and should therefore be regarded as a very realistic structural model.

After having derived/collected values for L_{skel} (0.11 μm), $\varepsilon_{\text{meso}}$ (0.69), and τ_{meso} (1.35), we now estimate the value for D_m using the Wilke–Chang equation^{S6} applied to ECA in pure ethanol. The Wilke–Chang equation describes the molecular diffusion coefficient D_{AB} for the solute ECA (subscript A) in the solvent ethanol (subscript B) as:

$$D_{AB} = 7.4 \cdot 10^{-8} \frac{(\varphi_B M_B)^{0.5} T}{V_{b,A}^{0.6} \mu_B} \quad (2.S4)$$

For the solvent, φ_B is the association factor, M_B the molar mass, and μ_B the dynamic viscosity, whose temperature-dependence can be approximated as:^{S7}

$$\mu_B(T) = \exp\left(-6.21 + \frac{1614}{T} + 0.00618 T - 1.132 \cdot 10^{-5} T^2\right) \quad (2.S5)$$

The molar volume at the normal boiling point $V_{b,A}$ can be derived using the critical volume $V_{c,A}$, critical temperature $T_{c,A}$, boiling point $T_{b,A}$, and acentric factor ω_A of the solute ECA:^{S8}

$$V_{b,A} = 7.047345 + 0.4 V_{c,A} + \left(0.01724 + \frac{15.3765}{T_{c,A}} + 0.004387 \omega_A\right) T_{b,A} \quad (2.S6)$$

All required thermophysical data for ECA can be found in the literature.^{S9} They are summarized in Table 2.S2 together with the resulting molar volume at the normal boiling point.

Table 2.S2. Thermophysical properties of ethyl cyanoacetate (ECA).

$V_{c,A}$ [mL mol ⁻¹]	$T_{c,A}$ [K]	$T_{b,A}$ [K]	ω_A [-]	$V_{b,A}$ [mL mol ⁻¹]
358.00	679.00	482.20	0.426	170.38

Returning to the Wilke–Chang equation, the ECA diffusion coefficient at different temperatures was estimated using the association factor of $\varphi_B = 1.5$ and a molar mass of $M_B = 46.07$ g mol⁻¹ for the solvent ethanol. The experimental values for the reaction rate constant k were determined in the temperature range $T = 10$ – 40 °C in steps of 5 °C. All temperature dependent values (including the targeted Thiele moduli) are summarized in Table 2.S3.

Table 2.S3. Ethanol viscosity, molecular and effective intraskeleton diffusion coefficients of ECA, as well as the rate constants of the rate-determining step in the Knoevenagel condensation, and the resulting Thiele moduli in the temperature range of 10–40 °C.

T [K]	μ_B [cPa]	D_{AB} [m ² s ⁻¹]	D_{eff} [m ² s ⁻¹]	k [s ⁻¹]	Φ [-]
283.15	1.39	5.72×10^{-10}	2.92×10^{-10}	2.50×10^{-3}	0.00032
288.15	1.26	6.44×10^{-10}	3.29×10^{-10}	3.00×10^{-3}	0.00033
293.15	1.14	7.22×10^{-10}	3.69×10^{-10}	3.42×10^{-3}	0.00033
298.15	1.04	8.08×10^{-10}	4.13×10^{-10}	4.04×10^{-3}	0.00034
303.15	0.95	9.01×10^{-10}	4.61×10^{-10}	4.53×10^{-3}	0.00035
308.15	0.87	1.00×10^{-9}	5.11×10^{-10}	4.97×10^{-3}	0.00034
313.15	0.79	1.11×10^{-9}	5.67×10^{-10}	5.64×10^{-3}	0.00035

Since the Thiele moduli in the reaction system are on the order of 10^{-4} , mass transfer limitations can be safely excluded. It means that the entire surface is practically instantaneously available, without delay, reflecting highest effectiveness (*i.e.*, an effectiveness factor of unity).

References

- (1) K. Kanamori, K. Nakanishi, Controlled pore formation in organotrialkoxysilane-derived hybrids: from aerogels to hierarchically porous monoliths. *Chem. Soc. Rev.*, **2011**, *40*, 754–770.
DOI: 10.1039/C0CS00068J.
- (2) T. Noisser, G. Reichenauer, N. Hüsing, In situ modification of the silica backbone leading to highly porous monolithic hybrid organic-inorganic materials via ambient pressure drying. *ACS Appl. Mater. Interfaces*, **2014**, *6*, 1025–1029.
DOI: 10.1021/am404005g.
- (3) K. Nakanishi, N. Tanaka, Sol–gel with phase separation. Hierarchically porous materials optimized for high-performance liquid chromatography separations. *Acc. Chem. Res.*, **2007**, *40*, 863–873.
DOI: 10.1021/ar600034p.
- (4) I. Tan, Z. Zarafshani, J.-F. Lutz, M.-M. Titirici, PEGylated chromatography: Efficient bioseparation on silica monoliths grafted with smart biocompatible polymers. *ACS Appl. Mater. Interfaces*, **2009**, *1*, 1869–1872.
DOI: 10.1021/am900461a.
- (5) A. Sachse, A. Galarneau, F. Fajula, F. Di Renzo, P. Creux, B. Coq, Functional silica monoliths with hierarchical uniform porosity as continuous flow catalytic reactors. *Microporous Mesoporous Mater.*, **2011**, *140*, 58–68.
DOI: 10.1016/j.micromeso.2010.10.044.

-
- (6) G. Hayase, K. Kugimiya, M. Ogawa, Y. Kodera, K. Kanamori, K. Nakanishi, The thermal conductivity of polymethylsilsesquioxane aerogels and xerogels with varied pore sizes for practical application as thermal superinsulator. *J. Mater. Chem. A*, **2014**, *2*, 6525–6531.
DOI: 10.1039/C3TA15094A.
- (7) J. García-Aguilar, I. Miguel-García, Á. Berenguer-Murcia, D. Cazorla-Amorós, Synthesis of robust hierarchical silica monoliths by surface-mediated solution/precipitation reactions over different scales: Designing capillary microreactors for environmental applications. *ACS Appl. Mater. Interfaces*, **2014**, *6*, 22506–22518.
DOI: 10.1021/am506595c.
- (8) E. Cuce, P. M. Cuce, C. J. Wood, S. B. Riffat, Toward aerogel based thermal superinsulation in buildings: A comprehensive review. *Renew. Sust. Energ. Rev.*, **2014**, *34*, 273–299.
DOI: 10.1016/j.rser.2014.03.017.
- (9) Y. G. Ko, H. J. Lee, J. Y. Kim, U. S. Choi, Hierarchically porous aminosilica monolith as a CO₂ adsorbent. *ACS Appl. Mater. Interfaces*, **2014**, *6*, 12988–12996.
DOI: 10.1021/am5029022.
- (10) A. Galarneau, A. Sachse, B. Said, C.-H. Péllisson, P. Boscaro, N. Brun, L. Courtheoux, N. Olivi-Tran, B. Coasne, F. Fajula, Hierarchical porous silica monoliths: A novel class of microreactors for process intensification in catalysis and adsorption. *C. R. Chimie*, **2016**, *19*, 231–247.
DOI: 10.1016/j.crci.2015.05.017.
- (11) C.-H. Péllisson, T. Nakanishi, Y. Zhu, K. Morisato, T. Kamei, A. Maeno, H. Kaji, S. Muroyama, M. Tafu, K. Kanamori, T. Shimada, K. Nakanishi, Grafted polymethylhydrosiloxane on hierarchically porous silica monoliths: A new path to monolith-supported palladium nanoparticles for continuous flow catalysis applications. *ACS Appl. Mater. Interfaces*, **2017**, *9*, 406–412.
DOI: 10.1021/acsami.6b12653.
- (12) H. Maleki, N. Hüsing, Current status, opportunities and challenges in catalytic and photocatalytic applications of aerogels: Environmental protection aspects. *Appl. Catal. B*, **2018**, *221*, 530–555.
DOI: 10.1016/j.apcatb.2017.08.012.
- (13) G. Guiochon, Monolithic columns in high-performance liquid chromatography. *J. Chromatogr. A*, **2007**, *1168*, 101–168.
DOI: 10.1016/j.chroma.2007.05.090.
- (14) D. Enke, R. Gläser, U. Tallarek, Sol–gel and porous glass-based silica monoliths with hierarchical pore structure for solid-liquid catalysis. *Chem. Ing. Tech.*, **2016**, *88*, 1561–1585.
DOI: 10.1002/cite.201600049.

-
- (15) T. Müllner, K. K. Unger, U. Tallarek, Characterization of microscopic disorder in reconstructed porous materials and assessment of mass transport-relevant structural descriptions. *New J. Chem.*, **2016**, *40*, 3993–4015.
DOI: 10.1039/C5NJ03346B.
- (16) H. Minakuchi, K. Nakanishi, N. Soga, N. Ishizuka, N. Tanaka, Effect of domain size on the performance of octadecylsilylated continuous porous silica columns in reversed-phase liquid chromatography. *J. Chromatogr. A*, **1998**, *797*, 121–131.
DOI: 10.1016/S0021-9673(97)00947-3.
- (17) M. Motokawa, H. Kobayashi, N. Ishizuka, H. Minakuchi, K. Nakanishi, H. Jinnai, K. Hosoya, T. Ikegami, N. Tanaka, Monolithic silica columns with various skeleton sizes and through-pore sizes for capillary liquid chromatography. *J. Chromatogr. A*, **2002**, *961*, 53–63.
DOI: 10.1016/S0021-9673(02)00133-4.
- (18) T. Hara, H. Kobayashi, T. Ikegami, K. Nakanishi, N. Tanaka, Performance of monolithic silica capillary columns with increased phase ratios and small-sized domains. *Anal. Chem.*, **2006**, *78*, 7632–7642.
DOI: 10.1021/ac060770e.
- (19) R. Skudas, B. A. Grimes, M. Thommes, K. K. Unger, Flow-through pore characteristics of monolithic silicas and their impact on column performance in high-performance liquid chromatography. *J. Chromatogr. A*, **2009**, *1216*, 2625–2636.
DOI: 10.1016/j.chroma.2009.01.079.
- (20) K. Nakanishi, Pore structure control of silica gels based on phase separation. *J. Porous Mater.*, **1997**, *4*, 67–112.
DOI: 10.1023/A:1009627216939.
- (21) K. Nakanishi, R. Takahashi, T. Nagakane, K. Kitayama, N. Koheiya, H. Shikata, N. Soga, Formation of hierarchical pore structure in silica gel. *J. Sol-Gel Sci. Technol.*, **2000**, *17*, 191–210.
DOI: 10.1023/A:1008707804908.
- (22) D. Stoeckel, C. Kübel, M. O. Loeh, B. M. Smarsly, U. Tallarek, Morphological analysis of physically reconstructed silica monoliths with submicrometer macropores: Effect of decreasing domain size on structural homogeneity. *Langmuir*, **2015**, *31*, 7391–7400.
DOI: 10.1021/la5046018.
- (23) A. Feinle, M. S. Elsaesser, N. Hüsing, Sol–gel synthesis of monolithic materials with hierarchical porosity. *Chem. Soc. Rev.*, **2016**, *45*, 3377–3399.
DOI: 10.1039/C5CS00710K.
- (24) J.-B. Pang, K.-Y. Qiu, J. Xu, Y. Wei, J. Chen, Synthesis of mesoporous silica materials via nonsurfactant urea-templated sol–gel reactions. *J. Inorg. Organomet. Polym. Mater.*, **2000**, *10*, 39–49.
DOI: 10.1023/A:1009404415925.

- (25) F. E. Bailey, H. G. France, Molecular association complexes of polymers. Urea and thiourea complexes of high molecular weight poly(ethylene oxide). *J. Polym. Sci.*, **1961**, *49*, 397–406.
DOI: 10.1002/pol.1961.1204915221.
- (26) E. Yilgör, E. Burgaz, E. Yurtsever, İ. Yilgör, Comparison of hydrogen bonding in polydimethylsiloxane and polyether based urethane and urea copolymers. *Polymer*, **2000**, *41*, 849–857.
DOI: 10.1016/S0032-3861(99)00245-1.
- (27) G. G. Hammes, P. R. Schimmel, An investigation of water-urea and water-urea-polyethylene glycol interactions. *J. Am. Chem. Soc.*, **1967**, *89*, 442–446.
DOI: 10.1021/ja00978a050.
- (28) E. G. Finer, F. Franks, M. J. Tait, Nuclear magnetic resonance studies of aqueous urea solutions. *J. Am. Chem. Soc.*, **1972**, *94*, 4424–4429.
DOI: 10.1021/ja00768a004.
- (29) S. Spange, D. Keutel, Untersuchungen zur Polarität wäßriger Harnstoff- und Zucker-Lösungen mit der Methode der vergleichenden Solvatochromie. *Liebigs Ann. Chem.*, **1993**, *1993*, 981–985.
DOI: 10.1002/jlac.1993199301156.
- (30) B. J. Bennion, V. Daggett, The molecular basis for the chemical denaturation of proteins by urea. *Proc. Natl. Acad. Sci. U. S. A.*, **2003**, *100*, 5142–5147.
DOI: 10.1073/pnas.0930122100.
- (31) K. A. Cychosz, R. Guillet-Nicolas, J. García-Martínez, M. Thommes, Recent advances in the textural characterization of hierarchically structured nanoporous materials. *Chem. Soc. Rev.*, **2017**, *46*, 389–414.
DOI: 10.1039/C6CS00391E.
- (32) Technisches Merkblatt 63251 – UHU PLUS ENDFEST, <https://www.uhu.de/content/dam/boltonadhesives/products/import/55/de/3950/50.pdf>, (accessed April 2018).
- (33) K. Nakanishi, H. Shikata, N. Ishizuka, N. Koheiya, N. Soga, Tailoring mesopores in monolithic macroporous silica for HPLC. *J. High Resolut. Chromatogr.*, **2000**, *23*, 106–110.
DOI: 10.1002/(SICI)1521-4168(20000101)23:1<106::AID-JHRC106>3.0.CO;2-1.
- (34) K. Nakanishi, H. Komura, R. Takahashi, N. Soga, Phase separation in silica sol–gel system containing poly(ethylene oxide). I. Phase relation and gel morphology. *Bull. Chem. Soc. Jpn.*, **1994**, *67*, 1327–1335.
DOI: 10.1246/bcsj.67.1327.
- (35) C. J. Brinker, Hydrolysis and condensation of silicates: Effects on structure. *J. Non Cryst. Solids*, 1988, *100*, 31–50.
DOI: 10.1016/0022-3093(88)90005-1.
- (36) D. W. Schaefer, Polymers, fractals, and ceramic materials. *Science*, **1989**, *243*, 1023–1027.

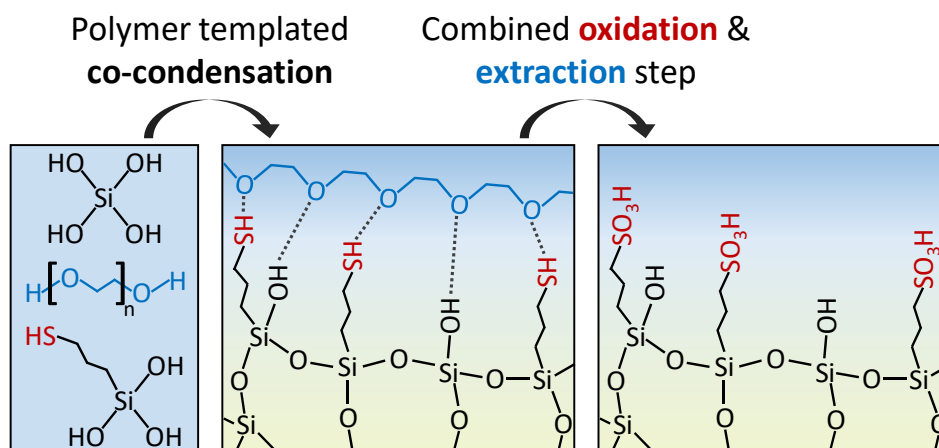
- DOI: 10.1126/science.243.4894.1023.
- (37) C. P. Haas, T. Müllner, R. Kohns, D. Enke, U. Tallarek, High-performance monoliths in heterogeneous catalysis with single-phase liquid flow. *React. Chem. Eng.*, **2017**, *2*, 498–511.
DOI: 10.1039/C7RE00042A.
- (38) D. Hlushkou, U. Tallarek, Transition from creeping via viscous-inertial to turbulent flow in fixed beds. *J. Chromatogr. A*, **2006**, *1126*, 70–85.
DOI: 10.1016/j.chroma.2006.06.011.
- (39) K. Hormann, U. Tallarek, Analytical silica monoliths with submicron macropores: current limitations to a direct morphology-column efficiency scaling. *J. Chromatogr. A*, **2013**, *1312*, 26–36.
DOI: 10.1016/j.chroma.2013.08.087.
- (40) A. Corma, S. Iborra, I. Rodríguez, F. Sánchez, Immobilized proton sponge on inorganic carriers: The synergic effect of the support on catalytic activity. *J. Catal.*, **2002**, *211*, 208–215.
DOI: 10.1006/jcat.2002.3692.
- (41) T. C. Keller, S. Isabettini, D. Verboekend, E. G. Rodrigues, J. Pérez-Ramírez, Hierarchical high-silica zeolites as superior base catalysts. *Chem. Sci.*, **2014**, *5*, 677–684.
DOI: 10.1039/C3SC51937F.
- (42) E. Angeletti, C. Canepa, G. Martinetti, P. Venturello, Amino groups immobilized on silica gel: an efficient and reusable heterogeneous catalyst for the Knoevenagel condensation. *J. Chem. Soc., Perkin Trans. 1*, **1989**, 105–107.
DOI: 10.1039/P19890000105.
- (43) X. Zhang, E. S. M. Lai, R. Martin-Aranda, K. L. Yeung, An investigation of Knoevenagel condensation reaction in microreactors using a new zeolite catalyst. *Appl. Catal. A: Gen.*, **2004**, *261*, 109–118.
DOI: 10.1016/j.apcata.2003.10.045.
- (44) T. Jackson, J. H. Clark, D. J. Macquarrie, J. H. Brophy, Base catalysts immobilized on silica coated reactor walls for use in continuous flow systems. *Green Chem.*, **2004**, *6*, 193–195.
DOI: 10.1039/B315764B.
- (45) R. Wirz, D. Ferri, A. Baiker, ATR-IR spectroscopy of pendant NH₂ groups on silica involved in the Knoevenagel condensation. *Langmuir*, **2006**, *22*, 3698–3706.
DOI: 10.1021/la053145y.
- (46) A. R. Bogdan, B. P. Mason, K. T. Sylvester, D. T. McQuade, Improving solid-supported catalyst productivity by using simplified packed-bed microreactors. *Angew. Chem. Int. Ed.*, **2007**, *46*, 1698–1701.
DOI: 10.1002/anie.200603854.

-
- (47) A. El Kadib, R. Chimenton, A. Sachse, F. Fajula, A. Galarneau, B. Coq, Functionalized inorganic monolithic microreactors for high productivity in fine chemicals catalytic synthesis. *Angew. Chem. Int. Ed.*, **2009**, *48*, 4969–4972.
DOI: 10.1002/anie.200805580.
- (48) A. Sachse, A. Galarneau, F. Di Renzo, F. Fajula, B. Coq, Synthesis of zeolite monoliths for flow continuous processes. The case of sodalite as a basic catalyst. *Chem. Mater.*, **2010**, *22*, 4123–4125.
DOI: 10.1021/cm1014064.
- (49) R. Munirathinam, J. Huskens, W. Verboom, Supported catalysis in continuous-flow microreactors. *Adv. Synth. Catal.*, **2015**, *357*, 1093–1123.
DOI: 10.1002/adsc.201401081.
- (50) W. Song, D. Shi, S. Tao, Z. Li, Y. Wang, Y. Yu, J. Qiu, M. Ji, X. Wang, Bio-inspired immobilization of metal oxides on monolithic microreactor for continuous Knoevenagel reaction. *J. Colloid Interface Sci.*, **2016**, *481*, 100–106.
DOI: 10.1016/j.jcis.2016.07.052.
- (51) D. Hlushkou, S. Bruns, A. Seidel-Morgenstern, U. Tallarek, Morphology-transport relationships for silica monoliths: From physical reconstruction to pore scale simulations. *J. Sep. Sci.*, **2011**, *34*, 2026–2037.
DOI: 10.1002/jssc.201100158.
- (52) D. Hlushkou, K. Hormann, A. Hölzel, S. Khirevich, A. Seidel-Morgenstern, U. Tallarek, Comparison of first and second generation analytical silica monoliths by pore-scale simulations of eddy dispersion in the bulk region. *J. Chromatogr. A*, **2013**, *1303*, 28–38.
DOI: 10.1016/j.chroma.2013.06.039.
- (53) H. S. Fogler, *Elements of Chemical Reaction Engineering*, 4th Ed., Prentice Hall, Upper Saddle River, NJ, **2006**.
- (54) J. Yoshida, Y. Takahashi, A. Nagaki, Flash chemistry: flow chemistry that cannot be done in batch. *Chem. Commun.*, **2013**, *49*, 9896–9904.
DOI: 10.1039/C3CC44709J.
- (55) J. S. Moore, K. F. Jensen, “Batch“ kinetics in flow: online IR analysis and continuous control. *Angew. Chem. Int. Ed.*, **2014**, *53*, 470–473.
DOI: 10.1002/anie.201306468.
- (56) S.-J. Reich, A. Svidrytski, D. Hlushkou, D. Stoeckel, C. Kübel, A. Hölzel, U. Tallarek, Hindrance factor expression for diffusion in random mesoporous adsorbents obtained from pore-scale simulations in physical reconstructions. *Ind. Eng. Chem. Res.*, **2018**, *57*, 3031–3042.
DOI: 10.1021/acs.iecr.7b04840.
- (57) S. L. Hruby, B. H. Shanks, Acid–base cooperativity in condensation reactions with functionalized mesoporous silica catalysts. *J. Catal.*, **2009**, *263*, 181–188.
DOI: 10.1016/j.jcat.2009.02.011.

-
- (S1) M. Thommes, K. Kaneko, A. V. Neimark, J. P. Olivier, F. Rodriguez-Reinoso, J. Rouquerol, K. S. W. Sing, Physisorption of gases, with special reference to the evaluation of surface area and pore size distribution (IUPAC Technical Report). *Pure Appl. Chem.*, **2015**, *87*, 1051–1069.
DOI: 10.1515/pac-2014-1117.
- (S2) D. W. Schaefer, Polymers, fractals, and ceramic materials. *Science*, **1989**, *243*, 1023–1027.
DOI: 10.1126/science.243.4894.1023.
- (S3) C. P. Haas, T. Müllner, R. Kohns, D. Enke, U. Tallarek, High-performance monoliths in heterogeneous catalysis with single-phase liquid flow. *React. Chem. Eng.*, **2017**, *2*, 498–511.
DOI: 10.1039/C7RE00042A.
- (S4) M. E. Davis, R. J. Davis, *Fundamentals of Chemical Reaction Engineering*, McGraw-Hill, New York, NY, **2003**.
- (S5) S.-J. Reich, A. Svidrytski, D. Hlushkou, D. Stoeckel, C. Kübel, A. Höltzel, U. Tallarek, Hindrance factor expression for diffusion in random mesoporous adsorbents obtained from pore-scale simulations in physical reconstructions. *Ind. Eng. Chem. Res.*, **2018**, *57*, 3031–3042.
DOI: 10.1021/acs.iecr.7b04840.
- (S6) C. R. Wilke, P. Chang, Correlation of diffusion coefficients in dilute solutions. *AIChE J.*, **1955**, *1*, 264–270.
DOI: 10.1002/aic.690010222.
- (S7) CHERIC, <http://www.cheric.org/research/kdb/hcprop/cmprch.php> (accessed April 2018).
- (S8) I. E. Maloka, Generalized liquid molar volume at the normal boiling point correlation. *Pet. Sci. Technol.*, **2005**, *23*, 133–136.
DOI: 10.1081/LFT-200028058.
- (S9) C. L. Yaws, *Thermophysical Properties of Chemicals and Hydrocarbons*, William Andrew, Norwich, NY, **2014**.

Chapter 3

In situ synthesis and characterization of sulfonic acid functionalized, hierarchical silica monoliths



Authors

Richard Kohns, Ralf Meyer, Marianne Wenzel, Jörg Matysik, Dirk Enke and Ulrich Tallarek

State of Publication

Submitted 16 April 2020 to *Journal of Sol-Gel Science and Technology*.

Abstract

Surface functionalization of porous materials with sulfonic acid (SO₃H) groups is of particular interest in applications involving ion exchange, acidic catalysis and proton conduction. Macroporous silica monoliths are ideal support structures for these applications, as they combine advection-dominated mass transport in the macropores with short diffusion lengths and a large surface area (available for functionalization) in their mesoporous skeleton. Here, we report on SO₃H functionalized sol-gel silica monoliths with bimodal pore systems exhibiting macro- and mesoporosity, prepared according to a simple, efficient in situ synthesis protocol. Based on the co-condensation approach, thiol groups were introduced homogeneously into the pore structure, followed by their oxidation to SO₃H groups and the simultaneous removal of the template. The macropore size, specific surface area and coverage with SO₃H groups are easily adjusted in this synthesis route. Importantly, the hybrid monoliths have a substantially narrower mesopore size distribution (relative standard deviation ~25%) than conventional sol-gel materials (>40%) and can be engineered crack-free in a robust column design (suitable for high-pressure flow-through operation) with mean mesopore size down to ~7 nm. They are characterized by IR spectroscopy, thermogravimetry and elemental analysis as well as ¹³C and ²⁹Si solid state NMR to corroborate the simple, efficient combination of sol-gel based material synthesis, surface functionalization and template removal (*i.e.*, polymer extraction). Complementary, inverse gas chromatography is presented as a new approach to characterize the incorporated SO₃H groups *via* surface energy analysis and particularly resolve changes in the Lewis acid-base characteristics engendered by that functionalization.

3.1 Introduction

Hierarchically porous silica monoliths with bimodal pore structure are widely used for chemical separation, thermal insulation, electrochemical processes, CO₂ adsorption and heterogeneous catalysis.^{1–9} Macro-mesoporous silica monoliths, in particular, are ideal support structures in these applications, because the macropores enable fast, advection-dominated transport through the material and the mesoporous skeleton provides a large external surface (thus, a large contact area) for efficient mass transfer between macroporous and mesoporous domains, as well as a large internal surface available for functionalization.¹⁰ Silica monoliths are also characterized by more homogeneous structural features (distribution of pore size and skeleton thickness) than alternative bimodal support structures like packed beds of mesoporous particles, which again enhances transport and overall performance.¹¹ Due to their high porosity, low bulk density, pore interconnectivity, mechanical stability and large surface, silica monoliths can be approached with various functionalization strategies.^{12,13}

Functionalization with organic species leads to organic-inorganic hybrid materials, whereby the synthesis routes can be quite versatile. A common strategy is to graft the surface with functional groups by traditional chemical bonding (involving the silanol groups of the silica surface), for which alkoxy silanes have proven to be well-suited linkers.^{14–17} However, this approach faces a number of disadvantages, such as the intrinsic drawbacks of multistep synthesis procedures, the inhomogeneous distribution of active sites and a low coverage due to pore blocking effects and hindered diffusion issues.¹⁸ Furthermore, it has been shown that the grafting procedure may not result in a homogeneous monolayer of the linkers, but rather in the formation of oligomers with ladder-like structures.¹⁹ An alternative is the co-condensation process, in which alkoxy silanes are hydrolyzed simultaneously with suitable silica precursors during sol–gel synthesis.^{7,20} The hydrolyzed precursors compete with each other during condensation and form a homogeneous porous hybrid material. The sol–gel process itself is extremely sensitive to parameter changes, so that even slight modifications regarding, for example, the polarity or pH affect the properties of the resulting monoliths. It implies that the synthesis has to be optimized individually for each material and functionality.^{14,21–23}

Functionalization of porous materials with sulfonic acid (SO₃H) groups is of special interest in applications involving ion exchange, acidic catalysis and proton conduction. Marshall *et al.*^{24–26} investigated the synthesis of sulfonic acid modified mesoporous materials (like MCM-41 and SBA-15) and their particular property of a high proton conductivity. Other studies focused on the preparation of SO₃H-functionalized mesoporous silicas (MCM-41, SBA-15, and KIT-6) for application in the heterogeneously catalyzed esterification of monoglycerides or fatty acids for the synthesis of biodiesel.^{27–29} Dias *et al.*³⁰ examined the dehydration of xylose to furfural with SO₃H-modified MCM-41 materials. The direct synthesis of sulfonic acid functionalized porous silicas based on the sol–gel process, however, has received little attention. Wilson *et al.*³¹ used the co-condensation method to prepare SO₃H-functionalized mesoporous materials applied in

the esterification of butan-1-ol with acetic acid. As one of the first, Xu and Lee³² adopted the co-condensation approach to synthesize SO₃H-modified, macro-mesoporous sol-gel monoliths (involving polymer-induced phase separation) intended for the microextraction of anesthetics followed by capillary electrophoretic separation. Apparently, the polymer has not been removed from the monolith prior to that application, which is expected to affect transport properties and impair the targeted functionality.

The preparation of sol-gel silica monoliths with bimodal pore size distribution can be divided into four steps: (1) the sol-gel transition with concurrent, polymer-induced phase separation to form a macro-microporous gel; (2) the widening process by hydrothermal treatment to enlarge micropores to mesopores and ripening the pore structure; (3) the solvent exchange and drying, which should yield a dry, mechanically stable monolith; and (4) calcination to remove organic matter on the inner surface.²¹ However, if the co-condensation method is adapted to incorporate organic groups into the pore system, then calcination cannot be applied, because the functional groups will also be removed. Therefore, an alternative process that guarantees efficient removal of the template (polymer) becomes one of the keys in a general route to these hierarchical hybrid materials.

We introduce a rapid and efficient synthesis procedure for the preparation of macro-mesoporous silica monoliths with homogeneously incorporated sulfonic acid functionalities by adapting the co-condensation sol-gel process. Through integration of a mild extraction step, the polymer can be removed without losing the organic functionality. Importantly, full oxidation of the initially introduced thiol groups to sulfonic acid groups occurs concurrently with the polymer extraction, resulting in hybrid monoliths with conveniently adjustable macropore size, specific surface area and SO₃H coverage. The simplicity and efficiency of this novel synthesis route are corroborated with a portfolio of characterization methods. Notably, inverse gas chromatography is a powerful approach to quantify by surface energy analysis the impact of the SO₃H groups on the interfacial properties of these hybrid materials and address, in particular, the changes in Lewis acid-base behavior occurring upon SO₃H functionalization.

3.2 Experimental

3.2.1 Chemicals

Tetraethoxysilane (TEOS, 99%) came from abcr (Karlsruhe, Germany). Poly(ethylene oxide) (PEO) with an average molecular weight of 100,000 was obtained from Alfa Aesar (Haverhill, MA). (3-mercaptopropyl)trimethoxysilane (MPTMS, ≥95%) and hydrogen peroxide (30%) were purchased from Merck (Darmstadt, Germany). Urea came from Caesar & Loretz (Hilden, Germany), sulfuric acid (95%) (AnalaR NORMAPUR[®] ACS, Reag. Ph. Eur.) and nitric acid (65%) from VWR International (Darmstadt, Germany). All reagents were used without further purification.

3.2.2 Synthesis

Sulfonic acid modified silica monoliths were prepared by a co-condensation sol–gel synthesis, adapting the synthesis procedure described in Kohns *et al.*¹⁴ In the prepared set of monoliths, only the PEO and MPTMS contents were varied. With increasing MPTMS content the TEOS content was reduced by the respective equivalent. Complementary, a reference material without MPTMS was synthesized. Starting compositions employed for the set of monolithic materials are summarized in Table S1 in the ESI.

First, PEO (1.5–1.8 g) and urea (2.4 g) were added to distilled water (18 g) under vigorous stirring. After stirring for 30 min at room temperature, sulfuric acid (1.26 g) and TEOS (12.7–14.6 g) were added. After an additional 30 min of vigorous stirring MPTMS (0–2.11 g) was added to the solution, which was stirred for 10 min. Each mixture was poured into a PTFE tube (7 mm i.d., filled to 10-cm height). PTFE inlets were placed in a small lab autoclave, which was put in an oven for gelation (24 h at 55 °C) and subsequent hydrothermal treatment (20 h at 120 °C). After cooling, wet gels were washed by submersion in stirred water, refreshed 4–5 times until pH was neutral (~5 h). Each gel was then placed in its own plastic vessel, submerged with water, and dried in an oven (24 h at 105 °C). The drying process is based on the procedure described in Kohns *et al.*³³ Dried monolithic rods had a diameter of ~0.5 cm and a length of ~9 cm and were trimmed to a length of 5 cm. Remaining pieces served as reference to evaluate the success of the oxidation/extraction procedure.

The removal of the polymer was performed according to the procedure described by Patarin.³⁴ Importantly, the reagents also oxidized the thiol to sulfonic acid groups. Briefly, each MPTMS-functionalized silica rod was stirred in a mixture of hydrogen peroxide (30%) and nitric acid (65%) at a ratio of silica : H₂O₂ : HNO₃ of 1 g : 37 g : 92 g at room temperature. After 1 h, the solvent was refreshed and the mixture heated to 60 °C for 18 h. Subsequently, silica rods were placed in a small lab Teflon autoclave with refreshed H₂O₂/HNO₃ solution and heated in an oven for 2 h at 120 °C. After cooling, the wet gels were washed by submersion in stirred water, refreshed 5–6 times (~5 h). Each rod was then placed in its own plastic vessel, submerged with water and dried in an oven (24 h, 105 °C) to obtain crack-free monoliths. For later comparison, several monolith pieces were calcined in a muffle furnace for 8 h, using a heating rate of 3 °C min⁻¹ from room temperature up to 600 °C.

3.2.3 Characterization

Silica rods were examined by mercury intrusion porosimetry (MIP) measurements on a Pascal 140/440 porosimeter (Thermo Fisher Scientific, Waltham, MA) over the pressure range of 0.015–400 MPa. Pore size distributions were derived from the MIP data with Pascal software according to the Washburn equation setting the mercury contact angle to 141°. The pressure range corresponds to pore diameters between 3.7 nm and 100 µm. Scanning electron microscope (SEM) images were recorded with a FEI Nanolab 200 (Hillsboro, OR). Sample

pieces were vapor-deposited with Au at 10 kV. This step was omitted for energy-dispersive X-ray analysis (SEM-EDX). Nitrogen physisorption measurements were carried out at $-196\text{ }^{\circ}\text{C}$ on an Autosorb-iQ sorption analyzer (Quantachrome Instruments, Boynton Beach, FL). Prior to the measurements, samples were evacuated for 10 h at $105\text{ }^{\circ}\text{C}$. Total pore volumes (V_{meso}) were obtained with the Gurvich rule at a relative pressure of $p/p_0 = 0.95$, specific surface areas (S_{BET}) were determined by means of the Brunauer–Emmett–Teller equation in a range of $0.05 \leq p/p_0 \leq 0.3$. Pore size distributions were derived from the adsorption branches of the physisorption isotherms using the non-local density functional theory (NLDFT) method with a cylindrical pore model.³⁵ Elemental analysis (CHNS) was conducted on a vario Micro cube (Elementar, Langensfeld, Germany). Thermogravimetry (TG/DTA) was carried out in a temperature range of $25\text{--}600\text{ }^{\circ}\text{C}$ with a $10\text{ }^{\circ}\text{C min}^{-1}$ heating rate using a Netzsch STA 409 (Selb, Germany). Diffuse reflectance infrared fourier transform spectroscopy (DRIFTS) was performed using a Vector 22 FT-IR spectrometer (Bruker, Billerica, MA) in the range of $700\text{--}4000\text{ cm}^{-1}$. Magic-angle spinning (MAS) ^{13}C and ^{29}Si NMR spectra were recorded on an Avance-III 400-MHz WB NMR spectrometer (Bruker BioSpin, Rheinstetten, Germany) equipped with a 4 mm MAS BB/1H probe at a Larmor frequency of 400.15 MHz for protons, 100.62 MHz for ^{13}C and 79.49 MHz for ^{29}Si , respectively. All spectra were collected at a spinning speed of 12 kHz at $20\text{ }^{\circ}\text{C}$ and referenced externally to TMS at 0 ppm. For cross-polarization (CP) experiments, 1024 scans were accumulated with a recycle delay of 5 s. Polarization transfer from protons to ^{29}Si and ^{13}C , respectively, was conducted for a contact time of 8 ms. For high-power decoupled (HPDEC) experiments, 256 scans were accumulated with a 90° pulse width of $6\text{ }\mu\text{s}$ (^{29}Si) and a recycle delay of 60 s. The offset was set at -50 ppm and the spectral width to 32 kHz in both experiments. During acquisition, heteronuclear decoupling was reached, using a $\text{SW}_f\text{-TPPM}$ at a radio-frequency field of 100 kHz.³⁶ Before conducting the NMR measurements, the monoliths had to be crushed. Inverse gas chromatography (IGC) experiments were carried out on a Clarus580 GC apparatus (PerkinElmer, Waltham, MA) equipped with flame ionization detector and controlled by IGC software (Adscientis SARL, Wittelsheim, France). To conduct the IGC measurements, the rods had to be transferred into a robust column format. For that purpose, the rods were embedded in a stainless-steel tubing ($10.6\text{ mm i.d./}12.6\text{ mm o.d.} \times 5\text{ cm length}$; Swagelok, Solon, OH) using UHU[®] PLUS 300 epoxy resin adhesive (UHU, Bühl, Germany) with a composition of 1:1 (v/v) tube binder and hardener, adapting the method from Kohns *et al.*¹⁴ Columns were completed by attaching zero-volume reducing unions (Swagelok) to the stainless-steel tubes (Figure 3.S1, ESI). Prior to the investigations, the columns were conditioned overnight at $80\text{ }^{\circ}\text{C}$ with a helium flow (20 mL min^{-1}). All IGC experiments were run at the same temperature and flow rate. Molecular probe molecules ($\text{C}_6\text{--C}_9$ *n*-alkanes, dichloromethane, chloroform, diethyl ether, acetonitrile and benzene) were injected at least three times onto each column to derive retention times. Methane served as inert reference.

3.3 Results and discussion

3.3.1 Pore space properties of the functionalized materials

To present a novel preparation sequence for sulfonic acid functionalized sol–gel monoliths with hierarchically structured pore systems, we adapted the strategy of a co-condensation synthesis procedure. The starting sol comprised a sulfuric acid solution of TEOS as silica precursor, water as solvent, PEO as porogen, urea as pore-size controlling agent (especially for mesopores), and MPTMS as functionalization precursor. MPTMS was added 30 min after starting the hydrolysis of TEOS, as it hydrolyses faster due to the methoxy groups. Following the well-known and established synthesis steps (gelation, hydrothermal treatment, washing, drying), an extraction and at the same time oxidation step was implemented in order to obtain hierarchically structured sulfonic acid functionalized silica rods.^{1,14,20,33} To confirm the success of the synthesis, samples were preserved untreated in their pristine state and (in some cases) subsequently calcined. The terminology for sample denotation is as follows: P-**X** stands for the initial weight of PEO and S-**X** for the initial volume of MPTMS. Abbreviations ext and c denote extracted and calcined. If not stated otherwise, results are presented for the modification after the oxidation/extraction procedure, referring to the sulfonic acid functionalized silica. All monoliths were examined by SEM and subjected to porosimetry analysis (Table 3.1).

Table 3.1. Porosimetry data for the sulfonic acid functionalized silica monoliths.

Sample	$d_{\text{macro}}^{\text{a}} /$ nm	$V_{\text{macro}}^{\text{a}} /$ $\text{cm}^3 \text{g}^{-1}$	$d_{\text{meso}}^{\text{a}} /$ nm	$V_{\text{meso}}^{\text{a}} /$ $\text{cm}^3 \text{g}^{-1}$	$\varepsilon_{\text{total}}^{\text{a}} /$ –	$S_{\text{BET}}^{\text{b}} /$ $\text{m}^2 \text{g}^{-1}$	$d_{\text{meso}}^{\text{b}} /$ nm	$V_{\text{total}}^{\text{b}} /$ $\text{cm}^3 \text{g}^{-1}$
P-1.5-S-1	8253	1.98	10	0.54	0.85	418	9	0.88
P-1.6-S-1	3547	2.25	10	0.72	0.87	428	9	0.95
P-1.7-S-1	2162	2.33	11	0.81	0.87	469	9	1.04
P-1.8-S-1	1202	2.46	12	0.87	0.88	470	9	1.10
P-1.7-S-1.5	4821	2.09	13	0.52	0.85	546	7	0.96
P-1.8-S-2	2353	2.07	13	0.38	0.84	576	7	1.00
P-1.7-S-0*	1100	2.33	21	1.08	0.88	195	26	1.21

^a Macropore size (d_{macro}) and volume (V_{macro}), mesopore size (d_{meso}) and volume (V_{meso}), as well as total porosity ($\varepsilon_{\text{total}}$) calculated from MIP data. d_{macro} and d_{meso} correspond to the median pore diameter (corresponding to 50% of the total intrusion volume increment).

^b BET surface area (S_{BET}), mesopore size calculated *via* NLDFT (d_{meso}), as well as total mesopore volume (V_{total}) based on nitrogen physisorption measurements.

* All data refer to the calcined material.

First, it is important to note that bimodal pore systems with interconnected pore structures were obtained for all synthesized samples. SEM images and MIP results for samples P-1.5-S-1 (lower end of polymer variation), P-1.8-S-1 (upper end of polymer variation) and P-1.8-S-2 (highest

MPTMS content) are compared in Figure 3.1. The images visualize that the polymer-induced phase separation conserved an interconnected pore structure resulting from spinodal decomposition. As the amount of polymer (PEO) increases, macropores and silica skeleton become much finer while the general morphology is preserved, as known for these sol–gel systems.^{1,21} The sponge-like pore structure is also recognized for the sample with the highest MPTMS content, although no state of spinodal decomposition could be frozen with a lower polymer content. This can be explained by the fact that MPTMS affects the polarity of the sol. This parameter (among others) has a significant influence on the gelation and phase separation.^{14,21,22}

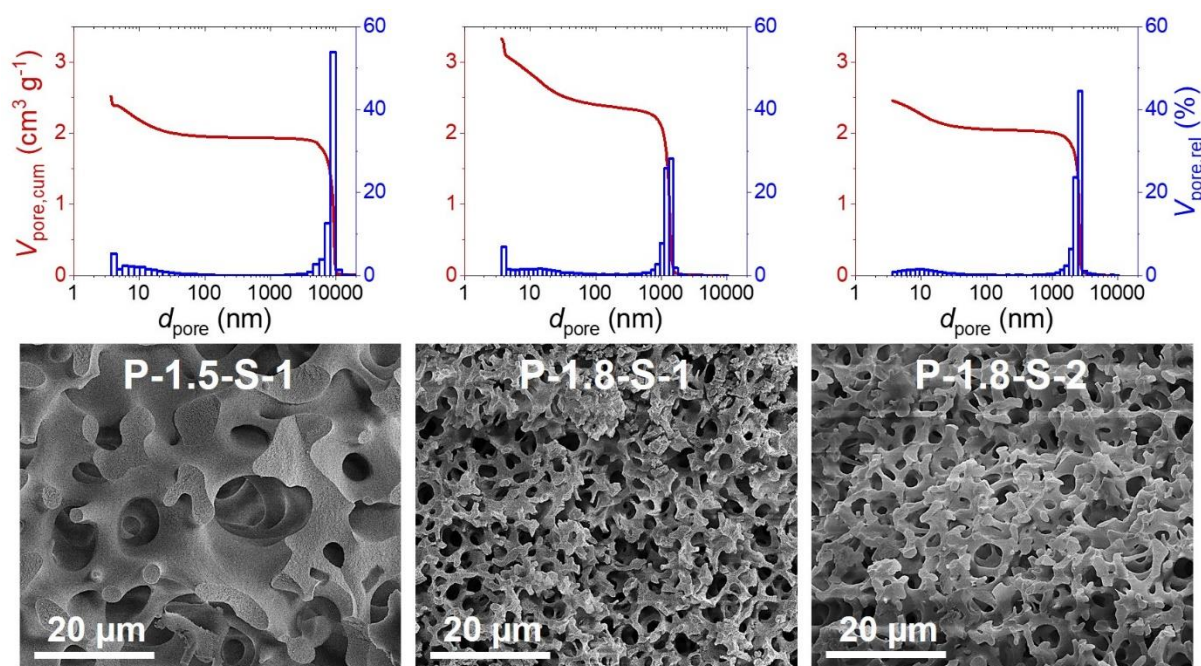


Figure 3.1. MIP analysis (mercury intrusion curves and pore size distributions as cumulative and relative pore volumes, respectively) and SEM images for selected sulfonic acid functionalized silica monoliths with hierarchically structured pore systems (Table 3.1).

The MIP-based pore size distributions correlate well with a visual analysis of Figure 3.1. The mean macropore size (d_{macro}) decreases with increasing PEO content from ~ 8.2 to ~ 1.2 μm (Table 3.1), reflecting a familiar trend.^{21,22,37} However, the macropore size is also influenced by the MPTMS concentration. With increasing amount of MPTMS, the size of the macropores increases, which becomes clear by comparing the respective samples with a PEO content of 1.7 or 1.8 g (Table 3.1): d_{macro} increases from ~ 1.1 μm (for the reference sample P-1.7-S-0) to ~ 2.2 μm (P-1.7-S-1) to ~ 4.8 μm (P-1.7-S-1.5). Similarly, with an increase in MPTMS concentration by a factor of two from sample P-1.8-S-1 to P-1.8-S-2, d_{macro} increases from ~ 1.2 to ~ 2.4 μm . Apparently, the MPTMS influences the sol–gel process in such a way (polarity) that a later state of spinodal decomposition is frozen, allowing larger pore structures to emerge. Interestingly, this behavior is opposite to that observed with urea.¹⁴ In that work, we found that increasing the urea content of the starting sol comprising a sulfuric acid solution of TEOS, PEO

and urea from 3 to 24 wt% decreased d_{macro} from 2.3 to 0.6 μm and the skeleton thickness from 2.0 to 0.4 μm . Supposedly, with increasing urea content, phase separation and gelation are retarded as well as shifted closer together, so that the formed monolithic structures represent a less evolved state of spinodal decomposition, preserving smaller macropores and a thinner skeleton.

The total porosities of the sulfonic acid modified materials are comparable to that of the calcined reference material of $\epsilon_{\text{total}} = 0.88$ (Table 3.1). However, the samples prepared with larger amounts of MPTMS (P-1.7-S-1.5 and P-1.8-S-2) do not that closely approach that value, which is mainly caused by their smaller mesopore volumes (V_{meso}). Mean mesopore sizes (d_{meso}) based on the MIP data are similar for all samples ($d_{\text{meso}} = 10\text{--}13\text{ nm}$), but the actual pore size distributions suggest that MIP is not appropriate for the investigation of the mesoporosity in these samples. It may be possible that organic matter inside the mesopores is compressed at the high pressures up to 4000 bar, which would bias the results except for the calcined reference material. Nitrogen physisorption measurements were therefore additionally conducted. Figure 3.2 shows the isotherms and derived pore size distributions for selected sulfonic acid modified, hierarchically structured sol–gel monoliths and the calcined reference sample P-1.7-S-0.

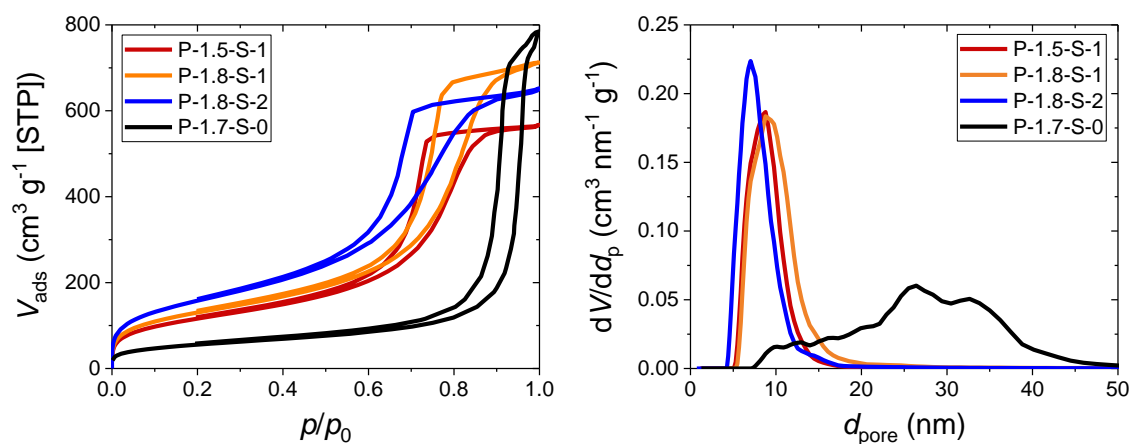


Figure 3.2. Nitrogen physisorption isotherms (left) and pore size distributions (right) for sulfonic acid functionalized silica monoliths and the calcined reference material (*cf.* Table 3.1).

The pore size distributions in Figure 3.2 reveal an impact of the MPTMS content on the mesopore formation. The reference material has a very wide distribution of pore sizes ranging from about 10 to 50 nm (mean pore diameter, $d_{\text{meso}} = 26\text{ nm}$). In contrast, the functionalized materials have relatively narrow pore size distributions, with $d_{\text{meso}} \approx 9\text{ nm}$ (decreasing to 7 nm as the amount of MPTMS is increased, Table 3.1). One reason for this observation may be that the formation of micropores is influenced during the sol–gel process, especially during condensation, resulting in smaller micropores with higher MPTMS concentrations.³¹ On the other hand, hydrothermal treatment could be affected, in which urea decomposes to ammonia,

resulting in a basic pore widening (syneresis and Ostwald ripening). During this process, micropores formed in the sol–gel step are widened to mesopores. It makes the pore system more stable and the material can also be easier dried with larger pores under ambient conditions.^{33,38} The functionalization that is covalently bonded to the surface could mitigate the effects of syneresis and Ostwald ripening, so that the pore widening is milder and more homogenous. At this point, it should be mentioned that the drying of crack-free monoliths was possible even with the smallest mesopores ($d_{\text{meso}} = 7$ nm). The simple drying method of Kohns *et al.*³³ was adapted here with a lower temperature (105 °C) to prevent damage of the organic component.

Narrowed mesopore size distributions, as observed in Figure 3.2, are advantageous in applications that rely on size-selective effects, such as size-exclusion chromatography³⁹ and catalysis under confinement.^{40,41} This has been demonstrated recently for the ring-closing metathesis of various dienes, where the catalyst was selectively immobilized inside the mesopores of the support.⁴² A narrow pore size distribution with carefully adjusted mean pore size (relative to the size of the dienes) is essential here to define a narrow operational window for optimal macrocyclization selectivity. Larger pores quickly increase the risk of unfavored oligomerization (decreasing the selectivity) and smaller ones ultimately impede the favored macro(mono)cyclization as well as diffusive transport into and out of the mesopores, which decreases conversion. For the materials compared in Figure 3.2, we note a substantial narrowing of the mesopore size distribution from the calcined reference material (standard deviation >10 nm, relative standard deviation >40%) to the functionalized materials, characterized by a standard deviation of only ~2 nm and a relative standard deviation of ~25%. If the calcined sample were subsequently functionalized *via* post-grafting, its wide mesopore size distribution would be largely retained.

The difference between the functionalized and pure silica materials is also seen in the isotherms in Figure 3.2. All isotherms belong to type IV, whereby the sulfonic acid functionalized materials display a clear H2(a) hysteresis. The other materials (not included) have a similar characteristic. In contrast, the hysteresis behavior of the pure silica materials can be assigned to type H1 (but for a disordered pore system). For this isotherm no plateau is reached, as the larger pores could not be completely filled during condensation.⁴³ The impact of the functionalization reagent on the pore space properties is also expressed in the specific surface areas (S_{BET}). The pure sol–gel material has a significantly smaller surface area (195 m² g⁻¹) than the functionalized materials (Table 3.1), for which S_{BET} increases to 418–470 m² g⁻¹ (mainly due to the smaller mesopore diameters, $d_{\text{meso}} = 9$ nm). Although the total pore volume of the non-functionalized material (1.21 cm³ g⁻¹) is not reached, V_{total} of the functionalized materials increases systematically from 0.88 to 1.1 cm³ g⁻¹ with the amount of polymer, which is consistent with the S_{BET} -values. The increase of the MPTMS content does not have a major effect on V_{total} , but S_{BET} increases further (up to 576 m² g⁻¹ for sample P-1.8-S-2) and becomes similar to values reported in the literature for pure and sulfonic acid modified bimodal sol–gel monoliths.^{3,32,44}

To understand the impact of the oxidation/extraction step, sample P-1.7-S-1 was exemplarily examined by nitrogen physisorption before that treatment (in pristine form), after the treatment (sulfonic acid functionalization), and after calcination. Isotherms and pore size distributions are summarized in Figure 3.S2 (ESI). We also recorded isotherms for the reference material P-1.7-S-0 in untreated and calcined forms for comparison. For sample P-1.7-S-1, mesopore size increases from $d_{\text{meso}} = 8$ nm (SH) to 9 nm (SO₃H) to 10 nm (calcined), whereas no change is seen for the reference material (Table S2, ESI). More importantly, the specific surface area of the pristine form is $273 \text{ m}^2 \text{ g}^{-1}$, rising to $469 \text{ m}^2 \text{ g}^{-1}$ after oxidation/extraction. After calcination, the specific surface area increases just slightly further to $479 \text{ m}^2 \text{ g}^{-1}$. By contrast, for the reference material P-1.7-S-0, S_{BET} only increases from 164 to $195 \text{ m}^2 \text{ g}^{-1}$. The sharp increase in S_{BET} for sample P-1.7-S-1 after the oxidation/extraction step strongly indicates the successful removal of the polymer from its pore system.

3.3.2 Efficiency of the *in situ* functionalization and extraction procedure

To examine our general synthesis procedure for its usefulness, various characterization methods were applied. Qualitative and quantitative techniques were selected to verify the approach and its individual steps. They provide results, which altogether allow to reach clear conclusions on the success of the presented synthesis procedure.

3.3.2.1 Elemental analysis and SEM-EDX measurements

The prepared materials were subjected to elemental analysis for a first assessment of the amount of incorporated sulfonic acid groups. These data also help to evaluate the extraction procedure that we implemented in order to remove the polymer. Table 3.2 summarizes the carbon, hydrogen and sulfur contents of pristine samples before and after the oxidation/extraction step. Nitrogen is not listed, because its content remained below the detection limit.

Table 2. Elemental analysis before and after the oxidation/extraction step.

Sample	pristine			extracted		
	C / %	H / %	S / %	C / %	H / %	S / %
P-1.5-S-1	12.9	2.3	2.9	3.9	1.5	2.5
P-1.6-S-1	13.5	2.4	2.9	3.6	1.6	2.7
P-1.7-S-1	14.1	2.5	2.8	3.9	1.5	2.8
P-1.7-S-1.5	15.8	2.9	4.1	4.8	1.7	3.8
P-1.8-S-2	16.1	3.0	4.0	4.8	1.8	3.8
P-1.7-S-0	3.5	0.8	0.0	1.1	0.7	0.0

A first qualitative identification can be based on the significant sulfur contents of all materials, except for sample P-1.7-S-0 (synthesized without MPTMS). As the MPTMS content increases (P-1.7-S-1.5), also the sulfur content increases from ~3 to ~4%. A further increase to twice the initial MPTMS amount (P-1.8-S-2), however, does not increase the sulfur content further in the formed material (Table 3.2). Because the condensation of additional MPTMS is unsuccessful, we assume that the system is saturated with functional groups. Based on the carbon contents of the pristine samples, the increasing amount of organic species (PEO, MPTMS) during the synthesis can be easily recognized. In comparison, the carbon content of the reference material (P-1.7-S-0) is much lower due to the absence of the functionalization reagent. Comparing extracted with pristine samples helps to verify the success of the extraction step. Carbon contents decrease significantly after extraction, as documented in a loss of 70–73%. The impact of the extraction step can be evaluated most clearly by inspecting the reference material, in which the amount of organic component is reduced by 69%. Therefore, the extracted reference material still contains carbon, suggesting that the polymer has not been completely removed. This is not that obvious for the functionalized materials, because we also introduce carbon with the propyl chain at the sulfur. On the other hand, the sulfur contents differ only slightly before and after the extraction step. Here, an exceptional loss of 14% is observed for sample P-1.5-S-1, but the sulfur loss for all other extracted samples remains below 6%.

With the determined sulfur contents, the loadings of the bulk materials with sulfonic acid groups can be calculated. For materials prepared with the standard amount of 1 ml MPTMS, the SO_3H loading increases slightly with increasing amount of PEO in the synthesis from 0.78 mmol g^{-1} for sample P-1.5-S-1 to 0.84 mmol g^{-1} (P-1.6-S-1) to 0.87 mmol g^{-1} (P-1.7-S-1). As expected, samples P-1.7-S-1.5 and P-1.8-S-2 have a higher SO_3H loading (1.2 mmol g^{-1}). Assuming that all sulfur atoms are on the pore surface, the number of SO_3H groups/ nm^2 can be estimated using the S_{BET} -values from Table 3.1 and the Avogadro constant. This allows to provide SO_3H loadings of 1.12 nm^{-2} (P-1.5-S-1), 1.17 nm^{-2} (P-1.6-S-1), 1.11 nm^{-2} (P-1.7-S-1), 1.31 nm^{-2} (P-1.7-S-1.5) and 1.24 nm^{-2} (P-1.8-S-2), which are comparable to those for purely mesoporous materials that were also synthesized through the co-condensation procedure.²⁴ There, it has been emphasized that co-condensation ensures significantly higher SO_3H loadings than achieved using common grafting methods. Interestingly, the monolithic materials prepared with the standard amount of 1 ml MPTMS all end up with very similar numbers of SO_3H groups/ nm^2 , despite their different morphological properties (particularly mesopore volume and specific surface area) caused by the different PEO contents used in their synthesis. It should also be noted that the pore widening process has no significant influence on the sulfur content (Table 3.S3, ESI).

Using the SO_3H loadings, sulfur and carbon contents can be interrelated to estimate the fraction of the organic component belonging to the functionalization. Considering the stoichiometry of the introduced functional chain (S:C = 1:3), about 17–19% of the residual carbon content is due to polymer, except for sample P-1.5-S-1 (27%). For materials prepared with larger amounts of

MPTMS, it is only ~10%. Therefore, we started further investigations of the extraction process by extending the duration of the hydrothermal treatment with $\text{H}_2\text{O}_2/\text{HNO}_3$ from 2 h to 4 and 6 h (Table 3.S4, ESI). These results showed that an extended hydrothermal treatment further reduced the carbon content, but also the sulfur content significantly (by ~28%). Consequently, extending the hydrothermal treatment for polymer extraction is no viable alternative, as the associated loss of sulfur (sulfonic acid groups) is undesirable. At this point, it cannot be clarified if the polymer remains on the surface of the materials (and prevents access to functional groups) or inside the pores due to diffusion limitations during the washing process.

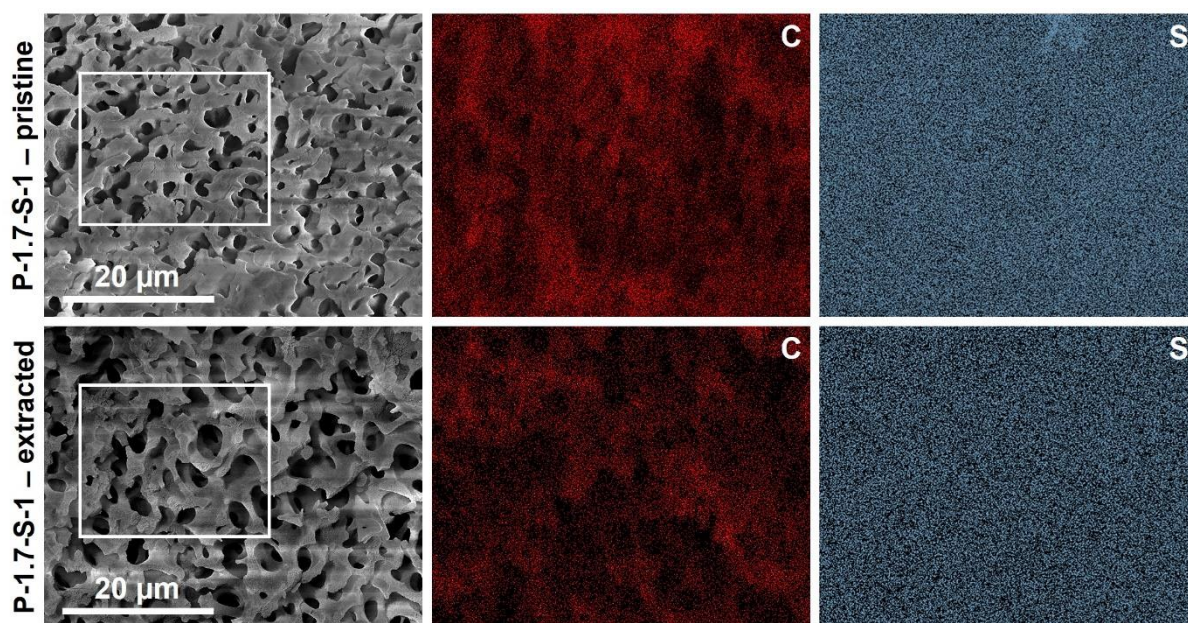


Figure 3.3 SEM-EDX images recorded for sample P-1.7-S-1 in its pristine form (top) and after the oxidation/extraction step (bottom), indicating carbon (red) and sulfur (blue) contents.

SEM-EDX measurements support the data from elemental analysis. Figure 3.3 shows SEM images and EDX mappings for the pristine and extracted forms of sample P-1.7-S-1. Red dots represent the presence of carbon atoms on the surface, which can be attributed to PEO (employed for the polymer-induced phase separation during the sol-gel synthesis) and the functionalization. Blue dots indicate the sulfur atoms incorporated by the functionalization reagent MPTMS during the gelation process. From the EDX mapping, it is seen that the functionalization is homogeneously distributed over the surface of the materials, which we explain with the effect of the *in situ* co-condensation. Further, based on Figure 3.3 it can be assumed that, while carbon atoms are removed to a substantial degree by the extraction step, the sulfonic acid functionalization remains largely intact. This suggests that a carefully timed extraction can indeed be used to selectively remove the polymer from the material, without impairing the functionalization.

Calculated compositions demonstrate this effect more clearly. The untreated sample (top row in Figure 3.3) consists of 24 at.% C, 1 at.% S, 52 at.% O and 21 at.% Si (rounded values). Here, the ratio between carbon and silicon contents appears uncharacteristic. However, we have to

recall that EDX is surface sensitive and the bulk of the material (which mainly consists of silicon and oxygen) cannot be detected in this way. After extraction (bottom row), the atomic composition is 15 at.% C, 1 at.% S, 56 at.% O and 26 at.% Si. The loss of organic matter is mainly attributed to the removal of polymer, as the sulfur content does not change. It is confirmed by the increase of the silicon content. More silicon can be detected after removing the polymer, which no longer obscures part of the surface.

For samples prepared with larger MPTMS amounts, SEM-EDX measurements were carried out to provide information particularly on the sulfur content. These materials were examined in the oxidized/extracted form. Sample P-1.7-S-1.5 has a sulfur content of 1.4 at.% (2.3 wt.%), which is an increase compared to sample P-1.7-S-1 (1.0 at.%, 1.7 wt.%). The increase is even stronger for sample P-1.8-S-2, which has a sulfur content of 1.6 at.% (2.5 wt.%). It shows that the sulfur content can be increased while preserving an interconnected pore structure.

For better evaluation of the polymer extraction step, SEM-EDX measurements were conducted for the reference material P-1.7-S-0 in pristine, extracted and calcined forms (Figure 3.S3, ESI). The pristine sample reveals 11 at.% C, 0.2 at.% S, 59 at.% O and 28 at.% Si. After extraction, the carbon content decreases to 1 at.%, while the sulfur content is constant at 0.2 at.%. The oxygen content increased (slightly) to 61 at.% and the silicon content to 36 at.%. After calcination, the atomic composition did not change with respect to the extracted sample (1 at.% C, 0.2 at.% S, 61 at.% O and 36 at.% Si). According to these results, the extraction process (which also serves to oxidize the thiol to sulfonic acid groups) is as effective as the calcination step in removing the polymer. The small amounts of carbon and sulfur remaining after extraction and calcination may be due to residues physisorbed on the surface. It could not be finally clarified why sulfur was detected. Quantification by SEM-EDX is difficult, because it is a surface sensitive method and furthermore represents a small region of the material. Due to these constraints, we rely on the quantification by elemental analysis.

3.3.2.2 FT-IR spectroscopy and thermogravimetric analysis

To verify specifically the oxidation of thiol to sulfonic acid groups (occurring simultaneously during polymer extraction) DRIFTS and TGA were applied. DRIFT spectra were collected for sample P-1.7-S-1 in pristine, oxidized/extracted and calcined forms (Figure 3.4a). All three samples exhibit vibrations typical for the silica skeleton: Si–O–Si stretching vibrations in the range of 1000–1250 cm^{-1} and the corresponding deformation vibrations at about 800 cm^{-1} . Additionally, all spectra show intense absorptions due to O–H stretching (3400–3600 cm^{-1}) and deformation vibrations ($\sim 1640 \text{ cm}^{-1}$) caused by adsorbed water.

The sharp band at $\sim 3750 \text{ cm}^{-1}$ in the calcined material can be assigned to Si–O–H stretching vibrations. The almost complete disappearance of this silanol vibration in pristine and oxidized samples suggests the successful incorporation of a covalently bonded functionalization. For the pristine material (blue) we note three additional absorptions: At $\sim 2580 \text{ cm}^{-1}$ the S–H vibration

of the thiol group (indicating successful functionalization) and in the range of 2850–2950 cm^{-1} and 1450–1500 cm^{-1} the C–H stretching and deformation vibrations, respectively, by the propyl chain of the functionalization and by the polymer. These vibrations can also be identified in the oxidized material (red), but they are much weaker. It suggests that the polymer has been largely removed, so that absorption either originates from the propyl chain of the functionalization or residual polymer. Most importantly, however, the explicit loss of the S–H vibration confirms a successful oxidation of thiol to sulfonic acid groups. Vibrations typical for the sulfonic acid, as shown by Marshall *et al.*²⁴ and Wilson *et al.*,³¹ could not be assigned, because they overlap with the strong Si–O–Si stretching vibrations (1145–1200 cm^{-1} for $-\text{SO}_2-\text{OR}$, $\sim 1050 \text{ cm}^{-1}$ for S=O). In comparison, the calcined sample (black) only shows vibrations typical for silica and adsorbed water, which indicates complete removal of organic moieties.

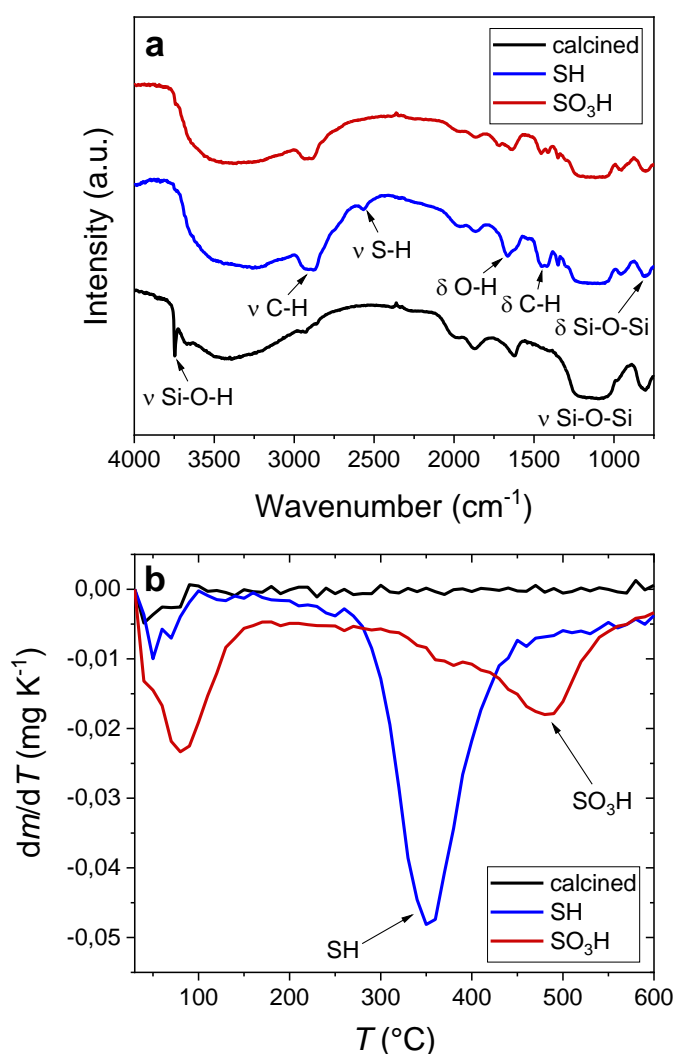


Figure 3.4. DRIFT spectra (a) and TGA curves (b) for sample P-1.7-S-1 in pristine (blue), oxidized/extracted (red) and calcined (black) forms.

The TGA data, plotted as differential mass loss in a temperature range of 30–600 °C (Figure 3.4b), support the conclusions derived from DRIFTS. All modifications of sample P-1.7-S-1 exhibit a peak below 120 °C caused by the loss of water, but in different intensity. The pristine sample (blue) reveals a thiol decomposition peak at ~350 °C (no further decompositions are recorded). The actual mass loss is high, because the polymer also starts to decompose in this temperature range. For the oxidized/extracted sample (red) a pronounced mass loss is observed, indicating the presence of the sulfonic acid functionalities. Decomposition begins at lower temperatures already (~340 °C), which suggests the presence of residual polymer. All these observations agree with the results of previous studies.⁴⁵

3.3.2.3 MAS NMR spectroscopy

NMR was used to corroborate our previous conclusions about the synthesis of the sulfonic acid functionalized silicas. These studies were performed exemplarily with sample P-1.7-S-1 before oxidation/extraction, after this treatment, and after the calcination step in order to compare the different surface modifications (thiol, sulfonic acid, and no functionalization). For this purpose, ¹³C and ²⁹Si spectra were recorded.

Figure 3.5a shows CP/MAS ¹³C NMR spectra of the sample before (blue) and after (red) extraction of the polymer (we did not expect any signals for the calcined material). The spectrum of the pristine material reveals three peaks at 11.3, 27.0 and 71.1 ppm. The first resonance at 11.3 ppm is caused by the carbon atom C₃ of the functionalization in direct neighborhood to the silicon atom. The peak at 27.0 ppm is due to the central carbon atom of the propyl chain (C₂) and the carbon atom C₁ that directly binds to the thiol group. Both resonances overlap, as known from the literature.⁴⁶ The peak at 71.1 ppm can be assigned to the carbon atoms of the polymer (C_{PEO}) that is still on the silica surface.⁴⁷ The treated material (red spectrum) also exhibits three signals, localized at 11.8, 17.6 and 53.3 ppm. However, the signal from the polymer is not visible any longer. It indicates the successful extraction of PEO, whereas our previous study by elemental analysis could not confirm this. The resonances at 11.8 and 17.6 ppm are caused by the carbon atom binding to the silicon atom (C₃) and the adjacent carbon (C₂). The peak at 53.3 ppm can be assigned to the carbon in direct neighborhood to the sulfonic acid functionality (C₁, strongly shielded by the oxygens), which agrees with data for sulfur groups from the literature.⁴⁶ Based on this insight, we conclude that the thiol groups have been converted into sulfonic acid groups and that the polymer has been removed at the same time, confirming the goals targeted with the adapted oxidation/extraction step.

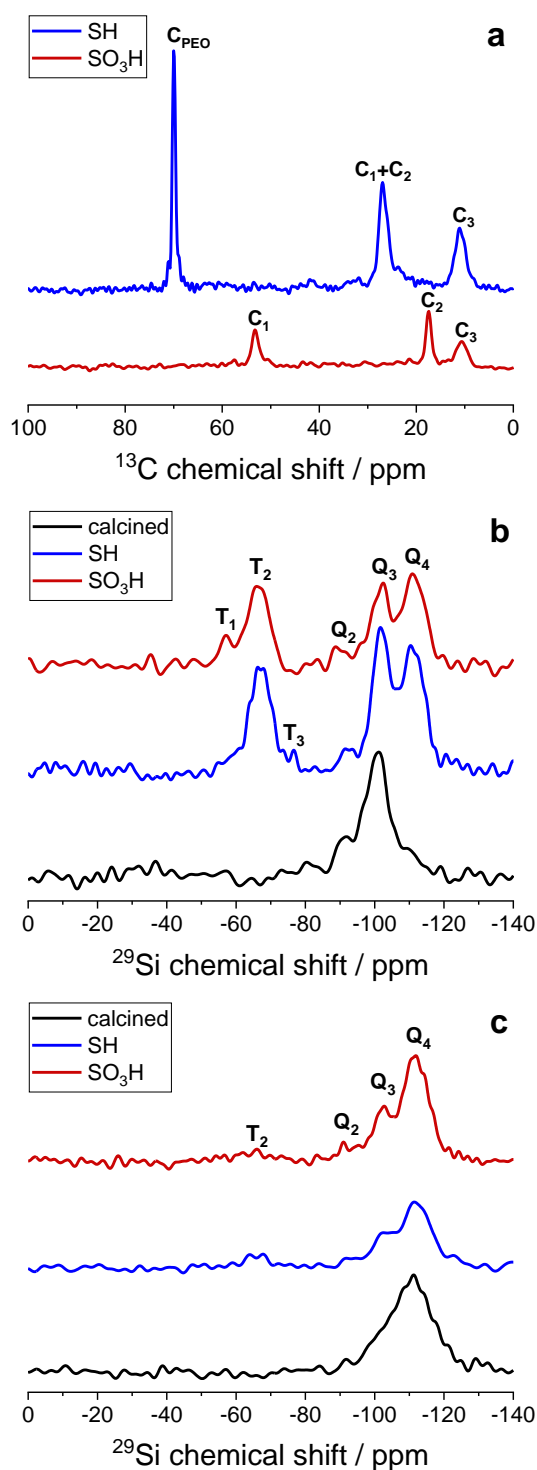


Figure 3.5. CP/MAS ^{13}C NMR spectra (a), CP/MAS ^{29}Si NMR spectra (b) and HPDEC/MAS ^{29}Si NMR spectra (c) collected from sample P-1.7-S-1 in pristine (blue), oxidized/extracted (red) and calcined (black) forms.

To support this qualitative proof of functionalization from Figure 3.5a, CP/MAS ^{29}Si NMR spectra (Figure 3.5b) were recorded in addition. They can be used to define connectivities between coupled nuclei and investigate the dynamics in solids. As the technique is based on heteronuclear dipolar interactions, it is sensitive to internuclear distances and the mobility of functional groups.⁴⁸ All three materials exhibit the typical signals of Q_4 (SiO_4), Q_3 (SiO_3OH) and Q_2 ($\text{SiO}_2(\text{OH})_2$) silicon species in their spectra (see Figure 3.S4 in the ESI for additional illustration). The calcined sample (black spectrum in Figure 3.5b) reveals no other signals than from the Q-species, which implies that the functionalization has been removed during the calcination step. The peak with the Q-species can be broad actually due to the heterogeneity of the silica skeleton regarding bond lengths and angles.⁴⁹ Taking a closer look at the spectra of the untreated functionalized sample (blue) and the oxidized/extracted sample (red), T-species can now be identified (*cf.* Figure 3.S4) and assigned in agreement with literature.⁵⁰ T_2 -signals ($\text{SiO}_2(\text{OH})(\text{CH}_2\text{R})$) around -66 ppm are prominent in both spectra. A T_3 -signal ($\text{SiO}_3(\text{CH}_2\text{R})$) is only detected for the untreated material (-76.6 ppm). Furthermore, the T_1 -signal ($\text{SiO}_1(\text{OH})_2(\text{CH}_2\text{R})$) is only weakly distinctive here (-57.6 ppm). On the other hand, no T_3 -signal is detected in the treated (SO_3H) material, whereas the T_1 -signal at -56.9 ppm is much more pronounced. This may be caused by bonds on the surface (primarily functionalization) that have been broken during the extraction step, whereby more single (T_2) and geminal (T_1) silanol groups were formed, which would be consistent with the loss of some sulfonic acid groups already indicated by elemental analysis and SEM-EDX.

This assumption is confirmed by the HPDEC spectra in Figure 3.5c. That technique can be used to derive quantitative evidence about the respective silicon species by a direct stimulation of each silicon atom. For this purpose, areas of the individual peaks in a spectrum were calculated by integration (exemplarily shown for the untreated sample P-1.7-S-1 in Figure 3.S4, ESI) and related to each other. From these relations, conclusions can be derived regarding the actual bonding in the materials that improve verification of the synthesis procedure. Based on the HPDEC spectra in Figure 3.5c, it is clear that the Q_4 species is the main constituent in all three modifications. This was expected, as it represents the bulk backbone of the monoliths. Furthermore, in both pristine (blue) and oxidized/extracted (red) materials, only T_2 -species are detected. Here, the signal for the sulfonic acid functionalized sample is weak, which further supports our assumption about the partial loss of functionalization in the extraction step. In the (blue) spectrum of the untreated material, two peaks are visible side by side (*cf.* Figure 3.S4). As they appear exactly in the range for T_2 -species, we took them as one T_2 ($\text{SiO}_2(\text{OH})(\text{CH}_2\text{R})$) signal.⁵⁰

Table 3.3. Relative peak areas of silicon species as quantified by HPDEC/MAS ^{29}Si NMR.

Sample	Q ₄ / %	Q ₃ / %	Q ₂ / %	T ₂ / %
P-1.7-S-1	72	18	4	6
P-1.7-S-1_ext	71	16	9	4
P-1.7-S-1_ext_c	91	7	2	–

Quantification becomes more meaningful with the percentages of the individual silicon species, as calculated from the peak areas and summarized in Table 3.3. As mentioned, the Q₄ is the most prominent species. It dominates with 91% in the calcined material compared to 72 and 71% in SH- and SO₃H-functionalized samples. The calcination step enhances the formation of siloxane bonds (Q₄) by dehydration of surface silanols. When cooling to room temperature, this process is somewhat reversed by atmospheric humidity, resulting in the low Q₃ and Q₂ quantities for sample P-1.7-S-1_ext_c. A comparison of the samples before and after the oxidation/extraction step shows that Q₄ quantities do not differ much. It should be noted that for each T-signal a Q₄-signal is detected, as a siloxane bond is added due to the functionalization reagent. Furthermore, the T₂-species decrease from 6 to 4% after the extraction, as suggested by our previous results. This is accompanied by a significant increase in Q₂-species (from 4 to 9%), which is consistent, because the silicon atom most likely replaces the cleaved functionalization by a hydroxyl group. As a consequence, a Q₂-species is formed from a T₂-species. Still, the T₂-signal is detected for the oxidized/extracted material (sample P-1.7-S-1_ext), which supports the presented synthesis scheme. It was not possible to quantify the site occupancy with respect to the condensation, as described by Ide *et al.*,⁵¹ because the surfaces of the materials were manipulated by the sample preparation (grinding) required for the NMR measurements. The generation of small particles increases the number of surface silanol groups (Q₃- and Q₂-species), because additional surface (previously bulk) is created and the ratio of T- to Q₃-species shifts. Nevertheless, the results of the NMR investigations are very instructive and demonstrate clearly that sulfonic acid functions were covalently bound to the surfaces of the prepared hierarchically structured silica monoliths to a significant extent.

The NMR investigations generally substantiate our approach. The ^{13}C spectra demonstrate that it was possible to extract the polymer and at the same time oxidize thiol to sulfonic acid groups. Complementary, the ^{29}Si spectra corroborate this important step by detecting silicon T-species, which represent the attachment of carbon atoms to silicon.

3.3.3 Inverse gas chromatography (IGC)

IGC is a source of physicochemical data for a variety of materials. The term indicates that the stationary phase of a chromatographic column is the material of interest and in turn examined through its interactions with well-known probe molecules. It was therefore necessary to prepare the monolithic rods in a column format suitable for the IGC equipment. The cladding approach

of Kohns *et al.*¹⁴ was used, in which the rods were first inserted into a stainless-steel tube and then embedded by epoxy resin. The attachment of zero-volume reducing unions completed the set-up (Figure 3.S1, ESI). For the IGC investigations, a series of probe molecules (C_6 – C_9 *n*-alkanes, dichloromethane, chloroform, diethyl ether, acetonitrile, benzene) were injected individually and at least three times onto all columns for the determination of retention times. Sulfonic acid functionalized materials with different SO_3H -loadings (samples P-1.7-S-1 and P-1.7-S-1.5) and the reference material without functionalization (P-1.7-S-0) were examined.

IGC characterizes the strength of interaction between an adsorbate and a solid surface through the total surface energy γ_s^t , covering dispersive (Van der Waals) and polar/specific (Lewis acid-base) interactions. To describe surface properties (*e.g.*, acidity, wettability) comprehensively, both terms (dispersive component γ_s^d and specific component γ_s^{sp} of the surface energy) have to be taken into account. The dispersive component can be calculated from interactions between *n*-alkanes and the solid surface. Dorris and Gray⁵² introduced calculations based on the linear relationship between free energy of adsorption and molecular weight of *n*-alkanes, the so called *n*-alkane line, to access the dispersive component of the surface energy. The specific component is determined from interactions of polar molecules with the surface. These interactions involve specific as well as dispersive contributions, which makes a distinction more difficult. Here, the dispersive component of the free adsorption enthalpy (as obtained from the *n*-alkane reference line) can be subtracted from the experimental free adsorption enthalpy to isolate the specific component. Details about these calculations are given in the ESI.

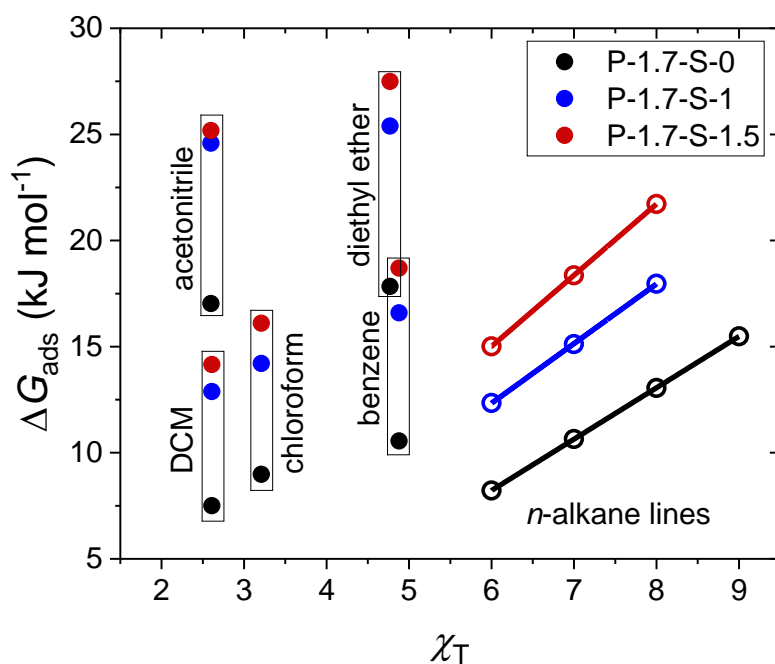


Figure 3.6. Free energy of adsorption for different polar and *n*-alkane probe molecules on non-functionalized silica P-1.7-S-0 (black) and sulfonic acid modified silicas P-1.7-S-1 (blue) and P-1.7-S-1.5 (red), temperature: 80 °C.

Free energies of adsorption (ΔG_{ads}) obtained by IGC reflect the strength of adhesive interaction with dispersive and specific contributions for each individual probe. By plotting ΔG_{ads} against the number of carbon atoms (expressed with the topological index χ_{T}), the interactions can also be represented graphically (Figure 3.6). The topological index was introduced to compare retention data of different probes despite their different molecular properties (such as adsorption area and interaction strength). Brendlé and Papirer^{53,54} developed the χ_{T} -parameter based on the Wiener index for linear, branched and cyclic alkanes, also taking polar eluents into account.

The data plotted in Figure 3.6 show that both dispersive and specific interactions are intensified with increasing amount of MPTMS in the synthesis and thus, with increasing sulfonic acid loading in the formed material. For example, the *n*-alkane line shifts significantly to higher ΔG_{ads} values (accompanied by an increasing slope), indicating stronger adhesion of the alkanes to the surface as we progress from sample P-1.7-S-0 to P-1.7-S-1.5. A clear influence of the introduced SO_3H groups is also seen for the polar probe molecules, ΔG_{ads} for sample P-1.7-S-1 increases strongly compared to the reference material. Interactions are intensified for Lewis-base (benzene, diethyl ether, acetonitrile) as well as Lewis-acid probes (DCM, chloroform). This indicates an increase in electron donor and acceptor capabilities of the materials upon silane incorporation. From the data in Figure 3.6, dispersive and specific components and the resulting total surface energy of the respective material can be calculated (Table 3.4).

Table 3.4. Dispersive ($\gamma_{\text{s}}^{\text{d}}$) and specific ($\gamma_{\text{s}}^{\text{sp}}$) components of the total surface energy ($\gamma_{\text{s}}^{\text{t}}$) and Gutmann constants K_{A} and K_{D} obtained by IGC at 80 °C.

Sample	$\gamma_{\text{s}}^{\text{d}}$ [mJ m ⁻²]	$\gamma_{\text{s}}^{\text{sp}}$ [mJ m ⁻²]	$\gamma_{\text{s}}^{\text{t}}$ [mJ m ⁻²]	K_{A}	K_{D}	$K_{\text{A}}/K_{\text{D}}$
P-1.7-S-0	35	87	122	0.57	0.38	1.5
P-1.7-S-1	47	168	215	0.77	0.48	1.6
P-1.7-S-1.5	67	179	246	0.77	0.48	1.6

The data in Table 3.4 confirm our expectations that the specific component ($\gamma_{\text{s}}^{\text{sp}}$) dominates over the dispersive component ($\gamma_{\text{s}}^{\text{d}}$) for silica due to the surface silanols (sample P-1.7-S-0). The total surface energy (122 mJ m⁻²) is composed of approximately one-third dispersive and two-thirds specific interactions. Upon functionalization (sample P-1.7-S-1), $\gamma_{\text{s}}^{\text{sp}}$ increases significantly, but also the dispersive part increases from 35 to 47 mJ m⁻², which can be attributed to the non-polar propyl chain of the introduced group. Rückriem *et al.*⁵⁵ have described the gain in polarizability for modified silica surfaces with each additional methylene unit. Nonetheless, the specific part increases much stronger and this also raises the total surface energy drastically to 215 mJ m⁻². By increasing the SO_3H loading (sample P-1.7-S-1.5), $\gamma_{\text{s}}^{\text{t}}$ rises further to twice the value of the reference material (246 mJ m⁻²), but the specific component does not increase as much as the dispersive component. Thus, the surfaces of the functionalized materials can be still described as polar, even as the interaction with non-polar probe molecules

is enhanced. To conclude, and with respect to characterizations already discussed, we can assume a covalently bonded sulfonic acid modification with different coverages on the surface of these hierarchically structured sol–gel silica monoliths.

Lewis acid-base characteristics of the monolith surfaces were subsequently analyzed using the concept of Gutmann.⁵⁶ Accordingly,

$$\Delta G_{\text{ads}}^{\text{sp}} \approx \Delta H_{\text{ads}}^{\text{sp}} = K_{\text{A}} \cdot DN + K_{\text{D}} \cdot AN \quad (3.1)$$

where $\Delta H_{\text{ads}}^{\text{sp}}$ is the enthalpy of sorption of a polar probe molecule, K_{A} is the electron-acceptor number (acid) of the investigated surface and K_{D} is the corresponding electron-donor number (base). DN and AN are Gutmann's donor and acceptor numbers used to quantify the acid-base properties of the probe molecules. DN -values are calculated by calorimetric measurements from the sorption of the probe molecules (electron donor) onto SbCl_5 (electron acceptor). AN -values are derived by ^{31}P NMR measurements from the chemical shift of Et_3PO (electron donor) in the presence of an electron acceptor.^{57–60} The enthalpy of sorption $\Delta H_{\text{ads}}^{\text{sp}}$ is obtained by IGC (using at least three different temperatures) with the following equation:

$$\Delta G_{\text{ads}} = \Delta H_{\text{ads}} - T\Delta S_{\text{ads}} \quad (3.2)$$

Repeating this procedure for each probe molecule to estimate K_{A} and K_{D} values would be very time-consuming. During these periods aging effects can occur for labile samples at the elevated temperatures required for the measurements.⁶¹ We therefore made a common simplification by using the specific interaction parameter $\Delta G_{\text{ads}}^{\text{sp}}$ for calculation of K_{A} and K_{D} . Both temperature dependent values can be received from the slope and the intercept of a linear plot of $\Delta G_{\text{ads}}^{\text{sp}}/AN$ against DN/AN , as illustrated in Figure 3.S5 (ESI).^{62,63} It should be noted that acid-base parameters for solid surfaces derived by IGC measurements depend on the employed approach and the DN and AN reference values.^{57,59} In that respect, all measurements were performed under identical conditions and with the same evaluation routines. K_{A} and K_{D} values resulting from IGC analysis are summarized in Table 3.4. The acid-base character of the monolith surfaces can be described by the ratio $K_{\text{A}}/K_{\text{D}}$. A ratio larger than 1.1 indicates acidic character of the surface, $K_{\text{A}}/K_{\text{D}} < 0.9$ reflects basic character.⁶⁴

The Lewis-acid parameter K_{A} increases from 0.57 to 0.77 after introduction of the sulfonic acid functionality into the pore network (Table 3.4), which is a clear sign that the surface has become more acidic. Generally, the density of surface silanol groups should decrease after binding of a functionalization, which should also cause K_{A} to drop. However, in our synthesis procedure K_{A} increases significantly, which indicates a more acidic surface and corroborates the introduction of the sulfonic acid groups, which are more acidic than the silanol groups. $K_{\text{A}}/K_{\text{D}}$ -ratios for the functionalized materials are just slightly elevated with respect to the non-functionalized sample. Apparently, the increase in acidity is compensated by the simultaneously increasing Lewis-base parameter K_{D} , as already noted with the ΔG_{ads} values for acidic probe molecules.

Bauer *et al.*⁶³ demonstrated a significant change in K_A/K_D -value for porous glass upon MPTMS functionalization (leading to the SH modification), where a strong basic character of the surface was observed. With respect to our synthesis, it is not possible to analyze the materials with their non-oxidized (SH) modification, because the polymer that is still in the pores prevents unbiased interaction of probe molecules with the surface. However, it can be concluded that the increase in MPTMS concentration does not affect acidity, because the K_A/K_D -value for sample P-1.7-S-1.5 remains at 1.6 and K_A at 0.77 (Table 3.4). It may be assumed that the surface is saturated with functional groups. Even though smaller changes are noticeable for these SO₃H loadings of 1.11 nm⁻² (P-1.7-S-1) and 1.31 nm⁻² (P-1.7-S-1.5), as detected by surface energy analysis (Table 3.4), Lewis acid-base parameters of these samples remain constant. The increase in polar interaction does not contradict constant acidity, because both acidic and basic polar probe molecules show stronger adhesive interactions for the higher SO₃H loading (*cf.* Figure 3.6).

3.4 Conclusions

Organic-inorganic hybrid sol-gel materials with hierarchical pore systems were synthesized by a simple, efficient synthesis route *via* co-condensation of TEOS and MPTMS, resulting in SO₃H functionalized macro-mesoporous silica monoliths. The polymer (template) used for generation of the macroporosity was removed with an extraction step, in which the introduced thiol groups were simultaneously oxidized to sulfonic acid groups, leading to hybrid materials with uniform distribution of the SO₃H groups inside the mesopores. The macropore size, specific surface area and coverage with SO₃H groups are conveniently adjusted in this synthesis route. For example, macropores formed by the polymer-induced phase separation were generated with median sizes from 1.2 to 8.2 μm at conserved mesopore diameters of 7–9 nm, and the materials offer specific surface areas of up to 576 m² g⁻¹. Using the co-condensation process, SO₃H loadings of 1.1–1.3 groups/nm² were realized by varying the initial MPTMS content. Higher MPTMS content also resulted in larger macropore sizes due to its influence on the phase separation. Importantly, the extraction of the polymer was facilitated while keeping most of the organic functionality intact. Altogether, it demonstrates that the co-condensation approach offers a simple, efficient route to functionalized sol-gel materials. Elemental analysis, SEM-EDX, thermogravimetry, DRIFTS, ¹³C and ²⁹Si solid state NMR, and IGC provided detailed qualitative and quantitative evidence on the formation of surface-bound SO₃H groups. With IGC, in particular, the effect of the SO₃H groups could be quantified by analyzing dispersive and specific components of the total surface energy as well as Lewis acid-base parameters of these surfaces. Notably, the changes in surface acidity upon SO₃H functionalization could be excellently monitored.

The prepared hybrid monoliths are primarily useful for processes involving ion exchange, acid catalysis or proton conduction, where morphological properties like macropore size and surface area will be easily adjusted in addition to the density of the SO₃H groups. However, their narrow mesopore size distribution further helps in applications that benefit from size-selective transport

like chromatographic (*e.g.*, biomolecular) separations or catalysis under spatial confinement. In this respect, the cladding approach applied to the monolithic rods in this work for IGC analysis also offers a robust column design for their convenient future use as a fixed-bed adsorber and/or reactor.

3.5 Supporting Information

Table 3.S1. Starting compositions of the *in situ* functionalized sol–gel silica monoliths.

Sample	m (H ₂ O) / g	m (Urea) / g	m (PEO) / g	m (H ₂ SO ₄) / g	m (TEOS) / g	m (MPTMS) / g
P-1.5-S-1	18.0	2.40	1.50	1.26	13.6	1.06
P-1.6-S-1	18.0	2.40	1.60	1.26	13.6	1.06
P-1.7-S-1	18.0	2.40	1.70	1.26	13.6	1.06
P-1.8-S-1	18.0	2.40	1.80	1.26	13.6	1.06
P-1.7-S-1.5	18.0	2.40	1.70	1.26	13.2	1.59
P-1.8-S-2	18.0	2.40	1.80	1.26	12.7	2.11
P-1.7-S-0	18.0	2.40	1.70	1.26	14.6	–

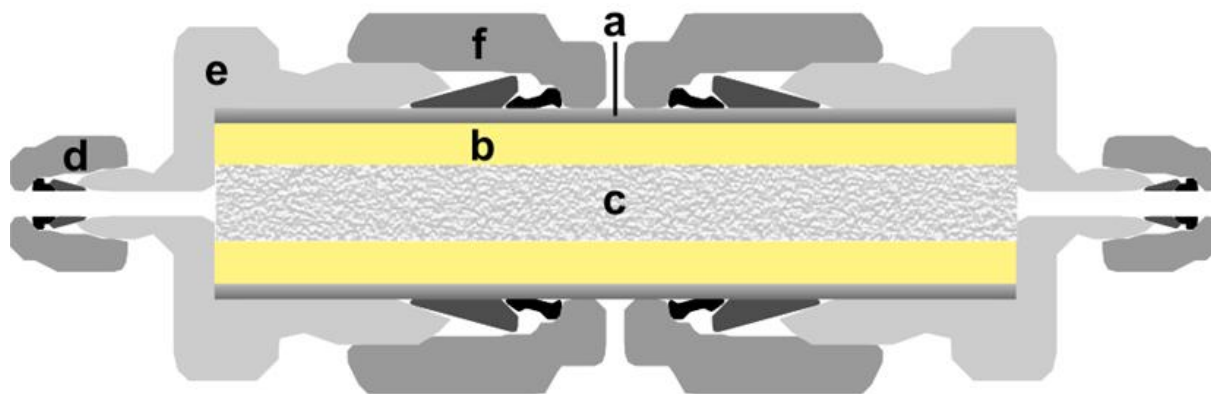


Figure 3.S1. Schematic drawing of the constructed column set-up.^{S1} (a) 1/2" o.d. stainless-steel tube (10.6 mm i.d. × 5 cm length), (b) UHU® PLUS 300 epoxy resin adhesive, (c) monolithic silica rod (5 mm i.d. × 5 cm length), (d) 5/16" nut hex with 1/16" o.d. tube, (e) 13/16" body hex, and (f) 7/8" nut hex with 1/2" o.d. tube.

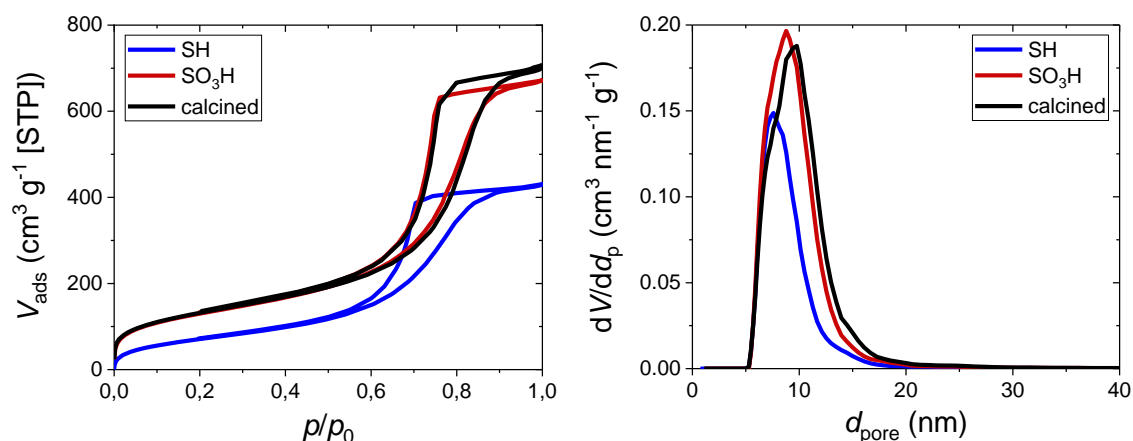


Figure 3.S2. Nitrogen physisorption isotherms (left) and pore size distributions (right) for sample P-1.7-S-1 in its respective modification: pristine (blue), oxidized/extracted (red) and calcined (black).

Table 3.S2. Influence of the extraction/oxidation step on the pore space properties as verified by nitrogen physisorption analysis.

Sample	$d_{\text{meso}} / \text{nm}$			$S_{\text{BET}} / \text{m}^2 \text{g}^{-1}$		
	SH ^a	SO ₃ H	calc.	SH ^a	SO ₃ H	calc.
P-1.7-S-1	8	9	10	273	469	479
P-1.7-S-0	26	–	26	167	–	195

^a The SH modification in the case of the reference material P-1.7-S-0 refers to the pure silica with the polymer still present.

Table 3.S3. Elemental analysis before and after hydrothermal treatment.

Sample	before			after		
	C / %	H / %	S / %	C / %	H / %	S / %
P-1.5-S-1	15.6	3.0	2.5	13.9	2.6	2.8
P-1.6-S-1	16.5	3.1	2.5	14.9	2.8	2.8
P-1.7-S-1	17.0	3.3	2.6	15.6	2.9	2.8
P-1.8-S-1	17.3	3.3	2.5	14.8	2.7	2.8

Table 3.S4. Efficiency of the extraction procedure. Comparison of reference material P-1.7-S-0 with the *in situ* functionalized sample P-1.7-S-1 based on elemental analysis.

Sample	reference			functionalized		
	C / %	H / %	S / %	C / %	H / %	S / %
P-1.7 (reference)	3.5	0.8	0.0	14.1	2.5	2.8
P-1.7_ext(2h)	1.1	0.7	0.0	3.9	1.5	2.8
P-1.7_ext(4h)	0.9	0.6	0.0	3.4	1.4	2.5
P-1.7_ext(6h)	0.8	0.6	0.0	2.9	1.3	2.0
P-1.7_ext(2h)-c	0.3	0.0	0.0	0.4	0.2	0.0
P-1.7_ext(4h)-c	0.1	0.0	0.0	0.1	0.0	0.0



Figure 3.S3. SEM-EDX images of the reference material P-1.7-S-0 in its respective modification: pristine (left), extracted (middle) and calcined (right).

The untreated pristine sample consists of 11 at.% (7.2 wt.%) C, 0.2 at.% (0.3 wt.%) S, 59 at.% (50 wt.%) O and 28 at.% (42 wt.%) Si (rounded values). After the extraction step, the detected composition of the sample is 1 at.% (0.6 wt.%) C, 0.2 at.% (0.3 wt.%) S, 61 at.% (48 wt.%) O and 36 at.% (50 wt.%) Si. Compared to the extracted sample, the calcined material has the same composition: 1 at.% (0.5 wt.%) C, 0.2 at.% (0.3 wt.%) S, 61 at.% (48 wt.%) O and 36 at.% (49 wt.%) Si.

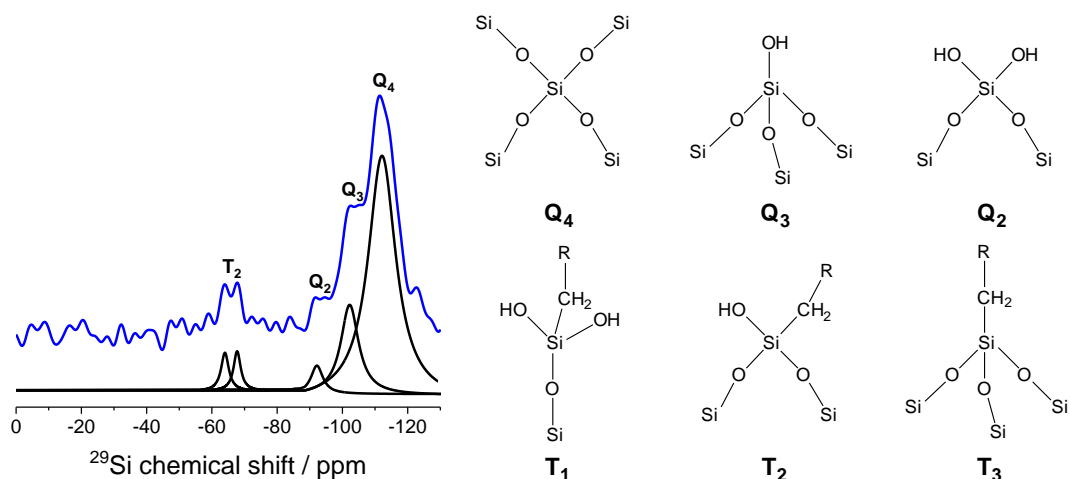


Figure 3.S4. Integrated HPDEC/MAS ^{29}Si NMR spectrum of the pristine sample P-1.7-S-1 (before the extraction step) and terminology for the silicon species.

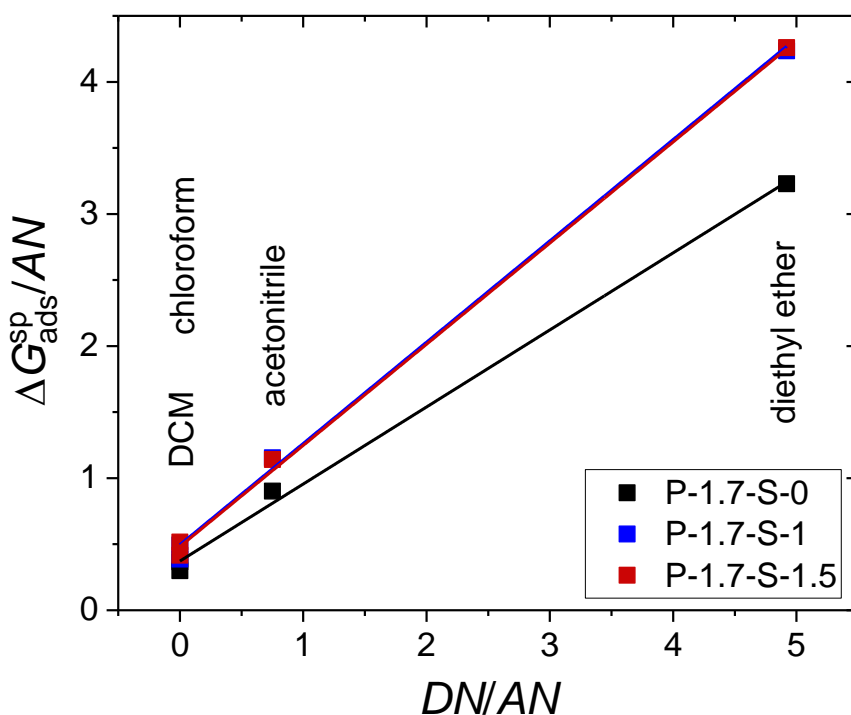


Figure 3.S5. Determination of the Lewis acid-base parameters K_A and K_D for the surfaces of non-functionalized (P-1.7-S-0) and sulfonic acid functionalized silica monoliths with different SO_3H loadings (P-1.7-S-1 and P-1.7-S-1.5) using Gutmann's approach (Equation (3.S1)).

The Lewis-acid parameter K_A is given by the slope of the linearized Gutmann plot, whereas the intercept with the vertical axis provides the Lewis-base parameter K_D :

$$\frac{\Delta G_{\text{ads}}^{\text{sp}}}{AN} = K_A \frac{DN}{AN} + K_D \quad (3.S1)$$

3.5.1 Determination of the total surface energy

The total surface energy γ_s^t has a dispersive (γ_s^d) and a specific (γ_s^{sp}) component. The dispersive component can be determined under IGC conditions of infinite dilution using *n*-alkane probe molecules, which then adsorb completely flat on the surface. The longer the hydrocarbon chain, the stronger the dispersive (also known as Lifshitz–van der Waals) interactions. The retention time t_N obtained with constant carrier-gas flow \dot{V} is a measure for the work of adhesion of the probe molecules and can be expressed by the retention volume V_N . Graphically, it is described as the volume necessary to purge the probe molecules from the column with respect to their individual adsorption-desorption equilibrium

$$V_N = \dot{V} j \left(\frac{T}{273.15 \text{ K}} \right) t_N \quad (3.S2)$$

where T denotes temperature and j the James–Martin mobile phase compressibility correction factor.^{S2} The retention volume V_N from Equation (3.S2) is used to calculate the free energy of adsorption ΔG_{ads} expressed as

$$\Delta G_{ads} = -RT \ln(V_N) + C \quad (3.S3)$$

where R is the universal gas constant and C is a constant that depends on a reference state for the adsorbed molecules (usually neglected in the determination of the free adsorption enthalpy). The slope of the *n*-alkane reference line (Figure 6), which characterizes the dependence of the free energy of adsorption on the number of CH₂ groups (the free energy of adsorption varies linearly with the number of carbon atoms^{S3,S4}) provides the dispersive component of the surface energy (γ_s^d) after using Equation (3.S4)

$$\gamma_s^d = \frac{[\Delta G_{ads}(\text{CH}_2)]^2}{4 N_A^2 (a_{\text{CH}_2}) \gamma_{\text{CH}_2}} \quad (3.S4)$$

where a_{CH_2} is the area of a methylene unit, N_A is Avogadro's constant and γ_{CH_2} is the surface energy of a solid based only on methylene units, *i.e.*, polyethylene.

The specific component of the surface energy can be calculated from interactions of polar probe molecules with the solid surface. These interactions have both specific (polar) and dispersive character. Therefore, as proposed by Donnet *et al.*,^{S5} the specific interaction parameter (ΔG_{ads}^{sp}) is determined by the difference between the free enthalpies of adsorption for the polar molecule (ΔG_{ads}) and the hypothetical or real *n*-alkane with the same topological index χ_T (ΔG_{ads}^d), which can be expressed as follows:

$$\Delta G_{ads}^{sp} = \Delta G_{ads} - \Delta G_{ads}^d \quad (3.S5)$$

The specific component of the surface energy (γ_s^{sp}) results from ΔG_{ads}^{sp} by applying the Van Oss theory,^{S6} leading to Equation (3.S6)

$$\Delta G_{\text{ads}}^{\text{sp}} = 2a_1N_A(\sqrt{\gamma_1^+ \gamma_s^-} + \sqrt{\gamma_1^- \gamma_s^+}) \quad (3.S6)$$

where a_1 is the cross-sectional area, γ_1^+ the Lewis-donor parameter and γ_1^- the Lewis-acceptor parameter of the probe molecule. The Lewis-acid (electron acceptor) parameter γ_s^+ and the Lewis-base (electron donor) parameter γ_s^- of the solid surface can be obtained with a nonlinear parameter approach presented in Bauer *et al.*^{S7} The calculation of γ_s^{sp} follows from Equation (3.S7) using both the Lewis-acid and the Lewis-base parameter and provides results in the same unit as the surface energy^{S8}

$$\gamma_s^{\text{sp}} = 2\sqrt{\gamma_s^+ \gamma_s^-} \quad (3.S7)$$

Finally, from the measured data, the resulting dispersive and specific components of the surface energy can be summed up, giving the total surface energy of the solid under study, as expressed by Equation (3.S8) (Table 4):

$$\gamma_s^{\text{t}} = \gamma_s^{\text{d}} + \gamma_s^{\text{sp}} \quad (3.S8)$$

Acknowledgement

The authors like to thank Niklas Olinski for preliminary lab studies.

References

- (1) K. Nakanishi, N. Tanaka, Sol-gel with phase separation. Hierarchically porous materials optimized for high-performance liquid chromatography separations. *Acc. Chem. Res.*, **2007**, *40*, 863–873.
DOI: 10.1021/ar600034p.
- (2) I. Tan, Z. Zarafshani, J.-F. Lutz, M.-M. Titirici, PEGylated chromatography: Efficient bioseparation on silica monoliths grafted with smart biocompatible polymers. *ACS Appl. Mater. Interfaces*, **2009**, *1*, 1869–1872.
DOI: 10.1021/am900461a.
- (3) A. Sachse, A. Galarneau, F. Fajula, F. Di Renzo, P. Creux, B. Coq, Functional silica monoliths with hierarchical uniform porosity as continuous flow catalytic reactors. *Microporous Mesoporous Mater.*, **2011**, *140*, 58–68.
DOI: 10.1016/j.micromeso.2010.10.044.
- (4) G. Hayase, K. Kugimiya, M. Ogawa, Y. Kodera, K. Kanamori, K. Nakanishi, The thermal conductivity of polymethylsilsesquioxane aerogels and xerogels with varied pore sizes for practical application as thermal superinsulator. *J. Mater. Chem. A*, **2014**, *2*, 6525–6531.
DOI: 10.1039/C3TA15094A.

-
- (5) E. Cuce, P. M. Cuce, C. J. Wood, S. B. Riffat, Toward aerogel based thermal superinsulation in buildings: A comprehensive review. *Renew. Sust. Energ. Rev.*, **2014**, *34*, 273–299.
DOI: 10.1016/j.rser.2014.03.017.
- (6) M. von der Lehr, C. F. Seidler, D. H. Taffa, M. Wark, B. M. Smarsly, R. Marshall, Proton conduction in sulfonated organic-inorganic hybrid monoliths with hierarchical pore structure. *ACS Appl. Mater. Interfaces*, **2016**, *8*, 25476–25488.
DOI: 10.1021/acsami.6b08477.
- (7) Y. G. Ko, H. J. Lee, J. Y. Kim, U. S. Choi, Hierarchically porous aminosilica monolith as a CO₂ adsorbent. *ACS Appl. Mater. Interfaces*, **2014**, *6*, 12988–12996.
DOI: 10.1021/am5029022.
- (8) A. Galarneau, A. Sachse, B. Said, C.-H. Péliesson, P. Boscaro, N. Brun, L. Courtheoux, N. Olivi-Tran, B. Coasne, F. Fajula, Hierarchical porous silica monoliths: A novel class of microreactors for process intensification in catalysis and adsorption. *C. R. Chimie*, **2016**, *19*, 231–247.
DOI: 10.1016/j.crci.2015.05.017.
- (9) H. Maleki, N. Hüsing, Current status, opportunities and challenges in catalytic and photocatalytic applications of aerogels: Environmental protection aspects. *Appl. Catal. B*, **2018**, *221*, 530–555.
DOI: 10.1016/j.apcatb.2017.08.012.
- (10) D. Enke, R. Gläser, U. Tallarek, Sol–gel and porous glass-based silica monoliths with hierarchical pore structure for solid-liquid catalysis. *Chem. Ing. Tech.*, **2016**, *88*, 1561–1585.
DOI: 10.1002/cite.201600049.
- (11) T. Müllner, K. K. Unger, U. Tallarek, Characterization of microscopic disorder in reconstructed porous materials and assessment of mass transport-relevant structural descriptions. *New J. Chem.*, **2016**, *40*, 3993–4015.
DOI: 10.1039/C5NJ03346B.
- (12) T. Noisser, G. Reichenauer, N. Hüsing, In situ modification of the silica backbone leading to highly porous monolithic hybrid organic-inorganic materials via ambient pressure drying. *ACS Appl. Mater. Interfaces*, **2014**, *6*, 1025–1029.
DOI: 10.1021/am404005g.
- (13) D. Stoeckel, C. Kübel, K. Hormann, A. Hölzel, B. M. Smarsly, U. Tallarek, Morphological analysis of disordered macroporous-mesoporous solids based on physical reconstruction by nanoscale tomography. *Langmuir*, **2014**, *30*, 9022–9027.
DOI: 10.1021/la502381m.
- (14) R. Kohns, C. P. Haas, A. Hölzel, C. Splith, D. Enke, U. Tallarek, Hierarchical silica monoliths with submicron macropores as continuous-flow microreactors for reaction kinetic and mechanistic studies in heterogeneous catalysis. *React. Chem. Eng.*, **2018**, *3*, 353–364.
DOI: 10.1039/C8RE00037A.

-
- (15) C. Xie, J. Hu, H. Xiao, X. Su, J. Dong, R. Tian, Z. He, H. Zou, Preparation of monolithic silica column with strong cation-exchange stationary phase for capillary electrochromatography. *J. Sep. Sci.*, **2005**, *28*, 751–756.
DOI: 10.1002/jssc.200400101.
- (16) A. El Kadib, R. Chimenton, A. Sachse, F. Fajula, A. Galarneau, B. Coq, Functionalized inorganic monolithic microreactors for high productivity in fine chemicals catalytic synthesis. *Angew. Chem. Int. Ed.*, **2009**, *48*, 4969–4972.
DOI: 10.1002/anie.200805580.
- (17) J. Timm, R. Marshall, A novel versatile grafting procedure: Toward the highest possible sulfonation degree of mesoporous silica. *Adv. Sustain. Syst.*, **2018**, *2*, 1700170.
DOI: 10.1002/adsu.201700170.
- (18) S.-J. Reich, A. Svidrytski, D. Hlushkou, D. Stoeckel, C. Kübel, A. Höltzel, U. Tallarek, Hindrance factor expression for diffusion in random mesoporous adsorbents obtained from pore-scale simulations in physical reconstructions. *Ind. Eng. Chem. Res.*, **2018**, *57*, 3031–3042.
DOI: 10.1021/acs.iecr.7b04840.
- (19) F. Bauer, S. Czihal, M. Bertmer, U. Decker, S. Naumov, S. Wassersleben, D. Enke, Water-based functionalization of mesoporous siliceous materials, Part 1: Morphology and stability of grafted 3-aminopropyltriethoxysilane. *Microporous Mesoporous Mater.* **2017**, *250*, 221–231.
DOI: 10.1016/j.micromeso.2016.01.046.
- (20) L. Yan, Q. Zhang, J. Zhang, L. Zhang, T. Li, Y. Feng, L. Zhang, W. Zhang, Y. Zhang, Hybrid organic-inorganic monolithic stationary phase for acidic compounds separation by capillary electrochromatography. *J. Chromatogr. A*, **2004**, *1046*, 255–261.
DOI: 10.1016/j.chroma.2004.06.024.
- (21) K. Nakanishi, Pore structure control of silica gels based on phase separation. *J. Porous Mater.*, **1997**, *4*, 67–112.
DOI: 10.1023/A:1009627216939.
- (22) K. Nakanishi, H. Komura, R. Takahashi, N. Soga, Phase separation in silica sol–gel system containing poly(ethylene oxide). I. Phase relation and gel morphology. *Bull. Chem. Soc. Jpn.*, **1994**, *67*, 1327–1335.
DOI: 10.1246/bcsj.67.1327.
- (23) A. Feinle, M. S. Elsaesser, N. Hüsing, Sol–gel synthesis of monolithic materials with hierarchical porosity. *Chem. Soc. Rev.*, **2016**, *45*, 3377–3399.
DOI: 10.1039/C5CS00710K.
- (24) R. Marschall, J. Rathousky, M. Wark, Ordered functionalized silica materials with high proton conductivity. *Chem. Mater.*, **2007**, *19*, 6401–6407.
DOI: 10.1021/cm071164i.
- (25) R. Marshall, I. Bannat, A. Feldhoff, L. Wang, G. Q. Lu, M. Wark, Nanoparticles of mesoporous SO₃H-functionalized Si-MCM-41 with superior proton conductivity. *Small*, **2009**, *5*, 854–859.

- DOI: 10.1002/sml.200801235.
- (26) R. Marschall, P. Tölle, W. L. Cavalcanti, M. Wilhelm, C. Köhler, T. Frauenheim, M. Wark, Detailed simulation and characterization of highly proton conducting sulfonic acid functionalized mesoporous materials under dry and humidified conditions. *J. Phys. Chem. C*, **2009**, *113*, 19218–19227.
DOI: 10.1021/jp904322y.
- (27) W. D. Bossaert, D. E. De Vos, W. M. Van Rhijn, J. Bullen, P. J. Grobet, P. A. Jacobs, Mesoporous sulfonic acids as selective heterogeneous catalysts for the synthesis of monoglycerides. *J. Catal.*, **1999**, *182*, 156–164.
DOI: 10.1006/jcat.1998.2353.
- (28) J.-P. Dacquin, A. F. Lee, K. Wilson, Pore-expanded SBA-15 sulfonic acid silicas for biodiesel synthesis. *Chem. Commun.*, **2012**, *48*, 212–214.
DOI: 10.1039/C1CC14563K.
- (29) C. Pirez, J.-M. Caderon, J.-P. Dacquin, A. F. Lee, K. Wilson, Tunable KIT-6 mesoporous sulfonic acid catalysts for fatty acid esterification. *ACS Catal.*, **2012**, *2*, 1607–1614.
DOI: 10.1021/cs300161a.
- (30) A. S. Dias, M. Pillinger, A. A. Valente, Dehydration of xylose into furfural over micro-mesoporous sulfonic acid catalysts. *J. Catal.*, **2005**, *229*, 414–423.
DOI: 10.1016/j.jcat.2004.11.016.
- (31) K. Wilson, A. F. Lee, D. J. Macquarrie, J. H. Clark, Structure and reactivity of sol–gel sulphonic acid silicas. *Appl. Catal. A*, **2002**, *228*, 127–133.
DOI: 10.1016/S0926-860X(01)00956-5.
- (32) L. Xu, H. K. Lee, Preparation, characterization and analytical application of a hybrid organic-inorganic silica-based monolith. *J. Chromatogr. A*, **2008**, *1195*, 78–84.
DOI: 10.1016/j.chroma.2008.04.068.
- (33) R. Kohns, N. Anders, D. Enke, U. Tallarek, Influence of pore space hierarchy on the efficiency of an acetylcholinesterase-based support for biosensorics. *Adv. Mater. Interfaces*, **2020**.
DOI: 10.1002/admi.202000163.
- (34) J. Patarin, Mild methods for removing organic templates from inorganic host materials. *Angew. Chem. Int. Ed.*, **2004**, *43*, 3878–3880.
DOI: 10.1002/anie.200301740.
- (35) K. A. Cychosz, R. Guillet-Nicolas, J. García-Martínez, M. Thommes, Recent advances in the textural characterization of hierarchically structured nanoporous materials. *Chem. Soc. Rev.*, **2017**, *46*, 389–414.
DOI: 10.1039/C6CS00391E.
- (36) R. S. Thakur, N. D. Kurur, P. K. Madhu, Swept-frequency two-pulse phase modulation for heteronuclear dipolar decoupling in solid-state NMR. *Chem. Phys. Lett.*, **2006**, *426*, 459–463.
DOI: 10.1016/j.cplett.2006.06.007.

- (37) N. Tanaka, H. Kobayashi, N. Ishizuka, H. Minakuchi, K. Nakanishi, K. Hosoya, T. Ikegami, Monolithic silica columns for high-efficiency chromatographic separations. *J. Chromatogr. A*, **2002**, *965*, 35–49.
DOI: 10.1016/s0021-9673(01)01582-5.
- (38) C. J. Brinker, G. W. Scherer, *Sol–Gel Science: The Physics and Chemistry of Sol–Gel Processing*, Academic Press, New York, **1990**.
- (39) F. Gritti, J. Hochstrasser, A. Svidrytski, D. Hlushkou, U. Tallarek, Morphology-transport relationships in liquid chromatography: Application to method development in size exclusion chromatography. *J. Chromatogr. A*, **2020**.
DOI: 10.1016/j.chroma.2020.460991.
- (40) F. Goettmann, C. Sanchez, How does confinement affect the catalytic activity of mesoporous materials? *J. Mater. Chem.*, **2007**, *17*, 24–30.
DOI: 10.1039/B608748P.
- (41) C. Yu, J. He, Synergic catalytic effects in confined spaces. *Chem. Commun.*, **2012**, *48*, 4933–4940.
DOI: 10.1039/C2CC31585H.
- (42) F. Ziegler, J. Teske, I. Elser, M. Dyballa, W. Frey, H. Kraus, N. Hansen, J. Rybka, U. Tallarek, M. R. Buchmeiser, Olefin methathesis in confined geometries: A biomimetic approach towards selective macrocyclization. *J. Am. Chem. Soc.*, **2019**, *141*, 19014–19022.
DOI: 10.1021/jacs.9b08776.
- (43) M. Thommes, K. Kaneko, A. V. Neimark, J. P. Olivier, F. Rodriguez-Reinoso, J. Rouquerol, K. S. W. Sing, Physisorption of gases, with special reference to the evaluation of surface area and pore size distribution (IUPAC Technical Report). *Pure Appl. Chem.*, **2015**, *87*, 1051–1069.
DOI: 10.1515/pac-2014-1117.
- (44) X. Ma, H. Sun, P. Yu, A novel way for preparing high surface area silica monolith with bimodal pore structure. *J. Mater. Sci.*, **2008**, *43*, 887–891.
DOI: 10.1007/s10853-007-2189-2.
- (45) D. Margolese, J. A. Melerio, S. C. Christiansen, B. F. Chmelka, G. D. Stucky, Direct Syntheses of ordered SBA-15 mesoporous silica containing sulfonic acid groups. *Chem. Mater.*, **2000**, *12*, 2448–2459.
DOI: 10.1021/cm0010304.
- (46) F. Freeman, C. N. Angeletakis, ^{13}C NMR chemical shifts of thiols, sulfinic acids, sulfinyl chlorides, sulfonic acids and sulfonic anhydrides. *Org. Magnet. Res.*, **1983**, *21*, 86–93.
DOI: 10.1002/omr.1270210204.
- (47) K. Yamamoto, A. Maruta, S. Shimada, Structure and molecular motion of poly(ethylene oxide) chains tethered on silica by solid-state ^{13}C NMR method. *Polym. J.*, **2001**, *33*, 584–589.
DOI: 10.1295/polymj.33.584.

- (48) W. Kolodziejski, J. Klinowksi, Kinetics of cross-polarization in solid-state NMR; A guide for chemists. *Chem. Rev.*, **2002**, *102*, 613–628.
DOI: 10.1021/cr000060n.
- (49) W. Lutz, D. Täschner, R. Kurzhals, D. Heidemann, C. Hübert, Characterization of silica gels by ^{29}Si MAS NMR and IR spectroscopic measurements. *Z. Anorg. Allg. Chem.*, **2009**, *635*, 2191–2196.
DOI: 10.1002/zaac.200900237.
- (50) T. Bein, R. F. Carver, R. D. Farlee, G. D. Stucky, Solid-state silicon-29 NMR and infrared studies of the reactions of mono- and polyfunctional silanes with zeolite Y surfaces. *J. Am. Chem. Soc.*, **1988**, *110*, 4546–4553.
DOI: 10.1021/ja00222a010.
- (51) M. Ide, M. El-Roz, E. De Canck, A. Vicente, T. Planckaert, T. Bogaerts, I. Van Driessche, F. Lynen, V. Van Speybroeck, F. Thybault-Starzyk, P. Van der Voort, Quantification of silanol sites for the most common mesoporous ordered silicas and organosilicas: total versus accessible silanols. *Phys. Chem. Chem. Phys.*, **2013**, *15*, 642–650.
DOI: 10.1039/c2cp42811c.
- (52) G. M. Dorris, D. G. Gray, Adsorption of *n*-alkanes at zero surface coverage on cellulose paper and wood fibers. *J. Colloid Interface Sci.*, **1980**, *77*, 353–362.
DOI: 10.1016/0021-9797(80)90304-5.
- (53) E. Brendlé, E. Papirer, A new topological index for molecular probes used in inverse gas chromatography for the surface nanorugosity evaluation. *J. Colloid Interface Sci.*, **1997**, *194*, 207–216.
DOI: 10.1006/jcis.1997.5104.
- (54) E. Brendlé, E. Papirer, A new topological index for molecular probes used in inverse gas chromatography. *J. Colloid Interface Sci.*, **1997**, *194*, 217–224.
DOI: 10.1006/jcis.1997.5105.
- (55) M. Rückriem, A. Inayat, D. Enke, R. Gläser, W.-D. Einicke, R. Rockmann, Inverse gas chromatography for determining the dispersive surface energy of porous silica. *Colloids Surf. A*, **2010**, *357*, 21–26.
DOI: 10.1016/j.colsurfa.2009.12.001.
- (56) V. Gutmann, Empirical parameters for donor and acceptor properties of solvents. *Electrochim. Acta*, **1976**, *21*, 661–670.
DOI: 10.1016/0013-4686(76)85034-7.
- (57) V. Gutmann, *The Donor-Acceptor Approach to Molecular Interactions*, Plenum Press, New York, **1978**.
- (58) F. L. Riddle, F. M. Fowkes, Spectral shifts in acid-base chemistry. 1. Van der Waals contributions to acceptor numbers. *J. Am. Chem. Soc.*, **1990**, *112*, 3259–3264.
DOI: 10.1021/ja00165a001.

-
- (59) E. Fekete, J. Móczó, B. Pukánsky, Determination of the surface characteristics of particulate fillers by inverse gas chromatography at infinite dilution: a critical approach. *J. Colloid Interface Sci.*, **2004**, *269*, 143–152.
DOI: 10.1016/S0021-9797(03)00719-7.
- (60) H. Grajek, J. Paciura-Zadrozna, Z. Witkiewicz, Chromatographic characterisation of ordered mesoporous silicas. Part II: Acceptor-donor properties. *J. Chromatogr. A*, **2010**, *1217*, 3116–3127.
DOI: 10.1016/j.chroma.2010.02.029.
- (61) C. F. Poole, *Gas Chromatography*, Elsevier, Oxford, 2012.
- (62) C. Saint Flour, E. Papirer, Gas-solid chromatography: a quick method of estimating surface free energy variations induced by the treatment of short glass fibers. *J. Colloid Interface Sci.*, **1983**, *91*, 69–75.
DOI: 10.1016/0021-9797(83)90314-4.
- (63) F. Bauer, R. Meyer, S. Czihal, M. Bertmer, U. Decker, S. Naumov, H. Uhlig, M. Steinhart, D. Enke, Functionalization of porous siliceous materials, Part 2: Surface characterization by inverse gas chromatography. *J. Chromatogr. A*, **2019**, *1603*, 297–310.
DOI: 10.1016/j.chroma.2019.06.031.
- (64) J. Lara, H. P. Schreiber, Specific interactions and adsorption of film-forming polymers. *J. Coating Technol.*, **1991**, *63*, 81–90.
- (S1) R. Kohns, C. P. Haas, A. Höltzel, C. Splith, D. Enke, U. Tallarek, Hierarchical silica monoliths with submicron macropores as continuous-flow microreactors for reaction kinetic and mechanistic studies in heterogeneous catalysis. *React. Chem. Eng.*, **2018**, *3*, 353–364.
DOI: 10.1039/C8RE00037A.
- (S2) A. T. James, A. J. P. Martin, Gas-liquid partition chromatography: the separation and micro-estimation of volatile fatty acids from formic acid to dodecanoic acid. *Biochem. J.*, **1952**, *50*, 679–690.
DOI: 10.1042/bj0500679.
- (S3) G. M. Dorris, D. G. Gray, Adsorption of *n*-alkanes at zero surface coverage on cellulose paper and wood fibers. *J. Colloid Interface Sci.*, **1980**, *77*, 353–362.
DOI: 10.1016/0021-9797(80)90304-5.
- (S4) B. Shi, Y. Wang, L. Jia, Comparison of Dorris-Gray and Schultz methods for the calculation of surface dispersive free energy by inverse gas chromatography. *J. Chromatogr. A*, **2011**, *1218*, 860–862.
DOI: 10.1016/j.chroma.2010.12.050.
- (S5) J. B. Donnet, S. J. Park, H. Balard, Evaluation of specific interactions of solid surfaces by inverse gas chromatography. *Chromatographia*, **1991**, *31*, 434–440.
DOI: 10.1007/BF02262385.
- (S6) C. J. Van Oss, M. K. Chaudhury, R. J. Good, Monopolar surfaces. *Adv. Colloid Interface Sci.*, **1987**, *28*, 35–64.

DOI: 10.1016/0001-8686(87)80008-8.

- (S7) F. Bauer, R. Meyer, S. Czihal, M. Bertmer, U. Decker, S. Naumov, H. Uhlig, M. Steinhart, D. Enke, Functionalization of porous siliceous materials, Part 2: Surface characterization by inverse gas chromatography. *J. Chromatogr. A*, **2019**, *1603*, 297–310.

DOI: 10.1016/j.chroma.2019.06.031.

- (S8) C. J. Van Oss, R. J. Good, M. K. Chaudhury, Additive and nonadditive surface tension compounds and the interpretation of contact angles. *Langmuir*, **1988**, *4*, 884–891.

DOI: 10.1021/la00082a018.

IV Conclusions and perspective

This cumulative dissertation includes three scientific studies dedicated to the concept of hierarchy and, more particular, with its characteristics and generation using the sol–gel process. The focus is on the understanding of the chemical and physical processes involved in the individual steps of the synthesis. The acquired expertise is used to highlight the qualities of hierarchically structured pore systems in the light of applications.

The first chapter enters the field of porous silica sol–gel materials in its variety of different pore structures. A suitable model system is introduced, which compares the macro–mesoporous support structure with the purely monomodal pore systems and illustrates when the advantages of hierarchy can be exploited. The substrate degradation reaction of acetylcholine to choline and acetic acid by acetylcholinesterase immobilized on the support surfaces shows that the mass transfer is strongly dependent on the macropore space and is also affected by its pore size. Consequently, a pore space hierarchy only has a beneficial impact when higher enzyme loadings are required, as it combines the highly permeable flow-through pores enabling advection-dominated transport with the large specific surface area for reaction due to the mesoporous domain. The second chapter reports on the synthesis of hierarchically structured, monolithic silica supports and the special role of urea in the sol–gel process. In addition to its usual role, which is the pore widening of the microporous skeleton into the range of mesopores due to decomposition to ammonia, urea exhibits a significant influence on the formation and size of the macroporous domain. Urea retards the phase separation more than gelation, so that an earlier state of spinodal decomposition is frozen, which yields smaller macropores and finer structural features. The resulting monoliths with submicron macropores can be used as continuous-flow microreactors due to a novel cladding procedure and subsequent functionalization. This allows to receive intrinsic reaction kinetics under quasi-homogeneous conditions for a Knoevenagel condensation test reaction, as external and internal diffusive transport limitations are eliminated. The third chapter focuses on a novel synthesis strategy for sulfonic acid functionalized hierarchical silica monoliths. Organic-inorganic hybrid materials are synthesized *via* co-condensation, whereby the macropore space is generated by the typical polymer-induced phase separation. The challenge of removing the polymer without loss of functionality is achieved by an extraction procedure that simultaneously creates sulfonic acid functions by oxidation of the introduced thiol groups, which results in an efficient and straightforward synthesis route. The confirmation of covalently bound surface functionalization and successful polymer extraction is verified by comprehensive characterization. Using inverse gas chromatography as a new approach, the acidity and surface energy changes of these hybrid materials upon sulfonic acid functionalization are documented.

All three studies demonstrate improved or novel synthesis strategies for the generation of hierarchically structured, monolithic silica materials. The individual steps of the monolith preparation, whether in the sol–gel process itself or in the post-treatments, have been refined,

saving time, costs and experimental efforts. These approaches have been used to create the tailor-made supports in terms of their porous properties, mechanical stability and handling. The understanding received in this way can be used for further scientific investigations, whether for basic research or technical applications. The following section offers an outlook with detailed perspectives and limitations for the overall methodology and the respective studies.

The preparation of the materials in all three studies is based on the sol–gel process, which can be divided into four general steps: (1) the sol–gel transition with concurrent, polymer-induced phase separation to form a micro–macroporous hydrogel; (2) enlargement of micropores to mesopores and reinforcement of the pore structure by hydrothermal treatment under basic conditions; (3) solvent exchange and drying, which should yield a dry, mechanically stable monolith; and (4) removal of the polymer located on the inner surface. This procedure is ideally suited for the preparation of porous materials with a wide range of characteristics. The properties can be specifically controlled by various modifications and thus adapted to the existing issue. The sol–gel process itself is extremely sensitive to parameter changes, so that even slight variations regarding, for example, gelation temperature, composition, polarity or pH affect the properties of the resulting monoliths. The synthesis duration can fluctuate greatly depending on the required porous characteristics, but in most cases the synthesis is completed within seven days. The synthesis routes described in chapters 1–3 protrude especially by their time and laboratory workload savings, whereby the hierarchical monoliths could be generated in less than four days. Particularly noteworthy at this point is the drying method presented in chapter 1 and generally used, enabling crack-free materials quickly and easily without extensive equipment. However, it is not always suitable. Small pores in the material can lead to tensions and cracks, especially if very small mesopores or even micropores are present, because the capillary stress during the drying process exceeds the stability of the pore network. By adjusting the drying conditions, as shown in chapter 3, even mesoporous systems with mean pore diameters of down to 7 nm can be dried stable, but this technique is reaching its limits. A solvent exchange, *e.g.*, from water to ethanol, can further reduce the capillary stress, which could help to dry crack-free monoliths with even smaller mesopores. Not only the external appearance of the prepared monoliths is of interest, above all the internal, porous properties are crucial for the interpretation of the collected reaction data. In all three studies rod-shaped monoliths with a length of up to 9 cm were synthesized. The porosity data from mercury porosimetry or nitrogen physisorption always indicate only the mean pore sizes of a small fraction of the rod. During synthesis, inhomogeneities can occur over the length of the rod, resulting in different porous properties within the monolith. Although the homogeneity of the materials was investigated and this was given within the scope of minor deviations, but defects cannot be completely excluded.

In all cases tetraethyl orthosilicate was selected to form the silica backbone. This chemical is relatively cheap, and the ethanol produced by hydrolysis is almost harmless. Nevertheless, it would also be possible to resort to the much lower-priced precursor water glass, especially if

this is obtained from a biogenic silica source like rice husk. This would be reasonable considering sustainability, bearing in mind that the synthesis conditions have to be adjusted due to the new educt. Additionally, alumina precursors could be used to generate aluminosilicates with Brønsted acid sites and create a catalytic active material without further modification.

Moreover, different inorganic, hierarchically structured materials could be considered. Porous carbon materials can be easily made by nanocasting strategy, a replica procedure, where a porous silica material is impregnated with a carbon precursor, followed by carbonization under non-oxidizing conditions. A macro–mesoporous carbon results of the silica monolith as positive replica on micrometer scale and negative replica on nanometer scale. Another possibility are porous glasses, which are mainly characterized by their mechanical stability. They can also be post-synthetically functionalized and used in heterogeneous catalysis, sensorics or chemical separation processes. The pore sizes can be controlled within the range of meso- and macropores, whereby the upper limit of macropores is reached much earlier than in the case of sol–gel materials. The hierarchy is created by pseudomorphic transformation, which causes in an additional mesopore space inside the originally nonporous glass walls. But the manufacturing of these glasses is very time consuming and tempering steps at high temperatures are necessary.

In chapter 2, a new cladding technique was developed to ensure an immaculate housing of the monoliths in order to use them as continuous-flow microreactors. This method was also applied in Chapter 3 to characterize the SO₃H functionalized monoliths using IGC. In contrast to the wrappings in glass, PTFE or PEEK tubes, which are widely reported in the literature, this procedure is a great advance, as it can withstand back pressures of >100 bar and thus even monoliths with submicron macropores can be investigated in flow-through mode. But there are also limitations for columns produced in this fashion. Especially the used epoxy resin adhesive provides a degree of defects. On the one hand, it tends to soften at a temperature of 100 °C, which means that certain reactions or studies with temperature variations are not practicable. Secondly, the epoxy resin adhesive is not stable against all solvents. With chlorinated solvents, such as chloroform or dichloromethane, it becomes brittle after long process times, which can cause leaking during flow experiments. During the housing process, small air bubbles could occur at the interface to the monolith, causing defects after hardening and thus the possibility of dead volumes. Furthermore, the construction of the column requires conventional machine processing, without this it would be difficult to produce a perfect column. Lastly, the length of the column would only be variable within a certain range. Due to the zero-volume reducing unions from Swagelok, the minimum required length of the monolith is 4.5–5 cm whilst the maximum length is limited by the synthesis.

All three studies have in common that the prepared porous materials have been functionalized either post-synthetically or *in situ* to obtain a catalytically active surface. The *in situ* functionalization has the advantage that the inserted active sites are homogeneously distributed over the monolith and strongly bound due to the co-condensation process, which also saves

laboratory workload. Post-synthetic functionalization always has the downside that the homogeneous distribution of the organic groups cannot always be guaranteed. With regard to the stop-flow functionalization mentioned in chapter 2, it would be likely that the condensation reaction starts earlier at the inlet and thus a concentration gradient of the active centers over the column length occurs. Although this has been addressed by cooling and a fast flow rate, this appearance cannot be excluded. Nevertheless, the characterization of this functionalization is still challenging, which is especially the case for quantification. In any study, elemental analysis was chosen, which is well suited to determine the mass fractions of certain elements, allowing the overall number of catalytic centers to be calculated. However, it does not give any information about the availability of these catalytically active sites. Even the consulted SEM-EDX analysis only allows conclusions about the elemental distribution on the silica surface.

Chapter 1 focused on the investigation of hierarchy in a porous system compared with monomodal pore structures. This study laid the foundation for the following chapters, as it was demonstrated for the first time how hierarchical pore networks enhance mass transfer and diffusion dependent processes by combination of functionality and transport efficiency. This was proven by the response times and resulting apparent reaction rates of the degradation reaction of acetylcholine to choline and acetic acid by the immobilized acetylcholinesterase, but these parameters are preceded by the assumptions of the indirect Lineweaver-Burk interpretation, because the direct Michaelis-Menten relationship was not valid. In addition, the apparent reaction rate was calculated back *via* the produced amount of acetic acid, which in total represents a few sources of error. Looking ahead, these studies should be transferred to the flow-through design of chapter 2. Then, due to pressure-driven flow through the hierarchical material, transport in macropores moves from diffusion-limited to advection-dominated and pure diffusion takes place only inside the thin mesoporous skeleton. This operation will allow to move from the apparent to the intrinsic reaction kinetics (as transport limitations are removed) and access parameters like the reaction order, rate constants, and activation energies. The comparison with the purely macroporous material in a continuous-flow application would also substantiate the presented conclusions.

In chapter 2, a new approach was reported, which describes the investigation of specially prepared hierarchical silica monoliths in a flow-through application including novel cladding and functionalization. For the synthesis of the porous monoliths urea was used as pore size controlling agent, whereby in addition to the usual mesopore widening, the macro pore size was adjusted. Urea was simply added to the aqueous starting solution in varying amounts to imply a homogeneous distribution in the later gel. The effect of urea on the macroporous domain has not been described so far and is due to the influence on the onset of gelation and phase separation. However, in order to completely exclude any other aspects, the different amounts of urea have to be dissolved in the same amount of water. Using the same volumes of these different concentrated aqueous urea solutions for the synthesis would be more accurate, because no volume changes would bias the sol formation.

The low activation energy ($E_a = 19.7 \text{ kJ mol}^{-1}$) obtained for the heterogeneously-catalyzed Knoevenagel condensation in chapter 2 compared to the literature reflects the near-instant access of the reactants to the large, active surface area of the monolithic microreactor. Consequently, the excellent transport properties of the prepared hierarchical silica monolith with submicron structural features enable quasi-homogeneous catalysis in continuous-flow mode with a high-performance fixed-bed support. However, it should be noted that the high surface area is not only accessible for the catalytic reaction but also for adsorption processes, which can distort the received data. In addition, the high surface hinders lateral heat transport. If highly concentrated solutions or highly exothermic reactions are used, the reaction heat can only be removed in the longitudinal flow direction. This could result in the formation of hotspots on the reactor, which in turn accelerates deactivation of the catalyst and thus limits productivity and reproducibility of the chemical process. This issue could be overcome by increasing the shared surface of the fixed-bed with the reactor walls. Nonetheless, this study opens the field for many other applications including, for example, much faster reactions than the Knoevenagel condensation adapted here, the use of smaller intraskeleton mesopores or even micropores, or the immobilization of enzymes with respect to chapter 1, *e.g.*, with wider mesopores ($>20 \text{ nm}$), which will also allow a relatively unimpeded transport, in general, of bulkier molecules and species, like peptides and proteins, or even metal clusters and nanoparticles. Furthermore, a study comparing monolithic fixed-beds with particular fixed-beds with different particle sizes and porosity (fully porous core-shell particles) in this continuous-flow design considering loading capacity, transport limitations, and hydraulic permeability would be an upgrade. By means of an extreme fast reaction, the Thiele-Moduli is increased in such a way that no reaction limitation exists and the performance would not be restricted by diffusive transport.

Chapter 3 presents a novel synthesis strategy for the preparation of sulfonic acid functionalized, hierarchical silica monoliths. The principle of co-condensation was utilized to incorporate the functional groups directly into the silica network, ensuring homogeneous distribution. The challenge of this route is that the polymer necessary for phase separation in the sol-gel process must be removed from the porous system without losing its functionalization. The usual calcination is not applicable for materials functionalized *via* co-condensation, as it pyrolyzes any organic matter. Therefore, an extraction procedure was implemented which removes the template (PEO) from the pore network in a mild manner and simultaneously converts the thiol groups introduced into the porous system to the targeted sulfonic acid functions. Altogether, this study demonstrates that the co-condensation approach offers a simple, efficient route to functionalized, hierarchical sol-gel materials. Nevertheless, there are also certain limitations for this method. The results reveal that the SO_3H loadings can be adjusted within a defined range ($1.1\text{--}1.3 \text{ groups/nm}^2$) and, according to the literature, are higher compared to post-synthetic functionalization. It was found that increasing the (3-mercaptopropyl)-trimethoxysilane (MPTMS) concentration is only beneficial only up to a specific point, but this investigation did not go into further detail. At this point, smaller intervals in the MPTMS

concentration should be considered and the concentration should be raised to clearly substantiate this trend. In the hydrolyzed state, silica gels have 4–6 silanol groups/nm², which can all be eligible for binding functionalization reagents. It therefore remains unanswered why only a maximum of 1.3 SO₃H groups/nm² could be generated on the surface and why the loading could not be enhanced more. In addition, a systematic investigation concerning the mesopore control would be conceivable. As shown, very narrow pore size distributions in the range from 7–9 nm could be obtained. It would be reasonable to vary the time of the hydrothermal treatment or to change the urea content in order to reach further differentiations in the mean mesopore size. In this context, the influence on the SO₃H load has to be examined too.

With IGC, a characterization technique for functionalized sol–gel monoliths was introduced that can describe the surface characteristics of the material in a new manner. The data showed that the total surface energy differed drastically from that of pure silica due to the SO₃H groups incorporated on the surface, and in addition an acidity gain due to the functionalization could be observed. It should be noted that the measurements were carried out at 80 °C and this temperature led to very long retention times and strong peak broadening for a couple of probe molecules. This complicated the evaluation of the data and, as a result, a certain error tolerance was assumed. With higher temperatures this phenomenon could be reduced, but the housing or especially the epoxy resin adhesive reaches its limit at 100 °C. Furthermore, the results of acid strength should be compared to findings of usual characterization techniques such as the temperature-programmed desorption of ammonia or pyridine in order to provide a reliable prediction of the surface acidity. Additional experiments could be performed to calculate adsorption isotherms and distribution functions of the adsorption energy.¹ From the adsorption isotherms, several information can be derived such as BET surface area and energetic heterogeneity. The assessed specific surface area (after applying BET linearization) can be compared to nitrogen physisorption data.

Chapter 3 introduces an excellent method for the preparation of SO₃H-modified silica monoliths, but this study refers exclusively to the synthesis. It is evident that these materials have to prove their ability. The generated hybrid monoliths are primarily useful for processes involving ion exchange, acid catalysis or proton conduction, where morphological properties like macropore size and surface area will be easily adjusted in addition to the dispersion of the SO₃H groups. However, their narrow mesopore size distribution further helps in applications that benefit from size-selective transport like chromatographic (*e.g.*, biomolecular) separations or catalysis under spatial confinement. With respect to chapter 2, the cladding approach applied to the monolithic rods for IGC analysis offers a robust column design for their convenient use as a continuous-flow microreactor. For SO₃H-catalyzed reactions intrinsic reaction kinetics can be determined or, by comparison with post-synthetically functionalized monoliths, the loading capacity, transport and diffusion limitations and hydrodynamic permeability can be investigated.

Another interesting approach would be to determine the attributes of the hierarchy and the influence of tortuosity in general by an appropriate test reaction.² Since the pore system yields homogeneously distributed active centers through this synthesis protocol, which were directly incorporated into the pore network and not subsequently grafted onto the surface, it is an ideal model for such investigations. The surface area was not subsequently changed and the cluster formation of functionalization groups was largely prevented. If all parameters regarding specific surface area, active site loading and porosity can be set constant and the macropore and/or mesopore size can be adjusted separately, changes in the kinetic data are only due to the variation of the pore size. Thus, the pore systems can be characterized and interpreted in a completely innovative way, and overall, this would create a very challenging field for the characterization of hierarchy.

However, a number of requirements have to be fulfilled to ensure this future approach. First, as already mentioned, the pore sizes have to be variable independently from the other properties. This is challenging, since the specific surface area and thus also the loading capacity of active sites are strongly dependent on the pore sizes, especially the mesopores. Moreover, the test reaction must be very fast and the reaction sequence should be able to be analyzed by the given instrumentation. The detection in chapter 2 was done with an inline diode-array detector, which means that the reaction must be UV-active. For very fast reactions, enzyme-catalyzed reactions would also be suitable, with attention to chapter 1. But the substrate degradation reaction using acetylcholinesterase is not UV-active and, in addition, the surface would be subsequently modified by the enzyme immobilization. A possibility for this investigations could be the reaction illustrated in Figure IV.1.

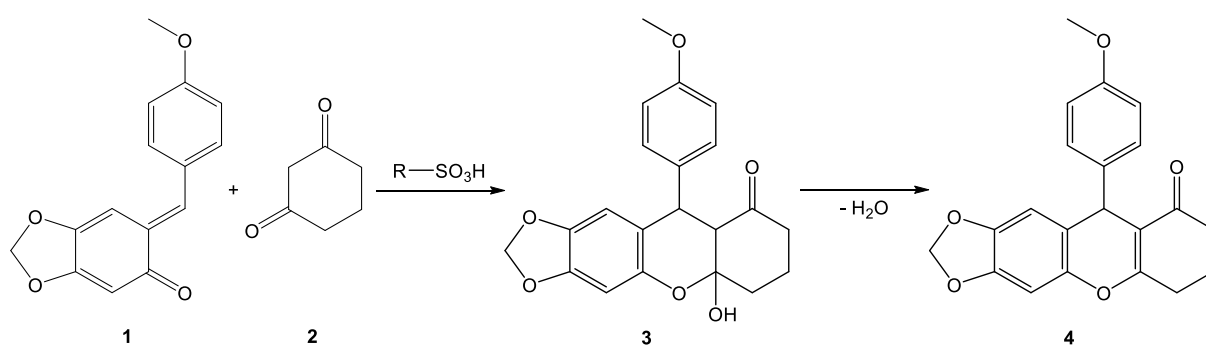


Figure IV.1. SO₃H-catalyzed (Brønsted acid) test reaction for characterization of hierarchical pore systems: Reaction of an *ortho*-quinone methide species **1** with 1,3-cyclohexanedione **2** results in a tetrahydroxanthenone **4** via a hemiacetalic intermediate **3**.

This reaction describes the synthesis of a 4-aryl-4*H*-chromene species. Molecules with chromene or xanthenone structures are widely found in natural products and used in many pharmacologically active substances with cytotoxic, anti-inflammatory, antibacterial, antiviral and antioxidant effects.³ The reaction proposed here is based on the reaction of an *ortho*-quinone methide **1**, which is formed *in situ* from an *ortho*-hydroxybenzyl alcohol, with 1,3-cyclohexanedione **2** to yield an hemiacetalic intermediate **3**. In a second step this intermediate

reacts under dehydration to a tetrahydroxanthenone species **4**. This reaction is worth considering because the *ortho*-quinone methide illustrated here is the only known bench stable agent of this substance class and is also the only colored one. The first reaction step to the intermediate is usually very fast using chiral binol-based phosphoric acids.³ The yellow intermediate is formed in a very short time (less than 5 min) from the deep orange or amber-colored educt (Figure IV.2). In the second reaction step, the solution gradually decolorizes to a weak yellow, whereby the reaction takes several hours. In conclusion, this is a fast, Brønsted-acid-catalyzed reaction with UV-active educt and product, which would satisfy all necessary conditions.

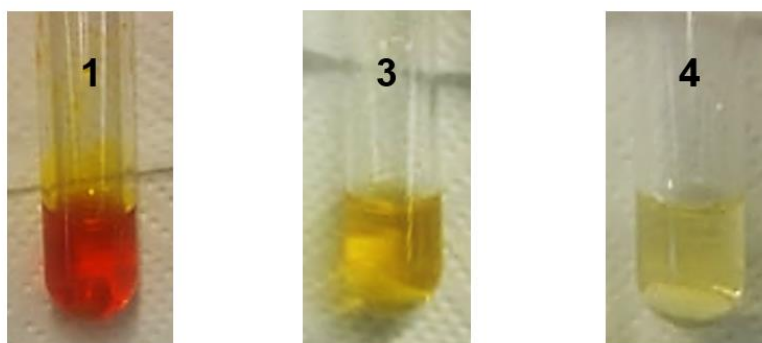


Figure IV.2. Preliminary investigations on the sequence of the considered test reaction (*cf.* Figure IV.1) of an *ortho*-quinone methide species **1** with 1,3-cyclohexanedione to a tetrahydroxanthenone **4** via a hemiacetalic intermediate **3** with SO₃H-functionalized silica granulate according to the synthesis protocol of chapter 3.

Preliminary investigations demonstrated that this reaction can also occur with the SO₃H-modified materials described in chapter 3. Before flow experiments can be started, however, a number of questions must be clarified. On the one hand, a suitable solvent is needed for the reaction, which enables both a fast reaction and does not damage the cladding. Moreover, it turned out that in some solvents the reaction was already autocatalytic, which would pose a major problem for later quantification. As usual in preparative organic synthesis, the change of solvents can affect the reaction rate. This in turn could cause a reduction in the speed of reaction and thus disqualify this approach for the intended application.

In summary, the presented work plays a major role in better understanding and applying the sol-gel process. By means of smart and straightforward synthesis routes, hierarchical pore structures could be better highlighted and exhibit their potential in reaction technology operations. The combination of material synthesis and applications allowed for the combination of preparative and instrumental chemistry. These studies are intended to contribute to the further advancement of these materials, which are beneficial in many ways, and to place them in the focus of many scientific disciplines.

References

- (1) F. Bauer, R. Meyer, S. Czihal, M. Bertmer, U. Decker, S. Naumov, H. Uhlig, M. Steinhart, D. Enke, Functionalization of porous siliceous materials, Part 2: Surface characterization by inverse gas chromatography. *J. Chromatogr. A*, **2019**, *1603*, 297–310.
DOI: 10.1016/j.chroma.2019.06.031.
- (2) D. Enke, F. Friedel, T. Hahn, F. Janowski, Transport properties of catalyst supports derived from catalytic test reaction. *Stud. Surf. Sci. Catal.*, **2007**, *160*, 455–462.
DOI: 10.1016/S0167-2991(07)80059-0.
- (3) O. El-Sepelgy, S. Haseloff, S. K. Alamsetti, C. Schneider, Brønsted-Säure-katalysierte konjugierte Addition von β -Dicarbonylverbindungen an in situ erzeugte *ortho*-Chinomethide – enantioselektive Synthese von 4-Aryl-4*H*-chromenen. *Angew. Chem.*, **2014**, *126*, 8057–8061.
DOI: 10.1002/ange.201403573.

V Appendix

V.I Curriculum Vitae

Persönliche Details

Name: Richard Kohns
Geburtsdatum: 17.10.1992
Geburtsort: Nordhausen
Nationalität: Deutsch

Ausbildung

01/2017 – heute Philipps-Universität Marburg (Marburg, Deutschland)
Promotion Chemie
Fachbereich Chemie, Prof. Dr. U. Tallarek

10/2014 – 11/2016 Universität Leipzig (Leipzig, Deutschland)
M.Sc. Chemie

10/2011 – 09/2014 Universität Leipzig (Leipzig, Deutschland)
B.Sc. Chemie

8/2002 – 06/2011 Herder-Gymnasium (Nordhausen, Deutschland)
Abitur

V.II Publikationsverzeichnis

- [1] C. P. Haas, T. Müllner, R. Kohns, D. Enke, U. Tallarek
“High-performance monoliths in heterogeneous catalysis with single-phase liquid flow”
React. Chem. Eng., **2017**, 2, 498–511. DOI: 10.1039/c7re00042a.
- [2] R. Kohns, C. P. Haas, A. Höltzel, C. Splith, D. Enke, U. Tallarek
“Hierarchical silica monoliths with submicron macropores as continuous-flow microreactors for reaction kinetic and mechanistic studies in heterogeneous catalysis”
React. Chem. Eng., **2018**, 3, 353–364. DOI: 10.1039/c8re00037a.
- [3] S. Yismaw, R. Kohns, D. Schneider, D. Poppitz, S. G. Ebbinghaus, R. Gläser, U. Tallarek, D. Enke
“Particle size control of monodispersed spherical nanoparticles with MCM-48-type mesostructure via novel rapid synthesis procedure”
J. Nanopart. Res., **2019**, 21, 258. DOI: 10.1007/s11051-019-4699-7.
- [4] T. I. Kwindt, S. Koppka, S. A. H. Sander, R. Kohns, D. Enke
“Effect of Al₂O₃ on phase separation and microstructure of R₂O-B₂O-Al₂O₃-SiO₂ glass system (R=Li, Na)”
J. Non-Cryst. Solids, **2020**, 531, 119849. DOI: 10.1016/j.jnoncrysol.2019.119849.
- [5] P. Hou, R. Kumar, B. Oberleiter, R. Kohns, D. Enke, U. Beginn, H. Fuchs, M. Hirtz, M. Steinhart
“Scanner-based capillary stamping”
Adv. Funct. Mater., **2020**, *accepted*. DOI: 10.1002/adfm.202001531.
- [6] R. Kohns, N. Anders, D. Enke, U. Tallarek
“Influence of Pore Space Hierarchy on the Efficiency of an Acetylcholinesterase-Based Support for Biosensors”
Adv. Mater. Interfaces, **2020**, *accepted*. DOI: 10.1002/admi.202000163.
- [7] H. R. N. B. Enniful, D. Schneider, R. Kohns, D. Enke, R. Vaiullin
“A novel approach for advanced thermoporosimetry characterization of mesoporous solids: Transition kernels and the serially connected pore model”
Microporous Mesoporous Mater., **2020**, *submitted*.
- [8] R. Kohns, R. Meyer, M. Wenzel, J. Matysik, D. Enke, U. Tallarek
“*In situ* synthesis and characterization of sulfonic acid functionalized hierarchical silica monoliths”
J. Sol-Gel Sci. Technol., **2020**, *submitted*.

V.III Erklärungen

Erklärung der Eigenleistung

Die vorliegende Dissertation mit dem Titel „Understanding sol–gel processing: Hierarchical silica monoliths towards applications in chemical reaction engineering“ wurde von mir, Herrn Richard Kohns, eigenständig angefertigt. Die Kapitel 1–3 basieren auf wissenschaftlichen Fachartikeln, die in Kooperation mit verschiedenen Koautoren verfasst wurden. Nachfolgend sind die Beiträge der einzelnen Koautoren für jedes Kapitel aufgeführt.

Kapitel 1

R. Kohns, N. Anders, D. Enke, U. Tallarek

Adv. Mater. Interfaces, **2020**, accepted on 26 March. DOI: 10.1002/admi.202000163

R. Kohns wirkte an wissenschaftlichen Untersuchungen, an der Beschreibung der Trocknungsmethode, der Datenanalyse sowie der Ausarbeitung, dem Review und der Editierung des Manuskripts mit. Dr. N. Anders erbrachte einen großen Anteil an den wissenschaftlichen Untersuchungen, der Konzepterstellung und der Methodologie. Prof. Dr. Dirk Enke trug wesentlich zur Konzepterstellung, der Bereitstellung wissenschaftlicher Ressourcen und Materialien, der Ausarbeitung des Manuskripts sowie an der Supervision bei. Einen wichtigen Beitrag zur Ausarbeitung des Manuskripts, dem Reviewprozess sowie an der Supervision erbrachte Prof. Dr. Ulrich Tallarek.

Kapitel 2

R. Kohns, C. P. Haas, A. Höltzel, C. Splith, D. Enke, U. Tallarek

React. Chem. Eng., **2018**, 3, 353–364. DOI: 10.1039/c8re00037a

Die Materialsynthese und -charakterisierung sowie die Entwicklung des Housing-Prozesses als auch die Ausarbeitung des Konzepts, der Methodik und des Manuskripts erfolgte durch Richard Kohns. Christian P. Haas erbrachte einen großen Anteil an der Ausarbeitung des Housing-Prozesses, des Konzepts und der Methodik, der Ausführung und Auswertung der HPSLC-Methodik, am Manuskriptdesign sowie am Reviewprozess. Christian Splith half bei wissenschaftlichen Untersuchungen und der Beschreibung der pH-abhängigen Phasenseparation. Dr. Alexandra Höltzel hatte einen großen Anteil an der Niederschrift des Manuskripts. Während Prof. Dr. Dirk Enke einen wichtigen Beitrag bei der Mitwirkung der Konzepterstellung, der Supervision und Bereitstellung von Materialien und Ressourcen leistete, erarbeitete Prof. Dr. Ulrich Tallarek das Konzept, stellte ebenfalls wissenschaftliche Mittel bereit und wirkte beim Review- und Editierungsprozess sowie an der Supervision mit.

Kapitel 3

R. Kohns, R. Meyer, M. Wenzel, J. Matysik, D. Enke, U. Tallarek
J. Sol-Gel Sci. Technol., **2020**, submitted.

Die wissenschaftlichen Untersuchungen, die Materialsynthese und -charakterisierung, die Ausarbeitung des Konzepts, der Methodik und des Manuskripts sowie dessen Review und Editierung erfolgten durch R. Kohns. R. Meyer half bei den wissenschaftlichen Untersuchungen mittels Inverser Gas Chromatographie und dessen Auswertung. M. Wenzel war verantwortlich für die Ausführung und Auswertung der MAS NMR Spektroskopie. Prof. Dr. Jörg Matysik wirkte an der Auswertung und Interpretation der MAS NMR Spektren mit. Prof. Dr. Dirk Enke wirkte bei der Konzepterstellung, der Bereitstellung wissenschaftlicher Ressourcen und Materialien sowie an der Supervision mit, während Prof. Dr. Ulrich Tallarek einen wichtigen Beitrag an der Konzepterstellung, dem Review und der Editierung des Manuskripts sowie an der Supervision leistete.

(Ort, Datum, Unterschrift des Promovierenden)

(Ort, Datum, Unterschrift des Betreuers)

Erklärung des selbstständigen Verfassens

Hiermit versichere ich, dass ich die vorgelegte Dissertation mit dem Titel

“Understanding sol–gel processing: Hierarchical silica monoliths towards applications in chemical reaction engineering”

selbstständig und ohne fremde Hilfe verfasst, keine anderen als die in ihr angegebenen Quellen oder Hilfsmittel benutzt, alle vollständig oder sinngemäß übernommenen Zitate als solche gekennzeichnet sowie die Dissertation in der vorliegenden oder einer ähnlichen Form noch bei keiner anderen in- oder ausländischen Hochschule anlässlich eines Promotionsgesuchs oder zu anderen Prüfungszwecken eingereicht habe.

Ich erkläre außerdem, dass eine Promotion noch an keiner anderen Hochschule als der Philipps-Universität Marburg versucht wurde.

Ort/Datum

Unterschrift
(Vor- und Nachname)

